



# Optical properties of point defects in hexagonal boron nitride

Thomas Pelini

## ► To cite this version:

Thomas Pelini. Optical properties of point defects in hexagonal boron nitride. Physics [physics]. Université Montpellier, 2019. English. NNT : 2019MONTS139 . tel-02986321v2

**HAL Id: tel-02986321**

**<https://tel.archives-ouvertes.fr/tel-02986321v2>**

Submitted on 3 Nov 2020

**HAL** is a multi-disciplinary open access archive for the deposit and dissemination of scientific research documents, whether they are published or not. The documents may come from teaching and research institutions in France or abroad, or from public or private research centers.

L'archive ouverte pluridisciplinaire **HAL**, est destinée au dépôt et à la diffusion de documents scientifiques de niveau recherche, publiés ou non, émanant des établissements d'enseignement et de recherche français ou étrangers, des laboratoires publics ou privés.

# THÈSE POUR OBTENIR LE GRADE DE DOCTEUR DE L'UNIVERSITÉ DE MONTPELLIER

En Physique

École doctorale I2S - Information, Structures, Systèmes

Unité de recherche UMR 5221

## Optical properties of point defects in hexagonal boron nitride

Présentée par Thomas PELINI  
Le 20 décembre 2019

Sous la direction de Guillaume CASSABOIS  
et Vincent JACQUES

Devant le jury composé de

Christophe CHAUBET, Professeur des Universités, L2C-Montpellier

Jean-Sébastien LAURET, Directeur de recherche, LAC-Paris

Abdelkarim OUEGHI, Directeur de recherche, C2N-Paris

Alberto ZOBELLI, Professeur des Universités, LPS-Paris

Clément FAUGERAS, Directeur de recherche, LNCMI-Grenoble

Vincent JACQUES, Directeur de recherche, L2C-Montpellier

Guillaume CASSABOIS, Professeur des Universités, L2C-Montpellier

Président du jury

Rapporteur

Rapporteur

Examineur

Examineur

Co-directeur de thèse

Directeur de thèse



UNIVERSITÉ  
DE MONTPELLIER



*À mon grand-père,  
Mes parents, ma soeur.*



## Remerciements

Le travail de recherche présenté dans ce manuscrit a été élaboré au sein de l'équipe NQPO au laboratoire Charles Coulomb à Montpellier, dont je remercie le directeur du laboratoire Pierre LEFEBVRE de m'avoir accueilli, et également tout le personnel administratif compétent sur qui j'ai pu compter ces trois années. Merci à Béatrice TOMBERLI, particulièrement pour mon installation dans l'équipe, à Jean-Christophe ART pour sa gestion impeccable de toutes les missions que j'ai effectuées, Stéphanie MARTEGOUTES pour les nombreuses commandes qui furent nécessaires à la construction du microscope, et enfin Christelle EVE et Régine PAUZAT ainsi que Patrick EJARQUE dont je garderai le souvenir de son goût pour la poésie. Je remercie aussi spécialement Lucyna FIRLEJ qui a su gérer les urgences de fin de thèse.

Mes remerciements vont en premier lieu à mes directeurs de thèse Vincent JACQUES et Guillaume CASSABOIS, pour m'avoir donné l'opportunité de travailler sur ce sujet et dans cette équipe, grandissante au fil de ma thèse, dans cette belle ville du Sud où le soleil trouve rarement refuge derrière un nuage. Si mon projet de thèse a été mené à bien, je le dois en grande partie à eux, qui ont tout fait pour que l'on puisse toujours avancer malgré les embûches techniques qui ont parsemé l'élaboration du microscope confocal dans l'UV. Je vous remercie chaleureusement pour votre encadrement empreint d'une disponibilité sans failles. Merci pour votre rigueur scientifique et remarques pertinentes ainsi que la richesse des discussions que l'on a pu avoir, cela a guidé mes pas jusqu'à la rédaction de mon manuscrit, et j'emporte précieusement ces apprentissages pour la suite de mon parcours. J'ai eu un plaisir ineffable à travailler dans l'équipe avec tous les autres étudiants et postdoc, et je sais que l'intelligence sociale que vous avez pour doser confiance, détente et sérieux y est pour beaucoup. Je veux aussi remercier à cet égard Isabelle PHILIP ainsi que Bernard GIL, à qui je dois aussi énormément pour ma recherche et son aide dans les derniers instants.

Au cours de mon doctorat, j'ai passé un temps considérable en salle de manip, et si j'ai acquis des méthodes rigoureuses en alignement optique, je le dois en partie à Anais DREAU qui m'a enseigné les secrets des techniques expérimentales, et ce avec une précision chirurgicale. Ce fut un réel plaisir de travailler avec elle, dans le noir des salles d'optiques. Nous avons eu l'occasion de tester en amont la faisabilité de la microscopie confocale dans l'UV dans la salle de manip de Christelle BRIMONT et Thierry GUILLET, que je remercie, et à cette occasion j'ai largement profité de son sens poussé de la planification et sa persévérance, indispensables outils lorsque le sujet de recherche revêtait un tel caractère exploratoire. Je me souviendrai avec amusement

---

de sa tendance à personnifier les éléments de manip (Alphonse, Basil...), que je lui emprunterai d'ailleurs peut-être.

Pierre VALVIN, merci de m'avoir laissé squatter ton bureau du bas de l'époque. Je crois que c'est là que nos discussions passionnées sur la musique et le piano ont premièrement émergé. C'était les balbutiements d'un long et exaltant chemin que l'on a parcouru ensemble, au cours duquel tu as eu la patience et le souci pédagogique de me transmettre tes connaissances techniques pointues sur bon nombre d'outils expérimentaux, des connaissances que je porterai avec moi par la suite. Laissant de côté les innombrables embûches en cours de route que l'on a surmontées ensemble, je garde en mémoire la première image sur le spectro, puis le premier scan en micro PL UV, et enfin la première image hyperspectrale: quelle accomplissement, quelle joie!

Enfin, cette expérience de recherche n'aurait pas été la même sans le bain ambiant de thésards. Cela a renforcé le sentiment d'apprentissage collectif lorsqu'on se posait entre nous les questions que l'on n'osait pas poser aux chefs, et m'a donné l'opportunité d'enseigner à mon tour les techniques et connaissances apprises. J'ai débuté dans l'équipe en stage de M2 avec deux autres doctorants, Saddem CHOUAIEB et Walid REDJEM, merci à vous pour tous les bons moments passés ensemble et l'entraide, jusqu'aux derniers jours de rédaction avec l'incontournable pause ping-pong. À mes débuts, j'ai aussi été accompagné par le fameux Luis Javier MARTINEZ RODRIGUEZ, Waseem AKHTAR, Isabell GROSS, Clément BEAUFILS et Phuong VUONG à qui je souhaite bonne continuation dans les positions académiques ou bien dans le privé qu'ils ont trouvé. Dans cette équipe multiculturelle, je me dois de remercier une triplette de Libanaises à savoir Rana TANOS, Angela HAYKAL et Christine ELIAS pour leur extrême bonne humeur déjà, et leur généreuse cuisine qu'elles n'ont jamais hésité à partager avec nous. Christine, sans qui les décibels dans la salle de manip n'auraient jamais atteint ces plafonds: notre collaboration de thésard a été haute en couleur, surtout dans l'UV! Puis il y a les anciens nouveaux, Alrik DURAND et Florentin FABRE, et les nouveaux tous frais Yoann BARON et Maxime ROLLO à qui je souhaite bon courage pour la suite de votre thèse dans cette famille NQPO. Mention spéciale pour Alrik, à qui je dois mon parcours initiatique avec python, ce geek.

Pour avoir accepté d'être rapporteur de ce travail de thèse, je remercie Jean-Sébastien LAURET ainsi qu'Abdelkarim OUERGHI. Merci également à Clément FAUGERAS et Alberto ZOBELLI pour avoir été examinateur à mon jury de thèse. Je souhaite remercier plus amplement Alberto, qui m'a accueilli dans son équipe au Laboratoire de Physique des Solides à Orsay à plusieurs reprises, et qui m'a donné l'occasion de pratiquer la microscopie électronique. Ça a été un plaisir de collaborer avec toi.

Tout au long de ces trois années, j'ai eu la chance de pouvoir enseigner à l'Université des Sciences de Montpellier, je remercie pour cela Christophe CHAUBET à la direction des enseignements en Physique. Cela a été un exercice riche qui m'a beaucoup apporté, à l'occasion duquel j'ai pu collaborer sur le plan pédagogique avec d'autres enseignants-chercheurs, dont Christophe bien sûr et aussi Laetitia DOYENNETTE que je remercie pour m'avoir laissée une marge d'initiative dans l'UE concernée; mais également avec

---

d'autres doctorants comme Adrien DELGARD et Chahine ABBAS.

Je tiens enfin à remercier Christian L'HENORET à l'atelier de mécanique qui a été d'une aide précieuse, sur le plan technique mais aussi temporel, pour la conception et réalisation des nombreuses pièces mécaniques nécessaires à la construction du microscope et aussi de m'avoir initié à quelques basiques en mécanique, et je veux souligner ici l'importance d'un atelier de mécanique au sein du laboratoire. Merci également aux électroniciens Rémi JELINEK et Yves TREIGUER pour leur aide. Je voudrais aussi remercier Christophe CONSEJO, ingénieur de recherche au laboratoire, pour m'avoir dépanné plusieurs fois et aidé avec enthousiasme.

Mes derniers remerciements vont à Julie, dont le soutien inconditionnel dans les dernières semaines d'écriture a été vital pour moi. Ta confiance en moi a été d'une grande aide dans les moments difficiles.

Bien sûr je me serais régalé à exploiter un peu plus cet outil de spectroscopie que j'ai monté, mais il me faut y renoncer, et aller vers d'autres aventures, expériences, recherches. Si je laisse à Montpellier une équipe passionnée et passionnante, j'emporte avec moi son souvenir impérissable.

---

# Contents

<b>Contents</b>	<b>i</b>
<b>Introduction</b>	<b>1</b>
<b>1 Hexagonal Boron Nitride</b>	<b>5</b>
1.1 Origins . . . . .	5
1.1.1 Boron nitride powder in the industry . . . . .	5
1.1.2 Hexagonal boron nitride in the semiconductor industry . . . . .	7
1.2 Structural properties . . . . .	9
1.3 Electronic band structure . . . . .	13
1.4 Photoluminescence of hBN . . . . .	14
1.4.1 Band edge exciton emissions . . . . .	15
1.4.2 Exciton recombination at stacking faults . . . . .	17
1.4.3 PL from deep defects . . . . .	18
1.5 Conclusion . . . . .	22
<b>2 Single defects emitting in the visible range</b>	<b>25</b>
2.1 Experimental setup . . . . .	25
2.2 Sample and typical results . . . . .	26
2.2.1 Sample . . . . .	26
2.2.2 Confocal maps of photoluminescence, dipole-like emission and photostability . . . . .	27
2.2.3 Photoluminescence properties . . . . .	29
2.3 Statistics of photon emission . . . . .	32
2.3.1 The second-order correlation function . . . . .	33
2.3.2 Experimental setup: HBT interferometer . . . . .	34
2.3.3 Discussion on the experimental procedures to access time-photon correlation . . . . .	36
2.4 Experimental results for the second-order correlation function . . . . .	38
2.4.1 Theoretical model for the photodynamics: the three-level system . . . . .	39
2.4.2 Derivation of $g^{(2)}(\tau)$ for a three-level system . . . . .	40
2.4.3 Procedure for fitting . . . . .	42
2.5 Photophysical properties of individual defects . . . . .	43
2.5.1 Expression of $r_{21}$ and $r_{31}$ with $a$ , $\lambda_1$ and $\lambda_2$ . . . . .	43
2.5.2 Power-dependent measurements of $g^{(2)}(\tau)$ . . . . .	44
2.5.3 Brightness of the source . . . . .	47

2.6 Conclusion	48
<b>3 Deep defects emitting in the UV range</b>	<b>51</b>
3.1 New levels in carbon-doped hBN crystals	51
3.1.1 Description of the experiments	51
3.1.2 Samples characteristics	53
3.1.3 Shallow-level emissions	56
3.1.4 Deep-level emissions	59
3.2 Confocal microscope at 266 nm / 4.66 eV	63
3.2.1 General overview of the experimental setup	63
3.2.2 What are the challenges to build a confocal setup in the UV?	68
3.2.3 Optimization of the optical excitation	69
3.2.4 Mitigation of chromatic aberrations	72
3.2.5 Performances of the microscope	76
3.3 Probing deep defects at a sub-micrometer scale in PL	79
3.3.1 The UV1-3 lines	79
3.3.2 Investigations of the 4.1 eV defect origin	86
3.3.3 Search for isolated emitters at 4.1 eV	92
3.4 Conclusion	97
<b>Conclusion</b>	<b>99</b>
<b>A Classical and quantum light, mathematical derivation of the second-order correlation function</b>	<b>103</b>
A.1 Classical light versus quantum light	103
A.1.1 Classification in terms of intensity fluctuation and correlation	103
A.1.2 The second-order correlation function: $g^{(2)}(\tau)$	104
A.2 Derivation of fundamental properties of $g^{(2)}(\tau)$	106
A.2.1 The classical case	106
A.2.2 The quantum case	107
<b>B Effect of the IRF on the histogram of photon correlations</b>	<b>109</b>
B.1 Position of the problem	109
B.2 Convolution of $g^{(2)}(\tau)$ and the IRF	111
<b>Bibliography</b>	<b>129</b>



## Introduction

THE understanding of the laws operating at the microscopic scale, originating from the first quantum revolution of the twentieth century, has allowed the emergence of new technologies and instrumental tools. Among them, we can cite the first realization of a solid-state Laser in 1960 by T. Maiman with a crystal of ruby [1], or the invention of the scanning tunneling microscope (STM) by G. Binnig and H. Rohrer at IBM in Zurich in 1981 [2]. These "tools" are now essential and participate in the elaboration of new nanotechnologies based on the manipulation and measurement of individual quantum systems. These new quantum devices, as part of the second quantum revolution, exploit the quantum logic and its counter intuitive aspects like quantum superposition and entanglement.

Single-photon sources formed by individual deep defects in wide bandgap semiconductors, also known as *artificial atoms*, are one of those emerging quantum systems. Electronic spins associated with these atomically small systems are at the heart of a broad range of emerging applications, from quantum information science, to the development of ultrasensitive quantum sensors. In this regard, the nitrogen-vacancy (NV) defect in diamond [3] has attracted considerable interest and led in particular to the elaboration of quantum protocols [4] and to highly sensitive magnetic field sensors [5], thanks to its spin-dependent photoluminescence. Single-photon emitters have also been found in silicon carbide (SiC) [6, 7], and more recently in our team in pure silicon with the G center (cf. thesis of W. Redjem).

In that context, hexagonal boron nitride (hBN), a lamellar material with a wide bandgap of  $\sim 6$  eV, is a promising platform for hosting single deep defects. The lamellar structure of this material offers an appealing alternative to standard cubic semiconductors because electrons and spins can be confined in a single atomic plane, thus offering enormous potential to engineer quantum functionalities. hBN has been used in the industry for more than seventy decades now, but has only recently attracted attention in the field of semiconductors, with the first synthesis of large monocrystals in 2004 by Watanabe and Taniguchi [8].

In the field of 2D materials, graphene has led to a colossal theoretical and experimental development that is now transferable to other 2D crystals. There is a large variety of candidates that are mechanically, thermally and electronically stable in ambient conditions [9, 10]. Among them, a promising family of materials, other than the atomically thin hBN and graphene, is the family of transition metal dichalcogenides (TMDC), which are ultrathin material composed of 3 atomic layers like  $\text{MoS}_2$  or  $\text{WSe}_2$ .

The interest in hBN arises from the possibility to combine different 2D materials into an heterostructure exhibiting new optical, electrical and magnetic properties different from the stand-alone bulk counterparts [10, 11], opening up the scope of possibilities in terms of opto-electronic devices [12]. The prospect of manufacturing such designed nano-architecture — known as *van der Waals heterostructures* — by stacking different layered crystals on top of each other via exfoliation or *in situ* epitaxial techniques, has launched a new era of material science at the beginning of this decade. A proof of concept for such an heterostructure was realized in 2012 with a superlattice of bi-layers of graphene and hBN stacked upon each other in sequence [13]. Besides, hBN presents a great affinity with graphene, as it is the best dielectric substrate for it [14], and is also used to enhance optical and electrical properties of TMDC materials by encapsulation [15, 16]. In the field of crystal growth, the research to obtain hBN crystals of increasing size and quality is very active, with recent papers reporting wafer-scale growth of single-crystals [17, 18].

In that context, it is essential to understand the structural, electronic and optical properties of hBN on the one hand, and to investigate its point defects for quantum technologies on the other. This manuscript deals with the spectroscopy of point defects in hBN.

Over the first chapter of this thesis, we present the fundamentals of hBN. We review the most-updated comprehension of the structural and electronic properties of the material. In particular, we present how the boron and nitrogen atoms are arranged in an honeycomb structure with  $sp^2$  orbitals configurations and describe the electronic band structure resulting thereof, in the bulk and the monolayer. Then, we present the characteristics of the bulk hBN photoluminescence at the energies of the bandgap and near-bandgap, showing the important coupling of the exciton with optical phonons. At last, we review the current knowledge relative to deep defects in hBN, emitting from the near-infrared to near-UV range.

Chapter two is dedicated to the study of single localized defects emitting at around 600 nm in a high-purity hBN crystal. We report on a highly efficient single-photon source, among the highest reported to date in solid-state systems. We study its photodynamics with photon correlations measurements, as well as its photoluminescence properties in regard to the phonon modes in the hBN lattice.

In the third and last chapter, we explore deep defects emitting in the ultraviolet range. First, we study shallow and deep levels in carbon-doped hBN samples by combining macro-photoluminescence and reflectance setup. We show the existence of new optically-active transitions and discuss the implication of carbon in these levels. The second section of this chapter is dedicated to the presentation of a new micro-photoluminescence confocal microscope operating at 266 nm under cryogenic environment. The design and performances of the optical system are described. In the third section, using this new setup, we go further into the examination of the deep levels, analyzing the relation between them and with the known point-defect at 4.1 eV. We use new crystals with isotopically-purified carbon doping as a strategy to investigate the long-standing question concerning the chemical origin of the 4.1 eV defect. Through this attempt, we bring to light the spatial dependence of the optical features for this specific emitter. Last but not least, we present our work dedicated to isolate the emis-

sion of a single 4.1 eV defect. We study the photoluminescence of thin undoped flakes, pre-characterized with an electron microscope, that contain a low density of emitters, and inspect in particular their photostability in these thin crystals.

Finally, we end this manuscript with a general conclusion and discussions.



## Hexagonal Boron Nitride

### 1.1 Origins

THE boron nitride is a binary chemical compound of the III-V family. It was first discovered and prepared by the English chemist W. H. Balmain in 1842 [19] by using molten boric acid and potassium cyanide, but unfortunately this new compound was unstable and required many attempts to obtain a stable boron nitride. The compound appeared as a white powder as a residue of the chemical protocol after dehydration. The optical microscope revealed a structure made of flakes easily slipping over each other and thus separable, and enabled to notice a random distribution in both size and shape, although a qualitative study on the orientation of the normales to the breaking faces indicates the existence of orientated bundles typical of the hexagonal crystal structure and to a lesser extent to the rhomboidal one. The Fig 1.1 illustrates these two macroscopic properties.



**Figure 1.1**

*Left: the BN white powder. Right: optical micrograph of BN flakes.*

#### 1.1.1 Boron nitride powder in the industry

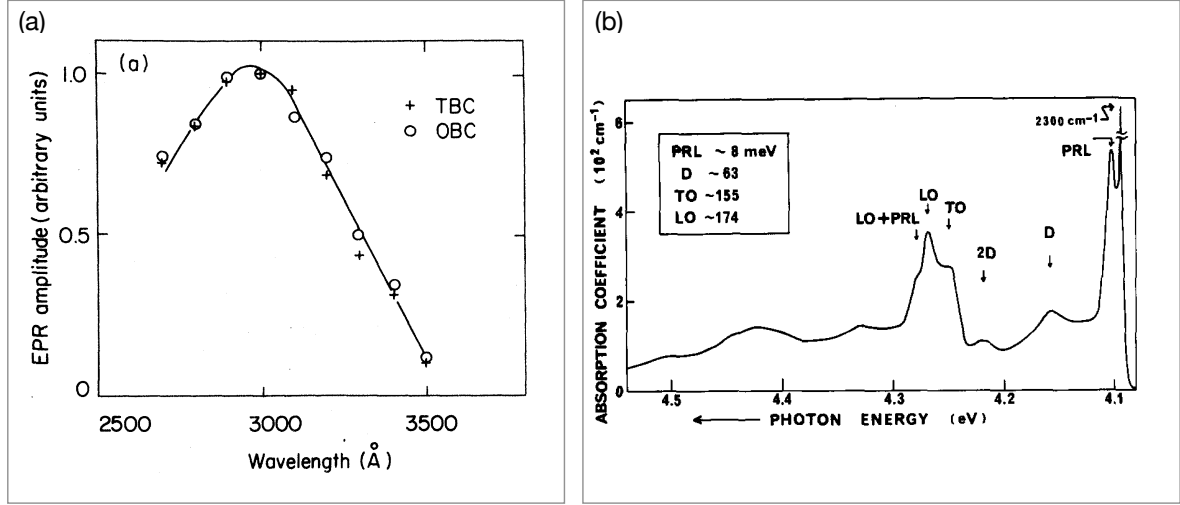
For nearly a hundred years studies on boron nitride remained in laboratory scale because of the technical difficulties of different production techniques and high cost of the material which is obtained with these synthetic methods. We have to wait for the onset

of the modern development of crystal growth technology, dating from the Second World War, which was boosted mainly by the demand for crystals for electronics, optics, and scientific instrumentation, for the growth technologies to be raised to a very high and advanced level to fulfill the increasing demands in crystal size and quality. Indeed, in the 1950s the Carborundum, the Union Carbide and the Norton Abrasives companies managed to prepare purified boron nitride powder [20] on an industrial scale for commercial applications with sophisticated hot pressing techniques [21].

The interests for this material in industry can be justified with these four properties among others:

- It is chemically inert,
- Its melting point is very high (2967 °C at ambient pressure [22-24]), making it first-class refractory material,
- The ease of sliding between adjacent crystalline planes (0001) in hexagonal form makes it a perfect solid-state lubricant up to 900 °C, better than graphite or MoS<sub>2</sub> that are burnt away at lower temperatures,
- It is attractive for the cosmetic industry for its quality whiteness, preferred to the kaolin, the silica or the alumina powder.

Besides this nascent interest in the industry, the newly available BN powder also encourages new fundamental studies. In 1956, Larach and Shrader used purified BN powders (particle size of approximately 100 nm) from the Carborundum Company and the Norton Company to perform various types of measurements with the aim of elucidating the emission spectrum in the UV to VIS range and determining the bandgap of the material by reflectivity technique [25]. Photoluminescence at low temperature and cathodoluminescence in the UV show a complex and broad spectrum with a multitude of peaks between 300 and 500 nm whose relative intensity change with excitation energy but positions remain stable, while the reflectivity measurement for wavelengths from 220 to 320 nm fails to show a bandgap absorption. Among others, we can also cite the remarkable studies from Katzir et al. [26] in 1975 on hot-pressed boron nitride (HPBN) obtained with powder of the Carborundum company. With UV light, they measure the excitation spectrum of the electron paramagnetic resonance (EPR) signal from the one- and three- boron centers (OBC, TBC), and find a maximum EPR amplitude for the energy of 4.1 eV or  $\sim 3000 \text{ \AA}$  [Fig 1.2(a)]. Assisted by quantum chemical calculation, they establish a model in which a carbon impurity introduces an energy level 4.1 eV below the conduction band. Upon excitation, electron excited from this level pass through the conduction band and fall into traps like the nitrogen vacancy, thus forming a TBC center. Later in 1981, Kuzuba et al. [27] study the characteristics of electron-phonon coupling for vibronic transitions in typical defects, ascribed to carbon acceptor at nitrogen site ( $C_N$ ) and nitrogen-site vacancy ( $V_N$ ). In the absorption spectrum [Fig 1.2(b)] associated with  $C_N$ , the zero-phonon line (ZPL) is identified at 4.095 eV and the spectral features at higher absorption energies are assigned to specific phonon modes.

**Figure 1.2**

(a) Excitation spectrum of the EPR signals of OBC and TBC, in HPBN as measured at 300 K [26]. (b) The absorption spectrum ( $E \perp c$ ) of the hBN single crystal at 2K in the energy range between 4.08 and 4.54 eV. Arrows indicate approximate positions of dominant sub-structures due to coupling with particular phonons [27].

### 1.1.2 Hexagonal boron nitride in the semiconductor industry

The semiconductor industry has only recently grown significant interests about this material with the successful growth of macroscopic monocrystals of hexagonal boron nitride, a technical achievement from Takashi Taniguchi and Kenji Watanabe at NIMS laboratory in Japan in 2004 [8]. They report on the growth of a pure hBN single crystal under high-pressure (5 GPa) and high-temperature (1750 °C) conditions, for a sample size of few cubic millimeters. Since then, miscellaneous advanced applications of this "new" material have flourished on a worldwide scale. Quite a major part of these applications is based on the integration of hBN in van der Waals heterostructure architectures. In addition to the already mentioned properties of hBN, the excellent electrical insulation (large breakdown voltage  $> 0.4$  V/nm [28]) and thermal conduction (20 W/mK [29]) are of particular interest for the semiconductor-based devices. It would be tedious to give an exhaustive description of the field of applications, we rather provide the reader with five seminal and recent papers we think give a relevant view of the wealth of applications [illustrations on Fig 1.3]. In Ref. [30], Hu et al. demonstrate that monolayers of hBN are highly permeable to thermal protons under ambient conditions thus unveiling the potential of hBN in many hydrogen-based technologies as an atomically thin membrane. Geim and Grigorieva [10] review the emerging research area related to van der Waals heterostructure (assembling of atomic planes of different crystals in a chosen sequence) in which hBN is most likely to play an important role due to its 2D geometry, along with graphene and transition metal dichalcogenides (TMDC). Beyond its use as a good dielectric substrate (the best for graphene [14]) or encapsulating layer, hBN is a natural hyperbolic material in the mid-IR range due the strong anisotropy of its permittivity tensor resulting from the intrinsic anisotropy of its 3D structure. It outperforms man-made hyperbolic materials, as discussed in Ref. [31] in the context of optoelectronics and photonics applications of 2D semiconductors,



while the more recent article from Caldwell et al. [32] presents the particular interest of hBN for this polaritonic property complemented with other valuable aspects like bright single-photon source and strong bandgap UV emission. The majority of these scientific developments are made possible by the continuously improved growth process of Takashi Taniguchi and Kenji Watanabe in Japan and their collaboration all over the world, as related in Ref. [33].

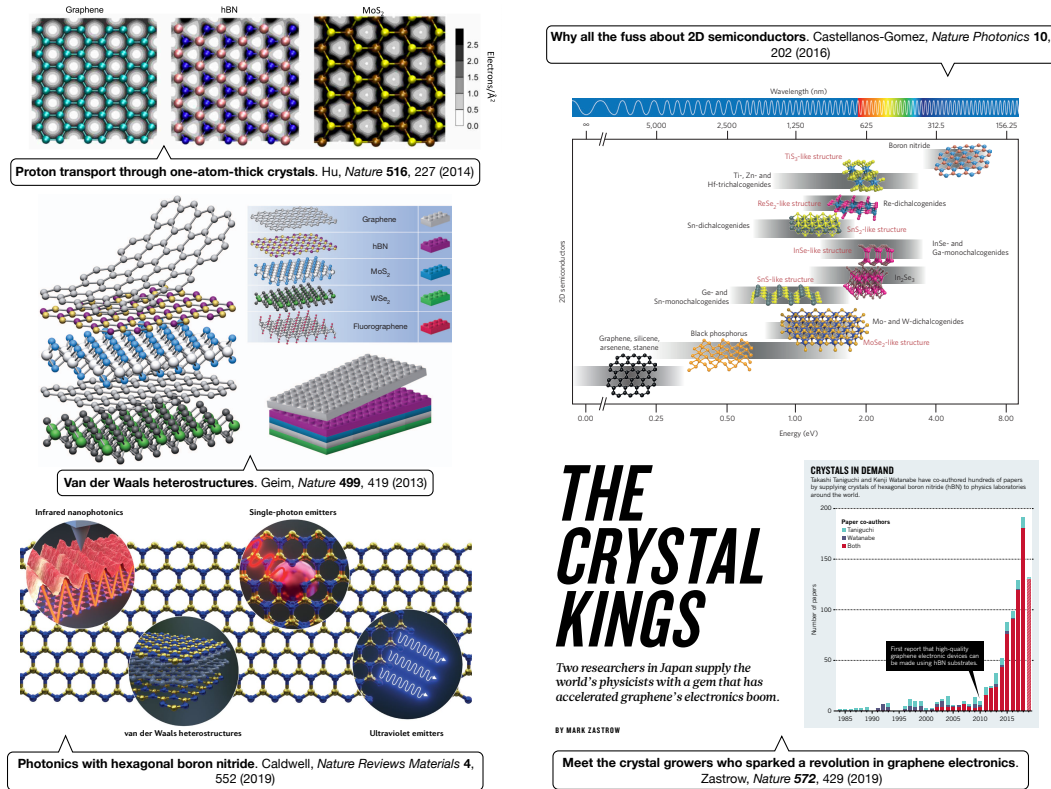


**Figure 1.3**

Hexagonal boron nitride as a macroscopic monocrystal, in its 2D and 3D forms, present a rich diversity of applications spanning the fields of nanophotonics, van der Waals heterostructure engineering, single-photon sources as well as technological niches like hydrogen-based technologies.

Among the numerous applications of hBN, we are going to focus specifically on the aspect related to single defects hosted in a solid-state matrix, as a road to engineer single-photon sources. Prior to this, we want to take some time to describe the structural and electronic properties of the material in order to better draw the landscape of its potential for the researcher in terms of opto-electronic performances as well as the difficulties one shall face in the pursuit of their quantitative determination.



## 1.2 Structural properties

To go beyond the simple observation of the macroscopic crystalline forms through optical microscope, the first experiment to do is X-ray diffraction (XRD). We have to wait the works of R. S. Pease in 1952 [34] on BN powder to dissipate all ambiguities about the crystallographic structure of BN. The structure proposed is a stacking of regular hexagons composed of alternating atoms of bore and nitrogen. Along the senary axis<sup>1</sup>, the atoms B and N periodically alternate one upon the other, as indicated above on Fig 1.4

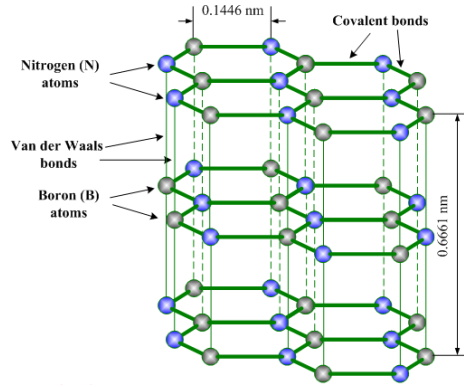


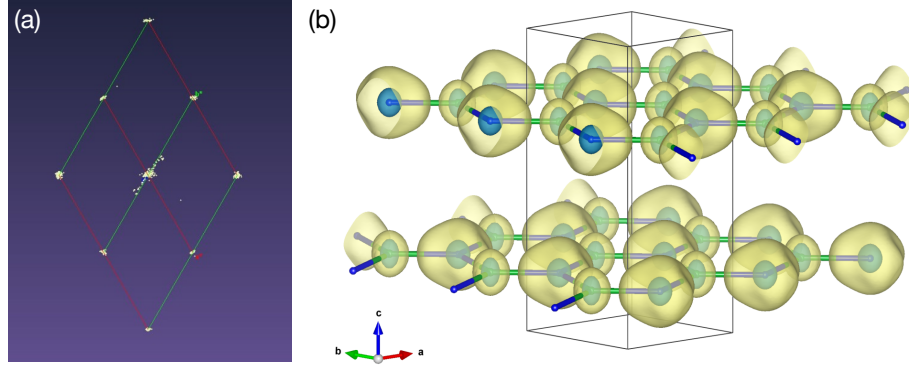
**Figure 1.4**

*Hexagonal boron nitride structure in the AA' configuration.*

The primitive cell is therefore of hexagonal symmetry, with cell parameters  $a = 1.446 \text{ \AA}$  and  $c = 6.661 \text{ \AA}$  at 300 K. Also according to Pease, the thermal expansion coefficient is negative within the plane and positive along the senary axis. The stacking sequence suggested by Pease is often noted AA', where A represents an hexagon of basis  $B_3N_3$  and A' the same hexagon in the adjacent plane but rotated by  $60^\circ$  along the senary axis of the crystal. It is worth noting here that the B and N atoms of a layer constitute an affine plane in the mathematical sense, similarly to the graphene, and unlike the 'monolayer' of a transition metal chalcogenide which are an arrangement of one atomic plane of the electro-positively charged transition metal capped with two planes of the chalcogen anion (three atomic planes), or the 'monolayer' of a III-VI compound which has two planes of chalcogen encasing two planes of gallium or indium (four atomic planes).

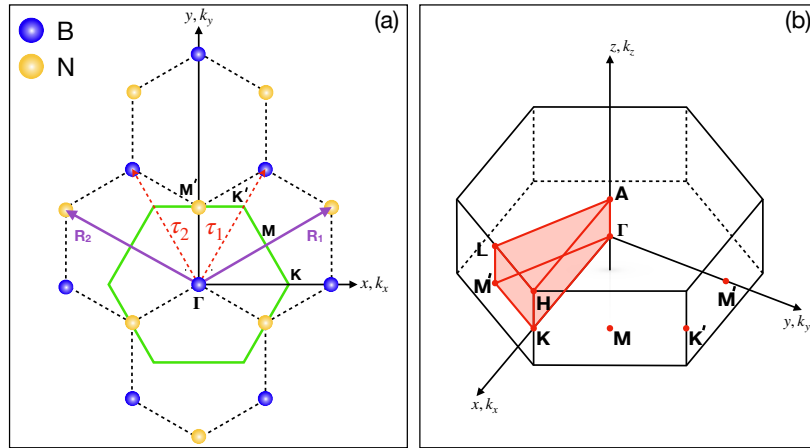
We have asked Arie Van der Lee from IEM in Montpellier, to reproduce the Pease experiment while using this time a monocrystal of hBN, with the modern technical tools for computer handling and processing of X-ray spectra [35]. The results of the experiments are presented hereinafter in Fig 1.5. The left image shows the reciprocal space computed via the spectrum of the diffraction spots of the beams, and the right image displays the electronic clouds corresponding to two successive reticular planes along the axis  $\langle 001 \rangle$  in the AA' stacking configuration, obtained with a modified Fourier transform.

<sup>1</sup>Symmetry axis along which a crystal gets the same spatial position back six times during a  $360^\circ$  rotation.


**Figure 1.5**

(a) Collapsed view of reciprocal space of hBN. (b) Electron density in a side view of two-layer hBN – derived from the maximum entropy method [35].

At this stage, it is possible to represent the crystalline stacking of BN and the crystallographic axes of the primitive cell  $\tau_1$  and  $\tau_2$  with  $(\tau_1, \tau_2) = 60^\circ$ , as well as the vectors of the reciprocal lattice  $R_1$  and  $R_2$  with  $(R_1, R_2) = 120^\circ$ , which are used to build the first Brillouin zone. For the purpose of clarity, we represent these parameters on a monolayer of hBN, Fig 1.6(a), thus neglecting the stacking along the  $c$  axis. The full representation is however represented in Fig 1.6(b). For calculations, orthogonal representation makes the work easier, we thus include the direct basis  $(x, y, z)$  and the reciprocal basis  $(k_x, k_y, k_z)$  which are usually defined as indicated on the figure. Last but not least, the high symmetry points  $\Gamma, M, K, K'$  of the reciprocal lattice are also included because they are important to describe the band structure.

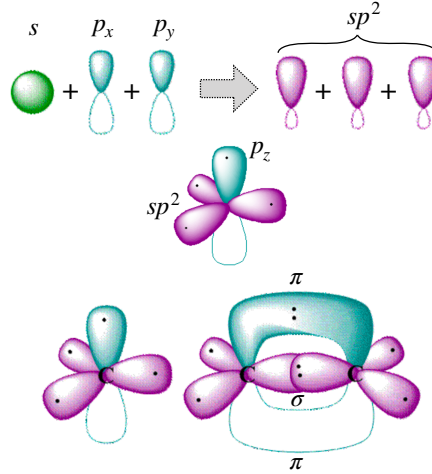

**Figure 1.6**

(a) Crystallographic axes and first Brillouin zone in the monolayer representation. (b) First Brillouin zone in 3D.

Let us make a small digression here. If we look at the atomic lines along the direction  $x$ , we observe alternating line of B or N depending on the ordinate  $y$ . If we were to consider the graphene, this alternation would not exist. Now if we look at the direction  $y$ , we not only notice an alternation of B and N atoms along the same lines but also of short

and long atomic distances. This is found in graphene as well. Behind these simple geometrical considerations there is an important result of the group theory: these elements of geometry account for the positive gap at the M point of the Brillouin zone in hBN and graphene, along with a zero gap at the K point for graphene and open gap for hBN.

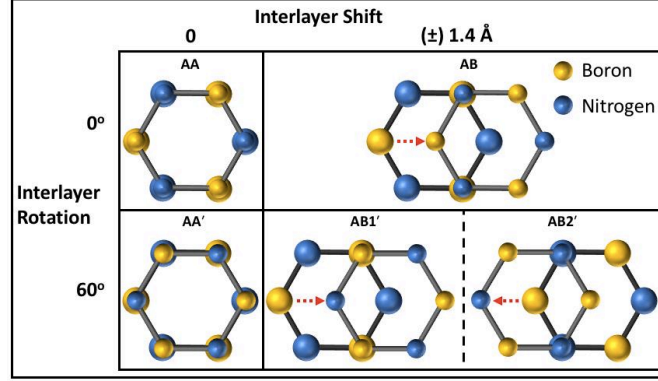
The hexagonal symmetry of the material is a consequence of the anisotropy of a chemical bond leading to the hybridization of type  $sp^2$ . Indeed, as in graphite and graphene, the covalent bonds in hBN are formed through the hybridization  $sp^2$ . Hybridization is a concept of valence bond theory in chemistry and consists, for an atom, of the mixing of its orbitals  $s$  and  $p$  with different weights in order to form new hybrid orbitals that account for the observed structure of molecules. In the particular case of hexagonal atomic layer, the  $2s$  orbital is combined with two  $2p$  orbitals of B and N atoms. The top part of Fig 1.7 represents the new orbital geometry resulting from the hybridization between orbitals  $p_{x,y}$  and  $s$ . The  $sp^2$  orbitals form  $\sigma$  bonds between B and N atoms along the plane of the layer, whereas the orbitals  $p_z$  are directed perpendicular to the nodal plane of the  $\sigma$  bonds, that is to say to the plane of the layer, and are going to participate in the interaction with the adjacent planes by forming  $\pi$  bonds.



**Figure 1.7**

Representation of the new hybrid atomic orbitals obtained by mixing two  $p$  orbitals with the  $s$  orbital. The  $sp^2$  orbitals make an angle of  $120^\circ$  between them and lie in a shared plane. On the bottom, illustration with two atoms of carbon of the formation of  $\sigma$  bond in the nodal plane ( $sp^2$  orbitals) and  $\pi$  bond ( $p_z$  orbitals). Adapted from [36].

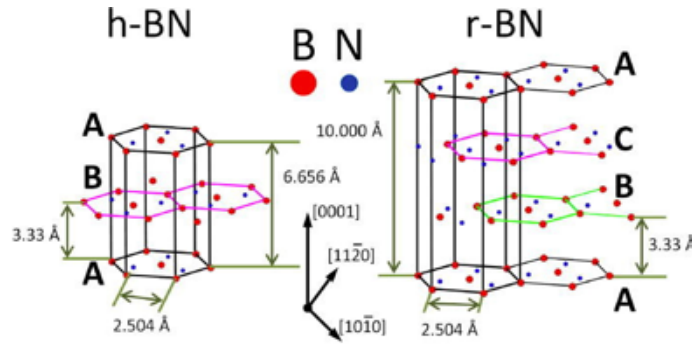
One consequence of this specific type of bonding is a weak lattice energy. Chemical bonds are strong in the plane (0001) and much more weak along the  $c$  axis. This anisotropy also affects the rigidity tensor, the measured value for the elastic modulus perpendicular to the  $c$ -axis direction [100] is  $c_{11} = 788.4$  GPa and for the elastic modulus along the  $c$ -axis direction [001]  $c_{33} = 24.5$  GPa, giving an in-plane/out-of-plane elastic modulus ratio of  $c_{11}/c_{33} \sim 32$  [37]. The elastic anisotropy of hBN is remarkably high, and this has to be compared with much lower values reported in other layered materials in which the layers are also weakly bound by van der Waals interactions. As for the component of type  $c_{12}$  (related to in plane [100] TA phonons), value of 170 GPa is calculated, and the theoretical values of  $c_{13}$  (non pure [110] direction TA phonons)


**Figure 1.8**

Schematics of the 5 high-symmetry stackings in bilayer hBN as sorted by interlayer rotation and shift [38].

and  $c_{44}$  (out-of-plane [001] direction TA phonons) are predicted to be very small in the order of 2.3 GPa to 3 GPa [39]. These small values of  $c_{13}$  and  $c_{44}$  demonstrate how the adjacent reticular planes can easily slip over each other, thus breaking the AA' stacking. Therefore, hBN can exist under different coherent stacking orders, close to AA', all based on the  $sp^2$  orbitals and with similar lattice energies [38], as represented on Fig 1.8. There are all obtained from AA' by interlayer shift or rotation or both.

Boron nitride can also be obtained in rhombohedral form [Fig 1.9], close to the hexagonal structure [40, 41], as well as under different crystal structures resulting from hybridization  $sp^3$  like the cubic and wurtzitic form (cf the thesis of Vuong [42] for more information). The cubic phase is a superhard material and crystals are small and


**Figure 1.9**

Comparison between crystal structures of hexagonal (left) and rhombohedral (right) boron nitride.

impure so we don't have particular interest in them [43]. The wurtzitic phase is quite unstable, but a recent study indicates the possibility to stabilize it under high pressure [44]. It is too soon to think about using w-BN in scalable application for information technology, and it will most likely remain the same in the future.

## 1.3 Electronic band structure

The bulk hBN is of hexagonal symmetry and has a centro-symmetric inversion of type  $D_{6h}$ , whereas the monolayer is non-centro-symmetric of type  $D_{3h}$ . The periodic stacking AA' requires to include two monolayers in the primitive cell and it induces a center of inversion at the exact barycenter of the two layers. This enhances the number of symmetry operations by introducing an axis of rotation-inversion of the 6<sup>th</sup> order. In order to construct the band structure of the bulk hBN, in the framework of the tight binding theory, one can begin with the Hamiltonian matrix representing the monolayer band structure, before diagonalization, and carefully build linear combinations of bonding and antibonding molecular orbitals by considering the properties of symmetry. The double matrix obtained by that means can then be diagonalized [45]. The justification for this method lies in the fact that  $D_{3h}$  is a subgroup of  $D_{6h}$ . The reader is invited to refer to the thesis of Vuong [42] Chapter I Section 2 for a more detailed discussion about the symmetries and the methodology to build the electronic band structure of the bulk from the coupling of two layers along the c axis. Here, we simply show the band structure in the monolayer case [Fig 1.10(a)] and the bulk case [Fig 1.10(b)] of hBN obtained by modern techniques.

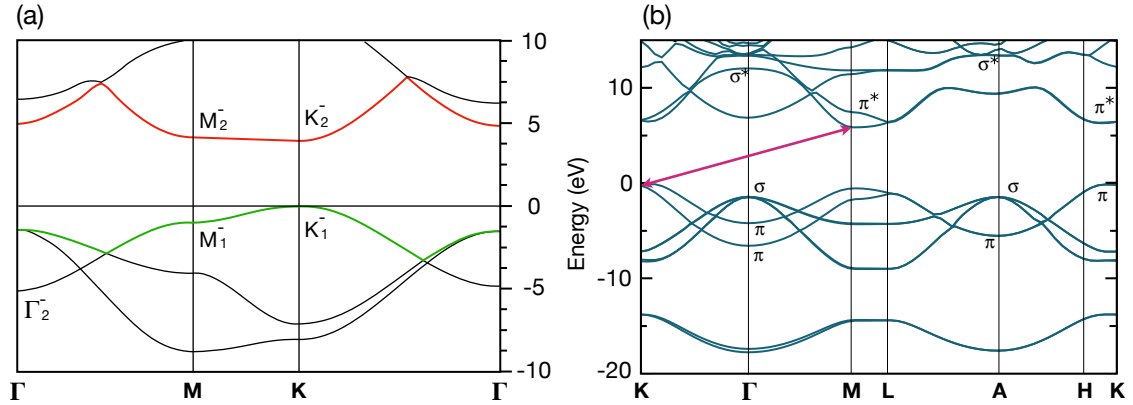


**Figure 1.10**

Calculated electronic band structure of 2D [46] (a) and 3D [47] (b) hBN. The electronic gap is direct in 2D at the K point of the Brillouin zone, while in 3D it is indirect with an upward transition from K to M.

In the case of the monolayer, the valence band in green on Fig 1.10(a) results from the bonding linear combinations of the  $p_z$  states of the bore and nitrogen while the conduction band (red) results from antibonding combinations. The "-" indicates that these molecular orbitals change sign under the symmetry operator  $\sigma_h$  that corresponds to the inversion symmetry relatively to the  $\sigma$ -bonds plane. We note that the maximum of the valence band and the minimum of the conduction band are vertically aligned at the K point of the Brillouin zone.

For the bulk case, we observe that the number of bands doubles. It is a consequence of the necessity to take two monolayers in the primitive cell, as discussed above, which double the number of atoms in it (from 2 to 4). Therefore there is two times more electronic orbitals that interact to give two times more electronic bands. Yet, the most

important change is the movement of the conduction band minimum from K to M in the Brillouin zone, as a consequence of the inter-plane interaction. Moreover, the maximum of the valence band moves slightly from K toward T (middle of the  $\Gamma - K$  path).

From these considerations on the theoretical band structure, we can state that the semiconductor BN has an indirect fundamental gap in  $k$ -space between a conduction band in M and a valence band near K, like indicated by the magenta arrow. The value of this indirect bandgap is  $\sim 6$  eV. Kolesko et al. have calculated that increasing the inter-reticular distance minimizes the coupling between layers thus returning to the situation found in the monolayer, that is to say a configuration with a direct gap in K [48].

In the past few years, it has been experimentally demonstrated that 2D semiconductors like the transition metal dichalcogenides ( $\text{MoS}_2$ ,  $\text{MoSe}_2$ ,  $\text{WS}_2$ ,  $\text{WSe}_2$ ,  $\text{MoTe}_2$ ) experience an indirect to direct bandgap transition when thinned to a monolayer [49–52]. Recently, in our team, using sample grown by molecular beam epitaxy (MBE) on HOPG, we have demonstrated the same crossover in monolayer hBN through macro-photoluminescence and reflectivity measurements [53], thus confirming the theoretical predictions [48, 54]. Now that we have pictured the electronic structure of the hBN, we can review the light emission properties in view of this analysis.

## 1.4 Photoluminescence of hBN

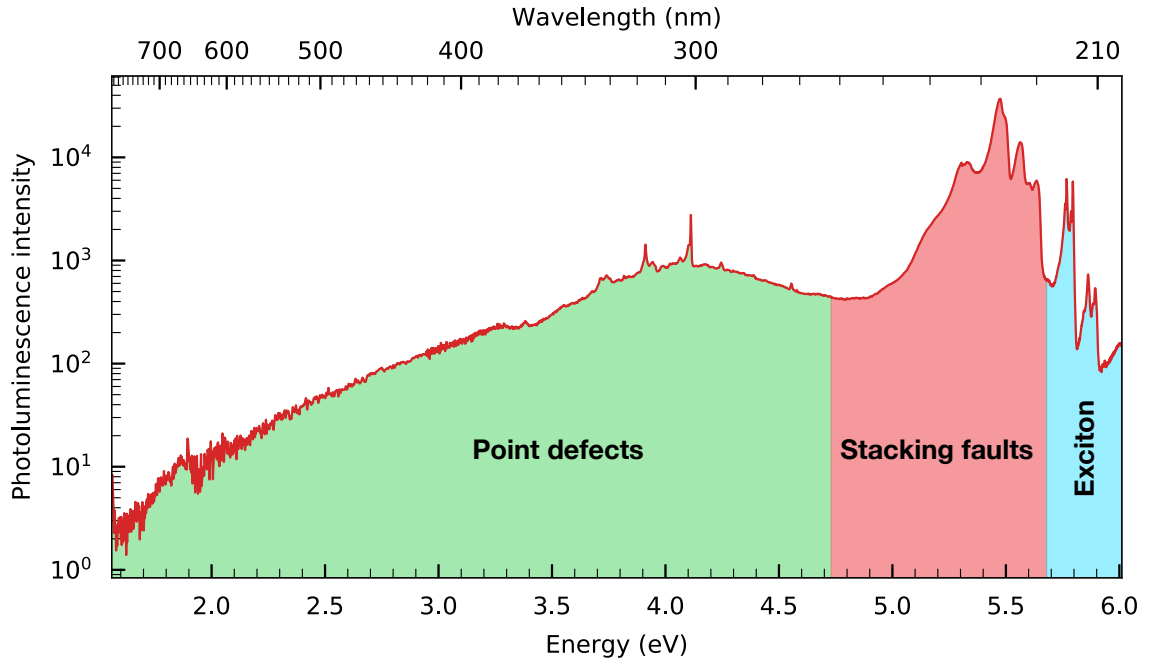


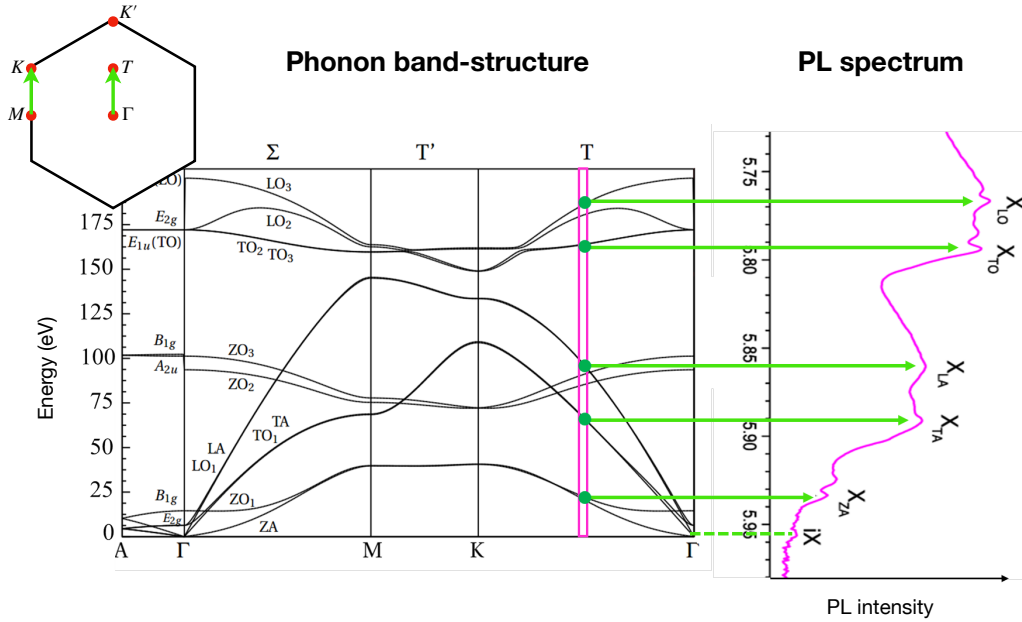
**Figure 1.11**

Spectrum of bulk hBN at 10K with an excitation at 6.3 eV recorded from 1.5 eV up to 6 eV. Three colored areas represent the features of the spectrum corresponding to excitonic bandgap emission, stacking faults recombination, and point defects emission, from high to low energies.

In Fig 1.11 above is reported a logarithm plot of the PL intensity typically recorded on bulk BN samples at low temperature using the 192 nm quadrupled radiation of a Ti-Sa laser. From the current understanding of the luminescent properties of hBN, the PL features can be split into three parts corresponding to specific origins for the optical emission: in the deep UV region we have the emission related to bandgap excitons (blue) and the exciton recombination at stacking faults (red), and in the moderate UV down to near-IR energies are the point defect related emissions (green).

### 1.4.1 Band edge exciton emissions

In the deep UV range, that is to say in the 6 eV to 5 eV range, one can distinguish two sub-regions. We focus here on the sub-region from 6 eV to 5.65 eV. We find a series of documented lines corresponding to the phonon-assisted intrinsic recombination [55], that are submitted to strict selection rules linked to the configuration of the PL experiment [35]. The energy spectrum of these lines is a complementary experimental evidence that definitively consolidate the indirect nature of the bandgap of hBN. At 5.955 eV, a very weak PL contribution iX (PL spectrum of Fig 1.12) can be detected. This forbidden recombination corresponds to the indirect exciton and indicates the value of the indirect excitonic band gap of hBN.

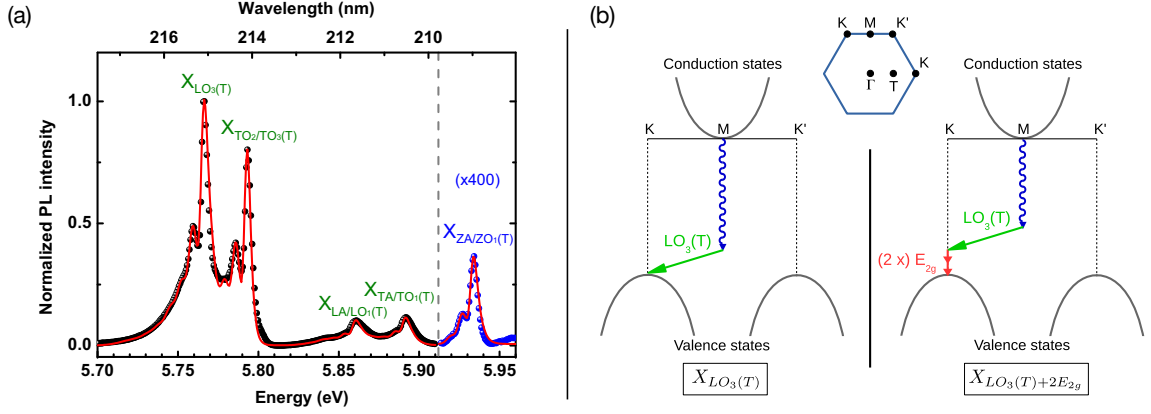


**Figure 1.12**

Photoluminescence spectra of BN (right side) plotted at the same scale as the phonon dispersion relation (left side) [56]. The energy of the photoluminescence line iX at 5.955 eV coincides with the zero phonon-energy.

These phonon-assisted recombination lines are all completed by a series of lower energy companions corresponding to a complementary energy relaxation process involving inelastic Raman scattering via the emission of one  $E_{2g}$  (on-axis atomic vibrations) Raman active phonon and overtones [57]; the process is illustrated on Fig 1.13(b).

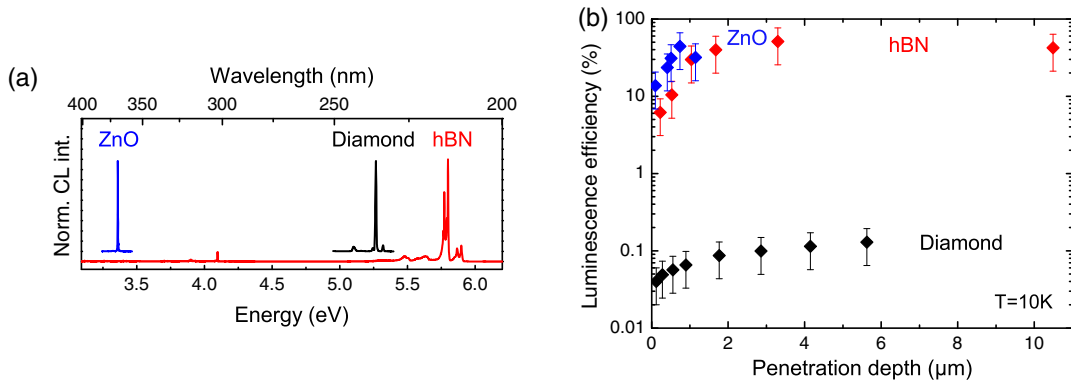



**Figure 1.13**

(a) Photoluminescence spectrum in bulk hBN in the deep ultraviolet under two-photon excitation at 3.03 eV, at 10 K. Experimental data (symbols), theoretical fit (red line).  $X_\mu$  stands for the replica involving the phonon mode  $\mu$  in the middle of the Brillouin zone around T points. (b) Schematic representations, in the single-particle picture of the electronic band structure, of the phonon-assisted recombination processes of the  $LO_3$  line (left part), and of the  $LO_3+2E_{2g}$  one (right part).

It is worth noting that the shape of the peaks in this series of phonon lines are not of the Lorentzian-shape kind, but they are instead fitted using Gaussian functions [Fig 1.13(a)] with a broadening parameter identically proportional through the whole series to the phonon group velocity at the middle of the Brillouin zone, as a third evidence of the about K-M configuration of the fundamental indirect bandgap.

Interestingly, when increasing the temperature the line-width of these phonon-assisted lines do not broaden according to a Bose-Einstein distribution (Bose-Einstein distributions probe the temperature-dependent population of the phonon bath), like it is traditionally found for semiconductors but follow a  $\sqrt{T}$  trend [58] as suggested by Toyozawa in a seminal paper in 1958 [59]. The Gaussian shape of the PL lines and


**Figure 1.14**

(a) Cathodoluminescence spectra of hBN, diamond and ZnO at 10K. (b) Luminescence efficiencies of ZnO, hBN, and diamond plotted as a function of electron penetration depth. (Borrowed from [60])



the  $\sqrt{T}$  dependence of their width both indicate a regime of strong-electron phonon interaction, in hBN. This is inferred by two recent first principle calculations [61, 62] which not only explain our experimental result and our identification, but also bring quantitative understanding of the high internal quantum efficiency (IQE) of intrinsic light-emission measured by Schué et al. in hBN [60] (cf. Fig 1.14), the strong IQE that lured Watanabe et al. and led them to suggest a direct band gap configuration [8].

### 1.4.2 Exciton recombination at stacking faults

In the 5.65 to 5 eV energy range, displayed on Fig 1.15(a) [63], roughly co-exist different extrinsic recombination processes: an impurity-related transition at 5.56 eV ( $D_2$ ), attributed to an optical transition in a boron-nitride divacancy ( $V_{BN}$ ), and another transition near 5.25 eV ( $D_6$ ) that is now attributed to a nitrogen vacancy rather than to a donor-acceptor pair (DAP) recombination as suggested before. Starting at 5.6 eV a series of bands are detected split by 147 meV which correspond to phonon overtones after the emission of the middle zone phonon LO(T)/TO(T), the complementary emission of a TO(K-K') phonon due to an efficient valley-orbit interaction process. These processes are illustrated in Fig 1.15(b). Calculation of the selection rules for overtone emission was published by Michel Hulin [64] and our measurement nicely fits with his predictions.

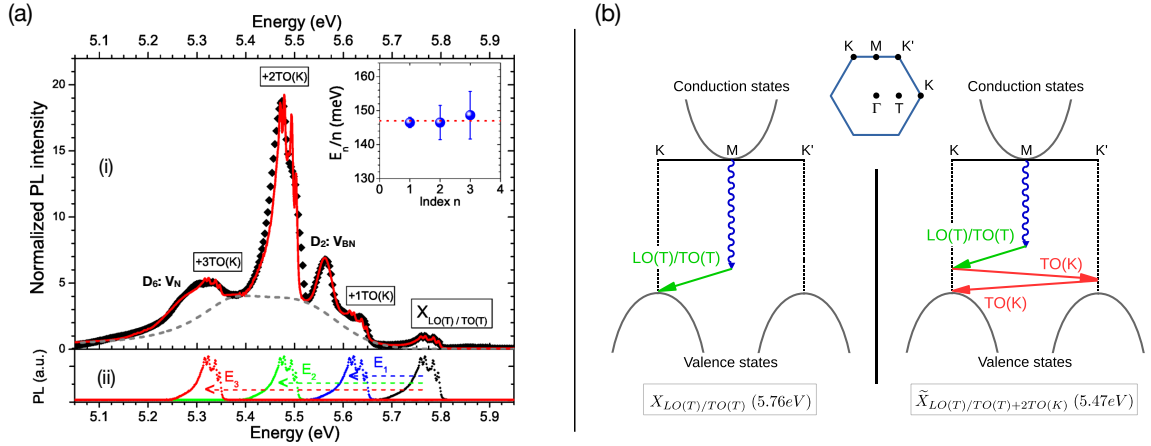


**Figure 1.15**

(a)(i) Normalized PL signal intensity in bulk hBN at 10 K, for an excitation at 6.3 eV (black diamonds), and fit (solid red line). The dashed gray line indicates the background signal intensity used in the fit, corresponding to the featureless defects emission in multiwalled boron nitride nanotubes ([65]). Inset: energy shift  $E_n$  divided by the replica index  $n$  versus  $n$ . (a)(ii) Emission spectrum of the  $X_{LO(T)/TO(T)}$  line at 5.76 eV (black diamonds), and three replicas used in the fit in (a)(i), obtained by a rigid energy shift of  $E_1$  (blue diamonds),  $E_2$  (green diamonds), and  $E_3$  (red diamonds). (b) Schematic representations, in the single-particle picture of the electronic band structure, of the phonon-assisted recombination processes of the  $X_{LO(T)/TO(T)}$  line at 5.76 eV (left part), and of the  $\tilde{X}_{LO(T)/TO(T)+2TO(K)}$  line at 5.47 eV (right part). (Adapted from [63])

One can legitimately be surprised regarding the intensity of these PL lines, due to complementary valley orbit scattering process, with respect to the near band edge

intrinsic phonon-assisted recombination. In fact as demonstrated by Bourrellier et al. [66] [Fig 1.16], the density of states required to explain this intensity is brought by the stacking faults existing in the BN crystal. The energy conservation process selects the ad hoc stacking faults and these lines are not observed in the absence of stacking faults, as observable in panels (d, e, f) of Fig 1.16 where the intensity of the 5.30, 5.46 and 5.62 eV emission is high along the lines interpreted as folds, and drops outside of these lines.

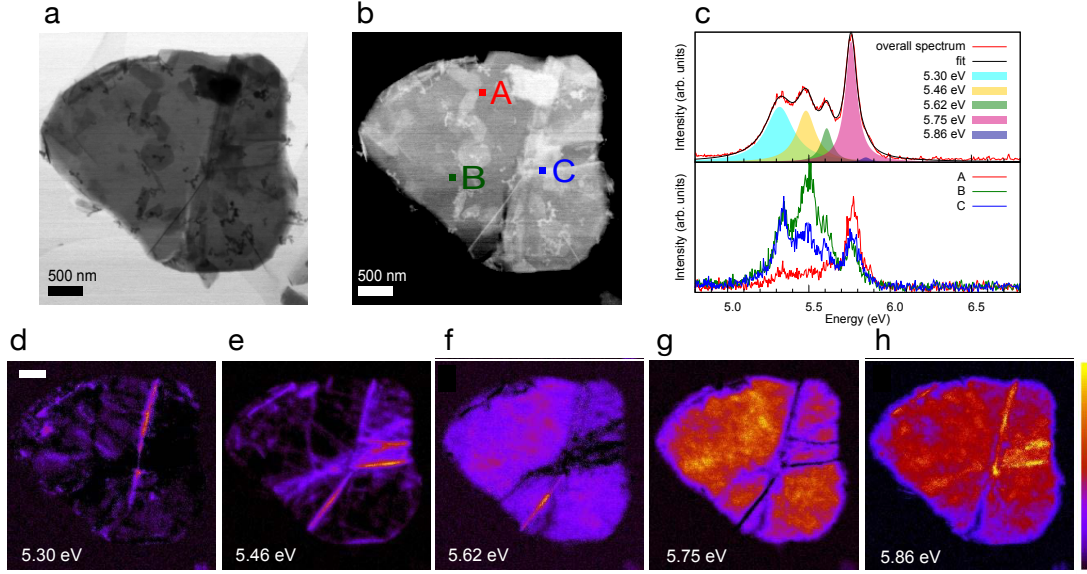


**Figure 1.16**

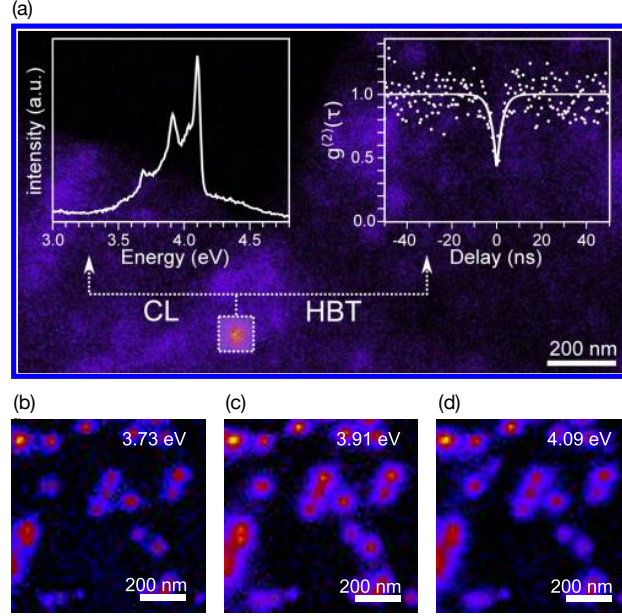
(a) Bright field and (b) dark field images of an individual BN flake. (c) Overall emission spectrum of the flake and individual spectra taken at specific probe positions indicated in panel (b). (d-h) Emission maps for individual emission peak. Intensity is normalized independently within each individual map. (Borrowed from [66])

### 1.4.3 PL from deep defects

#### Moderate UV range

In the moderate UV range, that is to say in the 5 eV to 3.3 eV range, one detect broad PL bands that are attributed to point defects when the crystal departs from perfection: vacancies, di-vacancies, anti-sites, combination of them. Regarding the defects giving a PL band, there is no unambiguous understanding for now. Interestingly, a series of sharp lines are detected at 4.1 eV and at energies below. Our attention was initially capture by their properties, Bourrellier et al. have performed cathodoluminescence measurement at 150 K and evidenced spatially localized zero-phonon assisted emission and phonon-assisted overtones [Fig 1.17(b,c,d)], as well as single-photon source behavior when excited by an electron beam [Fig 1.17(a)] [67].

Vuong et al. have done a preliminary investigation of the temperature-dependent light-matter interaction for ensembles of such color centers under light excitation [68]

**Figure 1.17**

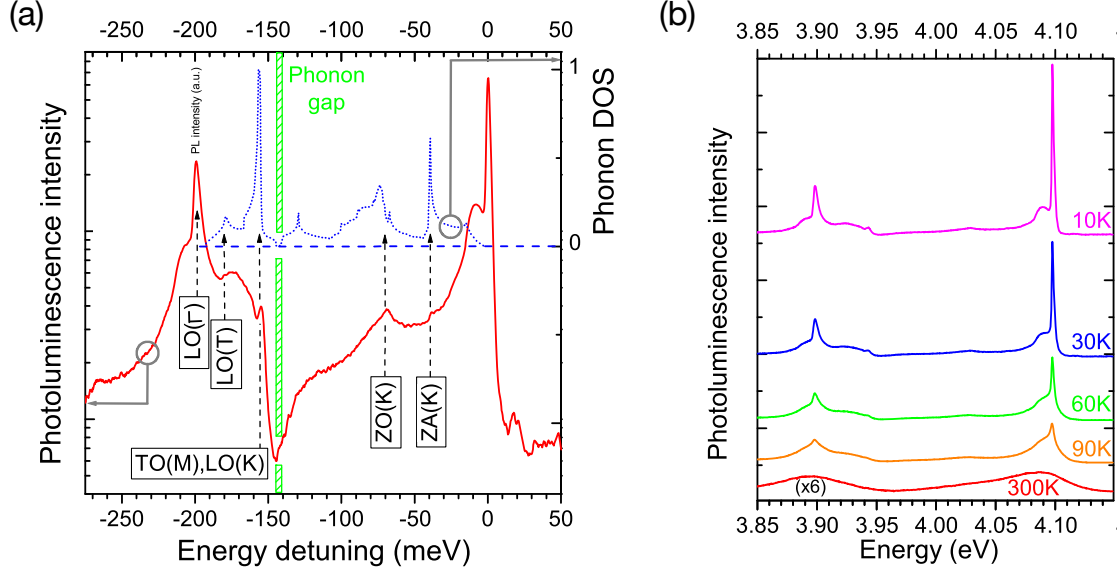
Cathodoluminescence spectrum of chemically exfoliated hBN flake suspended on a TEM grid (a-left) and normalized second-order correlation function (a-right) recorded on the emission spot in the white dotted square. (b,c,d) CL intensity maps of the peaks at 3.73, 3.91, and 4.09 eV, showing a perfect spatial match and therefore a unique origin [67].

and Koronski et al. have studied its localization by comparing the pressure dependence of the emitted light with the intrinsic behavior of the indirect bandgap of hBN [69]. The results obtained for the temperature study are shown on Fig 1.18(b), where the examination through a non-perturbative approach of the temperature dependence of the acoustic phonon sideband of the ZPL provides a value for the spatial extension of the defect  $\sigma \approx 2 \text{ \AA}$ , longer than the B-N bond length but shorter than the inter-layer distance in hBN. A peak-to-peak correspondence between the PL spectrum and the phonon density of states (phonon DOS) is presented on Fig 1.18(a), showing the phonon modes participating in the phonon-assisted emission of the defect at 4.1 eV. All these experiments plead in favor of a very localized level which in addition the density can be probed by tuning the growth protocol (doping, substrate, post processing treatment, irradiation). This is a good motivation for building an experimental platform of microscopy operating near 4 eV to probe single photon source emission by optical means rather than by cathodoluminescence.

### Near-UV to near-IR

In the near UV to visible range, that is to say in the 3.6 eV to 2 eV range, there are also a lot of signatures of defects.

In 2005, optoelectronic experiments have revealed that some defects in single crystals of hBN give rise to photoactive states within the BN bandgap at energy 3.6 eV [71]. The optical absorption and photoconductivity spectra in visible and UV region are


**Figure 1.18**

(a) Photoluminescence signal intensity at 10K (solid red line), on a semilog scale, for an excitation at 4.6 eV, as a function of the energy detuning with the zero-phonon line of the color center emitting at 4.1 eV, compared to the phonon density of states in hBN (blue dotted line) from [70]. (b) Photoluminescence spectrum of the 4.1 eV color center in hBN, for an excitation at 4.6 eV, from 10 to 300K [68].

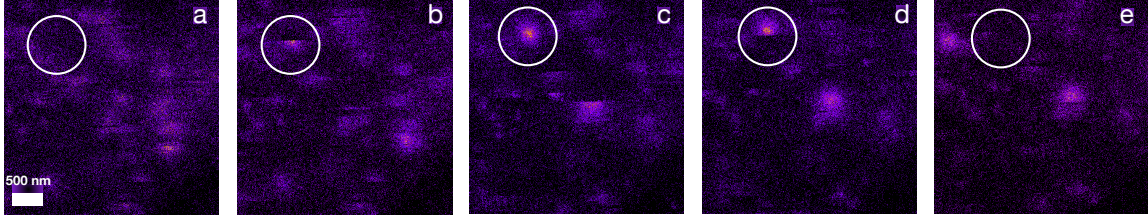
characterized by a steep rise at an energy threshold 3.6 eV. The shoulder at 3.6 eV indicating the presence of a donor or acceptor-like defect level within the band gap which traps free carriers that are photo-ionized by the excitation. Another study on photoinduced doping in heterostructures of graphene and boron nitride [72] have brought to light a strong photoinduced modulation doping effect in G/BN heterostructures with data supporting acceptor-like defects in hBN at 2.6 eV.

R. Bourrellier reported spectral lines between 2.1 and 2.3 eV [73], assigned to isolated defects that were generated under the electron beam irradiation. However, these defects exhibit emission instability under the electron beam as they are created and subsequently bleached over few scans like illustrated on the cathodoluminescence raster scans of Fig 1.19.

Deep defect related emissions at 3.03 and 3.77 eV have also been observed in time-resolved photoluminescence [74].

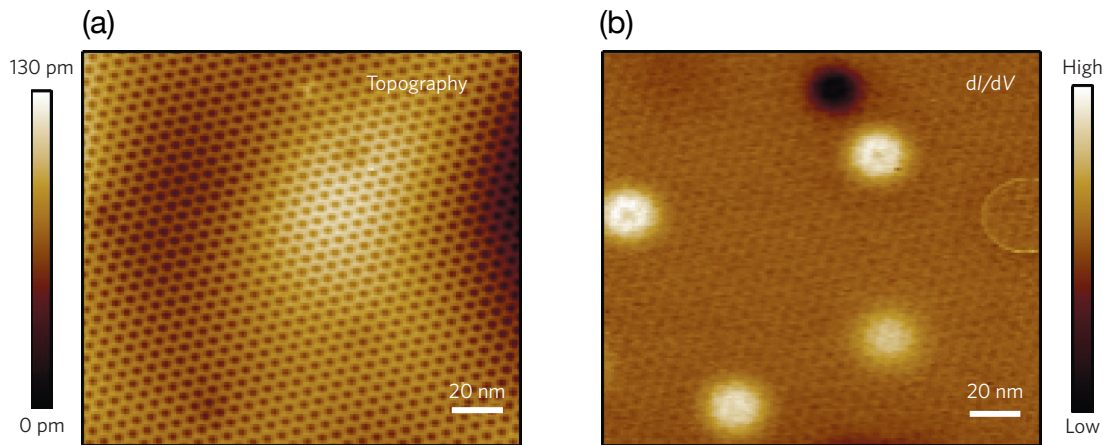
Heretofore, the studies on defects in the visible range have been limited to spatially averaged defect behavior. The investigation of individual defects at the nanoscale was first performed by Crommie et al. [75] in 2015. They showed for the first time individual/localized defects in bulk hBN in the visible range [75]. For that, they have used a STM microscope that had long been used for probing single atom or very small structure [76, 77]. However, it had never been used before with a bulk insulator material. To circumvent this issue the crystal was capped with a monolayer of graphene (which can be seen on Fig 1.20(a)), and they exploited the atomically thin nature of graphene



**Figure 1.19**

A CL filtered image is recorded on a area and present no localized emission (a). At the end of the second scan an emission spot is observed (white circle) (b). The emission spot is stable during the third scan (c) and then is destroyed through the fourth scan (d). Scan (e) shows that the spot has definitely disappeared [67].

to allow the visualization of defect phenomena in the underlying bulk boron nitride. The STM was used in spectroscopy mode ( $dI/dV$ , which reflects the probed material local density of states) in order to probe the charge state of the defects [Fig 1.20(b)]. Distance-dependent measurement of  $dI/dV$  was performed on different types of defects and allowed the assignment of bright and dark types of state. Ring defects were also identified and in this case they could measure the defect energy level with respect to the Dirac point energy of graphene and thus, knowing the energy position of the Dirac point respectively to the conduction band edge of BN, assess the energy position of the defect in the BN gap. Interestingly, they find that the energy level accounting for this defect lies  $\sim 4$  eV below the conduction band, similarly to the findings of Katzir et al. [26] presented in the beginning of this chapter 1.1.1, thus suggesting that the ring defect arises from a carbon impurity. Another important result is the possibility to alter in a reversible way the charge state of the defects or even neutralizing and ionizing them by applying an important electric potential above them with the tip of the STM.

**Figure 1.20**

STM topography (a) and corresponding  $dI/dV$  map (b) for a single layer of graphene deposited on top of a BN crystal. On (b) can be seen bright and dark dots as well as a ring [75].

The photodynamics of single emitters in the visible were first studied in early 2016

by Tran et al. [78] in multi and monolayer hBN crystals. Single emission centers are isolated in PL maps via a scanning confocal microscope [Fig 1.21(a)] operating at 532 nm and room temperature. In the multilayer case the zero-phonon line at 1.99 eV (623 nm) is clearly accompanied by two phonon replica at 1.83 and 1.79 eV (680 and 693 nm, respectively), not visible in the monolayer [Fig 1.21(b)]. The uniqueness of the localized luminescent center is evidenced by the recording of the second-order correlation function in both the multi and monolayer cases [Fig 1.21(c)]. The defect is claimed to be photostable in the multilayer case, and is very bright with a saturation intensity of few thousands of kilocounts per second. The defect emission is studied with a three-level model which provides a radiative lifetime of 3 ns and a metastable lifetime of 22 ns. Density functional theory (DFT) calculations directed the authors to assign the chemical origin of the emission to the  $N_B V_N$  center.

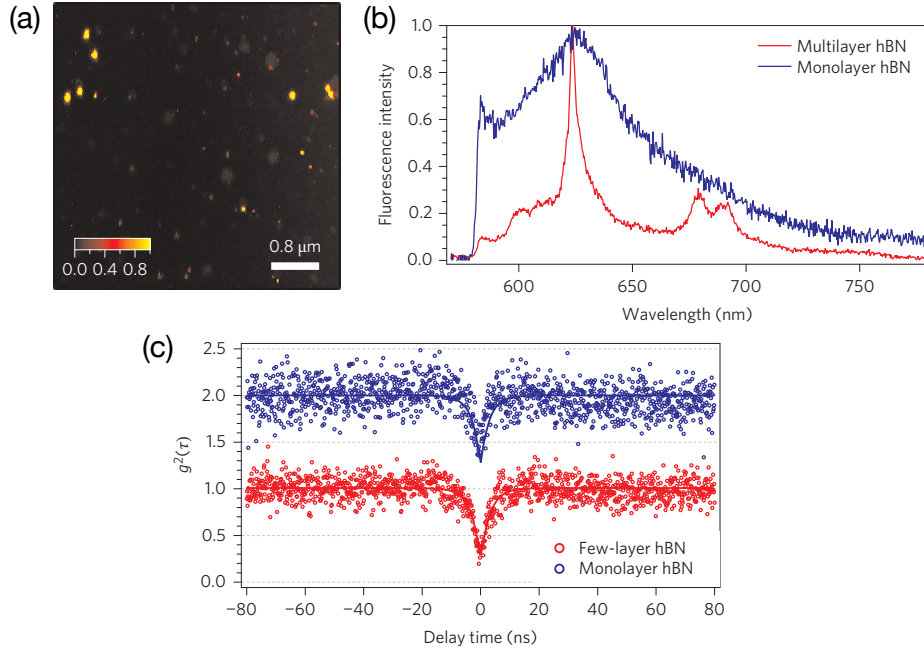


**Figure 1.21**

(a) Scanning confocal map of a multilayer hBN sample. (b) Room-temperature photoluminescence spectra of a defect center in hBN monolayer (blue trace) and multilayer (red trace). (c) Antibunching curves from an individual defect center in hBN monolayer (blue open circles) and multilayer (red open circles) [78].

## 1.5 Conclusion

We have first presented the structural properties of the layered material hBN as well as its electronic band structure. The atoms are tightly bound within a layer that interact weakly with the surrounding layers by van der Waals forces. In the bulk form, it is an indirect bandgap semiconductor with an indirect excitonic transition at  $E_{iX} = 5.955$  eV. Recently in our team, we have shown that hBN undergoes indirect to direct gap

transition when thinned to a monolayer, thus following the trend observed in other 2D-like materials.

Based on previous studies carried out in our laboratory, we have then presented and explained the intrinsic optical properties in the deep UV part of the PL spectrum of the bulk hBN, namely the exciton band edge emission and exciton recombination at stacking faults. As far as the former is concerned, the recombination of the indirect exciton is strongly assisted by phonon emission at the middle of the Brillouin zone (T), each of which additionally possesses a multiplet structure in the spectrum, due to overtones of the interlayer shear mode, specific to layered material. For the latter, multiple K-K' intervalley scattering with transverse optical phonons as well as final density of state provided by stacking faults in the crystal account for three of the peaks observed and their high intensity, while extrinsic origins, namely nitrogen vacancy and boron-nitrogen divacancy are supposedly responsible for the two others (D<sub>2</sub>, D<sub>6</sub>). This region of the spectrum is thus quite well understood, with experimental studies agreeing with theoretical one.

We have presented in the last part the emission related to point defects in hBN. Optically active defects are found over a large range of energies, from  $\sim 2$  eV to  $\sim 4$  eV. The properties of the defect at 4.1 eV has been studied in ensemble and its electronic-vibronic interaction is understood. Recently, cathodoluminescence in a STEM microscope have evidenced for the first time emission from such a single center, demonstrating the uniqueness of this defect. Under both photon and electron excitation, the color center exhibits a strong photostability. However under the electron beam, a broad background emission is created at the same energy, thus precluding the classical analysis of the photo-dynamics of the center. As for the emitters in the visible to near-IR range, they have been similarly evidenced in both photon and electron microscope, but manifest less stable behaviors, with photo-bleaching reported. Of particular interest, emitters around 2 eV present single-photon statistics, both in multi- and mono-layer hBN, indicating that the defect should lie within the atomic plane. Last but not least, the experimental proof that the charge state of defects at the surface of hBN crystal can be reversibly manipulated from "on" to "off" states is of great interest for the development of quantum nanotechnologies that requires electrical manipulation of single defects. Lastly, the knowledge on the origins of the defects, both in UV and visible to near-IR range, are however limited at this point.

In summary, the presence of isolated single color centers in hBN, a 2D material already exhibiting unique properties due to its large bandgap in the deep UV and its highly anisotropic structure, hold much promises in the view of elaborating hybrid quantum systems, potentially coupled to other 2D materials, integrating single color centers emitting from the near-IR to near-UV range.





## Single defects emitting in the visible range

IN THIS CHAPTER, I present the research carried out on isolated emitters in hexagonal boron nitride (hBN) by means of a scanning confocal microscope operating in the visible range at room temperature. Single point defects embedded in a solid-state matrix, acting as quantum source of light, are of great interest for quantum technology and sensor applications. Here, the photophysical properties of single-photon emitters are analyzed and their photodynamic behaviors studied through photon correlation measurements. The work accomplished in this chapter have led to the publication of an article in Phys. Rev. B in 2016 [79]. As explained in the first chapter of this thesis, at the time of this publication, the research activity on single defects in hBN was only dawning, with only one article reporting on the isolation of individual defects emitting in the visible range [78]. Since this seminal paper, an intense research activity has been devoted to the study of single-photon source in hBN, leading to a large number of publications [80–86].

### 2.1 Experimental setup

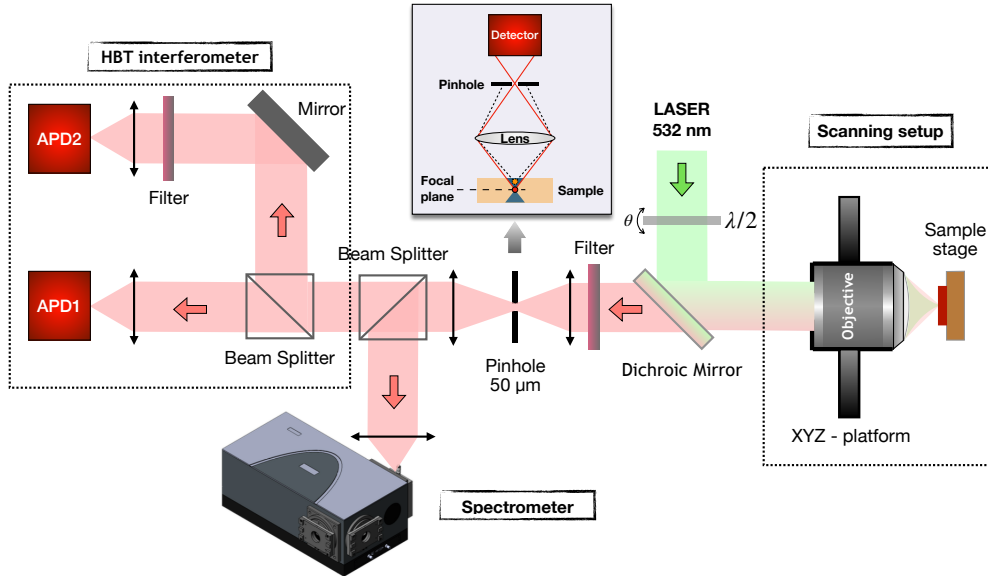


**Figure 2.1**

*Scheme of the experimental setup. Inset: illustration of how the pinhole permits to filter the light in the axial dimension.*

A scheme of the experimental setup is presented on Fig 2.1. We use a scanning confocal microscope operating under ambient conditions (300 K, 1 atm). Optical illumination is carried out at the wavelength  $\lambda = 532$  nm originating from the second harmonic of a Nd:YAG laser. The laser beam is focused onto the sample with a high numerical aperture (NA=1.35) oil-immersion microscope objective (Olympus) providing an excitation spot size in the order of  $300 \times 300$  nm<sup>2</sup>. The objective is mounted on xyz-piezoelectric platform. The photoluminescence (PL) response of the sample is collected by the same objective and spectrally filtered from the remaining excitation laser with a razor-edge long-pass filter at 532 nm (Semrock, LP03-532RU). The collected PL is then focused into a 50-nm-diameter pinhole conjugated with the focal plane of the objective. This permits to spatially filter the light in the axial dimension by selecting only beam rays coming from the focal plane (cf. inset of Fig 2.1), therefore improving the signal-to-noise ratio (SNR) of the collection system. Finally the PL is directed either to a spectrometer (Ocean Optics, QE Pro-FL) or to silicon avalanche photodiodes (Perkin Elmer, AQR-14) operating in the single-photon counting regime. The single-atom nature of the emitters was verified by measuring the second-order correlation function  $g^{(2)}$  using two avalanche photodiodes, APD1 and APD2, mounted in a HBT configuration. To avoid optical crosstalk between APDs, an interference phenomenon due to the backward emission of an infrared photon after a detection event, an additional filter is placed in front of APD2. The overall detection efficiency  $\zeta$  of the experimental setup, expressed as the product of the collection efficiency ( $\propto$  NA) by the optical transmission of the optics and by the quantum efficiency of the photodetectors (65% at 650 nm), is estimated to  $\zeta \sim 1\%$ . A half-wave plate  $\lambda/2$  set on a rotation mount positioned before the dichroic mirror enables the control of the excitation polarization.

## 2.2 Sample and typical results

### 2.2.1 Sample

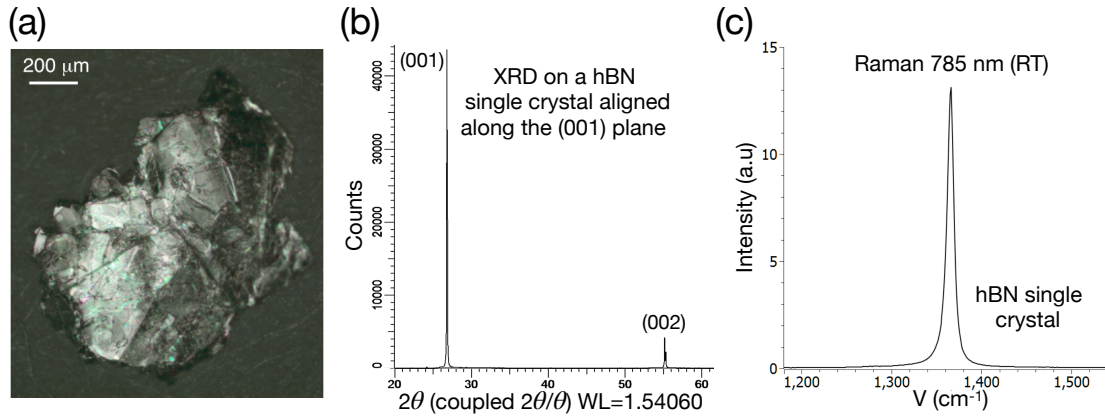


**Figure 2.2**

(a) Microscope image of a high-purity hBN crystal, as received from the commercial distributor. (b) X-ray diffraction showing a crystal orientation in the (001) plane, and (c) Raman spectrum displaying a peak at  $1365$  cm<sup>-1</sup> [28].

The hBN crystal utilized in the study presented in this chapter is a high-purity hBN monocrystal from the company HQ Graphene [28], with a size of about 1 mm, as shown on Fig 2.2(a). Both X-ray diffraction (XRD) and Raman spectroscopy are indeed very clean, and show a crystal highly oriented in the (001) plane, as well as a Raman peak centered at  $1365\text{ cm}^{-1}$  [Fig 2.2(a),(b)], as expected for a good crystallinity [87]. The sample is placed onto the sample holder and a drop of immersion oil is deposited on it before approaching the microscope objective until contact.

### 2.2.2 Confocal maps of photoluminescence, dipole-like emission and photostability

#### Map of photoluminescence

Typically, the confocal microscope was used to scan between 5 and 15  $\mu\text{m}$  below the surface of the hBN crystal in order to avoid background PL from contamination at the surface. Fig 2.3 displays a confocal image obtained with the confocal setup on a surface of  $12 \times 12\text{ }\mu\text{m}^2$  with a pixel size of  $50\text{ nm}^2$ . Several localized hot spots (yellow/orange) emitting photons above the background are discernible. Depending on the defect, the background represents from 5 to 50% of the signal. We notice that the density of hot spots is quite high. To study a single spot and make sure the defect is well isolated from other emitting centers, a more resolved confocal scan is performed in a narrower region around a particular spot, as presented in Fig 2.3.

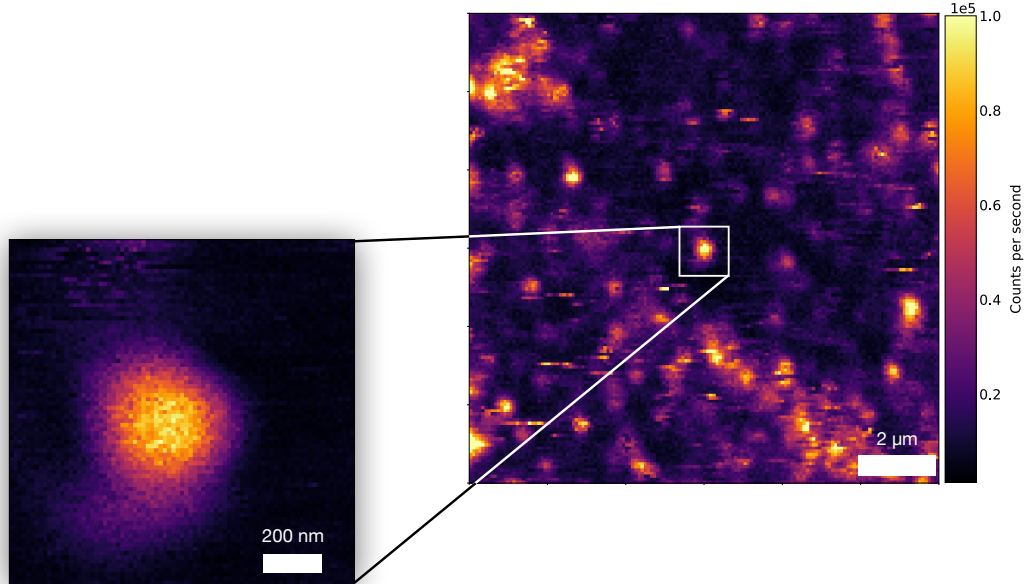


**Figure 2.3**

*Typical scan obtained with the confocal microscope. The brighter dots (in yellow/orange) indicate intense local emission of light.*

### Polarization investigation

To understand whether the localized emission spot consists of a single dipole or multiple dipoles, we performed excitation and emission polarization measurements. The excitation polarization measurement [Fig 2.4(a)] consists in recording the PL intensity emitted by the sample for different directions of the incident beam polarization  $\theta_{exc}$ , which is changed by a half-wave plate  $\lambda/2$  that rotates the fixed polarization  $\theta_0$  of the laser. After correction of the background, the PL intensity for each angle is plotted on a polar-projection diagram [Fig 2.4(b)]. This plot reflects the polarization dependence of the absorption of the emitter. For the emission polarization measurement [Fig 2.4(c)], the sample is illuminated at the maximum of absorption and the PL is recorded for only one emission polarization  $\theta_{em}$ , filtered by a polarizer. The data are plotted in Fig 2.4(d), and correspond to the angular diagram of emission. The diagrams reflect a well-defined dipole-like character for the defect isolated in Fig 2.3. The corresponding fits are obtained using a  $\cos^2(\theta)$  fitting function, and yield an excitation and emission polarization visibility of 89 and 78%, respectively; this is characteristic of a single linearly polarized dipole transition.

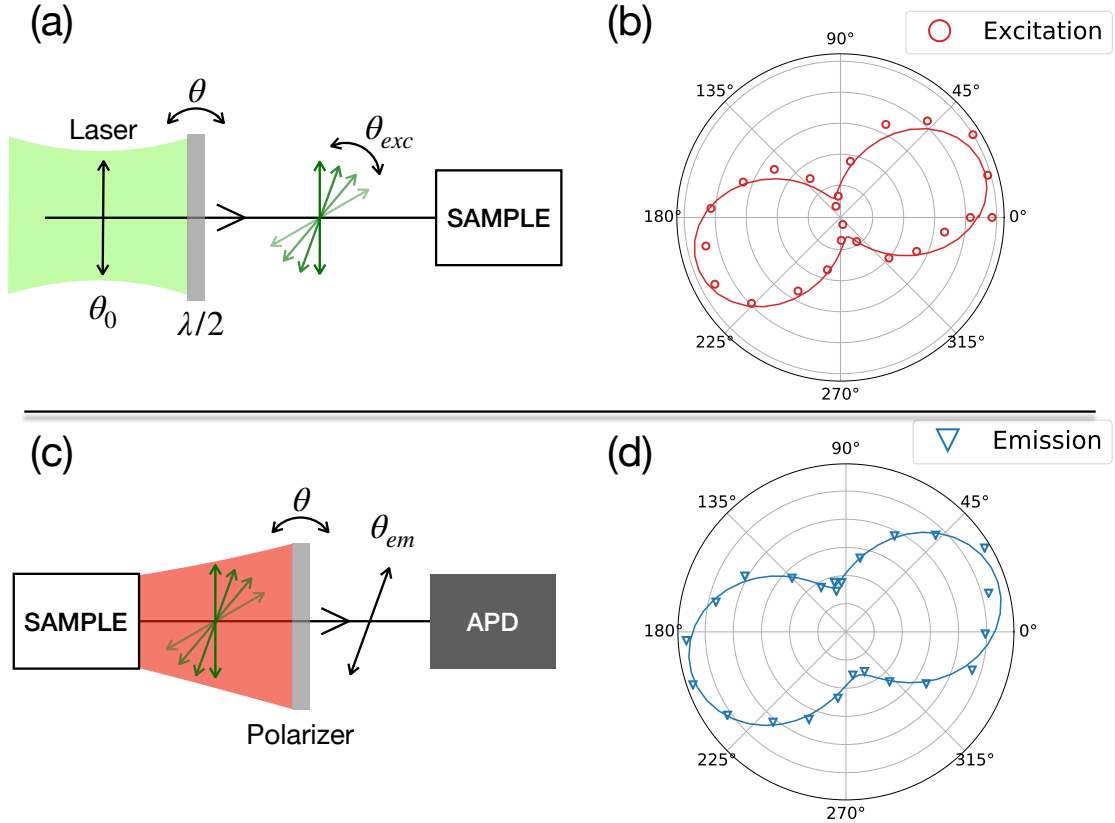


**Figure 2.4**

Schematic of the setup to perform excitation (a) and emission (c) polarization measurement, and corresponding angular diagrams for the excitation (b) and emission (d). The markers correspond to the data while the solid lines are fitting with a  $\cos^2(\theta)$  function.

### Photostability of the defects

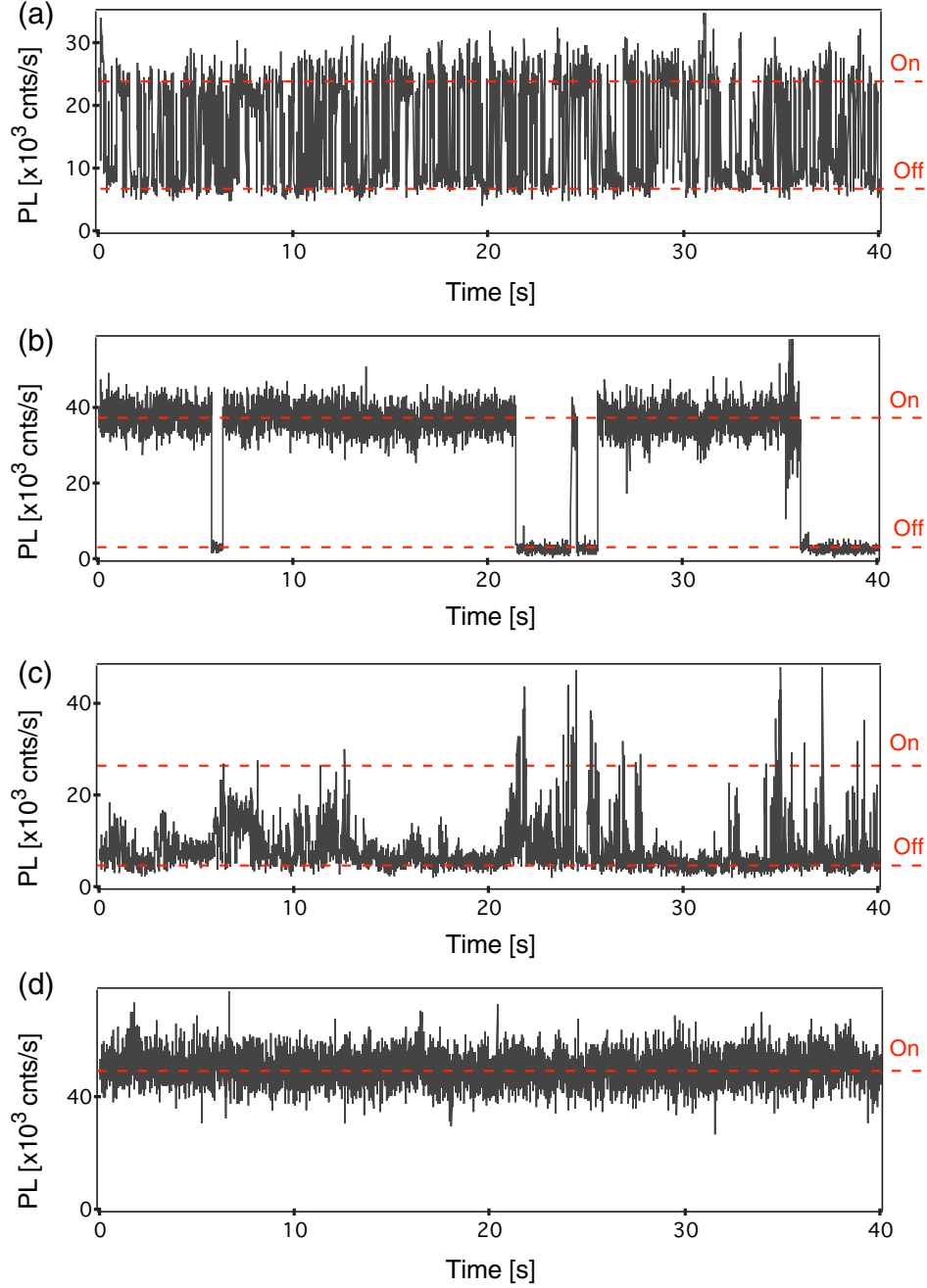
Considering the use of single defects for quantum technology, one property of paramount importance is the photostability over time. The isolated defect presented in Fig 2.3 exhibits a very stable emission over time, corresponding to the PL time trace shown on Fig 2.5(d). However, this is not the majority of cases and the other typical PL time traces recorded at low laser power from individual defects hosted in the crystal are represented on Fig 2.5. On each diagram, the continuous black line represents the oscillating PL evaluated on the vertical axis in kilocounts (kcnts) versus the time in seconds on the horizontal axis. The time binning is 10 ms and the laser power used is 10  $\mu$ W (measured right before entering the objective of the microscope). Most defects exhibit a pronounced blinking behavior, as it is often observed for solid-state emitters at room temperature like quantum dots [88], dye molecules [89] and deep defects in wide-bandgap materials [90]. The switching rate between the "on" and "off" states varies significantly from one emitter to another [Fig 2.5(a)-(c)], which suggests that the blinking dynamics are strongly linked to the local environment of the defect. This is consistent with the fact that 2D crystals are greatly exposed to the external environment. Such a blinking could originate from optically-induced charge state conversion mediated by a charge exchange with other defects acting as electron donors or acceptors and could be tempered by encapsulating the defect and annealing the crystal to reduce the charge traps [91]. Permanent photobleaching, in other words the irreversible conversion of an optically-active defect into a non-fluorescent entity, was also observed after few minutes of optical illumination for most emitters. However, around 5% of the emitters exhibit a perfect photostability over time [Fig 2.5(d)], even under high laser excitation power, as observed for few types of defects in diamond and SiC at room temperature [92]. This ratio might be improved through annealing procedures and chemical modifications of the sample surface [93]. On average, one stable defect could be found in each  $50 \times 50 \mu\text{m}^2$  scan of the sample.

### 2.2.3 Photoluminescence properties

#### Vibronic spectrum of the defects

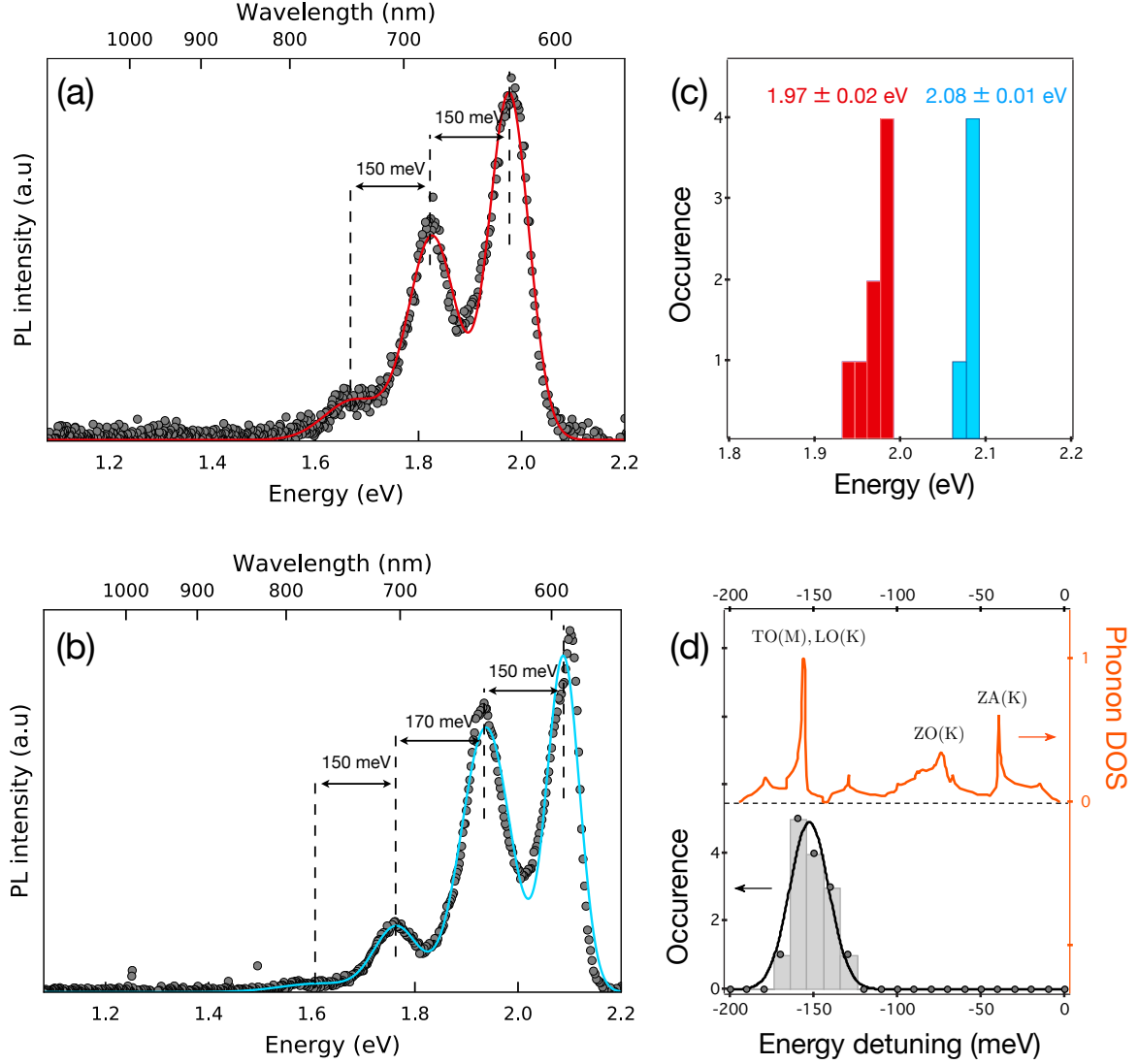
We now present in Fig 2.6(a)-(b) the typical emission spectra recorded at room temperature from individual emitters. On the vertical axis is represented the PL intensity in linear scale and on the horizontal axes the detection energy in eV (bottom) and wavelength in nm (top). On both spectra, three distinct peaks are observed with decreasing intensities from higher to lower energies. We identify the most-right peaks with the zero-phonon line (ZPL) of the defect and the low energy peaks with phonon replica. Each spectrum was fitted with a multi-Gaussian function to extract the spectral features. Two families of spectra with similar overall structure are identified: a first family with ZPL energy at  $1.97 \pm 0.02$  eV (629 nm) and width FWHM  $\sim 90$  meV [Fig 2.6(a)], a second family with a ZPL energy at  $2.08 \pm 0.01$  eV (596 nm) and width FWHM  $\sim 70$  meV [Fig 2.6(b)]. These average values and standard deviations are obtained from the statistics performed over 13 single defects, presented in Fig 2.6(c). We stress that no correlation could be found between the spectrum and the photostability of the defect.

We note a characteristic energy detuning of  $150 \pm 10$  meV between the phonon



**Figure 2.5**

Typical PL time traces recorded from different individual defects in a high purity hBN crystal. Horizontal axis represents time in second and vertical axis the number of counts per second on one APD. The laser excitation power is tuned to  $P = 10 \mu\text{W}$ . Bin size: 10 ms. (a) displays a very unstable behavior, it is called a blinking defect. (b) shows a bleaching behavior and (c) is an intermediate state. (d) is a stable defect with a relatively small standard deviation around the mean value of counting rate. The "on" and "off" horizontal dashed lines are guide line to indicate the photo-active and the photo-inert behavior of the emitter.

**Figure 2.6**

(a, b) PL spectra recorded from individual defects in hBN at room temperature under green laser illumination at 532 nm. The filled circles are experimental data while the solid lines are data fitting with multiple-Gaussian functions. (c) Histogram of the ZPL energy for a set of 13 single defects. (d) Bottom: Histogram of the energy detuning between the ZPL and the phonon replica. Top: phonon density of states (DOS) in hBN extracted from [70].

replica. A similar energy spacing was also reported in the case of single defects in multilayer hBN fakes [83, 94]. In fact, this value fairly matches an extremum of the phonon density of states in bulk hBN linked to transverse (TO) and longitudinal (LO) optical phonons at the K and M points of the Brillouin zone [Fig 2.6(d)] [70]. Our defects being linked to deep levels with a transition energy much smaller than the 6 eV bandgap of hBN, we expect an extension of the electronic wavefunction comparable to, or smaller than the lattice parameter of the hBN matrix [95]. As a consequence, the defect wavefunction in k-space is spread over the whole Brillouin zone with a sig-



nificant coupling to the zone-edge phonons, like at the K and M points (meaning high k-momentum). Since the interaction with optical phonons is much more efficient than with acoustic ones [63], we interpret the systematic 150 meV-energy detuning of the phonon replicas as resulting from a dominant coupling to the zone-edge optical phonons of highest density of states Fig 2.6(d).

### Different charge states

Individual defects in wide-bandgap materials can often be found in various charge states having very different optical properties. A well-known example is the NV defect in diamond, whose ZPL energy is shifted by  $\simeq 200$  meV depending of the charge state  $\text{NV}^0/\text{NV}^-$  of the defect [96, 97], and becomes even optically inactive in its positively-charged state  $\text{NV}^+$  [98, 99]. As discussed in the first Chapter Section 1.4.3, by using scanning tunneling microscopy (STM), it was shown that individual defects in hBN can also be found in positive, negative and neutral charge states [75]. Active charge state manipulation was even demonstrated by tuning the Fermi energy level with respect to the defect charge transition level by locally applying an electric field with a STM tip [100]. According to these considerations, we tentatively attribute the two groups of spectra shown in Fig 2.6 to different charge states of the same defect, while the small variation of the ZPL energy in each group ( $\pm 20$  meV) might result from local variations of the strain in the hBN matrix. It has actually been demonstrated that strain control allows spectral tunability of hBN single emitters over 6 meV, for a family of defects emitting around 2 eV [85]. Optically-induced charge state conversion towards a dark-state might also play an important role in the blinking/bleaching dynamics of the defect.

### Summary

To sum up, through spatially-resolved PL maps on bulk hBN crystal, we have shown the existence of point-like defects with single-dipole-type emission. In the PL map, the density of bright spots is quite high but the defects featuring a stable optical behavior represent only 5% of them. However, when it is the case, the defect is highly stable and reliable, even after few days or more. These defects form two families of spectra whose ZPL are shifted by  $\sim 100$  meV, and exhibit vibronic features arising from coupling with optical phonons (TO(M), LO(K)) at the edge of the Brillouin zone. We will now present the investigation on the single nature of these emitters, which requires to perform photon correlation measurements.

## 2.3 Statistics of photon emission

This section is dedicated to the presentation of the theoretical and experimental tools used to probe the photodynamics of the emitting centers detected in the confocal scans.



### 2.3.1 The second-order correlation function

The **second-order correlation function**  $g^{(2)}(\tau)$  (also referred to as the correlation function), is by far the most common quantity employed for determining the quality of a single-photon source as well as its properties. It is a measurement of the correlation in intensity of the light source, and is expressed as follows:

$$g^{(2)}(\tau) = \frac{\langle I(t)I(t+\tau) \rangle}{\langle I(t) \rangle \langle I(t+\tau) \rangle} , \quad (2.1)$$

where  $\langle \cdot \rangle$  denotes statistical averaging over time.  $I(t)$  is the electric field intensity at time  $t$ . To give a practical meaning to this function, we can think of it as answering the question: if I detect a photon at time  $t$  what is the probability to detect another photon at time  $t+\tau$ ? More precisely, it informs us on the degree of correlation between the number of photons detected at time  $t$  and at time  $t+\tau$ .

A very **important value** is the value at  $\tau = 0$ , which is linked to the probability of emitting two photons simultaneously. For a classical source of light, that is to say with a classical electromagnetic field, Eq 2.1 provides the two following fundamental relations 101:

$$g^{(2)}(\tau) < g^{(2)}(0) , \quad (2.2)$$

$$g^{(2)}(0) \geq 1 . \quad (2.3)$$

These two relations intrinsically define the regime of classical emission, and the violation of any of them is sufficient to claim that the light is of quantum nature.

In contrast, in the case of a quantum source of light, that is to say by considering the quantum electromagnetic field decomposed into annihilator and creator operators, one can find with eq. 2.1 the important relation:

$$g^{(2)}(0) = 1 - \frac{1}{N} , \quad (2.4)$$

where  $N$  represents the number of emitters participating in the emission process. In particular, we see that if  $g^{(2)}(0) < 0.5$  then  $N < 2$ , in other words  $N = 1$  and we are in presence of a single-photon source. If  $0.5 \leq g^{(2)}(0) < 1$  it means that there are several emitters. In resume, the essential criterion is:

$$\boxed{g^{(2)}(0) < 0.5 \implies \text{Single-photon source}} \quad (2.5)$$

These concepts and results are important for the interpretation of our measurements. The reader not accustomed to them may refer to Appendix A where we discuss the different types of light on the basis of the statistics of emission of the source, and derive the fundamental properties of the second-order correlation function for the cases of classical and quantum electromagnetic fields.

### 2.3.2 Experimental setup: HBT interferometer

To obtain the  $g^{(2)}(\tau)$  function, an optical interferometer is mounted, as originally designed by Robert Hanbury Brown and Richard Q. Twiss in 1956 for use in radio astronomy [102, 103]. In the following it is simply called HBT interferometer. Fig 2.7 depicts a scheme of the HBT setup. The incident light is split into two distinct paths by a beam splitter (BS), both paths leading the photons to two independent single-photon detectors (D1 and D2), and some form of timing or coincidence electronics counter. In order to access the value of  $g^{(2)}(\tau)$  close to  $\tau = 0$ , the time-counting accuracy of the detectors and electronics used must be excellent, in the order of hundreds of picoseconds or less.

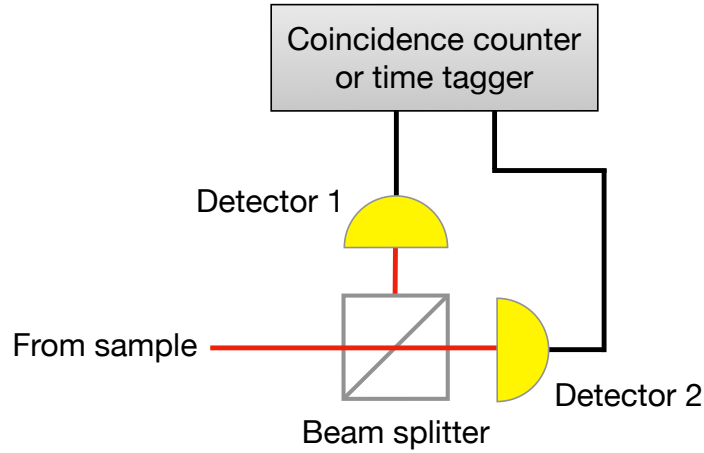


**Figure 2.7**

*HBT interferometer. The incident photons are separated in two paths by a beam splitter and sent to two discrete single-photon detectors, connected to a time tagger or a coincidence counter.*

The fact that the photons are recorded on two distinct detectors without making them interfere beforehand, is responsible for the loss of information about the phase. Consequently, the HBT interferometer is only about intensity correlation.

#### Working principle

To record the  $g^{(2)}(\tau)$  function, the principle is to build the histogram of time intervals corresponding to the delay between the detection of a photon on D1 and a successive one on D2. For that, we have at our disposal an acquisition card that is able to do two things: time tag all photon arrivals during a certain interval and store the data on memory (to be post-processed), or directly compute and register the time delay between two successive detections on D1 and D2. The two methods, upon appropriate normalization and in the correct conditions (cf. discussion in 2.3.3), yield an accurate representation of the second-order correlation function.

We see that in the case of a single-photon source, only one photon at a time is incident on BS, consequently there is no way for both detectors D1 and D2 to detect a

photon simultaneously because a single photon state can not be divided in two separated paths, thus  $g^{(2)}(0) = 0$ .

### Time accuracy limitations

Even though the single-photon detectors are ultra-fast counting devices, their electronics suffer the need to recover after the detection of a photon. This "deadtime" is inevitable and Perkin-Elmer gives a value of 40 ns for each APD. The value of the deadtime is always well beyond the dynamic range we aim at probing to unveil or not a phenomenon of antibunching, irrespective of the type of detector employed. It explains why it would be impossible to probe the short time correlation with only one detector, which would be blind during the deadtime after a first photon detection. The issue is circumvented by using two detectors: D1 starts the timer and then D2 starts to record quasi-instantly. Another limitation in our measurements is the minimum bin time of the histogram recorder, which was  $w = 200$  ps. However this value is generally small enough to record the dynamics of the emission. The limitation of any HBT interferometer is actually set by the time accuracy of the detector, called the time jitter of the electronics, which fundamentally limits the capability to probe the short time delay. It is measured by recording the instrument response function (IRF) of the setup. A

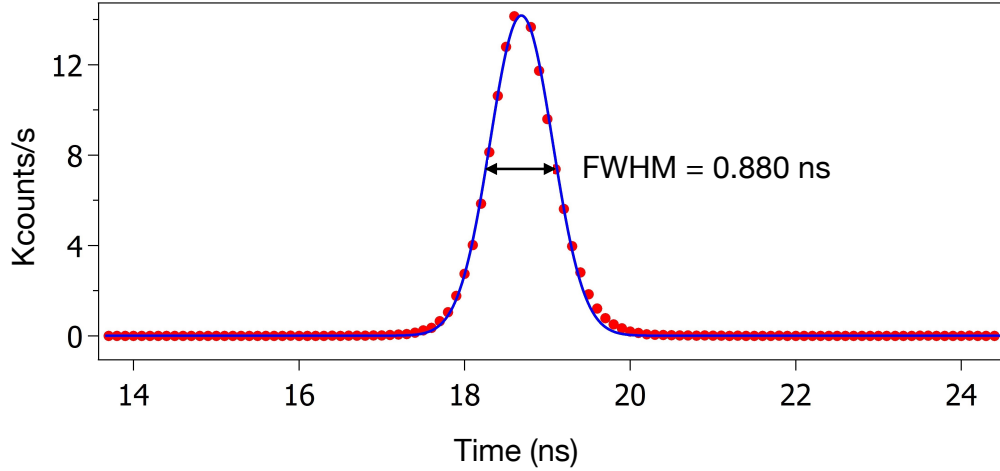


**Figure 2.8**

*Instrument response function (IRF) of the detection setup. 50 ps laser pulses are sent to probe the temporal broadening induced by the electronics of the detectors. Red circle are data whereas the solid blue line is a gaussian fit to the data. FWHM = 880 ps.*

short laser pulse of known width is sent through the detection setup, and the diagram of photon arrivals is reconstructed with the detector events. The pulse width need to be much shorter than the IRF. The IRF profile was obtained by using 50 ps laser pulses (attenuated to protect the detectors) and the result of the acquisition is shown on Fig [2.8](#): it displays a profile that corresponds to the convoluted Gaussian response of both APDs. Thus a Gaussian function is employed for fitting the data and the FWHM is obtained from the standard deviation  $\sigma$  of the function by:  $\text{FWHM} = 2\sqrt{2 \ln 2} \sigma \approx 2.355\sigma$ ,

which gives  $\text{FWHM} = 880$  ps. This is the average time response of the system.

To illustrate the limitations, let us take an example. Let a photon event happen on D1 at  $t = 0$ , the histogram recording goes off with D2 quasi-instantly and D1 is blind for  $\Delta t_{\text{deadtime}} = 40$  ns. A photon hits the detector D2 at  $t + \tau$  which triggers the coincidence counter to register a time delay event at  $\tau$ . Due to the time jitter, the detection system is incapable of distinguishing between values of  $\tau$  smaller than 880 ps, it will thus consider that the two events were simultaneous. Otherwise, the finite width of the IRF leads to an uncertainty around the zero time delay. We shall see later the consequences in the analysis of the data.

### 2.3.3 Discussion on the experimental procedures to access time-photon correlation

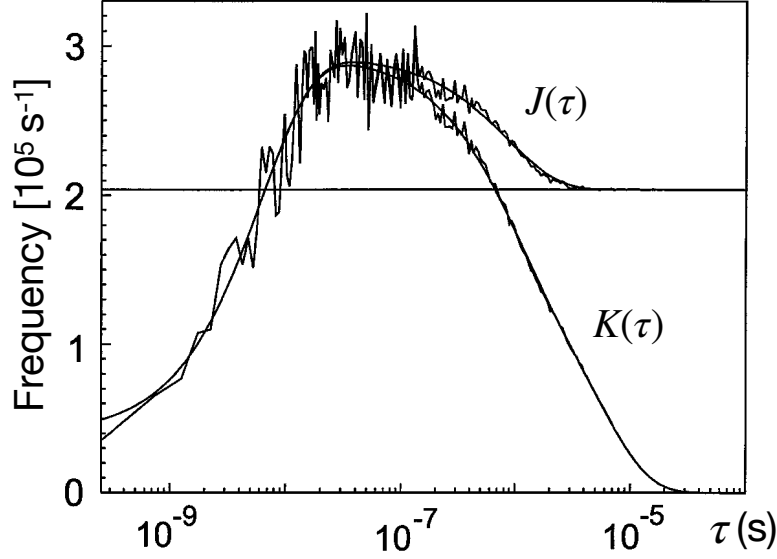
In order to probe the statistical fluctuations in intensity of the source, different experimental techniques have been developed, historically for single-molecule experiments [104, 105]. The specificity of the methods are due to the difference of probing two different quantities  $K(\tau)$  and  $J(\tau)$  [106, 107] that are both suitable to represent  $g^{(2)}(\tau)$  in their respective conditions of validity.  $K(\tau)$  is the probability to detect the first photon at time  $\tau$  given an initial detection at  $\tau = 0$ . This distribution is commonly recorded using a "start-stop" experimental scheme (described below). On the other hand,  $J(\tau)$  is the probability to record a photon at time  $\tau$  provided that there was a photon at  $\tau = 0$ . In other words, the latter quantity represents the number of photons detected at time  $\tau$ , independent of whether there was a detection event in between  $\tau = 0$  and  $\tau$ . The second-order correlation function  $g^{(2)}(\tau)$  is proportional to  $J(\tau)$  [106]:

$$g^{(2)}(\tau) \propto J(\tau) . \quad (2.6)$$

Hence,  $J(\tau)$  is the correct quantity to measure. The discrepancy between the two histograms is well illustrated on Fig 2.9, extracted from the article of Fleury et al. [107]. We see that for an emitting single-photon source with a detection rate  $R \sim 10^5 \text{ s}^{-1}$ , the histogram  $K(\tau)$  departs from the  $J(\tau)$  histogram for time delays exceeding 100 ns. If the emitting rate of the source is higher, then the discrepancy happens at even shorter time.

#### Short-time scale: the "start-stop" method

By far, the most common method to measure the  $g^{(2)}(\tau)$  is the "start-stop" method [105, 108]. The histogram  $K(\tau)$  of time interval between two-photon pair are recorded by triggering the start of the histogram with a detection event on D1 and subsequently stopping it with a photon detection on D2. The measurement is repeated a large number of times. This method is suitable only to probe the short-time scale, or more precisely it is accurate for  $\tau \ll R^{-1}$ , where  $R$  is the detection rate. Indeed, in this condition, the correlations are properly measured because it is rather unlikely to have more than one photon in the time interval  $R^{-1}$ , thus  $K(\tau)$  matches  $J(\tau)$  for  $\tau \ll R^{-1}$ . This condition is respected especially as the detection efficiency  $\zeta$  is small. If one attempt to record the correlation at longer time scale with the "start-stop" method, an artificial decrease of correlation will be observed.

**Figure 2.9**

Histograms  $K(\tau)$  and  $J(\tau)$ . The wiggly  $K(\tau)$  is the normalized histogram of the experimental interphoton times measured on a molecule. The wiggly  $J(\tau)$  was calculated using FFT. The smooth  $J(\tau)$  is a fit and the smooth  $K(\tau)$  is the corresponding prediction [107].

### No time scale restriction

In order to analyze the correlations of the light source without restriction to the short-time scale, we rather proceed by triggering the measurement with a photon detection on D1 and then by recording the time trace of photon arrivals on D2 during a time interval  $\Delta t$  in the order of few hundreds of  $\mu\text{s}$  to ms. The resulting histogram provides unnormalized  $J(\tau)$  after  $\mathcal{N}$  repetitions. The missing photon detections consequential to the deadtime of D2 that occurs during  $\Delta t$  are statistically filled by the high number of repetitions  $\mathcal{N} \sim 10^5$ . The acquisition card used in the experiment is a multiple-event time digitizer (FastComtec, P7889) with a large single sweep time range permitting to take data of up to 83 days with a time resolution of 100 ps.

Experimentally, an electronic delay  $\tau_d$  is introduced in order to obtain the full profile of the  $g^{(2)}(\tau)$  function at short time scale. It is usually achieved by physically lengthening the electronic cable of D2 (the STOP), but recent acquisition cards directly provide electronic delays. In this way, if two photons are emitted together, their collection will produce a count in the histogram at the binwidth corresponding to the delay  $\tau_d$ .

### Normalization of the histogram

Once acquired, the histogram of photon correlation must be properly normalized. The normalization should be such as if the emitting source would be of poissonian type, the normalized histogram would be flat at a value of 1. This normalization is essential for a correct analysis of the histogram representing  $g^{(2)}(\tau)$ .

To find the proper quantity to normalize  $J(\tau)$ , let us suppose that we have a poissonian distribution. After acquisition, each channel of the histogram is filled by approximately the same number of counts  $\bar{n}$  so that the histogram looks flat. The normalization would then only consist in dividing by  $\bar{n}$ . The histogram is composed of  $p$  channels of time width  $w$ . The integration time is  $\Delta t$  and is repeated  $\mathcal{N}$  times. We note  $N_T$  the total number of counts in the histogram and  $R$  the average count rate on the detector. We have:

$$N_T = R\Delta t\mathcal{N} = R(p \times w)\mathcal{N} . \quad (2.7)$$

And  $\bar{n} = N_T/p$ , so we obtain for  $\bar{n}$ :

$$\bar{n} = \frac{Rpw\mathcal{N}}{p} = Rw\mathcal{N} . \quad (2.8)$$

The second-order correlation function is thus finally obtained by dividing  $J(\tau)$  by  $\bar{n}$ :

$$g^{(2)}(\tau) = \frac{J(\tau)}{\mathcal{N}wR} . \quad (2.9)$$

## 2.4 Experimental results for the second-order correlation function

Fig 2.10 shows a very large scale measurement of the function  $g^{(2)}(\tau)$  over five temporal decades from an isolated PL spot of the hBN crystal. The data are normalized according to the procedure explained in Section 2.3.3. The data are represented in semi-log scale. The emitter was excited with a laser power  $P = 150 \mu\text{W}$  and the histogram was recorded with bin time of 200 ps. Measuring such a broad  $g^{(2)}(\tau)$  is a performance that requires a large-range time-to-digital converter acquisition card. Usually, second-order correlation functions are taken separately for short time — with  $K(\tau)$  — and long time — with  $J(\tau)$ . We recall that the electronic delay  $\tau_d$  represents the delay for a pair of photons emitted simultaneously.

One can first notice the antibunching occurring at  $\tau_d$ . According to the criterion given by Eq (2.5), the value  $g^{(2)}(\tau_d) \approx 0.25 < 0.5$  is a clear signature of single-photon emission from an individual defect. Nonetheless, it does not fall to 0. A first reason to explain this observation could be the background light originating from the host matrix itself around the defect. However, owing to a high signal-to-noise ratio ( $\text{SNR} > 20$ ), this possibility is dismissed [109]. As a matter of fact, it rather results from the electronic jitter of the detectors which is taken into account in the IRF of the detection setup [inset of Fig 2.10], as discussed above in Section 2.3.2.

The correlation function also reveals a large photon bunching  $g^{(2)}(\tau) > 1$ , revealing that the single photons are grouped by packet over a certain timescale. The bunching starts shortly after  $\tau_d$  and lasts for a very long time until  $\tau \sim 2 \times 10^4 \text{ ns}$ . We witness here the importance of normalizing with a poissonian distribution. Indeed, a short-time measurement would have displayed the bunching around  $\tau_d$  as a flat poissonian-like distribution and the normalization with the value of the falsely flat part would have provided a smaller value of  $g^{(2)}(\tau_d)$ . This error can lead to wrong conclusions about the

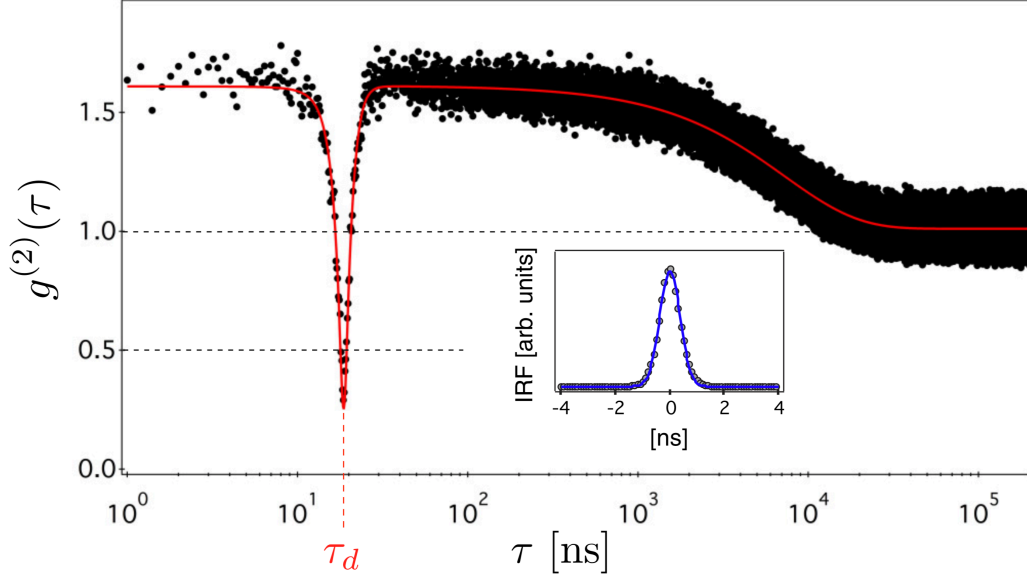


**Figure 2.10**

$g^{(2)}(\tau)$  function recorded from a PL spot for a laser excitation power  $P = 150 \mu\text{W}$  and a bin width  $w = 200 \text{ ps}$  and displayed on a log x-scale. Black dots are experimental data and the solid red line is data fitting using a three-level model while including the IRF of the detection setup, see next section.  $\tau_d \approx 20 \text{ ns}$  is the electronic delay.

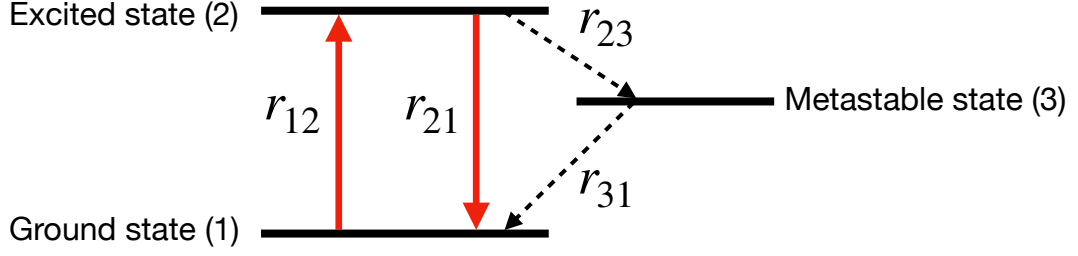
nature of the source.

Starting from this  $g^{(2)}(\tau)$  acquisition, the purpose is now to elaborate a model that accounts for the observed features. The simplest model one can think of is the two-level system — ground and excited state — which readily explains the antibunching phenomenon: after the emission of a first photon, the system is in his ground state and is unable to emit a second photon immediately. However, the bunching effect can not be described by this model, therefore indicating that another state has to be added to our basic two-level system. Moreover, owing to the very slow decay of  $g^{(2)}(\tau)$  after  $\tau_d$  to reach the value 1, we can already tell that the third level is a long-lived metastable state. Thus, in the following, the defect emission will be modeled by a three-level system, and the different transition rates determined in order to study the photodynamics of the emitter.

### 2.4.1 Theoretical model for the photodynamics: the three-level system

Fig 2.11 depicts the three-level system chosen to model the defect emission. The system is initially in its ground state (1). Under radiative excitation it goes in the excited state (2) with a transition rate  $r_{12}$ . Then, it can either be radiatively desexcited to (1) with a rate  $r_{21}$ , or get trapped into the metastable state (3) at rate  $r_{23}$ , from which it goes back to the ground state (1) with a rate  $r_{31}$ .




**Figure 2.11**

Schematic energy scheme showing the ground (1) state, excited singlet state (2), and metastable triplet state (3), and the various transition rates between the states.

### 2.4.2 Derivation of $g^{(2)}(\tau)$ for a three-level system

We now to give an expression of the second-order correlation function for the three-level system. For that, we translate the time-averaging of the intensity  $I(t)$  of the electric field in Eq (2.1) in terms of detection probability. It can be shown [110] that a meaningful expression for  $g^{(2)}(\tau)$  is:

$$g^{(2)}(\tau) = \frac{P_{12}(t, t + \tau)}{P_1(t) \times P_2(t + \tau)} \quad , \quad (2.10)$$

where  $P_{12}(t, t + \tau)$  refers to the joint probability of finding a photon on detector D1 at time  $t$  and then one photon on detector D2 at time  $t + \tau$ , and  $P_i(t_i)$  to the simple probability of finding a photon on detector  $D_i$  at time  $t_i$ . In the case of identical detectors, the index 1 and 2 can be omitted. Remembering the theory of probability, for two events  $A$  and  $B$  we have:

$$P(A | B) = \frac{P(A \cap B)}{P(B)} \quad , \quad (2.11)$$

where  $P(A | B)$  is the conditional probability of  $A$  given  $B$ . We can reformulate [2.10] as:

$$g^{(2)}(\tau) = \frac{P(t + \tau | t)}{P(t)} \quad , \quad (2.12)$$

with  $P(t + \tau | t)$  the probability to detect a photon at  $t + \tau$  providing that one photon has been detected at  $t$ , and  $P(t)$  the probability to detect a photon at time  $t$ . We shall now evaluate these probabilities for a single emitter.

The detection of one photon at time  $t$  is equivalent to the projection of the system in its ground state. Thus, the probability to emit a second photon at  $t + \tau$  is ruled by the evolution dynamics of the excited state population. Hence:

$$P(t + \tau | t) = P(\tau | 0) = \zeta r_{21} p_2(\tau) \quad , \quad (2.13)$$

with  $p_i(t)$  the population of state  $i$  at time  $t$  and  $\zeta$  corresponds to the total efficiency of our detection setup. We have  $p_1(0) = 1$ ,  $p_2(0) = 0$ . The probability of detection at



any time  $P(t)$  is going to be proportional to the steady-state probability  $p_2(\infty)$  of the system to be in the excited state:

$$P(t) = \zeta r_{21} p_2(\infty) . \quad (2.14)$$

And we get for  $g^{(2)}(\tau)$ :

$$g^{(2)}(\tau) = \frac{p_2(\tau)}{p_2(\infty)} . \quad (2.15)$$

An important remark is that the detection efficiency  $\zeta$  of the setup does not impact our capability to construct  $g^{(2)}(\tau)$ . Now considering the three-level defect system shown in Fig 2.11, we write the rate equations for the occupation probabilities  $p_i$  of the ground state, excited state and metastable state in a matrix form:

$$\partial_t \begin{pmatrix} p_1 \\ p_2 \\ p_3 \end{pmatrix} = \begin{pmatrix} -r_{12} & r_{21} & r_{31} \\ r_{12} & -(r_{21} + r_{23}) & 0 \\ 0 & r_{23} & -r_{31} \end{pmatrix} \times \begin{pmatrix} p_1 \\ p_2 \\ p_3 \end{pmatrix} . \quad (2.16)$$

We make the approximation of low transition rates to and from the metastable state (3) compared with the excited state to ground state decay rate:

$$(r_{23}, r_{31}) \ll r_{21} , \quad (2.17)$$

which means that we assume a slow population dynamic compared with the lifetime of the excited state (2). This is justified in regards of the long time scale at which the bunching occurs. We obtain [111, 112]:

$$\boxed{g^{(2)}(\tau) = 1 - (1 + a) \exp(-\lambda_1 \tau) + a \exp(-\lambda_2 \tau)} , \quad (2.18)$$

with  $a$ ,  $\lambda_1$  and  $\lambda_2$  defined as:

$$\begin{aligned} a &= \frac{r_{12} r_{23}}{r_{31} (r_{12} + r_{21})} , \\ \lambda_1 &= r_{12} + r_{21} , \\ \lambda_2 &= r_{31} + \frac{r_{12} r_{23}}{r_{12} + r_{21}} . \end{aligned} \quad (2.19)$$

From the expression (2.18) of the fitting function, it is clear that  $a$  stands for the photon bunching amplitude,  $\lambda_1$  for the decay rate of the antibunching, and  $\lambda_2$  for the decay rate of the bunching effect.

Interestingly, the expression obtained for  $g^{(2)}(\tau)$  evaluated at zero delay yields:  $g^{(2)}(0) = 0$ , which does not correspond to the  $g^{(2)}(\tau)$  measured on Fig 2.10. This stems from the fact that the IRF of the detection system has not been taken into account in the derivation of the  $g^{(2)}(\tau)$  function for the three-level model. The fit in red of the experimental histogram performed on Fig 2.10 is actually the convolution of the expression (2.18) with the IRF. The fitting procedure is explained in details below.

Also,  $\lim_{\tau \rightarrow \infty} g^{(2)}(\tau) = 1$ , which expresses a total loss of correlation for times much greater than  $[\lambda_1]^{-1}$  and  $[\lambda_2]^{-1}$  and thus a return to a poissonian statistics. This behavior

was expected because in the model no physical processes happen at larger time scale than the antibunching and bunching phenomena.

### 2.4.3 Procedure for fitting

According to the model established, the dynamics of emission is ruled by three photo-physic parameters  $a$ ,  $\lambda_1$  and  $\lambda_2$ . In order to determine their value and get insights into the dynamics, we need to fit the experimental histograms. Generally, the fitting process is split between short-time and long-time scale approximations of the correlation function.

#### Short-time approximation of $g^{(2)}(\tau)$

The short-time scale is defined for  $\tau \ll \lambda_2^{-1}$ . In this case, formula 2.18 reads:

$$g^{(2)}(\tau) \simeq (1 + a)(1 - \exp(-\lambda_1 \tau)) \quad . \quad (2.20)$$

From this function we extracted, for the  $g^{(2)}(\tau)$  of Fig 2.10 taken at  $P = 150 \mu\text{W}$ : a bunching amplitude  $a = 0.6$ , and the parameter  $\lambda_1 = 0.51 \text{ ns}^{-1}$ .

#### Long-time approximation of $g^{(2)}(\tau)$

The long-time scale is defined for  $\tau \gg \lambda_1^{-1}$ . In this case, formula 2.18 reads:

$$g^{(2)}(\tau) \simeq 1 + a \exp(-\lambda_2 \tau) \quad . \quad (2.21)$$

From this function we extracted, for the  $g^{(2)}(\tau)$  of Fig 2.10 taken at  $P = 150 \mu\text{W}$ , the parameter  $\lambda_2 = 0.14 \mu\text{s}^{-1}$ . Strikingly, there are three orders of magnitude of difference between  $\lambda_1^{-1}$  and  $\lambda_2^{-1}$  associated with the excited state (2) and the metastable state (3), respectively. This is an indication that the system can be trapped into the metastable level and stay for a much longer time than the radiative recombination between states (2) and (1).

#### Including the IRF

As discussed above, the full fitting function (2.18), or its short-time scale approximation (2.20), reaches 0 at zero delay, unlike the experimental histogram, and this arises from the IRF. To include the effect of the electronic jitter, a convolution between the fitting function and the IRF has to be applied. As the IRF has very small temporal width (FWHM = 880 ps) compared with the timescale at which happen the bunching in the correlation function, it is appropriate to use the short-time scale approximation for  $g^{(2)}(\tau)$  in the convolution product and then fit the data only for the antibunching. However, on Fig 2.10, the full convolution with the total expression of  $g^{(2)}(\tau)$  has been computed, and the function is obtained through the resolution of:

$$g_{IRF}^{(2)}(\tau) = \int_{-\infty}^{+\infty} \frac{1}{\sigma\sqrt{2\pi}} \exp\left(-\frac{(\tau - \tau')^2}{2\sigma^2}\right) g^{(2)}(\tau') d\tau' \quad , \quad (2.22)$$

where  $\sigma$  is the standard deviation of the IRF measured previously (Section 2.3.2) and given by  $\sigma \approx \text{FWHM}/2.355$ , with  $\text{FWHM} = 880$  ps. In the fit procedure,  $\sigma$  is a fixed parameter, determined experimentally. And  $g^{(2)}(\tau')$  is expressed with the electronic delay  $\tau_d$ :

$$g^{(2)}(\tau') = 1 - (1 + a) \exp(-\lambda_1|\tau' - \tau_d|) + a \exp(-\lambda_2|\tau' - \tau_d|) \quad . \quad (2.23)$$

The derivation of the analytical function  $g_{IRF}^{(2)}(\tau)$  is done in Appendix B. The result, shown on Fig 2.10, presents a perfect fitting of  $g_{IRF}^{(2)}$  with the experimental points. The fact that the sole convolution with the IRF is enough to fit the data without correcting for the background means that the single-photon source is very pure, the discrepancy with the theoretical value  $g^{(2)}(\tau_d) = 0$  arising, in a large proportion, from the fact that the IRF has a FWHM in the same order of time to that of the radiative dynamics.

## 2.5 Photophysical properties of individual defects

All the data in this section have been analyzed using the data analysis software Igor Pro [113] which is very convenient to compute complex fitting procedure, and provide a good flexibility in the handling of constraints for the fitting parameters.

For an isolated quantum emitter, the dynamics of excitation is dependent on the excitation power. Indeed, the power density at the defect position determines the density of modes of the electromagnetic field, which influences the population of the different quantum states of the system, thus the dynamics of transition through the modification of the decay rates  $r_{ij}$ . Let us first determine the radiative lifetime through the determination of  $r_{21}$ , then the metastable state lifetime by determining  $r_{31}$ .

### 2.5.1 Expression of $r_{21}$ and $r_{31}$ with $a$ , $\lambda_1$ and $\lambda_2$

#### Decay rate $r_{21}$

The fitting parameter  $\lambda_1$  is the contribution of two terms:  $\lambda_1 = r_{12} + r_{21}$  (2.19).  $r_{12}$  is related to the pumping rate and  $r_{21}$  has a dependence in the excitation power. In the limit of extremely weak pump power  $r_{12} \rightarrow 0$  and  $r_{21}$  is the **spontaneous decay rate** of the emitter. The radiative lifetime  $\tau_1 = r_{21}^{-1}(P = 0)$  of a single quantum emitter can then be inferred by extrapolating the value of the parameter  $\lambda_1$  for vanishing pump power. This is done by recording the histogram of time correlation at different laser power, extracting the parameter  $\lambda_1$  for each measurement, and building the diagram of  $\lambda_1$  versus power. The expression of  $\lambda_1$  as a function of P reads:

$$\lambda_1 = \alpha P + r_{21} \quad . \quad (2.24)$$

However, due to a short radiative lifetime, at increasing excitation power the antibunching becomes narrower than the IRF, thus strongly limiting the precision of this method for determining the radiative lifetime.

### Decay rate $r_{31}$

It is fruitful to notice that:

$$\lambda_2 = r_{31} + \frac{r_{12}r_{23}}{r_{12} + r_{21}} = r_{31} \left( 1 + \frac{r_{12}r_{23}}{r_{31}(r_{12} + r_{21})} \right) = r_{31}(1 + a) \quad , \quad (2.25)$$

hence:

$$r_{31} = \frac{\lambda_2}{1 + a} \quad . \quad (2.26)$$

We can then readily estimate the transition rate from the metastable state to the ground state from the fit. We can similarly study the power dependence of  $r_{31}$  through the determination of  $\lambda_2$  at different excitation power.

## 2.5.2 Power-dependent measurements of $g^{(2)}(\tau)$

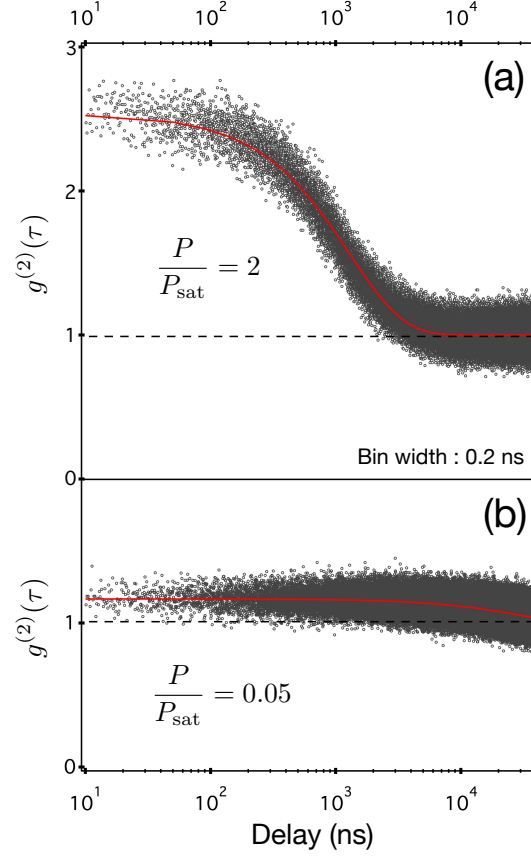
Fig 2.12 displays two histograms of photon correlations, for time delay up to  $4 \times 10^4$  ns = 40  $\mu$ s and bin width 0.2 ns, with  $P/P_{\text{sat}} = 0.05$  (bottom) and  $P/P_{\text{sat}} = 2$  (top), where  $P_{\text{sat}}$  is the saturation power determined and discussed later in Section 2.5.3. Each set of data is normalized according to equation (2.9) and fitted using the function  $g_{\text{IRF}}^{(2)}$  from Eq (2.22). The bunching amplitude (related to the parameter  $a$ ) is higher at high excitation power compared with low excitation power. It is an indication that upon rising the excitation pump, more population goes into the metastable state. The other difference is the delay value at which the histograms reach 1 (related to  $\lambda_2$ ). It looks shorter in the case of intense pump power.

This contrast in the histogram for two opposite regimes of excitation indicates a modification in the recombination dynamics of the metastable state and the excited state, driven by the pumping power.

### Radiative lifetime

As discussed in Section 2.5.1, the measurement of the radiative lifetime could, in principle, be performed with measuring  $\lambda_1$  for varying laser power. But here, the time-scale of the antibunching is in the order of the temporal width of the IRF, which preclude the use of this method.

The lifetime of the excited level was rather estimated through time-resolved PL measurements under pulsed laser excitation. This method is more accurate to determine the radiative lifetime of the emitter because the system evolves freely after excitation, without interacting with an electromagnetic field. A 50 ps laser pulse brings the system in the excited state at  $t = 0$  and we observe the system in a free evolution, so it can return to the ground state by emitting a photon after a certain period. After a time fixed by the repetition rate of the pulsed laser, a second pulse is emitted and we get a second photon emitted after a second time period. Repeating this experience, we get the PL diagram over time [Fig 2.13(b)]. The PL collected is proportional to the population of the excited state. At  $t = 0$  the process of emission of one photon is dependent on the radiative and non-radiative processes, in other words to the direct transition from (2) to (1) and to the trapping transition from (2) to (3). The PL decay is well fitted


**Figure 2.12**

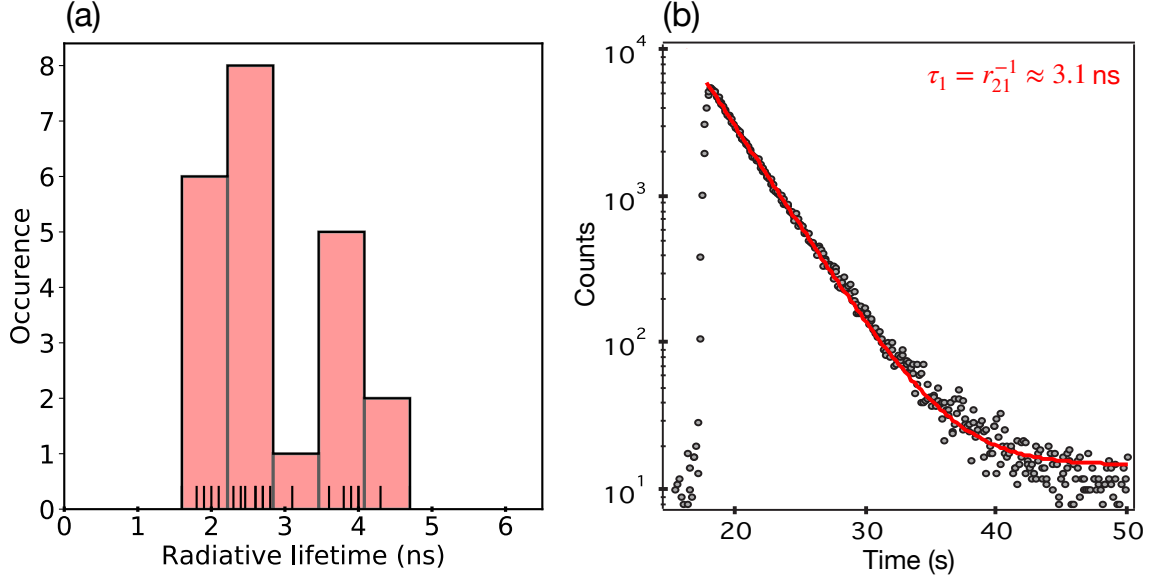
Second-order correlation function  $g^{(2)}(\tau)$  recorded for  $P/P_{\text{sat}} = 0.05$  (a) and  $P/P_{\text{sat}} = 2$  (b), for very long time delays and a bin width of the histogram of 0.2 ns. The data (black dots) are fitted using the full convoluted function of Eq (2.22) (red solid lines).

by a single exponential function  $\propto \exp -\Gamma t$  where  $\Gamma = \gamma_r + \gamma_{nr}$  with  $\gamma_r = r_{21}$  and  $\gamma_{nr} = r_{23}$ , leading to a value  $\Gamma = 3.1$  ns. Now we recall that to obtain the expression of the correlation function in the three-level model, we have made the approximation of low transition rates to and from the metastable state compared with the excited to ground state rate, consequently  $r_{23} \ll r_{21}$  and we get for the lifetime of the excited level:

$$r_{21}^{-1} \sim \Gamma = 3.1 \pm 0.1 \text{ ns} . \quad (2.27)$$

This value is in good agreement with the one measured in hBN flakes for individual defects showing similar spectral properties [80, 94].

Fig 2.13(a) shows the distribution of the radiative lifetime for an ensemble of 21 single defects. It seems that the distribution is bi-modal, but considering the small number of points, it is difficult to conclude on the existence of two families, moreover no correlation between one category of lifetime and photostability or spectrum family has been observed.


**Figure 2.13**

(a) Histograms of radiative lifetimes measured for 21 single defects. Each small vertical black ticks at the bottom represent an observation. (b) Decay of the excited state (2) recorded under optical excitation with 50 ps laser pulses. The solid line is data fitting with a single exponential function.

### Investigation on the metastable state

To gain insights into the dynamics of the metastable level, the characteristic parameters of the bunching effect ( $a$ ,  $\lambda_2$ ) were inferred from the fitting of the  $g^{(2)}(\tau)$  recorded at different laser power.

First, " $a$ " is directly plotted on Fig 2.14(a). The dependence on excitation power is clearly linear and positive. As a consequence, upon increasing the pump power the metastable state is more and more populated, which should result in a decrease of the photoluminescence recorded by the APDs.

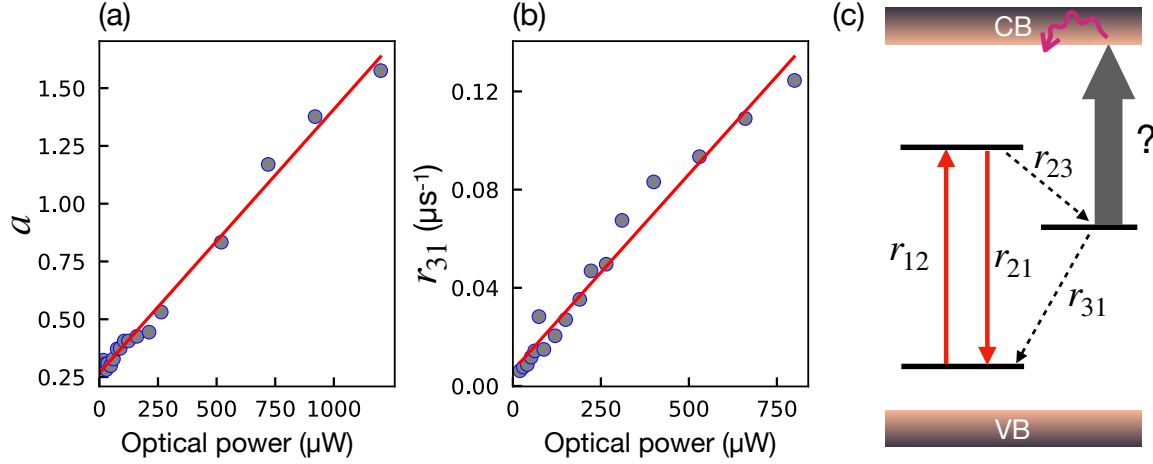
Using the relation (2.26), the evolution of  $r_{31}$  with the optical power is easily obtained and presented on Fig 2.14(b). The results indicate a pronounced increase in the decay rate  $r_{31}$  with the laser power, which suggests that optical illumination induces desheling of the metastable level. This effect is often observed for individual emitters in solid-state systems [107, 114]. By fitting the data with a linear power dependence of the desheling process, as:

$$r_{31} = r_{31}^0(1 + \beta P) \quad , \quad (2.28)$$

We get an estimation of the metastable level lifetime (at  $P = 0$ ):

$$[r_{31}^0]^{-1} = 180 \pm 60 \mu s \quad . \quad (2.29)$$

and  $\beta = 0.025 \pm 0.01 \mu W^{-1}$ . This value of the metastable lifetime is two orders of magnitude higher than the one found in NV centers at  $\sim 500$  ns. It brings the evidence that the metastable state is a long-lived trapping state for the system, the PL activity


**Figure 2.14**

(a) Parameter "a" as a function of the optical power. (b) Decay rate  $r_{31}$  of the metastable state as a function of the optical power. The red solid lines are data fitting with a linear function. (c) Schematic of possible processes occurring at high pumping rate.

is stopped during the occupation of this state where the center can stay for about  $10^5$  times longer compared to the radiative excited state (in the nanosecond order).

In terms of quantum efficiency of the single-photon source, it is quite fortunate that, although the non-radiative state is more populated with higher optical power, the decay rate from level (3) to ground state (1) increases with the excitation power, acting as a counter effect of the limitation induced by the trapping in the metastable state. The physical processes at stake in the deshelling mechanism are not well understood. On Fig 2.14(c), we depict the situation of the defect inside the gap. One possibility is the promotion of the electron in level (3) to the conduction band (black arrow), leading to a non-radiative recombination of the exciton with the valence band, or a radiative one but at wavelengths not recorded by the APDs. Also, the defect can couple to other defects or transit towards a different charge state, opening a channel for faster transition to the ground state (1).

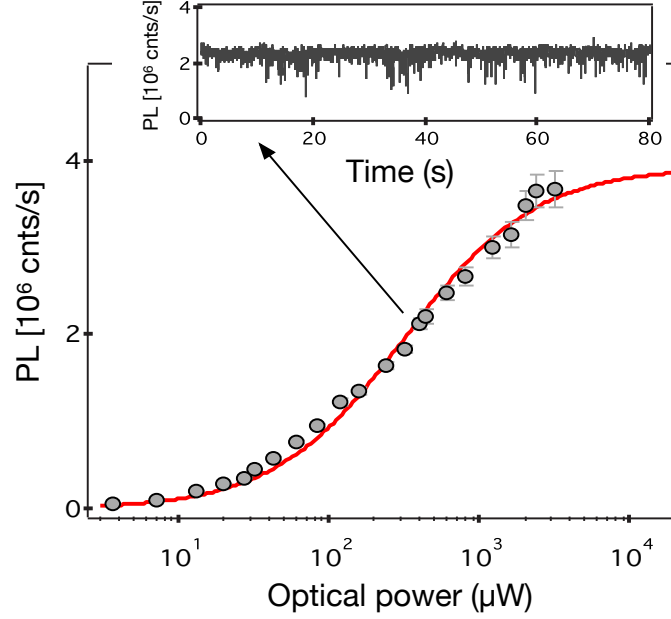
Let us now see the efficiency of the single-photon source by evaluating the emission rate at saturation.

### 2.5.3 Brightness of the source

Estimating the brightness of the source is important to compare it with other single-photon emitters. The PL rate  $R$  was measured as a function of the optical power  $P$  [Fig 2.15]. The horizontal axis is displayed in log-scale. Data fitting with a simple saturation function  $R = R_{\infty}/(1 + P_{\text{sat}}/P)$  leads to a saturation power  $P_{\text{sat}} = 310 \pm 20$  μW and an emission rate at saturation:

$$R_{\infty} = 3.9 \pm 0.1 \times 10^6 \text{ counts/s} , \quad (2.30)$$

similar to what is reported by other studies for the same type of defects [85, 94]. It corresponds to one of the brightest single photon source reported to date. For com-


**Figure 2.15**

*PL saturation curve of the defect. Inset: PL time trace recorded for a laser excitation power  $P = 400 \mu\text{W}$  performed on the same individual defect. The solid red line is the fit proposed in the main text. The dashed blue line shows the intensity at saturation for the NV center in diamond. The inset shows the stability of the emission at around 0.5 mW.*

parison, the emission rate at saturation is  $\sim 20$  times larger than the one obtained from a single nitrogen-vacancy defect in diamond with the same confocal microscope. Such high counting rates indicate that the short excited-level lifetime results from a strong radiative oscillator strength with near-unit quantum efficiency rather than PL quenching involving fast non-radiative decay processes ( $r_{23} \ll r_{21}$ ). Indeed, for the family of defects emitting at 596 nm (2.08 eV), the quantum efficiency (QE) has been experimentally measured at 87 % [115], which is among the highest QE recorded for a solid-state single-photon emitter.

## 2.6 Conclusion

In this work, we have studied a class of single defects in the wide bandgap semiconductor hBN on the angle of spectral measurement and photon statistics emission. Our approach has consisted in exciting the surface of a high-purity hBN monocrystal (HQ Graphene) by means of a single mode laser at 532 nm and a confocal microscope working in ambient conditions, and performing correlation measurements of emitted photons with a couple of APDs installed in the HBT configuration. The analysis performed with the help of the three-level system have brought insights into the dynamics of the quantum emitter.

Main important results consist in:

- A very bright single-photon source reaching  $4 \times 10^6$  counts/s at saturation power



310  $\mu\text{W}$ , resulting from a strong radiative oscillator strength, with excellent photostability. These defects have been proved to maintain their stability in a monolayer of hBN [82].

- Two families of defects exhibiting very similar spectrum, with ZPL at 1.97 eV and 2.08 eV, and phonon replica of constant energy shift 150 meV. These families may be considered as different charge states of the defect and the 150 meV detuning of phonon replica results from a dominant coupling to the zone-edge optical phonons of highest density of state.
- A dynamic of optical cycles marked by a long-lived non-radiative metastable state of  $\sim 200 \mu\text{s}$ . It appears to be very power dependent with a steep increase of the  $r_{31}$  decay rate with increasing excitation power, suggesting a deshelling of this level by the laser.

This analysis of the photophysical properties of the defect provides important information for understanding its structure using ab-initio calculations. These results pave the road towards applications of hBN, and more generally van der Waals heterostructures, in photonic-based quantum information science and optoelectronics.

We mention that we have not found optically-detected magnetic resonance (ODMR) in this hBN sample for this specific defect. However, more recent studies report on the magnetic-field dependent emission from single-photon source at room temperature for an emitting wavelength at  $\sim 725 \text{ nm}$  (1.7 eV) [86], and the first ODMR measured on single defect in hBN [116].

Concerning the chemical nature of these defects, recent calculations [117–119] suggest a carbon impurity substituting for a boron coupled to a nitrogen vacancy ( $\text{C}_B\text{V}_N$ ) or a nitrogen anti-site defect coupled to a nitrogen vacancy ( $\text{N}_B\text{V}_N$ ). However, electronic structure calculations in 2D materials remain challenging and uncertainty persists regarding the nature of the defects.



## Deep defects emitting in the UV range

IN CHAPTER I, we have presented the properties of luminescence of hexagonal boron nitride originating from point defects in the near ultraviolet, especially the deep defect emission at 4.1 eV. To date, there is no definitive understanding for this emission, although it was already observed in 1981 [120] with time-dependent photoluminescence experiments on hBN powder of poor quality compared with the current available crystals. As for other defects in different materials, the diversity in the experimental approaches is necessary to unveil the nature of such color centers. The specificity and originality of this defect lie in the fact that it emits in the UV, which explains at the same time the experimental difficulty to study it. In this chapter, we present an original study that makes use of isotopic purification in material doping to investigate the influence of carbon into the luminescence properties of hBN in the UV. We combine macro-photoluminescence and reflectance measurements to study new defects appearing in our carbon-doped samples, as presented in the first section of this chapter. As far as the detection of single emitters is concerned, the high concentration of the 4.1 eV defect usually recorded in bulk crystals led us to two developments. First, to build a photoluminescence confocal microscope operating at 266 nm (4.66 eV), presented in the second section. Secondly, to combine the characterization by cathodoluminescence of thin crystals with characterization by the micro-photoluminescence confocal microscope. We also used this new microscope to probe the spatial fluctuations at a sub-micrometer scale of the deep level emission in the UV. These two last investigations are the subject of the last section.

### 3.1 New levels in carbon-doped hBN crystals

In this section, we will present the results obtained by studying carbon-doped hBN crystals grown by precipitation method by means of two distinct spectroscopy techniques: photoluminescence and reflectivity. The measurements presented in this section are spatially resolved at a scale of tens of micrometers to millimeters. Considering the usual density of defects in the crystals, we thus probe ensembles of defects here.

#### 3.1.1 Description of the experiments

##### The complementary approaches of photoluminescence and reflectivity

The microscopic processes involved in photoluminescence and reflectivity are of distinct nature. The photoluminescence is the result of carrier relaxation and thermalization

processes after the system was put in an excited state, thus out of equilibrium. It is a particularly efficient technique to analyze semiconductors shallow levels and also deep levels when the radiative recombination process is intense enough [121]. Yet, the interpretation of the processes responsible for lines in the emission spectrum can sometimes be complex, therefore we complement our measurements with reflectance. In reflectance spectroscopy, we probe a material close to its thermodynamic equilibrium, that is to say the reflected signal intensity for a given excitation wavelength provides information about the dielectric constant of the material, and thus about the oscillator strength of the optical transitions. We will be using these two kinds of spectroscopy in order to gain better understanding of the underlying processes responsible for the features observed in our optical measurements. We will now present the experimental setup for these two techniques.

### Macro photoluminescence setup

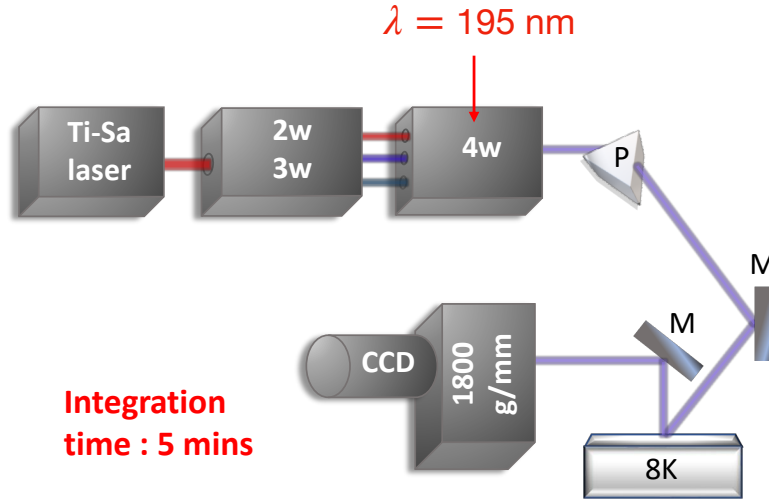


**Figure 3.1**

*Scheme of the macro-photoluminescence setup. A Ti:Sa oscillator is quadrupled through two successive wave-mixing units, and sent onto the sample inside the cryostat. An achromatic optical system couples the emitted light to a spectrometer equipped with a camera optimized for deep UV.*

We present on Fig 3.1 a scheme of the macro-photoluminescence setup. A cw mode-locked Ti:Sa oscillator with a repetition rate of 82 MHz is sent onto two successive wave-mixing devices: the first one provides the third harmonic signal that is subsequently mixed in the second unit with the first harmonic signal and tuned to give the fourth harmonic at a wavelength of 195 nm (6.35 eV) with a power of 30  $\mu\text{W}$ . A prism (P) is used to further separate the fourth harmonic from the other components, and a planar mirror (M) directs the beam toward the sample hold on a cold finger of a closed-cycle cryostat (temperature control from 8 K to room temperature). The spot diameter is on the order of 50  $\mu\text{m}$ . An achromatic optical system couples the emitted signal to the

detection system, composed of an  $f = 300$  mm Czerny-Turner monochromator, equipped with an 1800 grooves/mm grating blazed at 250 nm and with a back-illuminated CCD camera (Andor Newton 920), with a quantum efficiency of 50% at 210 nm. The spectral resolution is 0.8 nm or 2.5 meV at 200 nm.

### Reflectivity setup

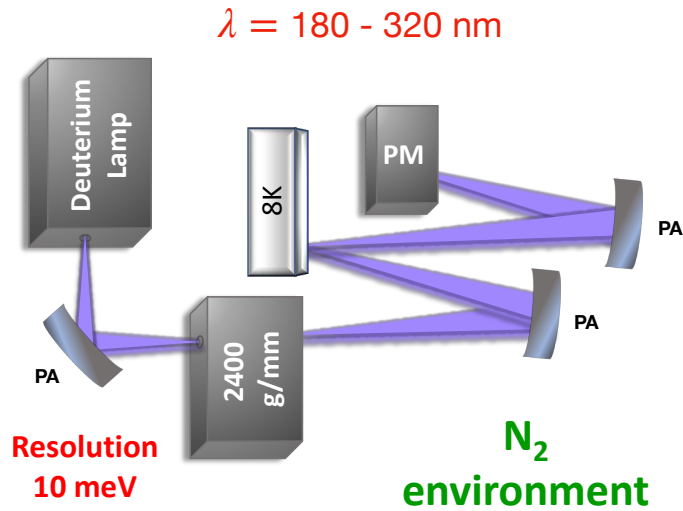


**Figure 3.2**

*Scheme of the reflectivity setup. A deuterium lamp is spectrally filtered through a monochromator and sent onto the sample with near normal incidence angle. The intensity of the reflected field is measured with a photomultiplier.*

We present our home-made experimental setup for deep UV reflectance on Fig [3.2](#). We use the field emission of a deuterium lamp (63163 Newport) spectrally filtered through a monochromator (Cornerstone CS130) with 100  $\mu$ m slits providing a spectral resolution on the order of 10 meV and a scan range going from 180 nm up to 320 nm. An achromatic optical system made of spherical mirrors coated for deep UV conducts the light onto the sample close to normal incidence, with a rectangular spot of size 100  $\mu$ m  $\times$  1.5 mm. The reflected field was collected by a photomultiplier (PM) connected to a preamplifier-transducer and a final lock-in amplifier. In order to remove absorption lines of  $O_2$  in the deep UV, the whole optical path was placed in a  $N_2$ -purged atmosphere. The cryostat was the same as in the macro-PL experiment. Due to the excitation field source (deuterium lamp) having a non-uniform intensity distribution over the wavelengths used in the experiment, we normalized the data by the measurement of the reflectivity spectrum on an Aluminum mirror deposited on the sample holder.

#### 3.1.2 Samples characteristics

We have carried out experiments on a batch of samples doped with carbon whose growth process involves different precursors. In order to avoid misinterpretation of results, it is

important to present the growth protocol as well as the potential effects of the different precursors on the PL spectra.

### Synthesis of the crystals

The team of James H. Edgar in Kansas State University provided us with carbon-doped hBN single crystals grown from a molten metal solution at atmospheric pressure with a modified version of the growth procedure described in references [17, 122]. Three metals were used: nickel, iron, and chromium. Nickel and iron are good solvents for boron, with maximum solubilities of 18.5 at.% and 17 at.%, respectively. Chromium is good for dissolving nitrogen. Mixing of both metallic solvents forms a eutectic (at 1345 °C for Ni and Cr). The boron source for all samples was either a commercial hBN powder or hot pressed boron nitride (HPBN), nominally fabricated from the same commercial powder. The carbon source was graphite powder, with the natural distribution of carbon isotopes, except for sample C40, which used  $^{13}\text{C}$  enriched graphite. We present the samples and their specificities on Table 3.1.

**Table 3.1**

*Growth parameters of the carbon-doped hBN crystals precipitated from a molten metal solution in a high-temperature furnace. HPBN denotes hot pressed boron nitride.*

Sample name	Graphite quantity	BN quantity	Solvents	Cooling rate	Atmosphere
C20	1.5 g graphite powder	0.5 g BN powder	10 g Fe + 10 g Cr	4 °C/h	H <sub>2</sub> + N <sub>2</sub>
C22	1.5 g graphite powder	0.5 g BN powder	10 g Ni + 10 g Cr	4 °C/h	H <sub>2</sub> + N <sub>2</sub>
C27	graphite piece	HPBN	17 g Fe + 17 g Cr	4 °C/h	H <sub>2</sub> + N <sub>2</sub>
C33	2.0 g graphite powder	1.0 g BN powder	20 g Ni + 20 g Cr	0.5 °C/h	CO + N <sub>2</sub>
C40	0.75 g $^{13}\text{C}$ powder	BN pressed boat	10 g Ni + 10 g Cr	0.5 °C/h	CO + N <sub>2</sub>

More specifically, the carbon-doped hBN crystals were precipitated from the molten metal solution in a high-temperature single-zone furnace. For growing the crystals of Table 3.1, the precursor powders with compositions listed in the second through fourth columns were loaded in either an alumina or a HPBN ceramic crucible, and transferred into the furnace. The furnace was evacuated and purged with the atmospheric gases listed in the sixth column multiple times to remove all residual oxygen. For growing pure hBN crystals, a small amount of hydrogen is typically added with the flowing nitrogen to reduce and remove any oxides from the source materials. However, to avoid excessive etching of the graphite source for growing these carbon-doped hBN crystals, carbon monoxide was used instead of hydrogen, as it reacts with and removes oxygen, but not carbon. The precursor powders were heated up to 1550 °C to form liquid phase and held at this temperature for 24 h to thoroughly dissolve the carbon, boron, and nitrogen into the molten metal solution. The crystals were then grown by cooling the system to 1300 °C at rates of 4 or 0.5 °C/h, as listed in the fifth column. During crystal growth, the atmospheric gases were continuously flowed to the system at a rate of 125 sccm, and the system was kept at 850 torr. After crystal growth, the system was then quenched to room temperature at 50 °C/h.

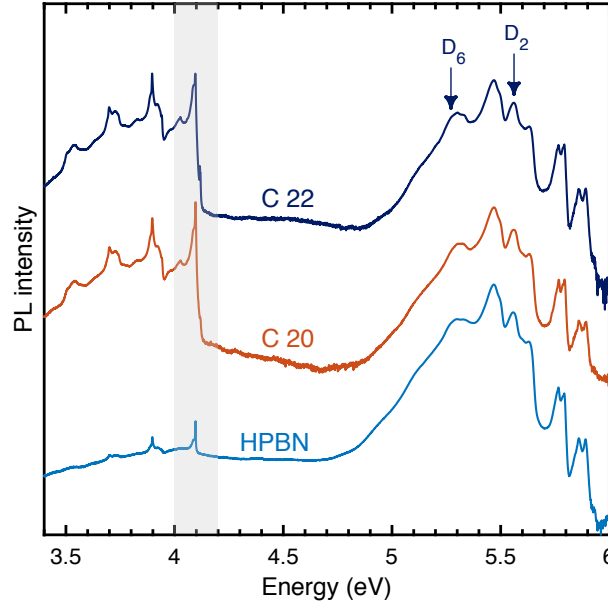


**Figure 3.3**

Macro-PL spectrum at 8 K (semilog scale), with an excitation energy of 6.35 eV, in bulk hBN synthesized either with iron (C22) or nickel (C20), and the hBN powder used as a precursor, here in the form of HPBN.

### Iron versus nickel as solvent

As alluded to earlier, the solubility of boron is higher in nickel than iron while the residual amount of carbon impurities in our Fe is smaller than in our Ni. To determine whether these parameters play a role in the crystals structural properties, we perform photoluminescence measurements over a wide range of energy.

We begin by comparing the 8 K PL features in the spectral range between 3.5 and 6 eV [Fig 3.3], recorded in cases of samples C20 (Fe-Cr solvent) and C22 (Ni-Cr solvent), and of the BN powder used as a precursor, here in the form of HPBN. The PL spectrum of the BN precursor displays emission lines near 4 eV (shaded region in Fig 3.3). These lines are also found in the PL spectra of C20 and C22. The lines form a more or less documented series, depending on the growth run, with in general the detection of a strong feature at 4.1 eV. We emphasize that these sharp lines were never recorded in the case of samples grown using the protocol of [123], which revealed the optical performances of monoisotopically boron-purified BN samples [124]. For these growths, elemental boron-10 and boron-11 as well as  $N_2$  were used instead of a BN powder. PL intensities have been plotted logarithmically in Fig 3.3. The PL spectrum below 5 eV corresponds to the recombination lines arising from deep levels. There is the well-known zero-phonon line (ZPL) at 4.1 eV with its accompanying phonon replicas at lower energies [68, 125]. Because of the heavy carbon-doping in our hBN crystals, the PL intensity of the 4.1 eV line is comparable to that of the stacking faults around 5.5 eV, in contrast to the peak observed in powder samples, if it is seen at all. This is in agreement with similar studies reported in [125] that led those authors to relate the 4.1 eV line to carbon/oxygen impurities. In Fig 3.3, the PL line shape is not influenced

by the chemical composition of the solvent (iron or nickel) within the inhomogeneous linewidth of our hBN crystals.

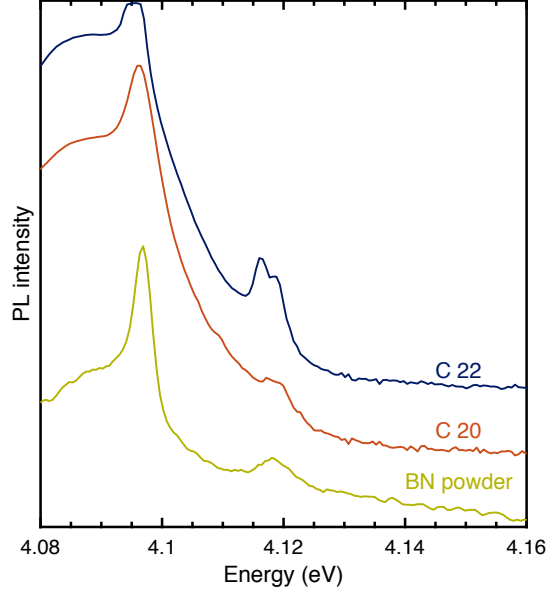


**Figure 3.4**

Zoom-in of the 4 eV region (linear scale) of the macro-PL spectrum in bulk hBN synthesized either with iron (C20) or nickel (C22), together with a hBN powder used as a precursor (BN Powder).

It is important to emphasize the occurrence of a doublet feature centered at 4.12 eV, with an interlevel splitting of  $\sim 2$  meV in sample C22 (grown using Cr-Ni), which is also recorded but weaker in sample C20 (grown using Cr-Fe), as shown in Fig 3.4. The PL feature of the BN powder displayed in Fig 3.4 indicates that it is also present in the precursor. Therefore, this doublet line is correlated to a contaminant contained in the BN precursor. It has nothing to do with the contamination of Fe, Ni, or Cr. The only difference between Ni and Fe as a solvent is the unsystematic recording of a weak and broad PL band at 4.6 eV when using the Ni-Cr solvent. We thus conclude that the use of Ni or Fe has only a marginal influence on the optoelectronic properties of our hBN crystals.

Now that we have cast out doubts concerning the effect of the solvent on structural properties through analysis of the photoluminescence over a wide range of energy, we will be focusing in the following on the impact of carbon-doping. We will first consider the shallow levels in the 5-5.7 eV range, and secondly deep levels around 4.1 eV.

### 3.1.3 Shallow-level emissions

Fig 3.5 displays on a semi-logarithmic scale the PL spectra recorded at 8 K for different samples, from top to bottom: a test undoped hBN crystal purchased from HQ Graphene (HQG), samples C22 and C27 (without CO), and sample C33 (with CO but with different C/BN ratios; cf. Table 3.1).



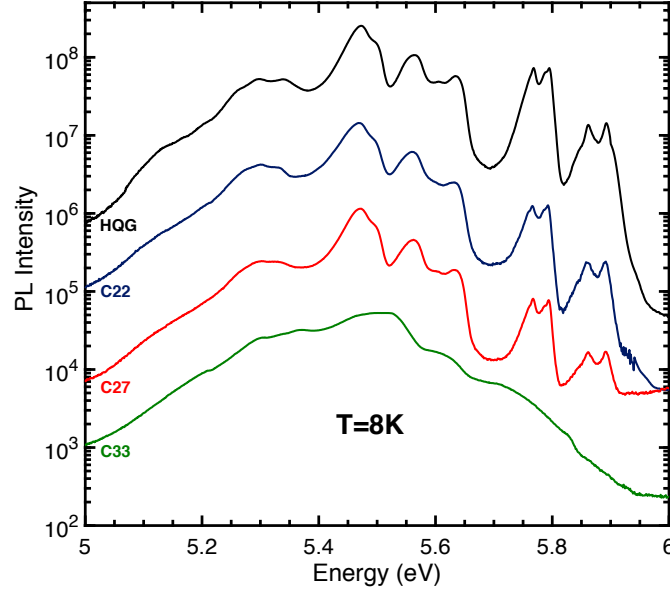


**Figure 3.5**

PL spectra recorded at 8 K in bulk hBN crystals for energies ranging between 5 and 6 eV (semilog scale). Spectra are vertically shifted for clarity. Growth conditions are given in Table I. HQG stands for a test undoped hBN crystal purchased from HQ Graphene.

The 5.7–6 eV energy range corresponds to the intrinsic part of the emission spectrum. This series of lines corresponds to the well-defined phonon-assisted optical transitions typical of indirect-bandgap semiconductors, and here, of the hexagonal BN stacking, with their specific spectral distribution that we have reviewed in Chapter 1 Section 1.4.1. Zooming in on each of these phonon-assisted recombination lines reveals a similar low-energy fine structure, due to the emission of phonon overtones involving the low-frequency Raman-active mode at the zone center [57].

Below the energy of the LO-assisted recombination (5.75 eV) starts the spectral range of defect-related emission, discussed in Chapter 1 Section 1.4.2. From 5.7 eV down to 5 eV, there is a series of discrete lines split from each other by about 147 meV. Transverse optical phonons at the K point of the Brillouin zone assist inter-K valley scattering, producing a series of discrete recombination bands because the stacking faults in bulk hBN [65, 66] provide a density of final electronic states in Fermi’s golden rule, and shape the envelope of the PL spectrum [63]. Two distinct lines, labelled D<sub>2</sub> and D<sub>6</sub> in the initial paper of Cassabois et al. [63] and noted on Fig 3.3, are also detected. They were tentatively attributed to the BN divacancy following [126].

The PL spectrum is almost identical for the first three samples (HQG, C22, and C27). In contrast, in the heavily doped C33 sample, the PL spectrum presents less defined features. The sharp and detailed series of phonon-assisted recombination lines above 5.7 eV is strongly broadened and hardly observable, and the defect-related emission lines are also broadened. More importantly, we note an apparent blue shift of the most intense line to 5.52 eV in C33, shifting from 5.47 eV in the other samples.

The higher carbon concentration in C33 may affect the crystal quality and result

in a decrease of the intensity of the intrinsic recombination lines together with a larger inhomogeneous broadening, which would contribute to washing out the series of phonon replicas above 5.7 eV. As a matter of fact, this may also impact the defect-related emission lines, but we note a distortion of the peak around 5.5 eV. In HQG, C22, and C27, the energy of the maximum is 5.47 eV with a high-energy shoulder at 5.5 eV [Fig 3.5], whereas we observe a broader asymmetric line in C33 with a maximum at 5.52 eV, an energy that corresponds to a minimum of the PL spectrum in HQG, C22, and C27. Finally, a secondary maximum appears at 5.37 eV in C33, as a high-energy shoulder of the 5.3 eV band, again at an energy where the PL spectrum of HQG, C22, and C27 displays a minimum. These observations suggest the existence of new transitions in the optical response of heavily carbon-doped hBN crystals.

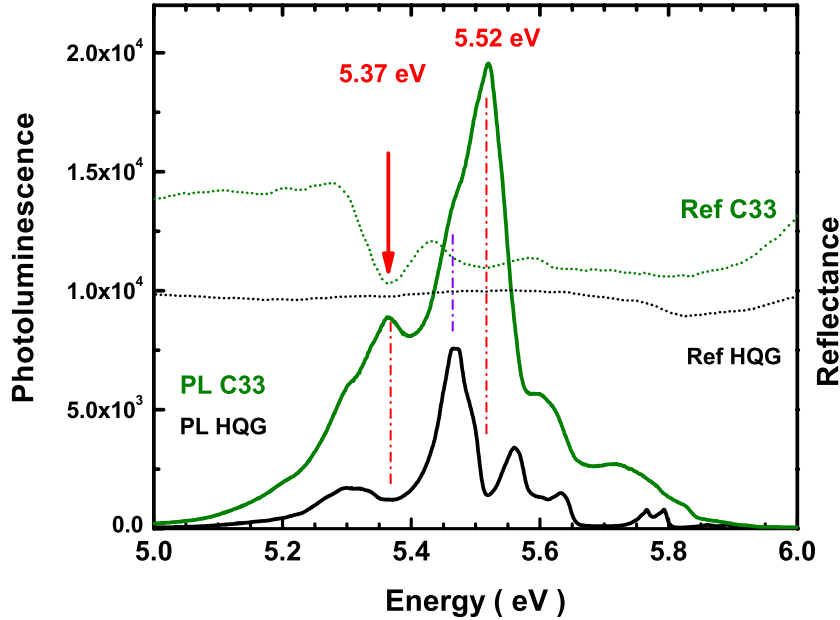


**Figure 3.6**

PL (solid lines) and reflectance (dotted lines) spectra on linear scales, recorded in a test undoped hBN crystal (HQG, black lines) and a heavily carbon-doped one (C33, green lines) at 10 K. Note the coincidences between the reflectance minima and the PL maxima in sample C33.

To test this hypothesis, we compare in Fig 3.6 the PL and reflectance spectra (on linear scales) recorded in HQG and C33. For HQG, the reflectivity (dotted black line) displays smooth variations with a rather flat spectrum in the spectral domain where the PL spectrum (solid black line) is on the contrary very rich with many lines due to intervalley scattering into excitonic states bound to stacking faults, as explained above. Such a difference between the spectra is fully consistent with the distinct nature of the microscopic processes involved in PL and reflectivity. Indeed, as explained in the beginning of this chapter, the reflectivity probes a material in its thermodynamic equilibrium whereas PL results from carrier relaxation and thermalization. The presence of

many defect-related lines around 5.5 eV, in the PL spectrum but not in the reflectance one, is a genuine signature of relaxation effects with resonances of intervalley scattering, further supporting the interpretation initially proposed in [63].

In contrast, the heavy carbon-doping in C33 not only modifies the PL spectrum (solid green line) but also the reflectance one (dotted green line). Strikingly, there are pronounced reflectance oscillations, in resonance with the new emission lines at 5.37 and 5.52 eV. This observation confirms the existence of new optical transitions associated with heavy carbon-doping in hBN crystals. The incorporation of carbon during the growth process produces complementary states with a high enough density and oscillator strength of their optical transition to significantly change the dielectric constant in the 5.3–5.6 eV energy region.

Following [126], we tentatively attribute the lines at 5.37 and 5.52 eV to an exciton bound to the defect formed by a carbon substituting for a nitrogen ( $C_N$ ). In [126], the optical absorption spectrum of hBN calculated by the Bethe-Salpeter equation predicted that native point defects or impurities induce novel optical transitions close to the band gap, corresponding to defect bound excitons. The heavy carbon-doping in C33 makes the  $C_N$ -bound exciton a strong candidate for the 5.37 and 5.52 eV lines.

### 3.1.4 Deep-level emissions

In this section we focus on the lower energy part of the spectrum presented in Fig 3.3, especially on the shaded region corresponding to the emission of the well studied defect at 4.1 eV. We discuss the presence of new spectral lines at higher energies between 4.1 and 4.2 eV.

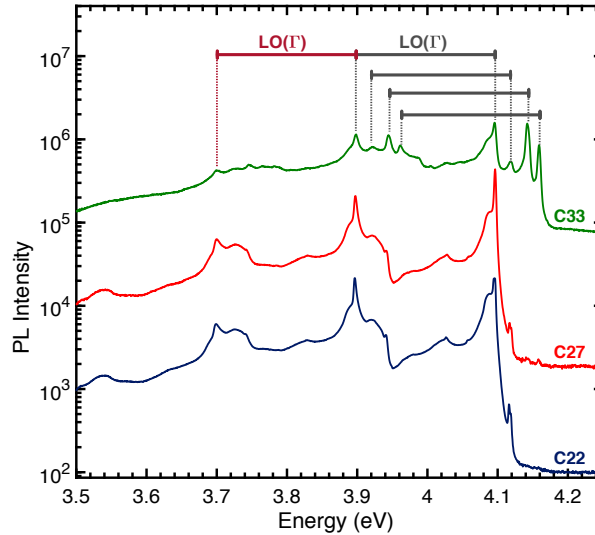


**Figure 3.7**

Full set of the PL spectra (semilog scale) of carbon-doped hBN samples in the 3.5–4.25 eV range. The spectra are vertically shifted for clarity. The horizontal bars have a 200 meV width, corresponding to the  $LO(\Gamma)$  phonon energy.

We display on Fig 3.7 the PL spectra of three samples in the 3.5-4.25 eV spectral range. Emission from the 4.1 eV deep level is always recorded with its sharp ZPL, phonon sidebands and prominent optical phonon replicas at 3.9 and 3.7 eV [68, 127]. A new line at 4.12 eV (called UV1) is observed with a doublet fine-structure splitting. In sample C27, there are additional weak lines at 4.14 and 4.16 eV (called UV2 and UV3, respectively), all three of these lines being much more intense in the heavily carbon-doped C33 sample. We also note that all of these lines broaden when increasing the amount of carbon involved in the growth protocol, which likely prevents us from observing any fine-structure splitting, if any, for UV2 and UV3. Finally, phonon replicas of UV1, UV2, and UV3 are detected, readily observed and red-shifted by 200 meV (LO( $\Gamma$ ) phonon) and 400 meV (2LO( $\Gamma$ ) phonons) from their ZPL.

The first indication that UV1-3 do not share the same microscopic origin as the 4.1 eV deep level comes from the vibronic part of their PL spectrum. The experimental data recorded in C33 are plotted on a linear scale in Fig 3.8 in order to better resolve the different line shapes of UV1-3 compared to the 4.1 eV line. At low temperature (8 K, top spectrum), we can distinguish the ZPL and the low-energy sideband in the emission spectrum of the 4.1 eV defect as described in Chapter 1 Section 1.4.3, although the carbon-doping leads to broadening of the ZPL. On the contrary, for UV1-3 no phonon sideband is observed and each of the UV1-3 lines can be fairly fitted to a symmetric profile, with a Gaussian function. Moreover, upon raising the temperature, the FWHM of UV1-3 increases from 6 meV at 8 K to 9 meV at 120 K. Such a temperature dependence contrasts with the phenomenology presented in Section 1.4.3 Fig 1.18, where we observed a 5.5 meV broadening in the 8-120 K range for the 4.1 eV defect [68], further suggesting a different microscopic structure in UV1-3 compared to the 4.1 eV defect.

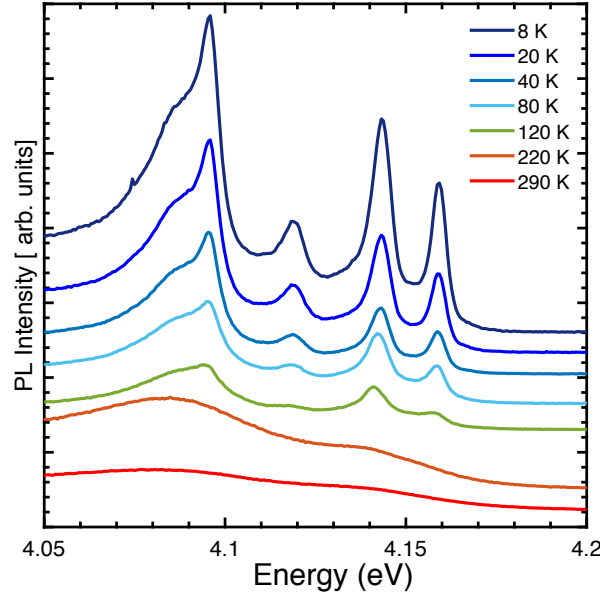


**Figure 3.8**

*Temperature-dependent PL measurements (linear scale) in the heavily carbon-doped hBN sample C33, in the 4.05 to 4.2 eV range. The spectra are vertically shifted for clarity.*

Furthermore, looking at the PL signal intensity as a function of temperature, we do

not record any cross-talk between the lines, with a constant intensity ratio among the set of optical transitions in the 3.8-4.2 eV range. This observation indicates the absence of interlevel crossing in the relaxation dynamics, either because the spatial separation of the defects is larger than the carrier diffusion length, or because they are formed in distinct mesoscopic domains due to the local fluctuations of the growth conditions during the synthesis of the hBN crystals.

We performed reflectivity measurements in this region of the spectrum in order to access the oscillator strength of the optical transitions observed. Results are shown on Fig 3.9, where we compare the PL and reflectance spectra recorded at 8 K in sample C33. The reflectivity signal exhibits a marked peak at 4.1 eV, testifying to a substantial oscillator strength. Because of the mirror symmetry between phonon-assisted absorption and phonon-assisted emission, we record a series of blue-shifted minima that are the high-energy analogs of the phonon replicas detected in the PL spectrum, with an interlevel spacing of 200 meV as discussed above. Note that the ZPL is broader in reflectance than in PL, thus smearing out the fine structure of the phonon replicas in reflectivity.

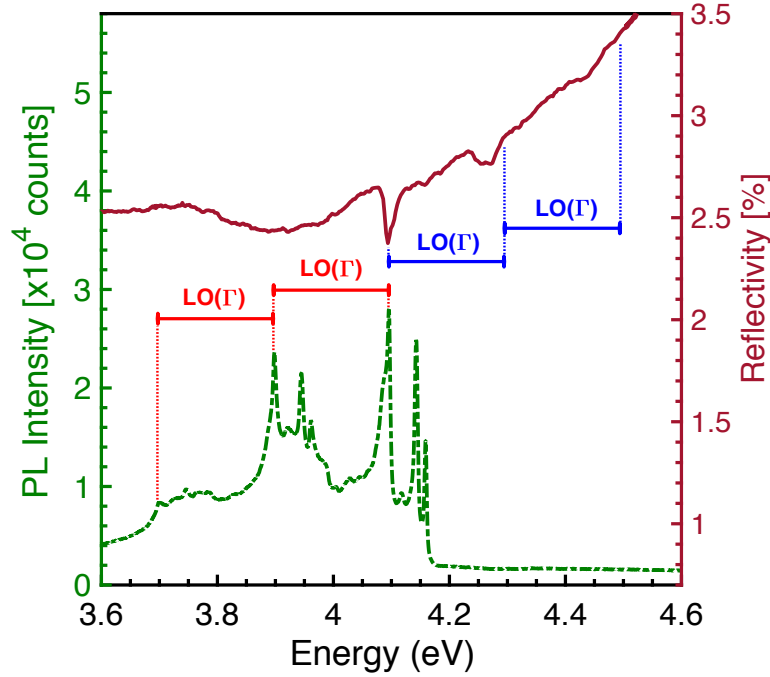


**Figure 3.9**

PL (green dashed line) and reflectivity (purple solid line) spectrum on linear scales, recorded at 8 K for sample C33 in the 4 eV region. The horizontal bars have a 200 meV width, corresponding to the  $LO(\Gamma)$  phonon energy. They are displayed in red for the red-shifted phonon-assisted emission (below 4.1 eV), and in blue for the blue-shifted phonon-assisted absorption (above 4.1 eV).

Surprisingly, nothing is detected for the UV1-3 deep levels in reflectivity. Although the PL lines of UV1-3 and the 4.1 eV defect are of comparable intensities in this sample, no reflectance minima are seen at the energies of the new carbon-related PL lines. This

effect may come from either a smaller oscillator strength or a lower density of the UV1-3 point defects. In both cases, the interpretation of the high PL signal intensity from UV1-3 implies a more efficient carrier relaxation in these novel carbon-related point defects.

### Summary

By means of macro-PL and reflectivity experiments, we have probed the emission spectrum of different carbon-doped crystals of hBN in the deep UV (5 eV to 6 eV) and the near-UV ( $\sim 4$  eV).

In the deep UV, namely in the part of the spectrum corresponding to exciton recombination assisted by inter-K valley scattering, we bring the evidence of new energy level transitions at 5.37 and 5.52 eV which are not observed in moderately doped samples. They have sufficient oscillator strength and are present in density high enough to modify the dielectric constant in the energy region 5.3-5.6 eV, as witnessed in reflectivity. We attribute the new level transitions to an exciton bound to a  $C_N$  impurity.

In the near-UV region around 4.1 eV, we reveal the existence of additional optical transitions at 4.12 eV (UV1), 4.14 eV (UV2), and 4.16 eV (UV3), to which carbon doping induces a strong increase in their PL signal intensity. These spectral lines are not documented in the literature. In contrast of the two levels introduced at higher energies in the spectrum, the reflectance spectra show no correlated features for the UV1-3 lines, indicating either a low density or weak oscillator strength. In the former case, recalling that the excitation spot is large and thus the signal is averaged over many locations, probing the sample at a smaller scale would enable to investigate the spatial variations of these deep levels and help to gain further insight into them.

To that end, we shall now present the  $\mu$ -PL confocal setup operating in the UV range, built during my thesis. Additionally to the gain in spatial resolution, the better spectral resolution of our confocal microscope will also help in revealing subtle details in the spectrum, if any. Besides, the sub-bandgap excitation energy at 4.66 eV (266 nm), is not only closer to the energy transition of the UV1-3 levels, but also allows the suppression of the 4-eV broad emission background [127], thus enhancing the visibility in this region of the spectrum.

## 3.2 Confocal microscope at 266 nm / 4.66 eV

### 3.2.1 General overview of the experimental setup

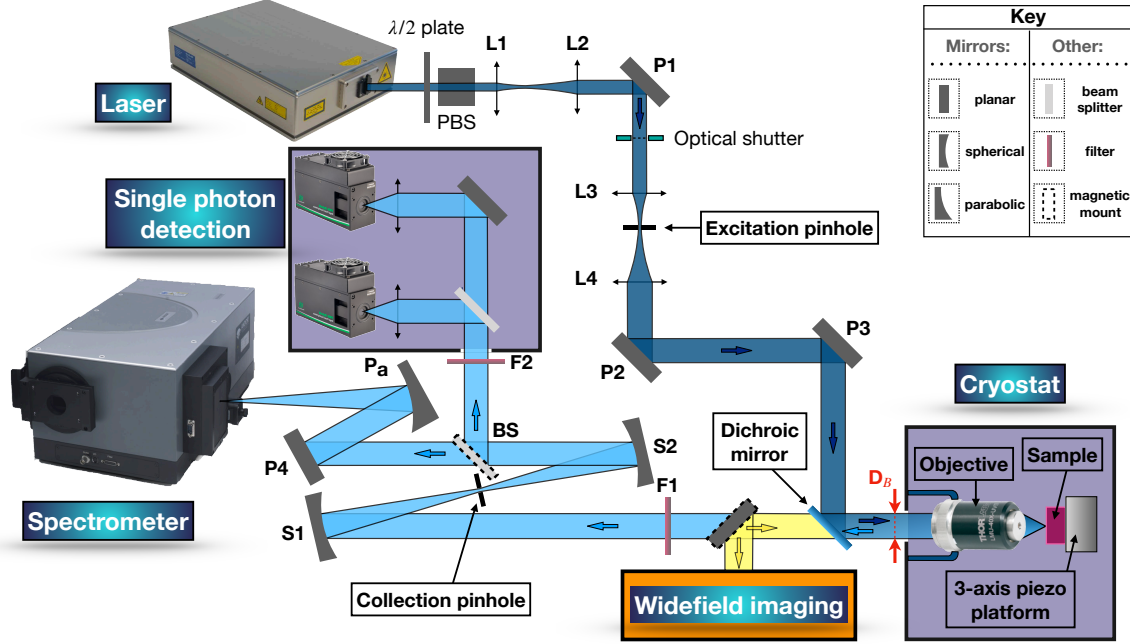


**Figure 3.10**  
Functional sketch of the confocal microscope.

We have built a confocal microscope in the ultraviolet range that works at cryogenic temperature and is coupled through an achromatic and geometrical aberration-free optical system with a spectrometer and a HBT interferometer (cf. Chapter 2) to assess the uniqueness of the point defect emitters. A scheme of the overall setup is shown on Fig 3.10, while a more detailed drawing for the cryostat and widefield imaging system is presented on Fig 3.11.

#### Laser source

The excitation source is a diode pumped continuous wave solid state laser (FQCW266-10, CRYLAS GmbH company). The optical emission results from a quadrupled Nd:YAG laser ( $\lambda=1064$  nm) thus providing an emission wavelength at 266 nm or 4.66 eV. The mode of the emitted light is a single longitudinal mode  $TEM_{00}$ , with a deviation from a gaussian beam shape characterized by a factor  $M^2 < 1.3$ , linearly vertically polarized and with a linewidth of less than 300kHz around 266 nm. A combination of a half-wave plate ( $\lambda/2$ ) and a polarized beam-splitter (PBS) allows the regulation of the laser power. The beam is enlarged a first time by a couple of lenses of different focal length (**L1**, **L2**).



### Spatial filtering

To obtain optimal performances, a pinhole diaphragm in the excitation path is used to improve the selectivity of the illumination in the sample field by spatially filtering the illumination beam. Another advantage of this pinhole is that it creates a point source for the excitation that is stable and remains immobile throughout measurement and alignment, the changes in pointing direction of the laser source producing only a modification of the laser intensity. In this purpose, a pinhole of 25  $\mu\text{m}$  is placed in the conjugated focal plane of a lens L3 ( $f=89.5$  mm) and L4 ( $f=136$  mm). The telecentric system formed by (L3, L4) provides a second enlargement of the beam. The focal length of L3 was chosen long enough in order to avoid spherical aberrations with high angles of diffraction which would introduce distortion of the spot and losses of energy. The lens L3 is installed on a XY translation stage with micrometer control of the position and on a Z linear translation stage in order to finely optimize the coupling with the fixed confocal pinhole. We reach a coupling of 86%.

### Beam walking and dichroic mirror

The excitation beam is then sent onto two planar mirrors (P2, P3) mounted on kinematic mounts with adjustable angles and in a  $45^\circ/45^\circ$  configuration, for beam walking. This couple of mirrors allows to make the beam parallel and centered with respect to the entrance pupil of the objective.

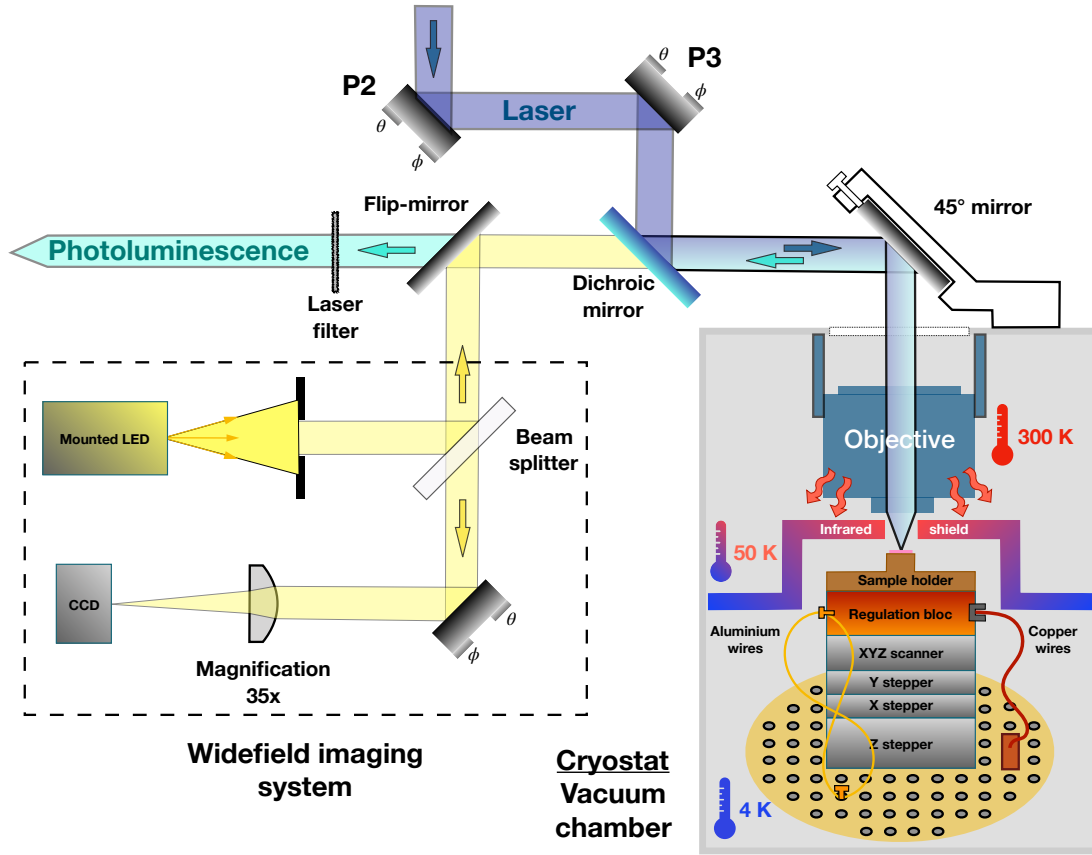
A dichroic mirror (Di01-R266 Semrock) is placed at an incident angle of  $45^\circ$ . It has a reflection coefficient of 94% for  $\lambda = 266$  nm and a transmission coefficient of 90% above  $\lambda = 277$  nm.  $D_B$  on Fig 3.10 indicates an iris diaphragm that enables to control the beam diameter before the objective.

### Microscope objective in a close-cycle cryostat

The microscope objective we use is a refractive objective with an effective focal length  $EFL = 5$  mm at 266 nm and numerical aperture  $NA = 0.5$  (LMU-40X-UVB, Thorlabs). The cryostat installed in the experiment is an helium close-cycle cryostat (OptiDry model) from MyCryoFirm. It has a large vacuum chamber with a cold gold-coated plate at 4 K at the bottom, on which lies the sample holder along with all the opto-mechanical devices (sample positioners, scanners), the probe and heater for temperature control (cf. Fig 3.11). This chamber possesses an upper turret, removable for samples installation and/or indoor optics adjustment. An in-house made mechanical piece was designed to hold a planar mirror at  $45^\circ$  on top of this turret, thus changing the propagation of light from horizontal to vertical direction, directing the beam towards the top window of the cryostat.

One fundamental aspect of our setup is the position of the objective inside the chamber of the cryostat. Indeed, in the UV range, aberrations introduced when a cone of light crosses a glass window are huge. In order to avoid any change of refractive index between the objective and the sample, the microscope objective was fixed inside the chamber to the top wall, like illustrated on Fig 3.11. However, in the cryostat, the walls are not cooled down, only the cold plate is connected to the cooling system. It means that the objective is at room temperature. This is why we need a thermal shield



**Figure 3.11**

*Drawing of the excitation part with the cryostat chamber and the widefield imaging system.*

at 50 K between the objective and the sample holder, to protect the sample from the black body radiation at 300 K of the objective.

### Scanning system

In the design of our confocal setup, the laser source and the objective are fixed, and we perform raster scans by recording the PL signal intensity for different positions of the sample by moving the sample. It requires a precise control of the position, the moving frequency and the repetition rate of the scanning stage. Moreover, the nanopositioners work under cryogenic temperature and vacuum. We use two types of positioners: three unidirectional steppers (2 ANPx101 & ANPz101 Attocube) to position roughly the sample and explore different regions, and one XYZ scanner (ANSxyz100 Attocube) to perform the scans. The steppers have a travel range of 5 mm at both high and low temperature whereas the scanner travel range is  $50 \times 50 \times 24 \mu\text{m}^3$  at 300 K and  $30 \times 30 \times 15 \mu\text{m}^3$  at 4 K. Both types of positioners are connected to their suitable controller. The scanner is controlled through an acquisition card with analog outputs (NI PCIe-6323) connected to the controller (Thorlabs MDT693B-3 channel) while the steppers are controlled independently through their own controller (Attocube ANC 300).

### Confocal collection

The photoluminescence of the sample is collected by the same objective and collimated towards the collection path. The light is first transmitted by the dichroic mirror, and then goes through a filter F1, an ultrastep long-pass edge filter (RazorEdge Semrock) with an optical density  $OD = 5$  at 266 nm, to remove the remaining laser light intensity. The confocality of the microscope is ensured by the collection pinhole positioned in the common focal plane of two spherical mirrors S1 and S2 ( $f=250$  mm). In this configuration, the light is therefore re-collimated by the second spherical mirror S2, and subsequently separated by a 50/50 beam splitter: one half is directed toward a couple of single-photon detectors and is filtered by the band-pass filter F2 300-340 nm with  $OD > 5$  outside the band (FF02-320/40 Semrock), and a second half toward a planar mirror P4 that directs the light to a  $24^\circ$  off-axis parabolic mirror  $P_a$  ( $f=209$  mm). This last mirror focuses the photoluminescence at the entrance slit of the spectrometer.

The diameter of the pinhole in collection, which fully determines the ability of the system to select one optical slice in the axial direction of the sample, has to be properly chosen. The choice is usually made so that the back projected image of the pinhole in the focal plane of the objective is equal or smaller than the excitation spot. If we neglect aberrations, the excitation spot size is given by the Airy disk radius calculated with the photoluminescence wavelength because we are considering the diffraction pattern caused by the light emitted from a point source in the sample. Thus, we apply the Abbe formula with  $\lambda_{PL} = 300$  nm (emission wavelength of the 4.1 eV defect) and the resulting Airy disk radius  $r^{\text{Airy}}$  equates to:

$$r^{\text{Airy}} = 0.61 \times \frac{\lambda_{PL}}{NA} = 0.61 \times \frac{300\text{nm}}{0.5} \approx 366\text{nm} \quad . \quad (3.1)$$

We finally obtain the size of the pinhole by applying the magnification factor related to the focal length of the objective and mirror S1:  $\frac{f_{S1}}{f_{\text{objective}}} \times 2 \times r^{\text{Airy}} = 250\text{mm}/5\text{mm} \times 2 \times 366\text{nm} \approx 37\mu\text{m}$ . Conventional sizes of pinhole being multiple of  $10\mu\text{m}$ , the choice was made to favor confocal stringency and work with a  $30\mu\text{m}$  wide confocal pinhole (80% of the Airy disk).

### Two channels for PL detection

After the confocal selection, we have two different ways of detecting the photoluminescence signal.

In the case of the reflection on the beam splitter BS [Fig 3.10], we use hybrid photomultiplier tubes (PMA Series PicoQuant) in photon-counting mode. The PMA have a 6 mm wide detection area, work for photon wavelengths between 220 and 650 nm, have a transit time spread of 50 ps, which is the ultimate time resolution achievable, and can handle count rate up to 10 MHz. The dark counts are under 100 counts/s. For raster scans of PL, only one of the detectors was used. However, to perform time-correlated single photon counting (TCSPC) measurements, we used both detectors mounted in the configuration of Hanbury Brown and Twiss (HBT) interferometer. The PMA are connected to a single-photon counting acquisition card (PicoQuant TH260).

In the second case of transmission by BS, we use a spectrometer that has a  $f=500$  mm Czerny-Turner system (Shamrock 500i B2) equipped with a turret containing three gratings with different groove density and blazed at different wavelengths. The one providing the best resolution has 1800 grooves/mm and is blazed at 250 nm: it provides a spectral resolution of 0.02 nm or 0.3 meV at 300 nm. The spectrometer is coupled to a back-illuminated UV-enhanced camera (Andor Newton DU940P BU2) with a quantum efficiency of 60% at 300 nm. The camera active pixel area is composed of  $2048 \times 512$  pixels of  $13.5 \times 13.5 \mu\text{m}^2$ . The advantage of using the spectrometer is to resolve the PL spectrum. We can spectrally filter the PL maps over a given spectral range, a type of analysis usually called SPIM. This will be further explained and illustrated in section [3.2.5](#). The time needed for such an acquisition is however much longer than the one with mono-channel photon detectors.

### Optical inspection with the widefield imaging system

An additional mirror placed on a magnetic mount ahead of the collection path is used to couple the objective with the widefield imaging setup. A close-up of this part is represented on Fig [3.11](#).

In order to visualize the sample surface under visible light and with an appropriate magnification, we set up a widefield microscope using a mounted LED (Thorlabs MCWHL5) which emits a cold light at 6500 K with a central wavelength at 430 nm. The image is formed on a CCD camera (Thorlabs DCC1545M) by a UV-coated lens. The magnification obtained is  $35\times$  which provides a spatial extent of  $45 \mu\text{m}$  wide and  $70 \mu\text{m}$  high.

### Computer control of the experiment

The experimental setup features a number of instruments that need to be controlled by a central unit for data acquisition. From shining a laser on a sample to obtain a SPIM image, there is a number of steps that goes from the development of an interface with a central unit, computer programs for data acquisition, data analysis and data visualization. I present below the programs that I have coded during my thesis.

There were two main programs to develop for the **data acquisition**. The first concerns the acquisition of raster scans of photoluminescence. One very inconvenient point is that the PMA, made to detect single photons, send low negative amplitude pulses ( $-75$  mV) with extreme short time resolution (700 ps) which make them undetectable by the acquisition card of the scanners (NI PCIE-6323). In consequence, the instruments have been synchronized for scan acquisition using the acquisition card PicoQuant-TH260, suitable for the signal sent by the PMs, with the NI card. The program has been coded in Labview with the DLL from Attocube and PicoQuant. The second program is the one used for SPIM acquisition. It requires to control in a synchronous manner the scanners and the spectrometer with the camera. Again the chosen interface is Labview because previous programs were already developed in that language.

A secondary program has been coded in Labview for control of the Attocube step-pers. Regarding the spectrometer, native program from Andor (Andor Solis) has been

extensively used for alignment and sample exploration especially for its numerous options in image mode. Temperature control has been conducted directly through the controller Cryo.Con 24C. Laser emitting power was always set to 8 mW for stability and effective used power was selected by a couple of a half-wave plate and a polarized beam splitter. The direction of the half-wave plate was controlled from the computer through a motorized rotation stage.

Concerning the **data visualization and analysis**, I have coded programs exclusively in Python programming language [128], working mainly with Numpy and Scipy libraries for data processing and analysis, Panda for data manipulation and Matplotlib for data visualization.

### 3.2.2 What are the challenges to build a confocal setup in the UV?

The many challenges to build such a confocal setup in the ultraviolet range stem from the optical aberrations, both spherical and chromatic, in the excitation as well as in the collection part of the optical system.

Indeed, materials used to build optics (lenses, mirrors, windows, beam splitters) become very dispersive media for the light in the UV. This is the reason why we installed the microscope objective inside the cryostat chamber, as explained earlier. Yet, this does not solve all issues related to spherical aberrations. The refractive objective we use in our system is significantly sensitive to spherical aberrations in that the focusing of the excitation beam into a small excitation spot in the sample field is remarkably dependent on the diameter  $D_B$  of the beam. While it is common to fully illuminate the entrance aperture of the objective to reach the best spatial resolution, here we need to assess the optimum value of  $D_B$  that minimizes the impact of spherical aberrations. We carefully deal with this issue in section 3.2.3.

Another consequence of optics becoming highly dispersive in the UV is that, while the excitation part deals with a monochromatic beam and for which we can use lenses to focus and re-collimate the light, the situation in collection is significantly different because the emitted light from our sample has a large spectral width that expands typically from 300 nm to 340 nm. In this regard, chromatic aberrations are a critical issue, and totally preclude the use of refractive optics for the collection of the photoluminescence. To get rid of this type of aberration we have used reflective optics such as concave and parabolic mirrors. We shall discuss the practical aspects of those in section 3.2.4. The microscope objective, made of a series of lenses, and used both for excitation and collection, suffers the same chromatic aberrations, particularly when it is question of focusing the laser light and collecting the PL light from the same focal point. This issue demands particular attention and will be tackled in section 3.2.4.

Besides, another necessity in the UV range is to work with UV-adapted optical components. The lenses L1-4 (LA-UV, Thorlabs) are made of UV grade fused silica offering a high transmission coefficient in the UV and low thermal expansion, and are coated with an anti-reflection layer, decreasing the reflection to 0.5%. The mirrors P1-

3 (NB1-K04, Thorlabs) are Nd:YAG laser line mirrors, perfectly adapted to our laser source, offering a high damage threshold to withstand the high-intensity beam in the excitation part. The reflection coefficient is greater than 99.75%. In the collection part, the mirrors S1-2 are UV-enhanced aluminum concave mirror (10DC500AL.2, Newport) with a reflection coefficient  $R > 90\%$  for wavelength between 250 nm and 600 nm. P4 is also a UV-enhanced aluminum mirror (PF10-03-F01, Thorlabs) with  $R > 90\%$  between 250 and 450 nm. Finally, the parabolic mirror  $P_a$  is made of bare aluminum (Edmund Optics) and is 40mm×40mm large. It has been specially coated for UV. Its reflectivity reaches 85% in the range 250 nm - 700 nm. These coatings are expensive, and sensitive to oxidization. Moreover they are less tolerant in angle of incidence which adds to the constraints, however they are of paramount importance when signals to be detected are very weak. Finally,

### 3.2.3 Optimization of the optical excitation

In this section, we deal with the impact of the excitation beam diameter on the spatial resolution. To obtain the smallest spot of excitation with a microscope objective, one usually illuminates the full entrance aperture of the objective, and we understand it well from basic knowledge on microscope resolution and Fraunhofer diffraction. However, due to importance of refraction phenomenon at 266 nm, spherical aberrations are occurring through the objective lenses and enlarge the excitation spot by modifying the distribution of intensity in the sample field. Thereby, the resolution given by the classical Abbe formula  $r_0 = 0.61 \times \frac{\lambda}{NA}$  is not applicable here.

In order to curb this detrimental effect, we control the entrance beam diameter  $D_B$  by placing an iris diaphragm on the excitation path before the top mirror of the cryostat (cf. Fig 3.10). By narrowing the beam we suppress the outer light rays on the pupil, thus diminishing spherical aberration effects. Yet, when the objective entrance pupil is not completely filled, the effective numerical aperture NA decreases and so does the diffraction-limited resolution (Airy disk radius increases). Therefore, one must find an optimum value for the resolution.

#### Simulation with an optical design software

We have used Zemax to numerically simulate the effect of  $D_B$  on the excitation spot size. Zemax is a professional optical design program [129] used to design and analyze imaging systems as well as illumination systems. It works by ray tracing-modeling the propagation of rays through an optical system. It can model the effect of optical elements (here, the objective) and produce standard analysis diagrams such as spot diagrams.

Fig 3.12(a) presents the dependence of the spot size with  $D_B$ . We have two elements in the figure. First is the case without spherical aberrations, represented by the solid orange curve. In this case the excitation spot radius is only limited by diffraction, it is the Airy disk radius. Second is the case with taking spherical aberrations into consideration, represented by the blue dots. In this case, the excitation spot radius departs from the ideal case because aberrations through the objective tend to deviate the peripheral rays, thus enlarging the spot. Therefore we need to redefine the spot radius. A consistent way of doing that is to consider, in the spot diagram, the radius

of the circle enclosing 84% of the total luminous intensity, a criterion chosen to be identical to that of the definition of the Airy disk (cf. Fig 3.13 for more details). The procedure for this redefined spot also performs an optimization along the axial direction (the so-called "refocused spot"), as a consequence the effective focal length changes a little bit during this process, however over the all range of  $D_B$  values in this figure, the variation of the focal length is less than  $1\text{ }\mu\text{m}$ .  $D_B$  ranges from 1.5 mm to 5 mm, the actual pupil diameter of the objective.

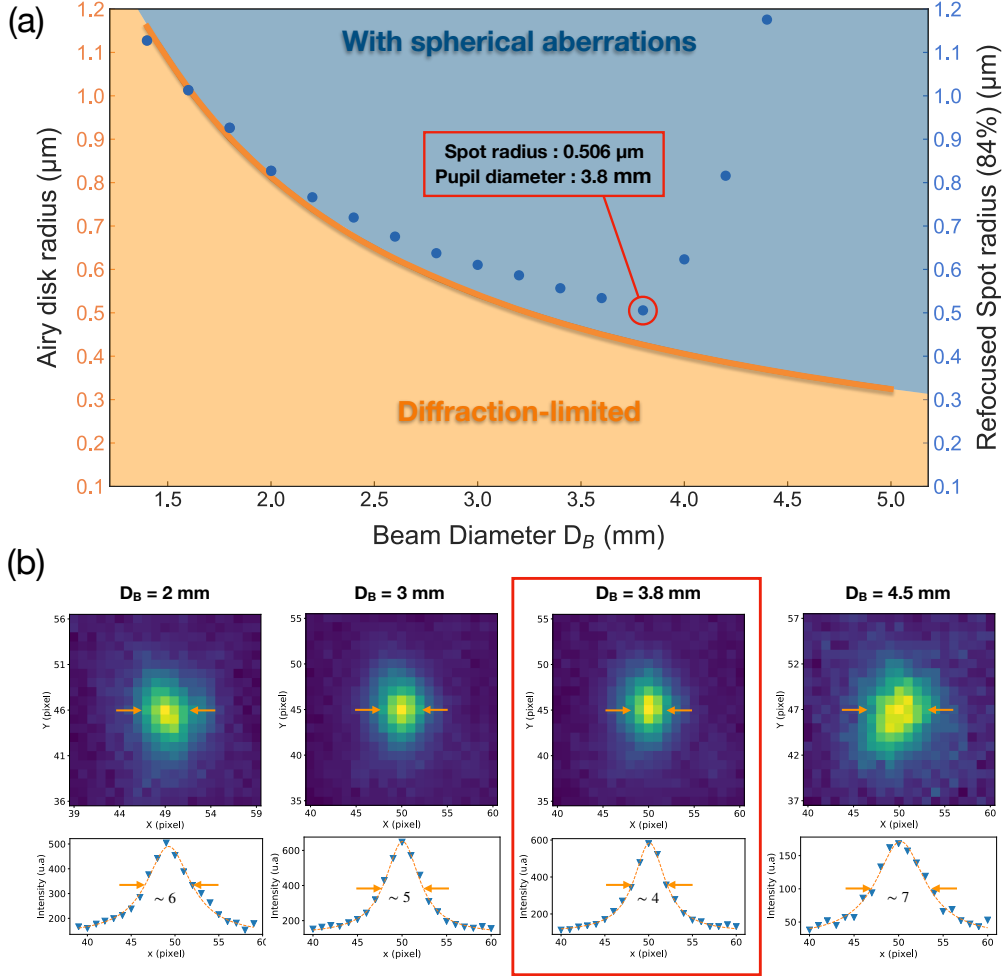


**Figure 3.12**

(a) Simulated diagram, using Zemax, of the excitation spot radius in the focal plane of the objective depending on the beam diameter ( $D_B$ ). The solid orange line represents the case without taking spherical aberrations into consideration (Airy disk), and the blue dots with spherical aberrations throughout the objective (refocused spot, see main text). (b) Experimental investigation of the effect of the beam diameter for  $D_B = 2, 3, 3.8$  and  $4.5$  mm. The upper panels are the images at zero order on the CCD camera of the spectrometer without the confocal pinhole in collection. The lower panels are a cross-section of the intensity profile with a Lorentzian fit, the FWHM in pixels is indicated by the orange arrows.

One can see that the Airy disk size (solid line) varies in a monotonous way with the beam diameter. This is well understood from Fraunhofer diffraction: the more



the incident beam illuminates the objective entrance aperture, the more the effective numerical aperture increases, the smaller the excitation spot. It reaches the value of 325 nm when  $D_B = 5$  mm, as expected.

In contrast, the refocused spot (blue dots) behaves in two distinct ways. For values of  $D_B$  less than 3.5 mm we are still in the Gauss conditions and the aberration effects are not visible, it follows the orange curve. Then, spherical aberrations become prominent and it rises significantly. Thereby, there is an optimum value of the beam diameter to obtain the smallest excitation spot. The optimum is found for  $D_B = 3.8$  mm, which provides a resolution of  $r_0^{\text{eff}} = 500$  nm at the sample surface.

### Experimental results

Fig 3.12(b) provides the experimental data when changing  $D_B$ . The upper panels show the images at zero order of the excitation spot onto the CCD of the spectrometer for several values of  $D_B$ , with the collection pinhole removed (otherwise we would image it instead of the excitation spot). The lower panels display a cross-section of the intensity profile with a Lorentzian fit. We note a good agreement with the simulation, the FWHM of the spot intensity decreases steadily until reaching a minimal value of  $\sim 4$  pixels for  $D_B = 3.8 \pm 0.1$  mm, and then rises rapidly to 7 pixels when reaching  $D_B = 4.5$  mm.

To bring more details on the procedure for defining the refocused spot radius, we present in Fig 3.13(a) the radial cumulative distribution of the intensity of the spot diagram in the focal plane of the objective, for  $D_B = 3.8$  mm (blue) and  $D_B = 4.4$  mm (red), and for the two cases with (dotted lines) and without (solid lines) spherical aberrations. For a given value of the radial distance, the curve indicates the percentage of the luminous energy contained in a circle of this radius. This is schematically illustrated in Fig 3.13(b) for a spot with aberrations, in purple. In the case of diffraction-limited resolution (not represented), the spot intensity follows the well-known Airy pattern<sup>1</sup>, whose radial distribution is recalled in the inset of Fig 3.13(b), where the Airy radius is simply defined by the distance from the center of the spot to the first zero of the distribution, and where the area between the two zeros represents 84% of the total intensity. In the spot diagram, however, we see that the spot is not included in the Airy disk because of aberrations, and we thus have determined the new radius forming the refocused spot (dotted line) that does contain 84% of the total luminous intensity.

In Fig 3.13(a), for  $D_B = 3.8$  mm (blue), corresponding to the optimum value determined above, we clearly see that the intersections of the solid and dotted lines with the 84% threshold give similar radii, as seen in Fig 3.12(a) where the blue dot is only 80 nm above the orange curve. For  $D_B = 4.4$  mm, the solid line indicates a smaller Airy disk radius as expected (because NA increases) but, in contrast of the precedent case, the intersection of the dotted line with the threshold at 84% gives a much larger refocused spot radius, in agreement with the fourth CCD image of Fig 3.12(b). Spherical aberrations tend to distribute more luminous energy in the secondary oscillations of the Airy pattern.

---

<sup>1</sup>For the common case of circular objective aperture, it involves the Bessel function of the first kind and order.

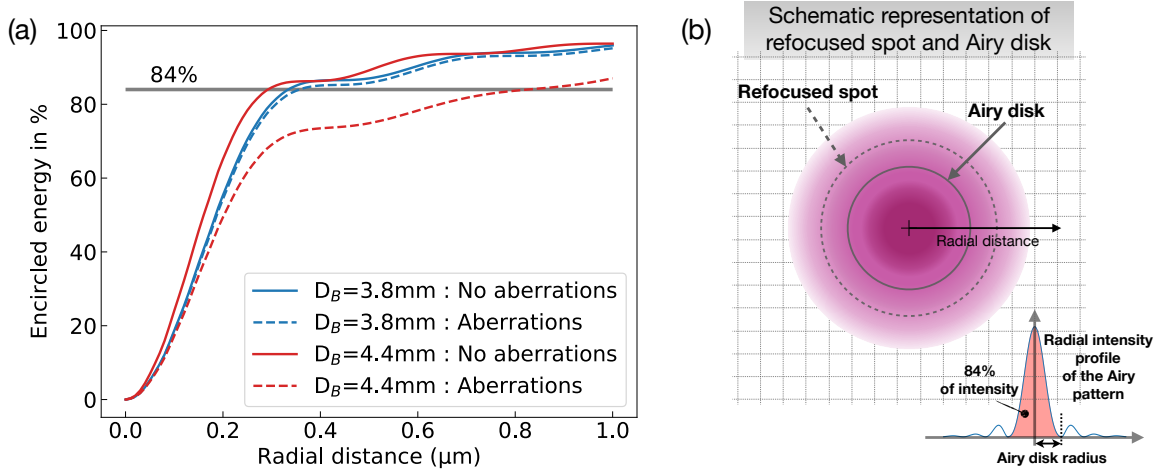


**Figure 3.13**

(a) Radial cumulative distribution of the luminous energy with (dotted lines) and without (solid lines) spherical aberrations, with  $D_B = 3.8\text{ mm}$  (blue) and  $D_B = 4.4\text{ mm}$  (red). (b) Illustration of a spot diagram in the focal plane of the objective. The dotted circle corresponds to the refocused spot radius encircling 84% of the total intensity distribution in purple. Inset: recall of the intensity distribution of the Airy pattern.

As said previously, the focus of the spot is slightly modified by the aberrations effect. We stress that between  $D_B = 5\text{ m}$ , that is to say the completely illuminated objective aperture, and  $D_B = 3.8\text{ mm}$ , the optimum beam diameter for the resolution, the axial shift calculated with Zemax is  $\sim 400\text{ nm}$ . It is not insignificant compared to the axial extension of the spot ( $\sim 2\text{ }\mu\text{m}$ ), therefore the iris diaphragm controlling  $D_B$  should be installed at the beginning of the alignment to optimize the confocal tuning.

### 3.2.4 Mitigation of chromatic aberrations

In this section we shall tackled the issue of chromatic aberrations occurring through the microscope objective, and then examine the collection system composed exclusively of mirrors.

#### Correction for the chromatism of the objective

The wavelength of the laser beam is  $\lambda_{\text{exc}} = 266\text{ nm}$ , while the typical emission wavelength is around  $\lambda_{\text{em}} = 300\text{ nm}$ . The refractive indices of materials, lenses are made of, vary more rapidly in the ultraviolet range compared to the visible range. It means that the effective focal length of the objective can be quite different for these two wavelengths.

To assess the necessity to compensate for chromatic aberrations in the objective, let us evaluate the change in focal length. To do so, we simulate the path of optical rays with Zemax. The program calculates that **the focal length of the objective for 266 nm is 11 μm shorter than the focal length at 300 nm**. To know whether or not this change in focal length has to be taken into account in the alignment, it is relevant to estimate the axial extension (along  $z$ ) of the confocal spot. Assuming that



the focused laser beam operates in the  $\text{TEM}_{00}$  mode and is directed along the  $z$  axis, the confocal volume is an oblate ellipsoid, which is an ellipse rotated around its longer axis. Similarly to the lateral resolution, the axial resolution is defined as the distance from the center of the 3D diffraction pattern to the first axial minimum (in object space dimensions). This definition is the axial equivalent of the Rayleigh Criterion, and reads:

$$r_z = \frac{1 \times \lambda}{n - \sqrt{n^2 - NA^2}} \approx \frac{2n\lambda}{NA^2} \quad , \quad (3.2)$$

where  $n$  is the index of refraction of the medium between the objective and the sample. The approximation that is done above simply results from a limited series expansion of the square root at the first order by factorizing by  $n$ , and stays true for value of  $NA$  less or equal to 0.5.

For our setup, the medium is the air  $n = 1$  and the formula (3.2) yields an axial resolution of  $r_z = 2 * 0.266 / 0.5^2 \sim 2 \mu\text{m}$ . This result confirms that we need to compensate for the chromatic aberrations of the objective. Indeed, the center of the spot is displaced by  $11 \mu\text{m}$  between excitation ( $\lambda_{\text{exc}}$ ) and collection ( $\lambda_{\text{em}}$ ) wavelengths which is more than 5 times the longitudinal extension  $r_z$  of the confocal volume.

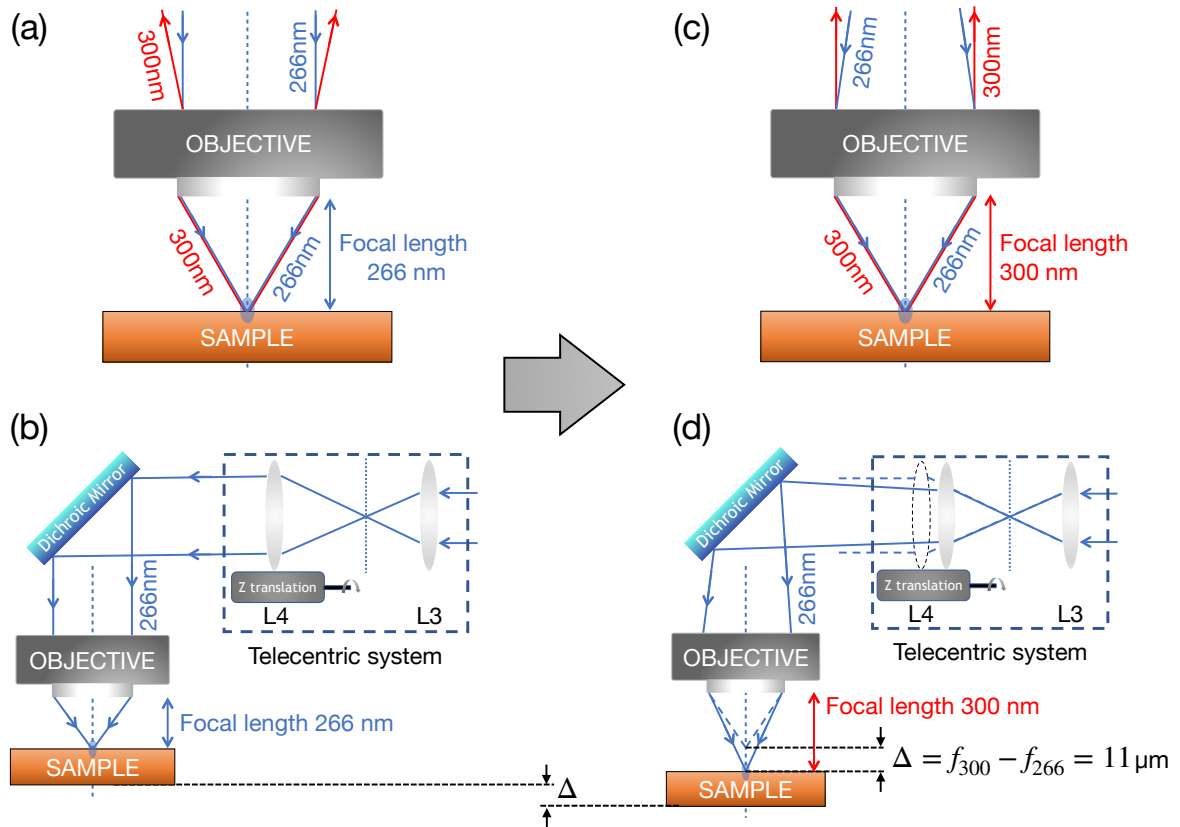


**Figure 3.14**

Scheme of the steps to compensate for chromatic aberrations of the objective. (a) Represents the inadequate situation where the laser beam is simply collimated at the entrance aperture, corresponding to lenses ( $L3$ ,  $L4$ ) of the telecentric system sharing a common focal plane (b). (d) Shows how the position of  $L4$  influences the divergence of the gaussian beam and thus the vertical position of the excitation spot. (c) Is the final sought configuration.

Fig 3.14 represents how to correct the chromatic aberrations of the refractive objective. Fig 3.14(a) shows the situation as it is just by focusing the collimated laser beam. The photoluminescence coming out of the sample diverges after the objective because the sample is placed at a closer distance than the focus at 300 nm. The divergence of the photoluminescence is very detrimental for the system. Indeed, after the objective the light goes through the glass window and different wavelengths (from 300 nm to 340 nm) will be further angularly dispersed, and will later have their foci at different distances even with an achromatic collection system. This situation corresponds to the experimental configuration where the distance between the two lenses (L3, L4) is the sum of their respective focal length for  $\lambda_{\text{exc}}$ , as represented in Fig 3.14(b).

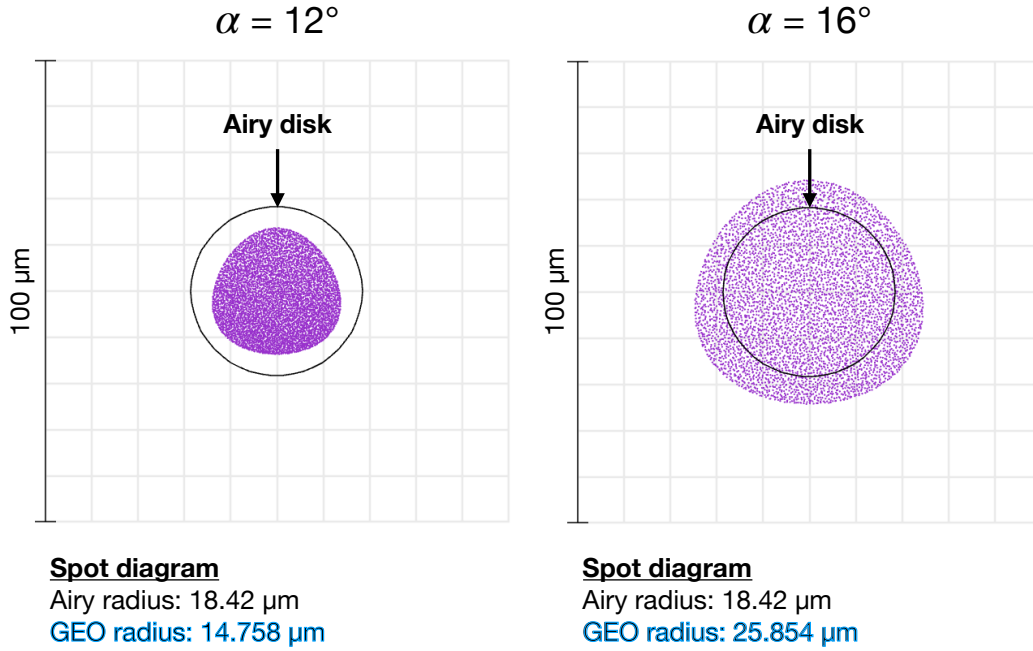
The goal here is to bring the focus of the laser for  $\lambda_{\text{exc}}$  at a distance corresponding to the focal length of the objective for  $\lambda_{\text{em}}$ . In this situation, the PL will exit the objective collimated.

The technique consists in using the telecentric system formed by (L3, L4) placed before the dichroic mirror. In Fig 3.14(b) the laser beam is collimated. But if one brings L4 closer to L3, as in Fig 3.14(d), geometrical optics stipulates that the beam will be divergent. It follows that the beam will be focused farther after the objective. We note  $\Delta$  the downward axial displacement of the excitation spot. At the same time, one needs to adjust the vertical position of the sample (with the steppers) in order to keep the excitation spot at the sample surface. The correct alignment is obtained when  $\Delta = 11 \mu\text{m}$ , that is to say when the focus of the laser matches that of the wavelength  $\lambda_{\text{em}}$ . This final situation is represented in Fig 3.14(c), where the excitation occurs with a divergent beam on the objective entrance pupil and the PL exits in a collimated beam. Experimentally, we have used a sample containing polar quantum dots (QDs), consisting of 10 monolayers of  $\text{Al}_{0.2}\text{Ga}_{0.8}\text{N}$ , with an emission peak at 300 nm. The QDs are strongly localized in depth (few nanometers), allowing for a sharp alignment.

### Achromatic collection system

We want to use this microscope to carry out studies on crystals emitting typically in the region 300 nm to 340 nm. The spectral width is large, and we have already stressed how dispersive the media can be at these wavelengths. Thus, having an aberration free system in collection is an essential prerequisite to preserve the resolution achieved in excitation. This is crucial both for the spatial and spectral resolution.

Therefore we only use mirrors in the collection path. With mirrors, chromatic aberrations are eliminated. However, in the case of concave mirrors (S1, S2), we must pay attention to the spherical aberrations that inherently occur when the light hit the mirrors with a non-zero incident angle. Since we need non-zero angle in the configuration of the experiment to set up the confocal filtering with the pinhole as well as to guide the light until the spectrometer, or towards the PMA detectors, it is necessary to determine which geometrical configuration of the mirrors allows an aberration-free optical system. We have performed optical simulation, using the software Zemax, to evaluate the limit angle of incidence on the concave mirrors (S1, S2) above which the effect of spherical aberrations deteriorate the resolution. In the simulation, the beam diameter is 5 mm (the entrance pupil diameter of the objective) and the wavelength 302 nm (ZPL of the 4.1 eV defect). Spot diagrams are shown on Fig 3.15 for  $\alpha$  angles, between incident

**Figure 3.15**

Spot diagrams in the focal plane of mirror  $S1$ , for angles between incident and reflected light at  $S1$  surface of  $\alpha = 12^\circ$  (left),  $16^\circ$  (right). Airy and geometrical (GEO) radii are given. The latter pertains to the calculated beam rays.

and reflected light, of  $12^\circ$  and  $16^\circ$ . The Airy disk radius is 18.4  $\mu\text{m}$  in both cases. It is clear that under  $12^\circ$  the aberrations introduce negligible effects, the geometrical radius (GEO) of the projected spot being smaller than the Airy radius, while above  $16^\circ$  they enlarge the spot beyond the diffraction-limited disk with a GEO radius 40% larger than the Airy one. It sets an upper limit of the angle for the experimental configuration. We chose to work with  $\alpha = 10^\circ$  to preserve an aberration-free collection.

In contrast, due to the constraints in the configuration of our setup, the focusing of the beam at the entrance of the spectrometer was made with an off-axis parabolic mirror (OAP)  $P_a$  (cf. Fig 3.10). An OAP is simply a side section of a parent parabolic mirror, as shown on Fig 3.16. However, unlike a centered parabolic mirror, an OAP mirror has an advantage in that it allows more interactive space around the focal point without disrupting the beam. Note that it is important to keep the incident beam parallel to the optical axis of the OAP, angular deviations producing comatic aberrations.

We use in our setup an OAP with  $24^\circ$  off-axis angle, enabling to work with high angles without introducing spherical aberrations.

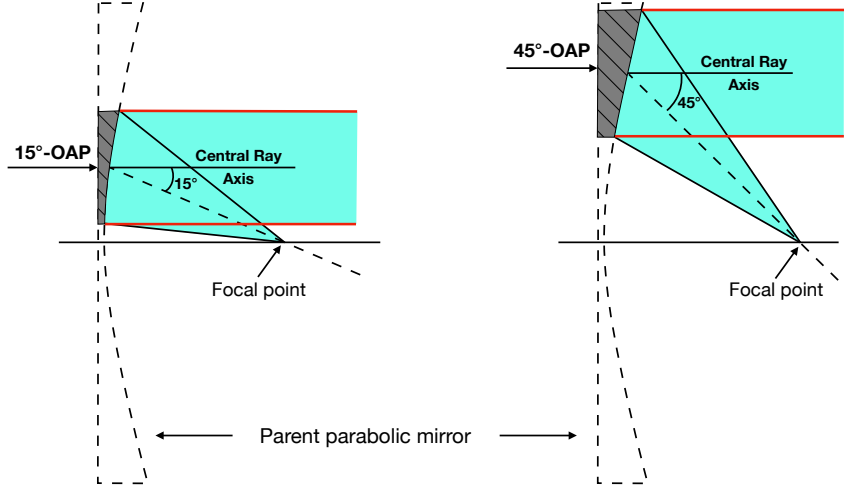


**Figure 3.16**

*Drawing of 15° and 45° off-axis parabolic mirrors (OAP). Parabolic mirrors are free of spherical aberrations.*

### 3.2.5 Performances of the microscope

We aim here at illustrating the different performances of the confocal microscope obtained with a crystal of hexagonal boron nitride (hBN).

#### Experimental conditions

The cryostat chamber is pumped down to  $10^{-4}$  mbar before cooling down. Between 100 and 150 K the pump valve is closed because cryopumping becomes more efficient than the turbo pump itself. We start working when reaching a temperature of about 5 K given by a temperature sensor located on the regulation bloc just beneath the sample holder. At this temperature the pressure is usually measured at  $2.5 \times 10^{-8}$  mbar.

#### Raster scan of PL with the PMA

Fig 3.17(a) presents a raster scan of photoluminescence recorded with the PMA detectors on a hBN flake over  $20 \times 20 \mu\text{m}^2$  area. The step size is 100 nm in both directions, and acquisition time per pixel is 50 ms. We observe a localized bright spot of emission (white square). A closeup scan is performed on the delimited region around this spot and shown on Fig 3.17(b). We evaluate the FWHM on this spot by plotting the cross-section of the intensity profile on Fig 3.17(c). A Gaussian fit to the experimental data (blue triangles) yields  $\text{FWHM} = 550$  nm, indicated by the orange arrows. This is a proof of concept for the achievement of the spatial resolution of our UV confocal setup. We are able to witness spatial features of less than 550 nm.

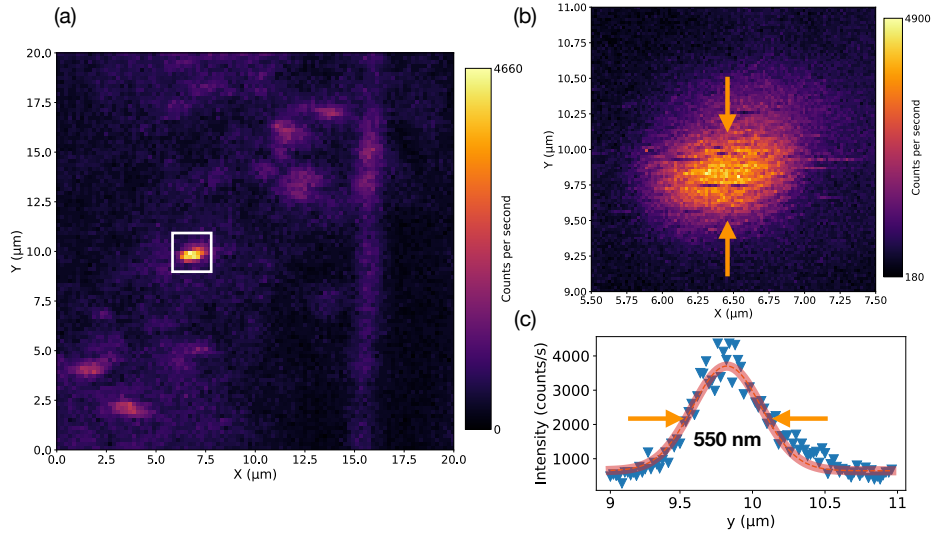


**Figure 3.17**

(a) Raster scan of photoluminescence recorded with the PMA detectors on a region of  $20 \times 20 \mu\text{m}^2$ . (b) Second scan with more pixel resolution on the white square of (a). (c) Vertical intensity profile of the scan along the vertical line indicated by the orange arrows on (b).

### SPIM images

With the spectrometer and the CCD camera in detection, we have the possibility to record one spectrum at every position of the scanners during the raster scan. This acquisition mode produces a 3D data set known as **spectral image** or shortly SPIM. Practically, these images are constructed by synchronizing the acquisition of the spectrometer and CCD with the piezoelectric scanners. A region of interest is determined on the sample, the spatial step size is usually chosen as  $1/3$  or  $1/2$  of the lateral spatial resolution and the spectrum acquisition time for each point is fixed relatively to the SNR, usually 0.5 to 5 s is necessary. The spectrum also needs to be recorded at least three times in order to remove spikes, originating from high energy particles, with a statistical treatment. The time needed to record a SPIM image is typically in the order of 10 to 25 hours depending on the size of the region of interest, the desired step size, the time of acquisition per spectrum and the reading speed of the CCD (varies the CCD noise).

The data processing of SPIM images allows the analysis of the correlation between spectral features and spatial localization, thus giving information on the impact of particular morphological elements at the surface on the spectral emission. Fig 3.18(b) shows the results of such an acquisition on bulk hBN at 4 K during 15 hours. The SPIM is acquired over the  $30 \times 30 \mu\text{m}^2$  region indicated by the blue square of the widefield micrograph Fig 3.18(a). The similarity between the two images indicates that the PL varies with surface morphology along the parallel lines. The SPIM is spectrally integrated between 302.49 and 302.80 nm (or 4.0946 and 4.0988 eV), that is to say around the ZPL of the 4.1 eV defect, and the step size in each direction is 200 nm. The spectrum of Fig 3.18(c) is taken at the pixel position indicated by the yellow square on the SPIM. We note the narrow ZPL, more visible in the inset. A Gaussian fit of the data points is calculated and provides  $\text{FWHM} = 0.87 \text{ meV}$ , corresponding to the

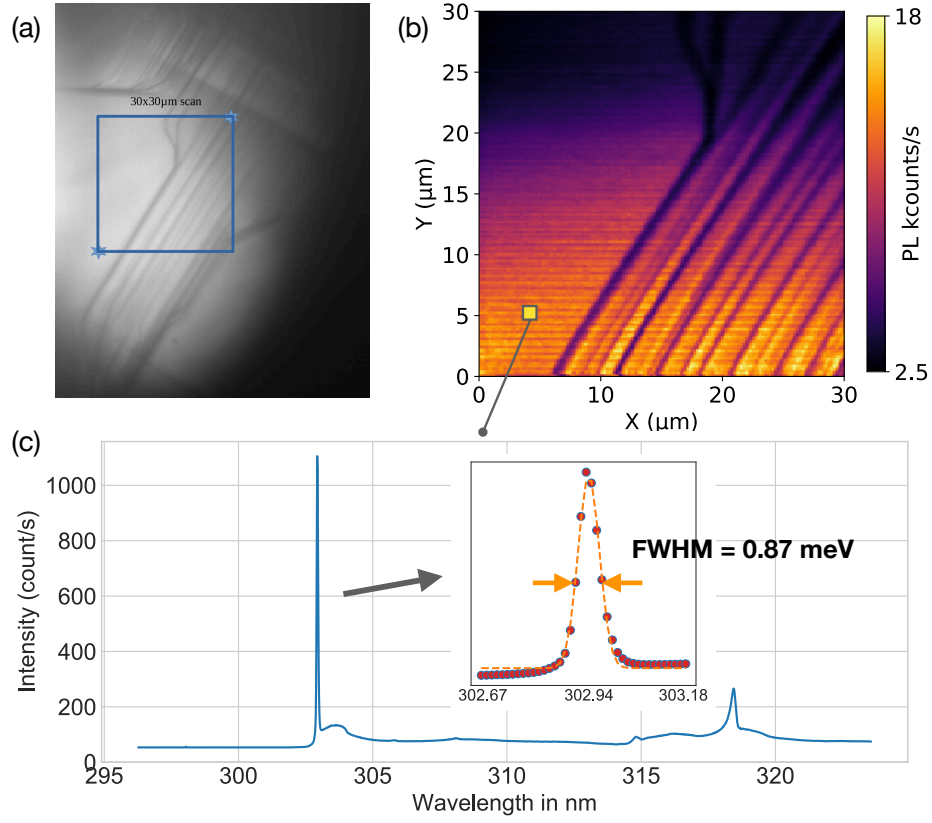


**Figure 3.18**

(a) Widefield image of a region of the hBN crystal. The blue square indicates a region of  $30 \times 30 \mu\text{m}^2$  on which is performed the SPIM acquisition (b). (c) is the spectrum extracted from the yellow pixel on (b). Inset: zoom on the ZPL of the emission and Gaussian fit (orange dotted line).

spectral resolution of our setup limited by the width of the slits of the spectrometer which were closed to  $20 \mu\text{m}$  (this is the minimum width and the one used for SPIM acquisition).

### 3.3 Probing deep defects at a sub-micrometer scale in PL

IN THIS SECTION, we present the studies carried out with the confocal microscope in the UV range, described in Section 3.2. We first investigate the new transitions unveiled in macro PL and reflectivity, and then focus on the 4.1 eV line with the aim of investigating the involvement of carbon in the structure of the defect. Finally I will present the search for single emitters at 4.1 eV in very thin flakes of hBN.

The spectrometer is set with the grating 1800 grooves/mm blazed at 250 nm, providing a spectral resolution of 0.02 nm or 0.3 meV at 300 nm (cf. Section 3.2.1). In this configuration, the full spectrum range is 27 nm (353 meV) around 310 nm (4 eV).

#### 3.3.1 The UV1-3 lines

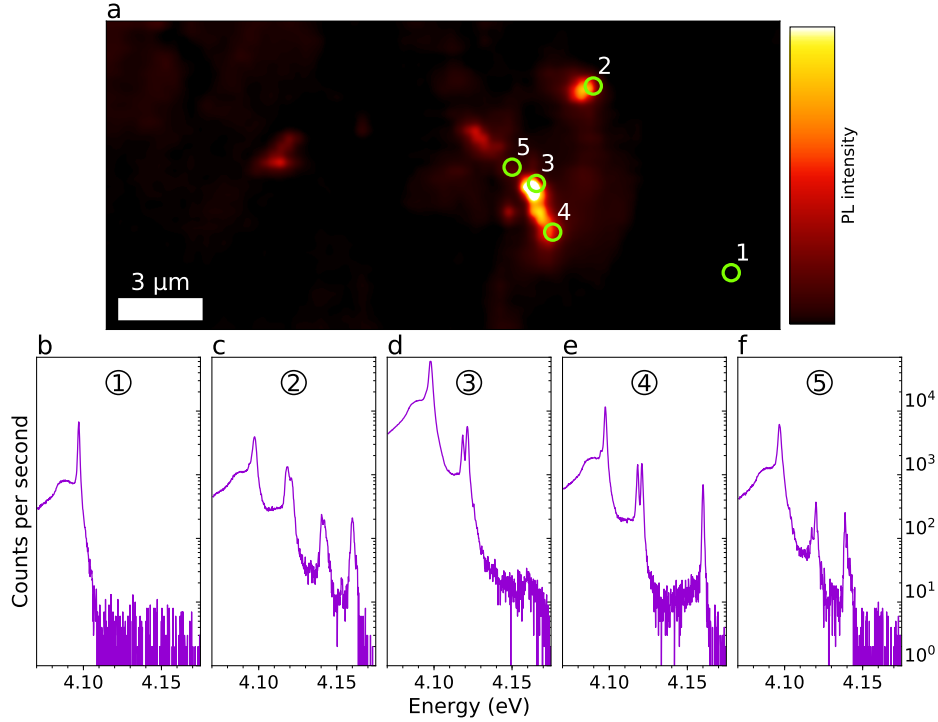


**Figure 3.19**

(a) Spatial variations of the PL signal intensity recorded by an UV scanning confocal microscope in sample C27, at 10 K, for an excitation power of 0.35 mW. The PL signal is integrated from 4.112 to 4.175 eV, with a 5 s integration time per acquisition point. (b)-(f) PL spectrum on a log scale recorded at the five different locations indicated by circles in (a).

We present here the measurements by our UV scanning confocal micro-PL setup related to the new transitions above 4.1 eV. We first studied the spatial variations of the UV1-3 PL signal intensity in sample C27, at 10 K. Carbon-doping in this hBN crystal is moderate to minimize broadening of the PL lines (cf. Table 3.1). In Fig 3.19(a), the PL map is plotted after integration of the signal intensity from 4.112 to 4.175 eV in order to better visualize the presence of the novel carbon-related UV1-3



lines. With this color code related to a spectral range excluding the 4.1 eV defect, we stress that the regions appearing dark correspond to a large PL intensity of  $\sim 5 \times 10^3$  counts per second for the 4.1 eV ZPL. In terms of the intensity of the UV1-3 lines, sample C27 is thus more or less homogeneously dim except for very bright domains. The 4.1 eV defect is also rather uniform and intense with a local increase in some bright regions of Fig 3.19(a), as detailed below.

The PL spectra of five representative regions are provided in the lower panels (b)-(f) of the figure. In the homogeneous part of the sample (circle 1), only the 4.1 eV line is detected with a sharp ZPL and the low-energy acoustic phonon sideband Fig 3.19(b). We note the high signal-to-noise ratio with a dynamical range of three decades between the maximum of the ZPL at 4.1 eV and the noise level at higher energy. Such a precision is important in view of claiming the contribution of the novel carbon-related UV1-3 lines is negligible within our signal-to-noise ratio.

Circles 2, 3, and 4 are located in the bright white regions. As expected, we observe that the UV1-3 lines have a PL signal intensity always lower than the 4.1 eV defect, in agreement with the macro-PL measurements presented in Fig 3.7. Our spatially resolved PL measurements reveal the striking absence of spatial correlation between the UV1-3 lines: all three are detected at point 2, only UV1 at point 3, UV1 and UV3 at point 4, and UV1 and UV2 at point 5. We thus conclude that the novel emission lines related to carbon-doping in hBN do not come from the same defect, rather they originate from three independent defects. This is crucial information and a key indication that one has to look for three novel microscopic configurations in order to account for the micro-PL measurements in Fig 3.19.

Eventually, we point out the doublet structure of UV1, which is much better resolved in Fig 3.19 than in Fig 3.4. Thanks to the low carbon doping and correspondingly narrow defect lines, as well as the spatial resolution of our microscope, the spectra recorded in positions 3 and 4 show that UV1 is a doublet with a splitting of 2.7 meV and a FWHM of 1.7 meV for the two components. No well-defined fine structure for UV2 and UV3 is detected in sample C27.

We now show the similar measurements performed on the heavily carbon-doped sample C33 in identical conditions to those of Fig 3.19. We first notice the increased inhomogeneity with many domains giving a large PL signal intensity for the UV1-3 lines. Moreover, there is a significant broadening with a typical FWHM of the order of  $\sim 10$  meV compared to 1.7 meV measured in Fig 3.19(d) and (e). Nevertheless, the 4.1 eV defect maintains a narrow ZPL as seen in Fig 3.20(c) and (e), not only where the UV1-3 lines are hardly observable, but also in locations where they are intense [Fig 3.20(f)] or even dominate the PL spectrum [Fig 3.20(b),(d)]. This phenomenology suggests that the UV1-3 defects are not only independent from each other but also uncorrelated to the 4.1 eV deep level. Besides, all three additional lines present no change when varying the polarization angle of the excitation laser.

We can also notice on Fig 3.20(c) the unusual shape of the ZPL peak, with a doublet structure. Actually, in the region surrounding spot 2 in Fig 3.20(a), we find a second peak in the ZPL structure. We recorded 11 spectra on a  $\sim 2 \mu\text{m}$  long horizontal line shown in Fig 3.21.

From bottom to top, we see the emergence of a second peak at lower energy, with a



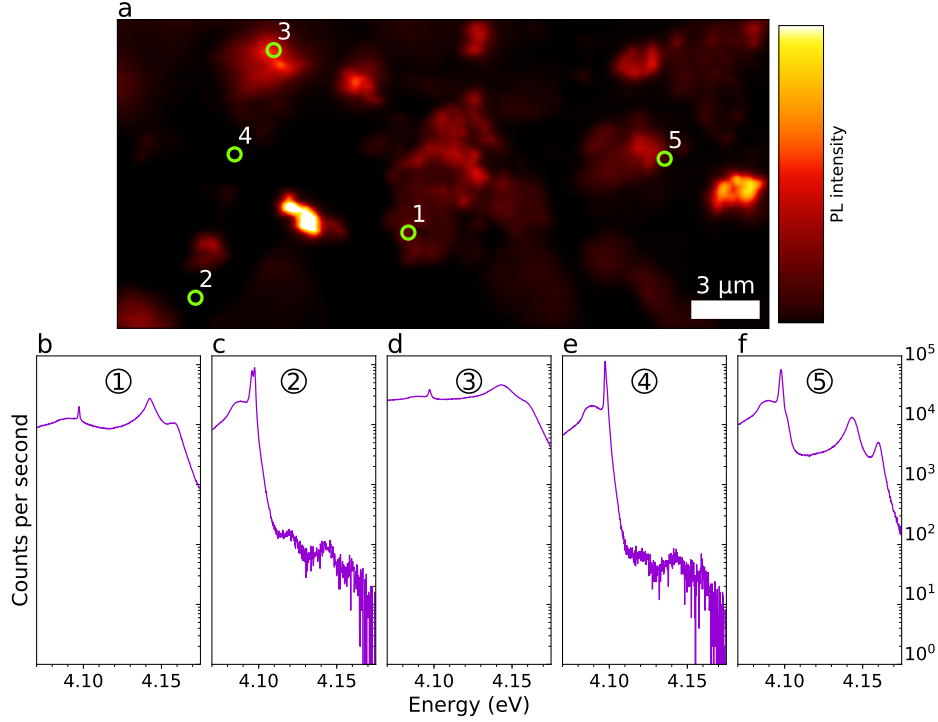


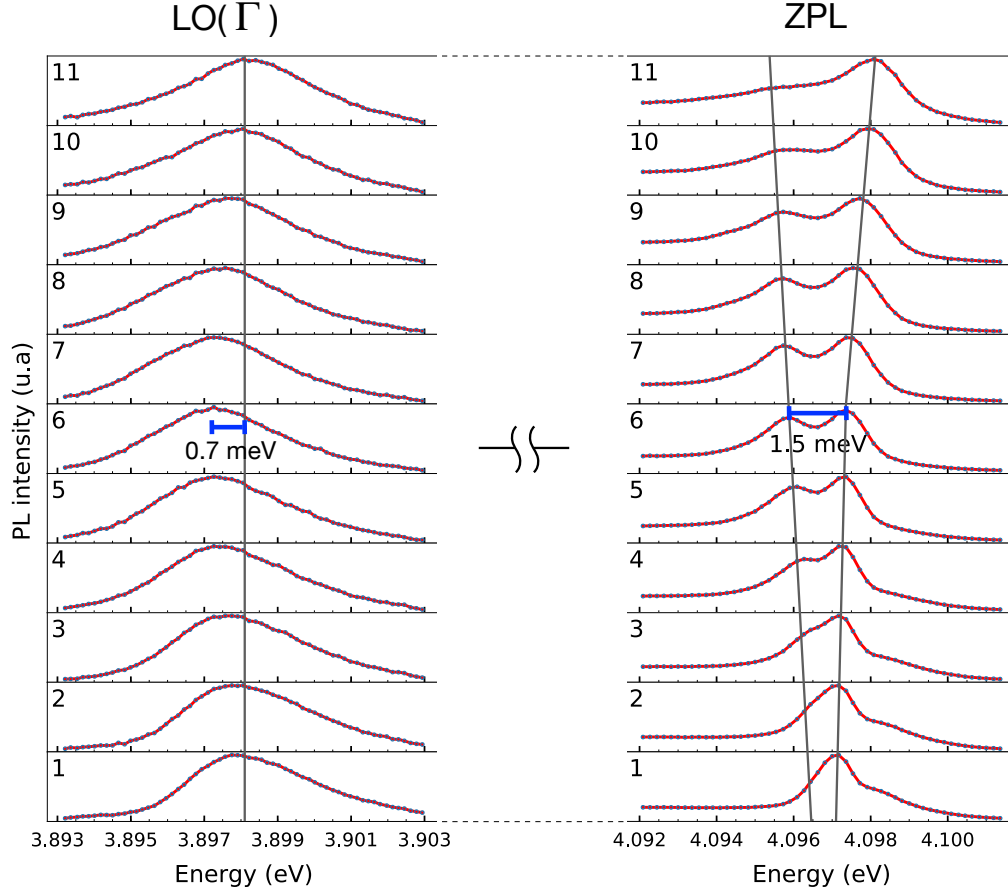
**Figure 3.20**

(a) Spatial variations of the PL signal intensity recorded by an UV scanning confocal microscope in the heavily carbon-doped sample C33, at 10 K, for an excitation power of 0.35 mW. The PL signal is integrated from 4.112 to 4.175 eV, and there is a 2.5 s integration time per acquisition point. (b)-(f) PL spectrum on a log scale recorded at the five different locations indicated by circles in (a).

splitting of 1.5 meV in the spectrum 6 where the two peaks have the same intensity, and then its progressive disappearance. No similar structure at the LO( $\Gamma$ ) phonon replica at 3.898 eV was discernible because of the broader profile of the phonon replica ( $\sim 5$  meV instead of  $\sim 1$  meV for the ZPL). However the phonon replica does red-shift by 0.7 meV from 1 (3.8981 eV) to 6 (3.8974 eV) where the doublet structure exhibits a maximum of contrast, and then return to its initial value by blue-shifting from 8 (3.8974 eV) to 11 (3.8981 eV). The FWHM of the replica also constantly increases from 1 (4.6 meV) to 11 (6.3 meV) following the trend of the ZPL doublet splitting illustrated by the gray lines on Fig 3.21. We don't know if this doublet structure emerges from an intrinsic phenomena or from the spatial variation of the emission. In the latter case, giving the  $\sim 500$  nm excitation spot diameter, it would be an indicator of the sub- $\mu$ m scale at which the ZPL position varies. This will be further investigated in the next section 3.3.2.

### Doublet structure of the UV1-3 lines

We have discussed above the doublet structure of the UV1 line in C27. We present below on Fig 3.22 a spectrum showing a well-resolved fine structure for the three lines UV1-3, recorded on sample C40 doped with  $^{13}\text{C}$  (cf. Table 3.1) at 4 K. PL maps integrated in the range 3.83-4.18 eV (ZPL + UV1-3) and 4.11-4.17 eV (UV1-3) are shown on Figs


**Figure 3.21**

Series of spectra recorded at 200 nm from each other. The horizontal energy range selects only the ZPL (right) and its phonon replica  $LO(\Gamma)$  (left). The horizontal blue bars at the spectrum 6 indicates energy splitting of 1.5 meV between the two ZPL and an energy shift of 0.7 meV for the phonon replica. Gray lines are guidelines for the eyes.

[3.22](#)(a) and (b), respectively. We can see that the emission from the additional lines are localized on what resemble structural deformations, like folds on the crystal surface as already observed in cathodoluminescence in hBN [\[66\]](#). On few particular points along these deformations, the spectrum displayed a well resolved doublet structure for UV1 and UV3, and on even fewer points a doublet structure for UV2. Fig [3.22](#)(c) displays the spectrum from the pixel selected on Fig [3.22](#)(b) (black square). The doublets UV1 and UV3 are fitted with a double gaussian function, yielding a splitting energy of 1.7 meV and 1.3 meV for UV1 and UV3, respectively. The width for both peaks is FWHM  $\sim 0.8$  meV. UV2 has a peak to peak splitting of 0.5 meV, and is shifted from the mean position usually recorded at 4.14 eV by  $\sim 3$  meV. Unfortunately, no analysis as a function of temperature could be done on these doublets, because the temperature change was causing a drift of the scanners.

We note that the above value of 1.7 meV for the splitting of UV1 is smaller than the one found in C27 in Fig [3.19](#) (2.7 meV), at same excitation power and temperature. To analyze the variations of the PL spectrum of the UV1 doublet, we have carried out statistical measurements over 45 well-defined doublets found in a  $30 \times 30 \mu\text{m}^2$  PL map

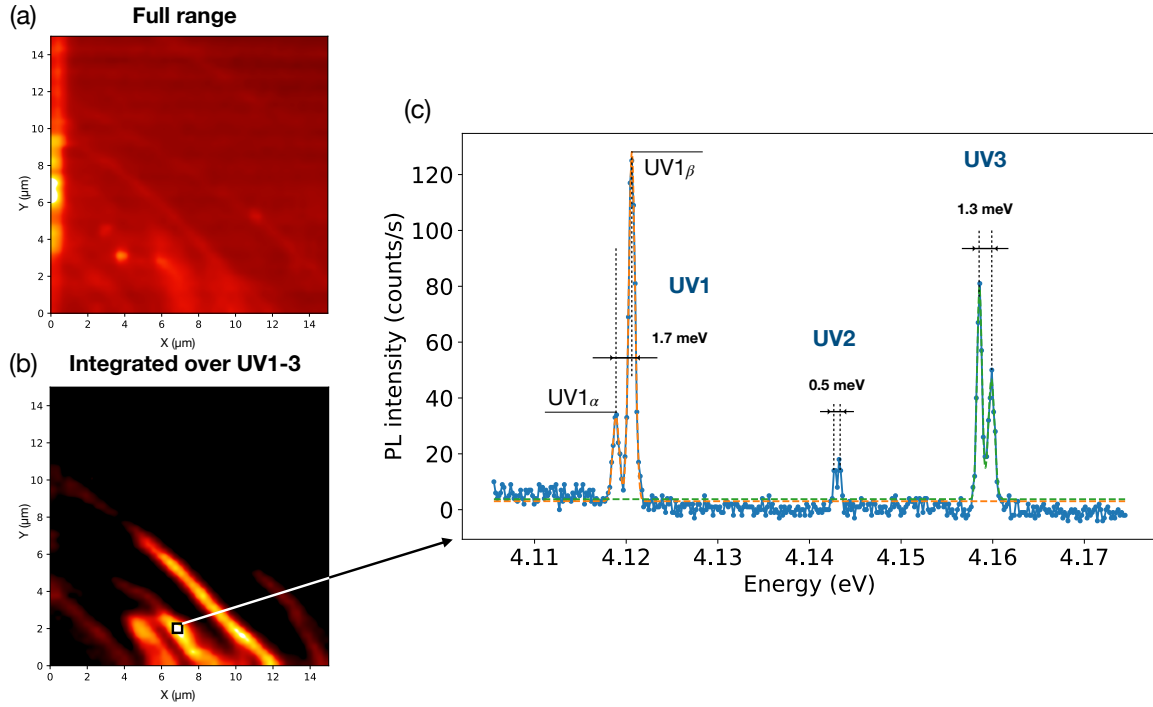


**Figure 3.22**

PL intensity map of sample C40 at 4 K integrated over the full spectrum (from 296 to 323 nm) (a) and over the UV1-3 lines (b), for an excitation power of 0.35 mW. (c) Spectrum recorded at the pixel position indicated by the black square on (b). The solid orange and green line are the double gaussian fits for UV1 and UV3, respectively.

of sample C27. The low and high energy components of the doublet are called UV1<sub>α</sub> and UV1<sub>β</sub>, as illustrated on Fig 3.22(c). The statistical analysis of the distribution of peak position and width for UV1<sub>α/β</sub> as well as the splitting values ( $\Delta E$ ) is presented in Table 3.2.

**Table 3.2**

Statistical analysis of the doublet UV1 over 45 spectra recorded on sample C27 at 4K and excitation power 0.35 mW. In the analysis, UV1<sub>α/β</sub> are independently fitted with a Lorentzian function and linear background.

	UV1 <sub>α</sub>			UV1 <sub>β</sub>			Splitting UV1
Feature	Position (nm)	Position (eV)	FWHM (meV)	Position (nm)	Position (eV)	FWHM (meV)	$\Delta E$ (meV)
mean	301.06	4.1183	1.5	300.86	4.1211	1.4	2.8
std	0.01	0.0002	0.5	0.02	0.0002	0.3	0.1
min	301.02	4.1180	0.8	300.82	4.1206	0.9	2.4
max	301.07	4.1188	3.2	300.89	4.1215	2.1	3.1

The mean value for the splitting of UV1 is  $\Delta E = 2.8$  meV, while the width of each component is  $\sim 1.5$  meV. These values indicate that the characteristics of the doublet UV1 in sample C27 are significantly different from the one in sample C40 discussed above. Indeed, the splitting  $\Delta E = 1.7$  meV in C40 (cf. Fig 3.22(c)) is 30% smaller than the minimum value found in C27, and the width of UV1<sub>α/β</sub> in Fig 3.22(c) is 50% lower than in C27. Giving the different compounds stoichiometry used in the growth

process for C27 and C40, and especially different concentrations of carbon (Table 3.1), the results of this analysis provides an additional evidence of the implication of carbon in the emergence of the new deep levels.

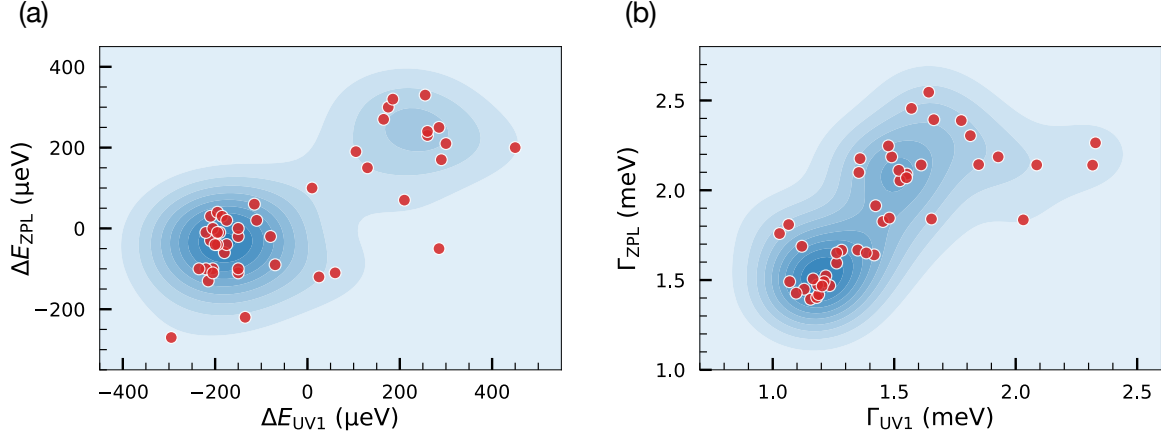


**Figure 3.23**

(a) Correlation plot of the shifts  $\Delta E$  of the UV1 line and ZPL of the 4.1 eV defect. The average UV1 energy is 4.1197 eV, and the average ZPL energy is 4.0974 eV. (b) Correlation plot of the widths  $\Gamma$  of the same peaks as in (a).

Correlations between the variations in the spectral line of the 4.1 eV defect and in the UV1 level have also been investigated. Fig 3.23(a) is the scatter plot with ZPL shift of the 4.1 eV defect assigned to the vertical axis and energy position shift of the center of the doublet UV1 on the horizontal one, and Fig 3.23(b) is the scatter plot of the width of the ZPL and the mean value of the  $UV1_{\alpha/\beta}$  widths. The data points in red are completed by a bivariate kernel density estimation in bluish hue to make the distribution more visible when data points pile up at the same location. For both plots, the distribution is mainly unimodal and no linear tendency is observed within the standard deviation of the values. If both transitions were maintaining an energy relation by phonon emission or absorption, for instance, this should be witnessed in these scatter plots with a clear linear trend.

We finally conclude that no correlation exists whatsoever between the UV1 line and the 4.1 eV defect.

## Summary

The study at low temperature at a sub- $\mu\text{m}$  scale of our carbon-doped hBN crystals confirms the existence of the three new transitions UV1-3 at 4.12, 4.14 and 4.16 eV, above the 4.1 eV defect. Although they are generally separated by a constant 20 meV interval, we have shown that they have different origins and are uncorrelated to each other and to the 4.1 eV defect. In moderately doped samples (C27, C40), a well-defined doublet structure is observed for the UV1 line more regularly than for the UV2-3 lines. A statistical analysis of the low energy component  $UV1_{\alpha}$  and the high energy component  $UV1_{\beta}$  of the UV1 doublet have brought two elements. First, the width of each sub-peak increases from sample C40 to C27 to C33, supposed to contained increasing amount of carbon, thus highlighting the role of carbon in these transitions.

Second, no significant correlation between the ZPL of the 4.1 eV defect and UV1 is observed, definitely confirming different origins.

We are thus dealing with a new class of point defects in hBN crystals. This raises fundamental questions about the exact influence of carbon, which is clearly involved here: is carbon itself incorporated into the defect structure, and in which crystallographic configurations with four point defects? Does carbon play only a side effect and promote the formation of deep levels without any embedded carbon atom? Since new shallow levels were observed in heavily carbon-doped hBN (Section 3.1.3) and interpreted as excitons bound to  $C_N$ , one may wonder if the UV1-3 lines are themselves the true candidates for point defects made of carbon, and if, on the contrary, the 4.1 eV defect is carbon-free.

As a perspective, it appears that the combination of advanced optical spectroscopy with nanoscale electron microscopy will be a promising strategy for unveiling the nature of the defects. Additionally, the examination of the density of the UV1-3 levels in similar samples having undergone annealing or other post-process treatments could equally bring illuminating elements in the present quest.

As far as theoretical development is concerned, a recent study [130] on various point defects in a planar molecular cluster of boron and nitrogen, using *ab initio* calculation employing density-functional theory (DFT) methods, presents two interesting candidates. For UV1: a Stone-Wales [131] defect  $SWC_B C_N$  composed of an adjacent pair of carbon placed in the middle of two heptagons, as represented on Fig 3.24(a), that has a HOMO-LUMO absorption line at 4.12 eV. For UV2: 4 carbons in a *cis* pattern  $C_{4\text{ cis}}$  [Fig 3.24(b)], with a HOMO-LUMO absorption at 4.14 eV. Both transitions have a good oscillator strength ( $\sim 0.3$ ) and a state localized on the defect, which is consistent with an experimental sharp peak. Moreover,  $C_{4\text{ cis}}$  has the particularity of having a second excited state around 5.3 eV, thus close to the shallow level observed at 5.37 eV, but is more delocalized. In the same idea, simulating the lattice deformation to mimic the effect of interstitial carbon atoms could bring important elements for the understanding of the origins of these new levels.

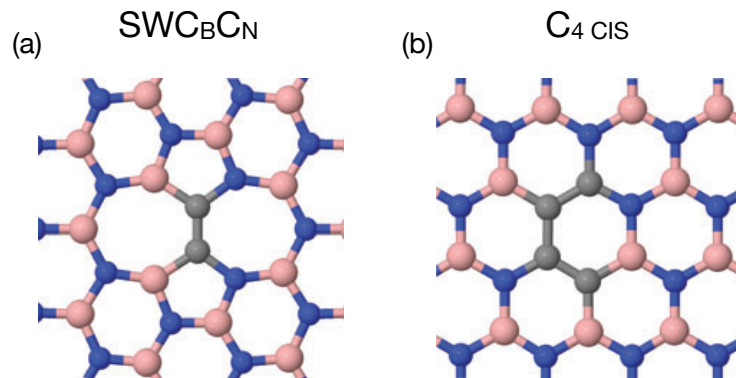


**Figure 3.24**

(a, b) Representation of point defects due to substitutional carbons [130]. Boron in pink, nitrogen in blue and carbon in gray.

### 3.3.2 Investigations of the 4.1 eV defect origin

Despite an active research activity, the chemical origin of the emission at 4.1 eV in hBN is still debated. Carbon is often considered to be involved as a substitutional atom for boron or nitrogen [67, 125, 127], and recent theoretical works using large finite-size molecular cluster with TD-DFT suggests multiple neighboring carbon substitutions like  $C_B C_N$  or  $C_{4_{cis/trans}}$  rather than simple substitution [130], in agreement with the observation via an electronic microscope showing that C atoms are only seen to substitute for B-N pairs and not for isolated vacancy [132].  $C_B C_N$  is also strongly supported by first-principles calculations based on hybrid density functionals that account for the experimentally observed ZPL position, radiative life and Huang-Rhys factor [133]. Some have also suggested donor-to-acceptor pair (DAP) transition between a shallow  $V_N$  donor and a deep  $C_N$  acceptor [134], while others have cited oxygen as potentially responsible for the emission [125] or  $V_B O_N$  complex [135]. In contrast, no correlation between impurity concentration (C, O) and deep level emission intensity at 4.1 eV has been measured in a recent study where the authors performed trace impurity analysis [136]. They rather suggested the intrinsic defect boron-vacancy ( $V_B$ ), similarly to the theoretical work of Attacalite et al. [126]. Moreover,  $C_N$  has been excluded on the basis of density functional theory with a hybrid functional [137]. In summary, it is not overstated to say that the origin of the emission at 4.1 eV remains highly conflicting.

In this controversial context, we use isotopic purification, a powerful tool in semiconductor physics enabling the fabrication of chemically and isotopically pure crystals and crystals doped with isotopically pure impurities [138]. We have carried out experiments on hBN crystal grown with isotopically controlled carbon doping in order to further test if carbon is a constituent of the defect emitting at 4.1 eV. More specifically, we have performed high-resolution measurements of the energy of the ZPL in hBN crystals doped either with  $^{13}\text{C}$  (sample C40, Table 3.1) or with  $^{nat}\text{C}$  (sample C27, Table 3.1), meaning the natural mixture of 99% in  $^{12}\text{C}$  and 1% in  $^{13}\text{C}$ , thus close to pure  $^{12}\text{C}$  doping.

The justification for this study on isotopic controlled doping is the fact that for point defects the isotopic selectivity of the atoms forming the defect can shift the zero-phonon line. Several mechanisms may explain this isotopic shift, such as a modification of the confinement or the electron-phonon interaction [138]. Quantitatively, the energy shifts are very small. For instance, the boron-bound exciton in silicon presents an isotopic shift of the order of 1  $\mu\text{eV}$  when switching from  $^{10}\text{B}$  to  $^{11}\text{B}$  [138], but it can be much larger as for G-centers in silicon with an isotopic shift of  $\sim 15 \mu\text{eV}$  between  $^{12}\text{C}$  and  $^{13}\text{C}$  doping [139], or even  $\sim 600 \mu\text{eV}$  between  $^{28}\text{Si}$  and  $^{30}\text{Si}$  for the SiV center in diamond [140].

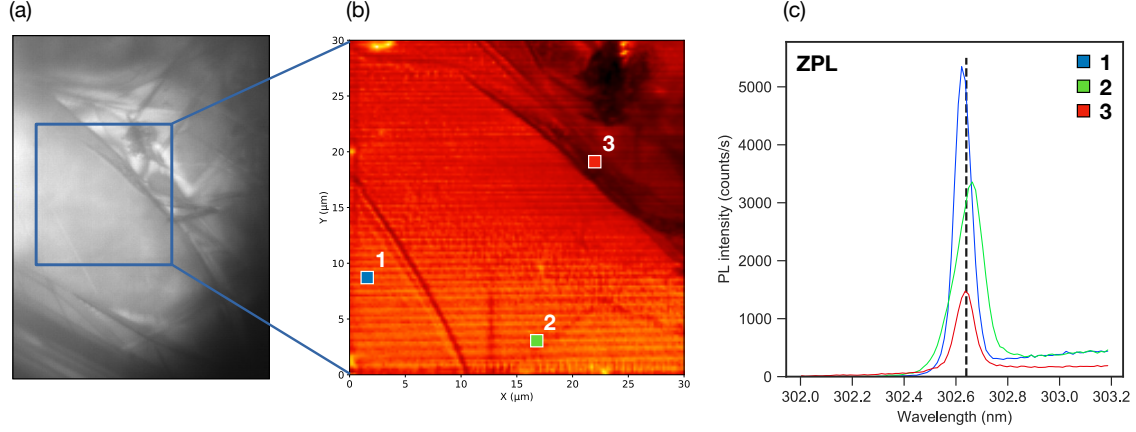
In the case of hBN doped either with  $^{nat}\text{C}$  or  $^{13}\text{C}$ , the search for an isotopic shift of the 4.1 eV line requires high-spectral resolution measurements. Moreover, one has to pay attention to possible variations of the ZPL energy within a given sample before comparing  $^{nat}\text{C}$ - and  $^{13}\text{C}$ -doped hBN in order to exclude any artifact due to a shift not coming from the isotopically controlled doping.

Following this reasoning, we will first study the spatial variations of the energy and linewidth of the ZPL in sample C40, and secondly compare the statistical analysis of



our data recorded in  $^{nat}\text{C}$ - and  $^{13}\text{C}$ -doped hBN crystals (C27 and C40, respectively).

### Spatial inhomogeneity

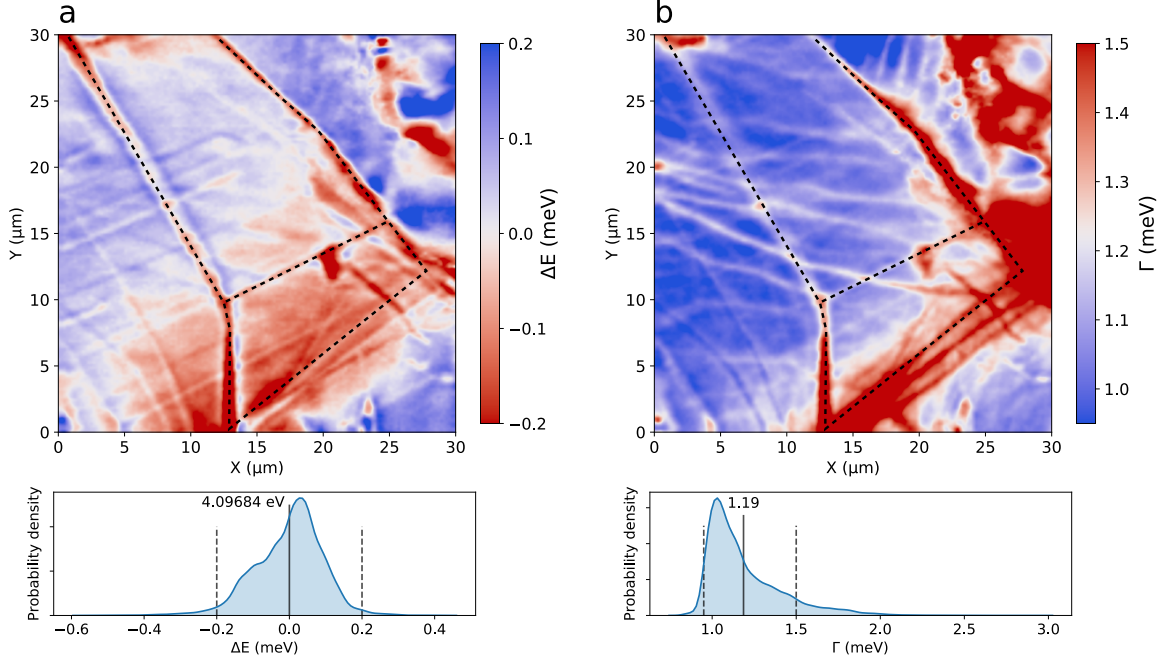


**Figure 3.25**

(a) Micrograph taken with the optical microscope. (b) PL scan recorded in the region identified by the blue square in (a). (c) The spectrum around the ZPL of the 4.1 eV defect taken at the locations indicated by the colored squares in (b).

On the surface of sample C40, we find a region exhibiting both good apparent crystallinity and structural deformations (stacking faults) with the widefield microscope (described in Section 3.2.1), as shown on the micrograph of Fig 3.25(a). On the region indicated by the  $30 \times 30 \mu\text{m}^2$  blue square, we recorded a map of the PL intensity at 10 K with our UV scanning confocal micro-PL setup [Fig 3.25(b)], here sharply integrated around the ZPL of the 4.1 eV defect (4.0946-4.0988 eV). The image shows a slowly decreasing intensity from bottom to top. We explain that with the variation of the crystal axial position in the depth of field of our confocal microscope, thus decreasing the excitation density from bottom to top. This is even more visible in the top right corner that corresponds to the stacking fault region, with higher contrast of intensity. For each of the  $150 \times 150$  positions, we acquired the PL spectrum over an integration time of 3 s, resulting in a total acquisition of 27 h for the full scan. Three pixels are selected on the scan and their respective spectrum around the ZPL is displayed on Fig 3.25(c). Apart from different intensities, we note that they all have a different ZPL position, distributed around the vertical dotted line, and different width. The shift between the most separated peaks (blue and green) is  $\sim 0.56$  meV. In order to better analyze the spatial shift of the ZPL position along with the width of the peak, the ZPL of each of the  $150 \times 150$  spectra was then fitted with a Gaussian function. With  $\sim 5 \times 10^3$  counts at the maximum of the ZPL, the standard deviation for the estimation of the ZPL energy and width was 6 and 10  $\mu\text{eV}$ , respectively. Fig 3.26 displays the analysis of the set of data.

In Fig 3.26(a) we show the spatial energy shift  $\Delta E$  of the ZPL relative to the average value of 4.09683 eV in this region. The variations of the ZPL full width at half-maximum


**Figure 3.26**

Upper panels: spatial variations of the shift  $\Delta E$  (a) and broadening  $\Gamma$  (b) of the ZPL in a  $30 \times 30 \mu\text{m}^2$  region of sample C40 at 10 K. The energy shift is calculated relatively to the average ZPL energy at 4.09684 eV. Black dotted lines are guidelines for the eyes. Lower panels: full distribution of the ZPL shift  $\Delta E$  (a) and broadening  $\Gamma$  (b). Vertical solid lines indicate the mean of the distribution while dotted lines indicates the interval chosen for plotting the spatial variations.

$\Gamma$  are plotted in Fig 3.26(b). The first finding is that the fluctuations of the ZPL energy over the  $30 \times 30 \mu\text{m}^2$  scanned region have an amplitude as large as 1 meV (see the full distribution on lower panel of the figure). These fluctuations contribute to the inhomogeneous broadening of the 4.1 eV line. With an average FWHM on the order of 1.2 meV [Fig 3.26(b)], the  $\pm 0.2$  meV variations of the ZPL energy are consistent with the 1.9 meV value of the ZPL width previously reported by macro-PL measurements in [68], but here we notably demonstrate the sub- $\mu\text{m}$  scale at which the ZPL energy varies.

Interestingly, the ZPL shifts appear spatially correlated with the ZPL broadening. Indeed, where the ZPL position is red-shifted in (a) (redder) it is also broadened in (b) (also redder). Although there is not a one-to-one correlation, the overall pattern is the same in Figs 3.26(a) and (b), with lines of different orientations in close analogy to the luminescence maps recorded by cathodoluminescence [66]. We interpret these lines as folds or extended defects in the lamellar structure of our hBN crystal, a point of view supported by the widefield micrograph of Fig 3.25(a).

The spatial correlation of the ZPL shift and broadening suggests they correspond to the real and imaginary parts of the same perturbation. This common origin is further supported by a similar magnitude (in the 0.1 meV range here), and this variation presumably originate from mechanical strain related to the stacking faults in hBN.



We present in Fig 3.27 the same analysis done in a  $30 \times 30 \mu\text{m}^2$  region of sample C27 at 10 K, with  $75 \times 75$  spectra recorded. The average ZPL energy is 4.09702 eV. We note a greater heterogeneity in this region of sample C27 compared with the one presented for sample C40, with a maximum amplitude for  $\Delta E$  of 1.8 meV, and for  $\Gamma$  of 3 meV. Strikingly, the tendency discussed above for the correlation of the ZPL shift and broadening, tend to reverse in these images: blue-shifted areas of the ZPL [Fig 3.27(a)] matching broader ZPL areas [Fig 3.27(b)]. Again, this is no perfect correlation.

From a structural point of view, the images in Fig 3.27 present no straight lines as in Fig 3.26 that we attributed to folds arising from stacking faults in the crystal. These straight lines make easier the interpretation of strain-induced variations. In contrast, the shapes observed in Fig 3.27 suggest disparate aggregation of carbons during the growth process, which could influence, directly or indirectly, the spectral features of the defects. However, we lack of experimental characterization concerning the distribution of carbons throughout the crystal, whether it is homogeneously distributed or not, thus the previous statement has to be taken only as an attempt of interpretation.

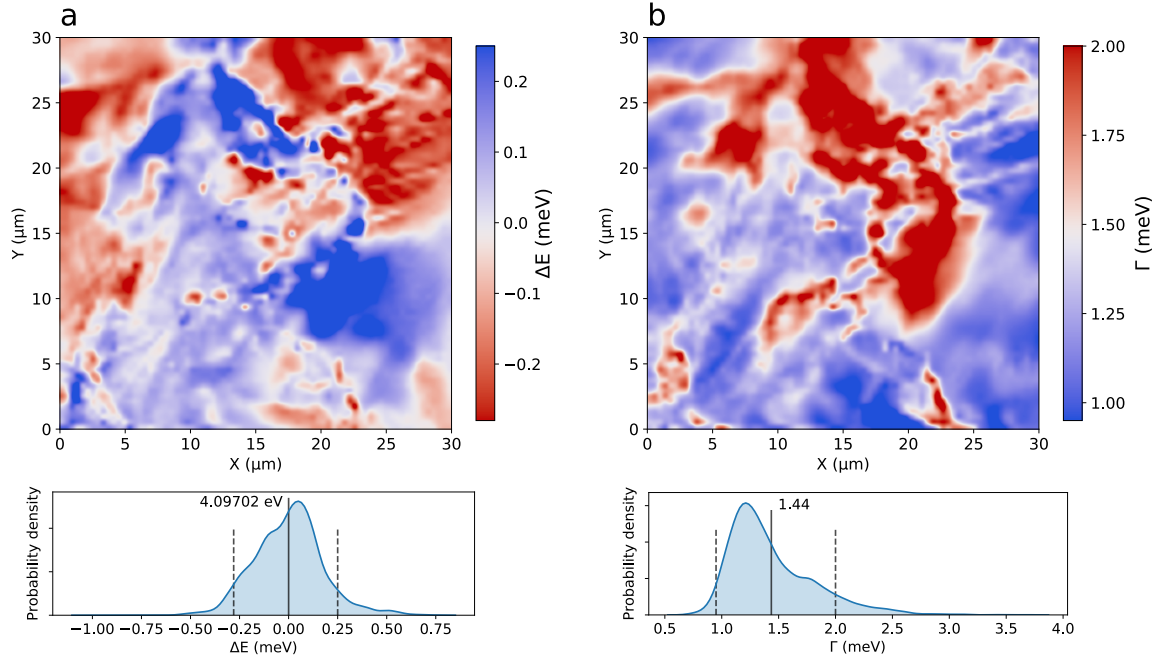


**Figure 3.27**

Upper panels: spatial variations of the shift  $\Delta E$  (a) and broadening  $\Gamma$  (b) of the ZPL in a  $30 \times 30 \mu\text{m}^2$  region of sample C27 at 10 K. The energy shift is calculated relatively to the average ZPL energy at 4.09702 eV. Lower panels: full distribution of the ZPL shift  $\Delta E$  (a) and broadening  $\Gamma$  (b). Vertical solid lines indicate the mean of the distribution while dotted lines indicates the interval chosen for plotting the spatial variations.

Over the same area of sample C40 Fig 3.26, we could acquire the data set with the spectrometer tuned at the wavelength of the Raman-active mode at  $\sim 1370 \text{ cm}^{-1}$  (170 meV). The maps, shown on Fig 3.28, are featureless except for the wave pattern that we attribute to an artifact during the hours-long scanning time. There are random

fluctuations in the range of  $\pm 60 \mu\text{eV}$  for the energy shift ( $\Delta E$ ), and  $\pm 0.15 \text{ meV}$  for the FWHM ( $\Gamma$ ). This may come from the reduction of the stress-induced energy shift for phonons compared to electrons [141, 142].

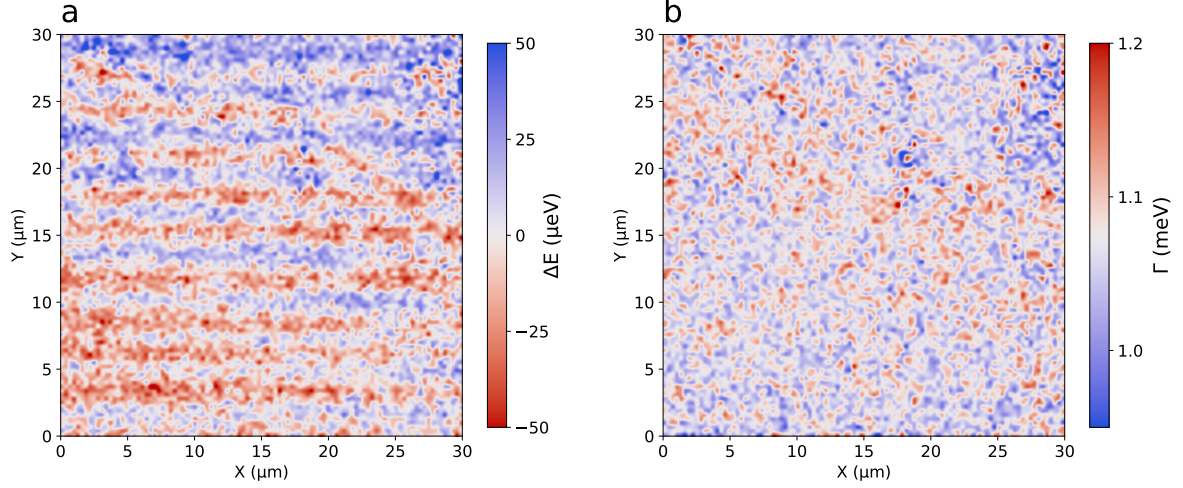


**Figure 3.28**

Spatial variations of the shift  $\Delta E$  (a) and broadening  $\Gamma$  (b) of the Raman-active mode of hBN at  $1370 \text{ cm}^{-1}$  ( $170 \text{ meV}$ ) in a  $30 \times 30 \mu\text{m}^2$  region of sample C40 at 10 K. The average Raman-mode energy is  $169.78 \text{ meV}$ .

Although detrimental to our objective of resolving an isotopic shift in  $^{nat}\text{C}$ - and  $^{13}\text{C}$ -doped hBN crystals, the sensitivity of the ZPL energy to the presumable perturbation caused by strain is an important piece of information for elucidating the structure of the point defect leading to the  $4.1 \text{ eV}$  emission. In this context, PL experiments as a function of pressure could provide interesting complementary inputs [69] for identifying the nature of the defect and reaching a quantitative interpretation of our measurements.

### $^{13}\text{C}$ - and $^{nat}\text{C}$ doping

Keeping in mind the spatially-resolved ZPL fluctuations in Fig 3.26 and Fig 3.27, we will now compare the ZPL energy in hBN crystals doped either with  $^{nat}\text{C}$  and  $^{13}\text{C}$ . Fig 3.29 shows the probability density of detecting the ZPL at a given energy. Following the data analysis described previously, we have computed the statistical distributions of the ZPL energy in two  $30 \times 30 \mu\text{m}^2$  regions, arbitrarily selected in each crystal.

We first note the different shapes and widths of the four statistical distributions, which can be narrow or asymmetric in the two types of samples. More importantly, there is no spectral separation indicative of an isotopic shift of the ZPL, within the inhomogeneous broadening of the  $4.1 \text{ eV}$  line. This is further supported by the mean value of the ZPL energy in  $^{13}\text{C}$ - and  $^{nat}\text{C}$ -doped hBN crystals calculated for ten  $30 \times 30 \mu\text{m}^2$  regions in each sample, and represented by an horizontal bar of  $100 \mu\text{eV}$  on Fig 3.29. Moreover, there does not seem to be any specific feature of the spatial fluctuations of the ZPL energy from  $^{13}\text{C}$ - to  $^{nat}\text{C}$ -doped hBN crystals. As explained in the previous section, this suggests mechanical strain or inhomogeneous carbon distribution impacts the ZPL position independently of the carbon isotopes.

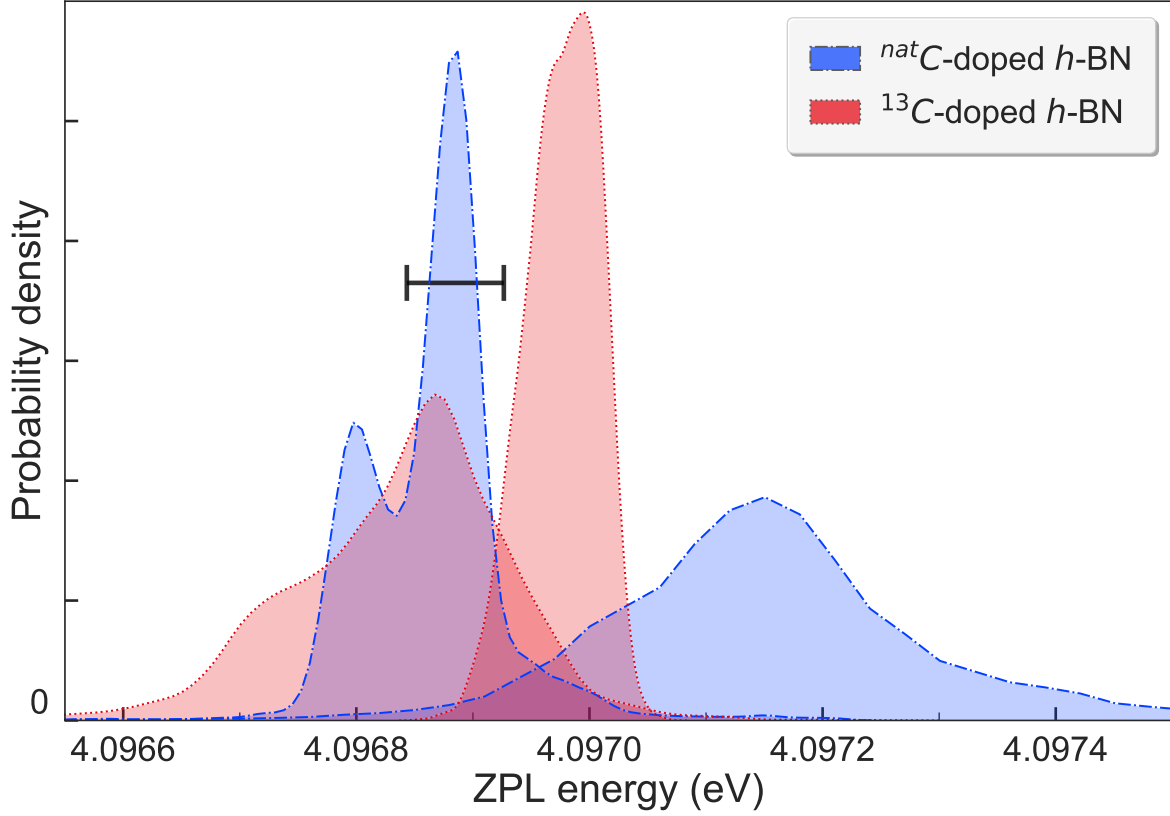


**Figure 3.29**

Statistical analysis of the ZPL energy in  $^{nat}\text{C}$ - and  $^{13}\text{C}$ -doped hBN crystals: the normalized probability density of the ZPL energy is plotted for four  $30 \times 30 \mu\text{m}^2$  regions: two in a  $^{13}\text{C}$ -doped crystal (C40, red data), two in a  $^{nat}\text{C}$ -doped crystal (C27, blue data). The 100  $\mu\text{eV}$  large horizontal bar indicates the difference of the mean values of the ZPL energy in  $^{13}\text{C}$ - and  $^{nat}\text{C}$ -doped hBN crystals, the mean values being calculated for a total of ten  $30 \times 30 \mu\text{m}^2$  regions.

### Summary

Thanks to our spectral resolution, spatial resolution, and the high signal-to-noise (SNR) and signal-to-background (SNB) of the spectral line corresponding to the ZPL of the 4.1 eV defect in bulk hBN, we could draw maps illustrating the spatial variations of the shift and broadening of the ZPL, demonstrating that the spatial fluctuations of the ZPL is in a sub- $\mu\text{m}$  scale. These maps show interesting features with localized correlations of the two parameters along specific structural deformation, that we interpret as folds arising from stacking faults in the crystal. At this extended defects, stress is most likely responsible for the observed variations of both  $\Delta E$  and  $\Gamma$ . Notably, the maximum amplitude for the energy shift is in the order of 1 meV, with typical variations happening at the scale of 0.1 meV. Unfortunately, the statistical study on  $^{13}\text{C}$ - and  $^{nat}\text{C}$ -doped hBN crystals of the ZPL energy shift presents similar variations in both type of samples. We thus conclude that there is either no isotopic shift, or a finite one but smaller than the inhomogeneous broadening. Isotopic selectivity in carbon-doping has not brought any proof to confirm or infirm the presence of carbon in the structure of the defect emitting at 4.1 eV. However, we hope that the quantitative measurements presented here will be

useful for testing various models in future calculations.

### 3.3.3 Search for isolated emitters at 4.1 eV

In this section, we present the investigations we conducted to isolate the emission of a single point defect at 4.1 eV using the micro-PL confocal setup operating at 266 nm (4.66 eV). This study is motivated by the little knowledge concerning the photodynamics of this deep defect in hBN. Museur et al. [127] measured by time-resolved PL experiments a radiative decay for the luminescence originating from ensembles of defects of  $\sim 1.1$  ns, confirming an early study from 1981 [120]. This fast decay was later also measured by Meuret et al. [143] from the bunching peak decay curve in the autocorrelation function of the cathodoluminescence intensity. More recently, Bourrel-lier et al. [67] reported the first detection of the emission from a single 4.1 eV defect by cathodoluminescence in a STEM<sup>2</sup> microscope (cf. Chapter 1 Section 1.4.3), and by recording the second-order correlation function they could extract the lifetime of a single emitter from the antibunching yielding a value of 2.5 ns. However, under electron irradiation the broadband emission around 4 eV, originating from intrinsic defects, rises and decreases the signal-to-background ratio, ultimately limiting the signal-to-noise ratio [67]. It has been demonstrated that under an excitation energy of  $\sim 5.2$  eV this broadband emission is quenched in photoluminescence experiments [127]. In our experiment, photo-excitation operates at energy below this threshold. Moreover, the radiative recombination at point defects inside the bandgap in a cathodoluminescence experiment (with electrons carrying energy in the order of tens of thousands electron-volts) is a complex phenomenon to analyze because it often involves several processes of desexcitation, while in photoluminescence experiment we operate close to resonance with the level transition, enabling the study of the photodynamics in similar conditions in which a single-photon source would be used in applications.

### Combining photon microscopy with electron microscopy

During my thesis, I had the opportunity to do several visits at the LPS<sup>3</sup> in Paris in the team of Alberto Zobelli and Mathieu Kociak, specialists in electron microscopy and especially in cathodoluminescence (CL). The purpose was to use the STEM microscope operating at 150 K, and try to find isolated emitters at 4.1 eV and record the signal of CL simultaneously with performing electron energy loss spectroscopy (EELS). By measuring the energy loss experienced by the incident electrons during their interaction with the matter, EELS provides information on the chemical bonding, optical and electronic properties, and especially on the chemical composition of the specimen. As discussed previously, carbon is one favorite candidate for the origin of the point defect, thus we used samples from NIMS in Japan, highly doped with carbon, giving a yellow hue to the crystal. Unfortunately the sample were contaminated by another source of carbon, making the analysis of the EELS spectrum insignificant.

However, in another attempt of combining the powerful tool of electron- and photon-microscope, Alberto Zobelli and Steffi Woo pre-characterized thin flakes of hBN with

<sup>2</sup>Scanning transmission electron microscope.

<sup>3</sup>Laboratoire de Physique des Solides, Orsay - France.

the STEM microscope and sent them to us. We will present first the characterization done with the STEM-CL microscope and secondly the study with our PL microscope.

### Samples and pre-characterization

An undoped single crystal of hBN from Taniguchi and Watanabe (NIMS) was liquid-phase exfoliated in isopropanol for 15 min; 3 drops of hBN dispersion was placed onto a 300-mesh copper TEM grids with lacey carbon support. In the annular dark field (ADF) image of Fig 3.30(a) we can see flakes supported by the lacey carbon grid. The transparency of the flake in the bright field (BF) image Fig 3.30(b) is an indicator of the small thickness in the order of tens of nanometers. Having thin flakes is an essential element in the purpose of isolating a single emitter. CL measurements were

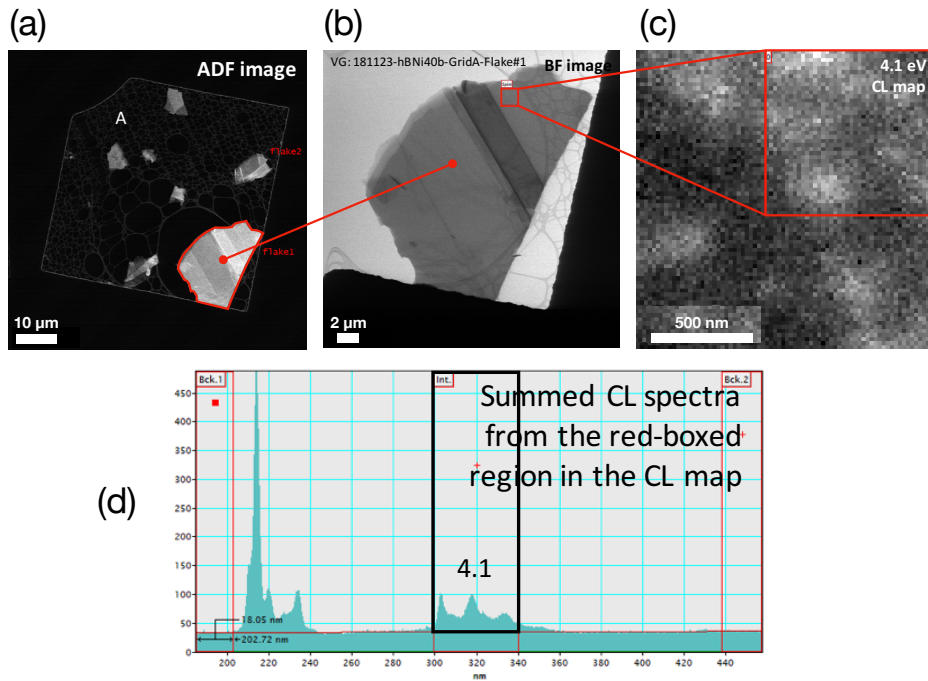


**Figure 3.30**

Annular dark field (ADF) image of flakes deposited on a TEM grid (a), closeup of a flake in bright field (BF) imaging mode (b), filtered CL map on a small region (c) corresponding to the signal intensity integrated over the wavelength range inside the rectangular box of the CL spectrum (d).

done at 60 kV and with nitrogen cooling (150 K) in random scan mode for spectrum imaging [144]. Fig 3.30(c) is a CL map performed on the red square of the BF image and integrated on a spectral range encompassing the 4.1 eV defect and its two phonon replica, as illustrated by the black rectangle in the CL spectrum of Fig 3.30(d). The spectrum is obtained by averaging the signal over the red-boxed region of Fig 3.30(c). The red square on the CL map is  $\sim 700$  nm large and presents a structured emission distribution with a more or less isolated spot on the bottom left.

Basically, the pre-characterization was meant to produce a cartography of the isolated deep emitters at 4.1 eV on the flakes that could potentially be resolved and studied with our PL microscope. We will now present the results of our measurements.



### Images with the UV confocal microscope: emission at the borders of the flakes

The TEM grid was installed in our cryostat and fixed to the sample holder with silver paint. The silver paint has a strong broad emission from 330 nm to longer wavelengths when excited with our laser at 266 nm, this fact precluded to study most of the areas characterized by STEM-CL, thus we only studied the flakes lying on the copper structure of the grid.

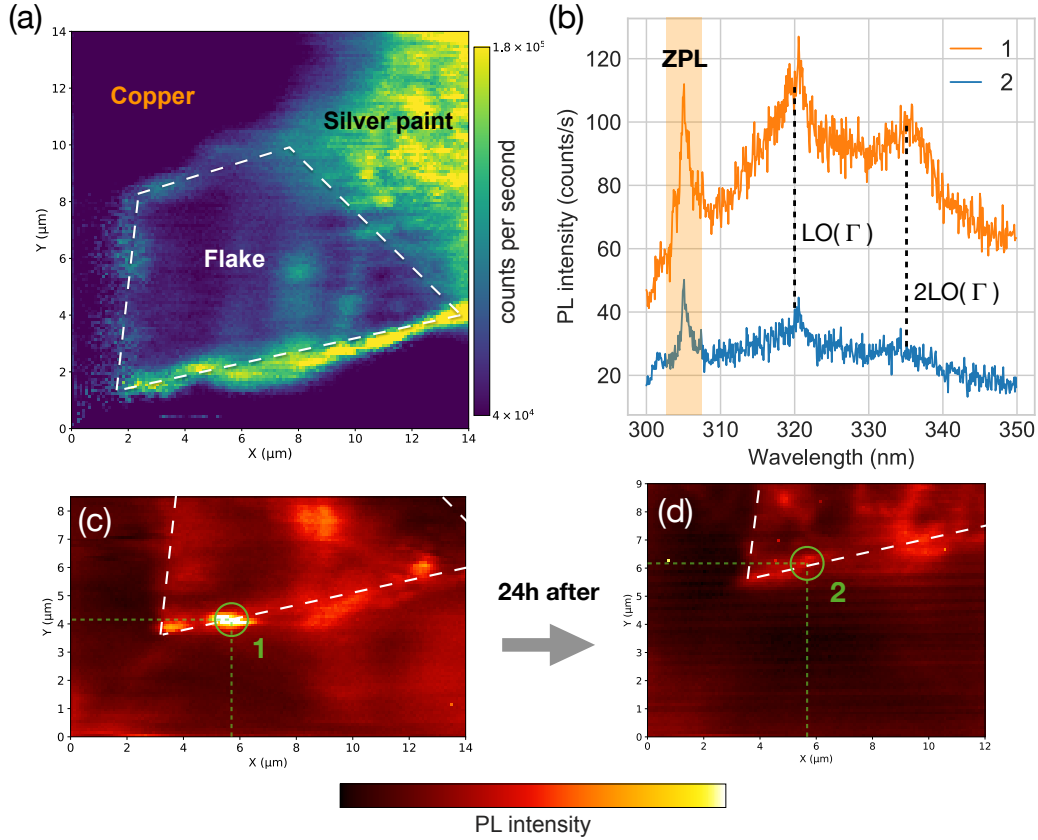


**Figure 3.31**

(a) Raster scan of PL on a flake lying on the copper structure. (b) Spectrum 1 is acquired at the brightest pixel of the circle in (c) and spectrum 2 at the brightest pixel of the circle in (d). The filtered PL image (c) was recorded just after (a), and (d) was recorded 24 hours after (c). The PL signal is integrated between 300 and 340 nm. The vertical upward shifts of the flake between the three scans is due to a drift of the steppers.

On Fig 3.31(a) we present a raster scan of PL recorded with the photomultipliers at 4 K on a region of a flake lying on the copper (delimited by the white dotted lines). We first notice a spatially-inhomogeneous emission, with high PL signal from the border of the flake presenting a maximum signal-to-background ratio of  $\sim 10$  and region where there is no emission from the deep defect, which was never observed in bulk material (Section 3.3.1). The fact that the signal is more intense on the border is actually a general observation in our measurements. There are several ways of interpreting that: either the PL collection efficiency is higher on the border because the light can freely

propagates out of the crystal and be collected, or this is the result of intrinsic phenomena, which may be related to polarization direction or stacking order at the border, or dangling bonds providing electrostatic potentials for impurity and thus promoting the formation of defects, enhancing the emission intensity.

After this first scan, we recorded a PL image with a pixel size of  $100 \times 100 \text{ nm}^2$ , presented on Fig 3.31(c) after integration of the PL signal between 300 and 340 nm so as to include the ZPL and the two LO( $\Gamma$ ) phonon replicas of the 4.1 eV defect. Strikingly, there is an important loss of emission on the bottom border of the flake. We focus our attention on the bright spot indicated by the green circle. The spectrum of the emission at the brightest pixel in this circle is shown on Fig 3.31(b) (1, orange). Strikingly, the profile is very different from what is usually recorded in bulk crystal, with a first phonon replica more intense than the ZPL, and a broadening ten times greater with  $\text{FWHM} = 10 \text{ meV}$  instead of  $\sim 1 \text{ meV}$ . We also note the appearance of a broad background raising underneath the defect emission. Last but not least, the overall profile is red-shifted compared with usual measurement performed at 4 K (the ZPL is at 305 instead of 302 nm). In fact, the PL spectrum is similar to the CL spectrum of Fig 3.30(d) recorded at 150 K in the STEM microscope. One hypothesis is that the flake, in this configuration where it is suspended over the lacey carbon grid, may not be fully thermalized with the copper structure lying on the sample holder, thus red-shifting the emission and broadening the line. However, in macro-PL experiment no such dependence on temperature is observed, as it was discussed in Section 1.4.3. Thus, this could be a behavior specific to low number of emitters, or due to the modified coupling to phonon in very thin flakes of hBN.

We now look at the third PL image [Fig 3.31(d)] recorded at the exact same conditions and with same parameters, but 24h after Fig 3.31(c). Remarkably, there is an important decline in the intensity of the bright region. Indeed, as evidenced on the blue spectrum of Fig 3.31(b) from the same brightest pixel, the intensity for the ZPL has decreased by a factor 2 but the integrated area undergoes a much more severe decrease. This phenomenon is not specific to this flake but was generally observed on those few-tens-of-nanometers-thick flakes.

To sum up, the emission originating from point defects emitting at 4.1 eV decreases between successive scans, especially when the emission takes place at the borders of the crystal. This unveils a phenomenon of bleaching for the 4.1 eV deep defect under laser excitation in these chemically exfoliated flakes. Besides, this conclusion lead us to favor an intrinsic cause for the emission at the borders, because several scans on the same region result in the quenching of the emission.

### Emission from localized centers inside the flakes

In certain cases however, we could find isolated emitters within a flake exhibiting stable emission over time. The XY PL scan of Fig 3.32(a), performed with the bandpass filter 300-340 nm, displays a bright localized emission at  $X = 6.5 \mu\text{m}$  and  $Y = 10 \mu\text{m}$ , over a more or less dim area. This spot is well localized and has a more or less rounded shape with  $\text{SNR} \sim 26$ , as shows the closeup scan of Fig 3.32(b). The intensity profile of the vertical cross-section is presented on Fig 3.32(d). A Gaussian fit to this profile yields a width of  $\text{FWHM} = 550 \text{ nm}$ , which indicates that the size of the spot is limited

by the lateral resolution of the confocal microscope (Section 3.2.3). Fig 3.32(c) is a XZ scan in-depth of the thin flake, showing a spot extension in Z of  $\sim 1.5 \mu\text{m}$ , which corresponds to the axial resolution of the confocal setup (Section 3.2.4). Motivated by these observations, we have recorded the  $g^{(2)}$  function on this emitter. Despite hours of integration time with a tracking system, we did not observe a dip at the zero delay of the second-order correlation function, suggesting the emission originates from multiple point defects.

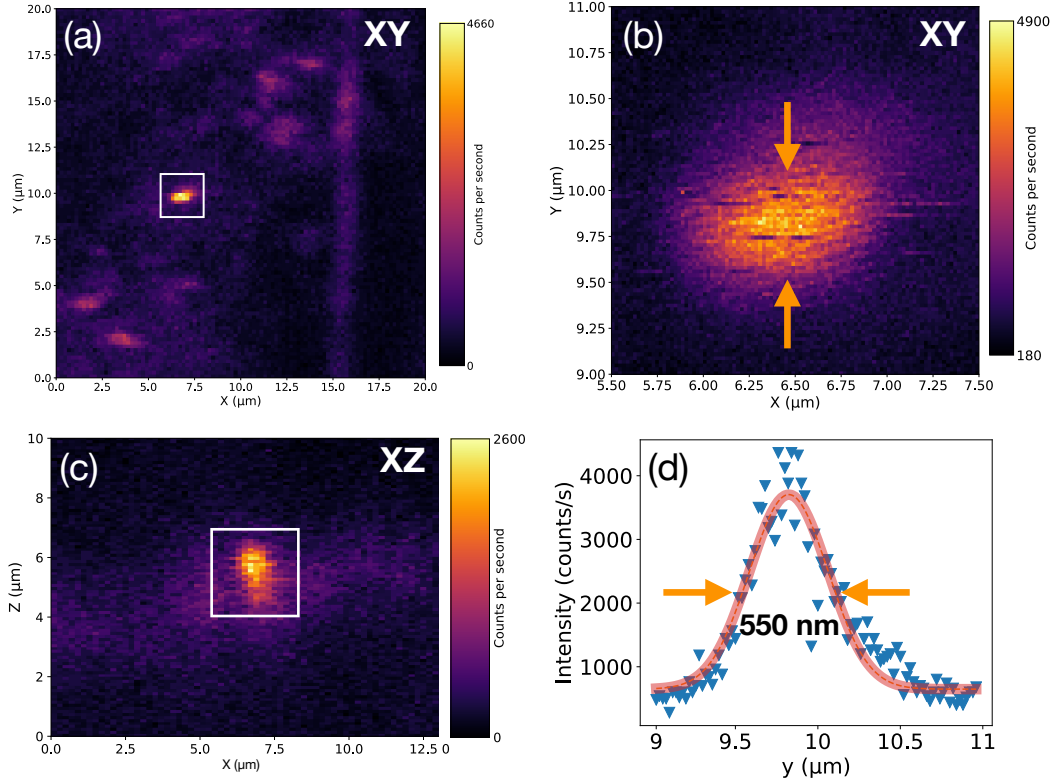


**Figure 3.32**

XY PL scan on a flake (a) and a zoom on the bright spot indicated by the square (b) complemented by a XZ scan in depth (c). Temperature is 4 K, excitation power 0.3 mW. (d) Intensity profile of the vertical cross-section on (b) at  $X = 6.5 \mu\text{m}$ .

### Summary

In bulk material, the emission at 4.1 eV is ubiquitous, indicating a high density of emitters. Here, we make use of a STEM-CL microscope to characterize thin flakes of hBN, obtained by liquid phase exfoliation of a monocrystal, as a preliminary to ensure that it is possible to find localized emissions in regions in the order of  $\sim 500 \text{ nm}$ , that is to say small enough for being resolved with the UV confocal setup.

In these samples, as a general observation, there is a pronounced emission at the borders of the flakes, that we attribute to intrinsic causes, structural deformations favoring the formation of defects. This observation has also been reported for single defects around 600 nm in hBN flakes of similar size, where the authors always observe the emission at flake edges [145]. However, the PL mapping of the same region at



different time brings evidence of PL quenching in these areas, suggesting that the 4.1 eV defect is subjected to bleaching phenomenon, as most defects are. Interestingly, no such behavior is witnessed in bulk material, which may be due to more stable configuration. In this case, concerning the origin of the defect, it would rather be in favor of interstitial impurity, or impurity complexes, because there would be no reason for a substitutional atom to be less stable in thin layers compared to bulk for a lamellar material. However, recent calculations [137], using density functional theory with a hybrid functional, show that the formation energy of interstitial carbon is very high, and greater than that of substitutional carbon impurities ( $C_N$ ,  $C_B$ ). Moreover it predicts a low migration barrier (below 1 eV), finally suggesting that the interstitial carbon impurities would either diffuse out of the sample or migrate until getting annihilated by a vacancy to form  $C_N$  or  $C_B$ . Giving that this migration barrier energy (1 eV) is largely provided with an electron beam, and that the defect at 4.1 eV is observed to be immobile during electron scan, we can rule out the hypothesis of interstitial carbon atoms, and speak in favor of substitutional ones.

Despite the unstable emission at the borders, we manage to find isolated spots, away from the borders, with sizes limited by our spatial resolution, that is to say  $\sim 500 \text{ nm}^2$ . These bright spots manifest stable emission over time, although we could not detect an antibunching in the measurements of the  $g^{(2)}$  function, indicating that the spots are not single-photon sources.

We finally note the uncommon profile in the spectrum of the emitter in these samples. Maybe the thermalization in the configuration for this specific measurements (TEM grid on sample holder) has to be incriminated, and another test with a different configuration could bring an answer. For example, flakes deposited on  $\text{SiO}_2$  substrate that we could directly stick on the sample holder, although in that case the characterization by STEM-CL would not be possible, but using the same procedure for exfoliation and deposition on the substrate should produce similar flakes with similar low density of emitters at 4.1 eV.

## 3.4 Conclusion

In this chapter, the optical properties in the UV of hBN crystals have been investigated by means of photoluminescence (samples from Kansas State University and NIMS) and reflectivity measurements (Kansas State University).

**First**, in samples grown by precipitation techniques at normal pressure, we have shown that the incorporation of carbon in the growth process is associated with the emergence of new optical transitions in the optical spectrum. We summarize the observations in two parts, first for the shallow levels and secondly for the deep levels:

- For the sample presenting the highest concentration of carbon, shallow levels are observed at 5.37 and 5.52 eV, in the deep UV region. The reflectivity spectrum in this region, that provides information on the dielectric constant of the material, suggests that the oscillator strength and density of these shallow levels has to be substantial as correlated peaks for these transitions are noted. The attribute these new shallow transition to an exciton bound to a  $C_N$  impurity.

- For all samples doped with carbon, new deep levels emerge at 4.12, 4.14 and 4.16 eV (named UV1, UV2 and UV3, respectively), and are more prominent in the heavily carbon-doped one. These levels produce no modification of the dielectric constant of the material, and this observation is consistent with the moderate to low density of these lines witnessed in the spatially-resolved PL maps obtained with the UV confocal microscope. With this same microscope, spectra taken with high spectral resolution point out the existence of a sub-structure in these lines, consisting of the splitting of each of them. Through the examination of the spectrally-filtered micro-PL maps taken on different samples and the comparison of the localization of the UV1-3 lines and the 4.1 eV defect, we argue that these deeps transition are uncorrelated to each other and to the point defect at 4.1 eV. This statement is further confirmed with a statistical analysis of the correlation between the doublet structure of UV1 and the spectral features of the 4.1 eV emitter.

**Secondly**, we focused on the 4.1 eV defect. The analysis of spatially-resolved PL maps of the point defect reveals that the energy and width of the ZPL vary at a sub-micrometer scale, while presenting correlation in their variations along specific lines interpreted as folds arising from stacking faults in the crystal lattice. According to this observation, we suggest that strain induces both the ZPL and width modification. In a second part, photoluminescence of  $^{13}\text{C}$ -doped and  $^{12}\text{C}$ -doped samples are compared in an attempt of discerning a modification of the ZPL energy of the 4.1 eV defect depending of the carbon isotope used in the growth process. We report that there is either no isotopic shift, or a finite one but smaller than the inhomogeneous broadening observed in both samples.

**Lastly**, we tried to isolate the emission from a single point defect at 4.1 eV in thin flakes obtained from undoped monocrystals of hBN (NIMS). Here, we used cathodoluminescence performed in a STEM microscope to make sure that the density of emitters was low enough for a single emitter to be isolated with the spatial resolution of our confocal microscope. Isolated spots are observed within the flake, emitting photoluminescence well above the background ( $\text{SNR} \sim 26$ ) and exhibiting good photostability. However, these spots are not associated with single emitters because the second-order correlation function  $g^{(2)}(\tau)$  manifest no antibunching feature in the conditions of the experiment.

At the borders of the flakes, the emission is generally stronger but unstable: bleaching along the borders happens over several subsequent scans. One explanation, still to be investigated, may be related to the dipole direction of the emitter. Indeed, if the defect has a polarization axis out of plane, at the border the laser polarization may becomes more aligned with the dipole direction of the defect because the crystal lattice bends in these regions.

## Conclusion

DURING this thesis, the optical properties of point defects in hexagonal boron nitride have been studied.

First, a confocal microscope operating with a green laser at 532 nm in ambient conditions allowed us to study an individual emitter acting as a room temperature single-photon source in the visible. We have identified two families of isolated emitters on the basis of their photoluminescence spectra. Apart from the energy shift of their spectrum, the two families present similar behavior, with in particular excellent photostability and well defined dipole-like emission. The originality of our approach consisted in analyzing the photodynamics of the emitters over five temporal decades, which brought to light the existence of a long-lived metastable state. Yet, we find a high quantum efficiency of the radiative transition with one of the most intense source of quantum light in a solid-state platform ( $\sim 4 \times 10^6$  counts/s). This study definitely opens up the perspective of applications with hBN in the world of photonics science. Interestingly, the intrinsic structure of hBN allows for an easier integration of its photonic capacity in heterostructure composed of others similarly thin semiconductors.

Secondly, the exploration of the optical response in a higher energy range, from 3.5 to 6 eV, have brought evidence for the existence of shallow and deep levels in carbon-doped crystals. In particular, novel transitions in the deep UV appear at 5.37 and 5.52 eV with high enough oscillator strength to modify the dielectric constant in this energy region, as demonstrated by reflectivity. These transitions are only observed in the case of high carbon doping. On the basis of theoretical absorption spectra including the effects of point defects and impurities we attribute these newcomers to an exciton trapped by a  $C_N$  impurity. In the near-UV, we have observed three novel lines at around 4.12 eV (UV1), 4.14 eV (UV2), and 4.16 eV (UV3). Although the intensity of these deep levels seems to increase with carbon doping, even exceeding the intensity of the 4.1 eV defect in the case of highly doped crystals, we observe no structure in the reflectivity spectra, which suggests either a low density or a weak oscillator strength of these levels.

A confocal microscope at 266 nm with sub-micrometer spatial resolution operating at cryogenic temperature has been built. In the UV, the aberrations have drastic effects and pushed us to design an original setup with adapted optics and elaborate protocols to align it. The unique performances of this new microscope have been used to further explore the properties of the point defects emitting in the UV.

By acquiring spatially and spectrally-resolved PL map, we examine the localization of the UV1-3 lines. We attest that the deep levels are scarce in moderately doped samples, and become more frequent upon increasing doping. The UV1-3 lines present an intriguing  $\sim 20$  meV energy spacing, and have a similar coupling to optical phonon LO( $T/\Gamma$ ) as the 4.1 eV defect. We prove that there are not only independent of each other, but also of the 4.1 eV defect. Therefore, we are in presence of a new class of point defects in hexagonal boron nitride. This raises fundamental questions about the role of carbon into these new levels, which is undoubtedly involved here. Is carbon implied only during the growth process by promoting the formation of the defects, or is it part of the final crystallographic configuration?

Then, we questioned the implication of carbon in the 4.1 eV defect. Nearly no variations of the photoluminescence profile and ZPL features are observed through the series of carbon-doped samples. We tackled this long-standing question from another angle with two types of sample: a first one doped with purified  $^{13}\text{C}$  powder, and a second one with  $^{12}\text{C}$  powder. The different isotope composition in the two crystals was expected to induce a statistical shift in ZPL energy. At the end, no definitive statement can be made, because there is no spectral separation indicative of an isotopic shift of the ZPL, within the inhomogeneous broadening of the 4.1 eV line. Nonetheless, we show important results concerning this last point: correlation of the energy shift and broadening of the 4.1 eV defect ZPL are observed along specific lines on the sample, interpreted as folds of the crystal lattice originating from stacking faults. The correlation along these lines are attributed to stress-induced effects.

Finally, we have used electron microscopy to help find isolated defects in thin flakes of undoped hBN crystals. The purpose was to map the areas in cathodoluminescence where the density of emitters at 4.1 eV was low enough to permit the collection of photoluminescence from a single defect. We report on the observation of very localized PL emission in the flakes, within the spatial resolution of our confocal microscope. It presents a high signal-to-noise ratio ( $\sim 26$ ) and very stable emission (hours, days). However, no antibunching is measured in the histogram of photon correlations measurement. In that respect, further investigations with improved experimental configuration will certainly allows a better thermalization with the cold plate as well as easier inspection of the flakes. Another finding in these very thin flakes is that the emission is predominantly located at the borders and bleaches over several scans, unlike what is seen in bulk material.

As far as the confocal microscope is concerned, significant improvements could be achieved with the installation of a new microscope objective made of reflective optics, like a Cassegrain telescope, and with a higher numerical aperture. The former allows for a full aberration-free collection system, cancels the need for chromatic correction in excitation and also enlarges the spectral bandwidth in collection. The latter allows for a better spatial resolution and collection efficiency of the PL, thus harboring the hope of detecting an individual emitter in the UV in hBN.

Concerning the 4.1 eV defect, temperature-dependent measurements, polarization in emission and especially ODMR measurements remain to be done at the scale of localized emitter as observed in thin flakes. ODMR would enable to probe the spin states of the point defect, providing important information in the search of its origin,

and potentially revealing interesting spin configuration for quantum applications. The prospect of having individual defects acting as single-photon source or with controllable spin states confined to a single layer is desirable for device fabrication, as it can improve ultimate control over emitter placement and coupling to photonic and plasmonic cavities.

Besides, in a near future, it is also planned to update all the optics towards deep UV excitation at 200 nm, thus above the bandgap of hBN. This will open up a scope of possibilities, particularly for the study of excitonic emission by spatially-resolved map of PL performed on few layers to monolayer samples.



## Classical and quantum light, mathematical derivation of the second-order correlation function

### A.1 Classical light versus quantum light

IN the nature exist different physical processes to emit light. One can think of the simplest examples like a fire or a star, or recent invention like the laser, or even more specific source like the photoluminescence coming from the excitation of a single suspended molecule. The physics of these various sources of light are now well understood, and it is customary to make the distinction between classical source and non-classical, or quantum, source of light. Classical light corresponds to electromagnetic field that can be described by classical physics, it includes thermal light emitted from a blackbody source (fire, star), and coherent light (laser). While quantum light corresponds to emission of photons whose behavior requires the quantum theory to be properly described. It includes squeezed states, general photon-number (or Fock) states, and specifically **single-photon states**.

#### A.1.1 Classification in terms of intensity fluctuation and correlation

An efficient way to identify the type of light is to examine how the photons are distributed in time by the source. By looking at this distribution, the statistic of emission of the source, we are able to determine what kind of source has emitted the photons.

The statistic of emission refers to the intensity fluctuation over time, which depends on the emission process. The most basic type of process is the Poissonian process<sup>1</sup>. It can be illustrated with an experiment into which the occurrence of an event (emission of a photon) does not influence the occurrence probability of another event, that is to say the events are independent. In terms of **correlation**, there is no correlation in the intensity of the source, it means that the source present very little intensity fluctuation, in other words it is a stable source of photons, or a coherent source, which is the most stable source of light in classical optics. The laser falls into that category. However, it is remarkably easier to have unstable sources, and in this case the intensity fluctuation is greater, with a tendency to emit multiple photons at a time. This phenomenon is called "bunching" and in most cases the process is said to be super-Poissonian. The intensity correlation is positive. Thermal sources of light fall into that category.

<sup>1</sup>From the name of the French physicist and mathematician Siméon Denis Poisson, 1781-1840.

Both of the above types of processes are the classical processes of emission. A third one, the sub-Poissonian process, represents a quieter than perfectly coherent process. It can therefore only be described by quantum optics, and the observation of sub-Poissonian statistics is inevitably a clear signature of quantum nature of light [146]. The observation of sub-Poissonian statistics very often occurs concomitantly with an anti-bunching behavior, that is to say the photons are never emitted by groups.

To help illustrate the differences, we show on Fig A.1 the three cases. From bottom to top, the blue photons (a) follow a bunched type of statistic, the red photons (b) represent a random-type or coherent-type of light, and the green photons (c) the anti-bunched type of light.

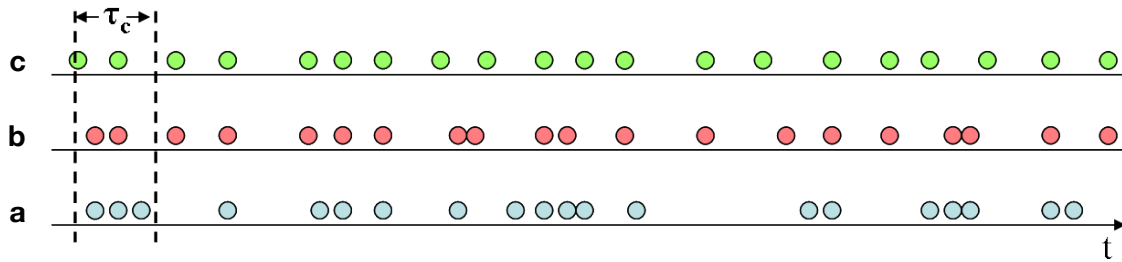


**Figure A.1**

*Illustration of the different statistics of emission for a source.  $\tau_c$  represents a typical interval to evaluate the photon emission fluctuation. (a), (b), (c) represent the bunched type, coherent type and anti-bunched type, respectively.*

Although we have associated sub-Poissonian process with anti-bunching, it is worth noting that both are distinct effects, and sub-Poissonian statistics can display bunching effect, as carefully demonstrated and discussed by Zou and Mandel [146].

### The case of a single emitter

A single emitter in a solid-state matrix is a case of quantum source. This can be easily understood from the fact that after a first photon emitted, the emitter is in its ground state and is unable to emit a second photon for some time following the primal emission. It is noteworthy that this physical fact is also responsible for the limitation of the single-photon source emission rate.

#### A.1.2 The second-order correlation function: $g^{(2)}(\tau)$

Now that we have explained and illustrated in terms of photon statistics the meaning of a quantum source of light versus a classical source of light, it is time to introduce the mathematical function  $g^{(2)}(\tau)$ , namely **the second-order correlation function** (also referred to as the correlation function). It is by far the most common quantity employed for determining the quality of a single-photon source as well as its properties. To give a practical meaning to this function, we can think of it as answering the question: if I detect a photon at time  $t$  what is the probability to detect another photon at time



$t + \tau$ ? More precisely, it informs us on the degree of correlation between the number of photons detected at time  $t$  and at time  $t + \tau$ .

**A very important value** is the value at  $\tau = 0$ , which is linked to the probability of emitting two photons simultaneously. If we come back to the time distribution of photons presented on Fig A.1, we can assign the three types of statistics to three interval of values of  $g^{(2)}(\tau = 0)$ :

$$\begin{aligned} \text{(a) bunched light: } & g^{(2)}(\tau = 0) > 1 \\ \text{(b) coherent light: } & g^{(2)}(\tau = 0) = 1 \\ \text{(c) anti-bunched light: } & g^{(2)}(\tau = 0) < 1 \end{aligned} \tag{A.1}$$

A resume of the different types of statistics of emission and photons grouping behavior is represented on Fig A.2. In particular, Fig A.2(b) highlights the importance of correctly normalizing  $g^{(2)}(\tau)$ : if such a source is bunched over a much longer time scale than the anti-bunching (so that the bunching peak looks flat over the measured delay range), then a source may appear to have sub-Poissonian statistics, when in fact  $g^{(2)}(\tau = 0) > 1$ .

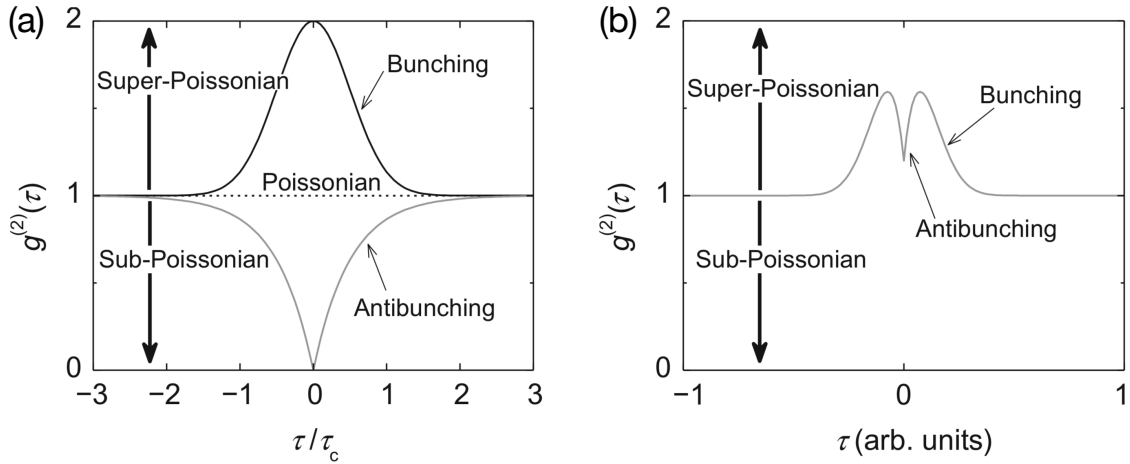


**Figure A.2**

(a) Diagrams showing the relationships among bunching, anti-bunching, sub-, super- and Poissonian photon statistics. Plotted are three ideal sources: a chaotic, thermal-like source (solid black curve), a coherent source (dotted black curve), and a single-photon source (solid gray curve).  $\tau_c$  is the coherence time of the bunched and anti-bunched sources. (b) Illustration of how a source could be anti-bunched without exhibiting sub-Poissonian photon statistics. [Figure extracted from [147]]

## A.2 Derivation of fundamental properties of $g^{(2)}(\tau)$

It can be shown that a meaningful expression for  $g^{(2)}(\tau)$  is 110:

$$g^{(2)}(\tau) = \frac{P_{12}(t, t + \tau)}{P_1(t) \times P_2(t + \tau)}, \quad (\text{A.2})$$

where  $P_{12}(t, t + \tau)$  refers to the joint probability of finding a photon on detector D1 at time  $t$  and then one photon on detector D2 at time  $t + \tau$ , and  $P_i(t_i)$  to the simple probability of finding a photon on detector  $D_i$  at time  $t_i$ . In order to highlight the difference between the classical and quantum case, it is nonetheless necessary to express  $g^{(2)}(\tau)$  in his rigorous mathematical form.

### A.2.1 The classical case

In classical optics, the temporal correlation of the intensity variable between two time  $t$  and  $t + \tau$  takes the form:

$$g^{(2)}(\tau) = \frac{\langle E^*(t)E^*(t + \tau)E(t + \tau)E(t) \rangle}{\sqrt{\langle |E(t)|^2 \rangle \langle |E(t + \tau)|^2 \rangle}} = \frac{\langle I(t)I(t + \tau) \rangle}{\langle I(t) \rangle \langle I(t + \tau) \rangle}, \quad (\text{A.3})$$

where  $\langle \cdot \rangle$  denotes statistical average over time.  $I(t) = E^*(t)E(t)$  is the electric field intensity at time  $t$ , with the superscript  $*$  indicating the complex conjugate. Let us derive some interesting properties from the expression (A.3).

The Cauchy–Schwarz inequality implies:

$$\langle I(t)I(t + \tau) \rangle \leq \sqrt{\langle I(t)^2 \rangle \langle I(t + \tau)^2 \rangle}. \quad (\text{A.4})$$

Moreover, for a stationary process of emission:  $\langle I(t_1)^2 \rangle = \langle I(t_2)^2 \rangle \forall (t_1, t_2)$ . Therefore, we obtain the inequality:

$$\langle I(t)I(t + \tau) \rangle \leq \langle I(t)^2 \rangle, \quad (\text{A.5})$$

and dividing by  $\langle I(t) \rangle^2$ , we finally have:

$$\boxed{g^{(2)}(\tau) \leq g^{(2)}(0)}. \quad (\text{A.6})$$

This important inequality shows that for the classical correlation function the maximum is reached at  $\tau = 0$ . It translates the tendency of photons to come by packets (bunching phenomenon) in classical source of light.

Also, using the subsequent inequality:

$$\langle (I(t) - \langle I(t) \rangle)^2 \rangle \geq 0 \Leftrightarrow \langle I(t)^2 \rangle \geq \langle I(t) \rangle^2, \quad (\text{A.7})$$

we obtain for  $\tau = 0$ :

$$\boxed{g^{(2)}(0) \geq 1}. \quad (\text{A.8})$$

The classical second-order correlation function is necessarily greater than 1 at time  $\tau = 0$ . It is worth noting that the value  $g^{(2)}(0) = 1$  is representative of the absence of correlation between two simultaneous detections. A positive correlation would be a value greater than 1. With that being said, it is now evident that "negative correlation" with value smaller than 1, or more properly anti-correlation, is not a permitted phenomenon for classical source of light.

### A.2.2 The quantum case

In the Glauber formalism of quantum optics, Eq (A.3) becomes for a given mode of the electromagnetic field [101, 148]:

$$g^{(2)}(\tau) = \frac{\langle E^-(t)E^-(t+\tau)E^+(t+\tau)E^+(t) \rangle}{\langle E^-(t)E^+(t) \rangle \times \langle E^-(t+\tau)E^+(t+\tau) \rangle} , \quad (\text{A.9})$$

where  $E^{+/-}$  are the field operators defined by the annihilation  $\hat{a}$  and creation  $\hat{a}^\dagger$  quantum operators. The process of emission is still considered to be stationary. The equation (A.9) can be rewritten as:

$$g^{(2)}(\tau) = \frac{\langle \hat{a}^\dagger(t)\hat{a}^\dagger(t+\tau)\hat{a}(t+\tau)\hat{a}(t) \rangle}{\langle \hat{a}^\dagger(t)\hat{a}(t) \rangle^2} . \quad (\text{A.10})$$

It is tempting to try to express  $g^{(2)}(\tau)$  in terms of the time-dependent number operator  $\hat{n}(t) = \hat{a}^\dagger(t)\hat{a}(t)$ . However, because  $\hat{a}$  and  $\hat{a}^\dagger$  do not commute, the normally ordered operators in this expression cannot be rearranged like in Eq (A.3). Nonetheless, in the special case of  $\tau = 0$  and by using the commutation relation  $[\hat{a}, \hat{a}^\dagger] = 1$ , it is possible to write:

$$g^{(2)}(0) = \frac{\langle \hat{n}(\hat{n} - 1) \rangle}{\langle \hat{n} \rangle^2} . \quad (\text{A.11})$$

where  $\langle \hat{n} \rangle$  is the mean number of photon in the mode considered. Finally, by using the notation  $\mu \equiv \langle \hat{n} \rangle$  and  $(\Delta n)^2 \equiv \langle \hat{n}^2 \rangle - \langle \hat{n} \rangle^2$  for the variance of the photon statistics:

$$g^{(2)}(0) = 1 + \frac{(\Delta n)^2 - \mu}{\mu^2} . \quad (\text{A.12})$$

Thus  $g^{(2)}$  is a measure of the relative magnitude of the mean and the variance of the photon statistics. The relation (A.12) is an algebraic illustration of the discussion in Section A.1.1. Indeed, for a poissonian source the mean and variance are equal:  $\mu = (\Delta n)^2$  and thus  $g^{(2)}(0) = 1$ . For a source that exhibits a super-Poissonian statistics, the variance in photon number is larger than the mean and  $g^{(2)}(0) > 1$ . Finally, in the case of a sub-Poissonian photon source, the variance is smaller than the mean, as a result  $g^{(2)}(0) < 1$ . As we have demonstrated with relation (A.8), classical light fields are constrained to  $g^{(2)}(0) \geq 1$ , and this is why sub-Poissonian statistics, in other words an anti-correlated photon distribution, can only be described by a quantized electromagnetic field.

### The case of a single emitter

In the particular case of a **single emitter** with discrete energy levels, the emission of a photon can be represented by a pure single-photon Fock state  $|\Psi\rangle = |1\rangle$ , for which we know that the variance is null:  $(\Delta n)^2 = 0$ . The formula (A.12) then reads:

$$\boxed{g^{(2)}(0) = 1 - \frac{1}{\mu}} . \quad (\text{A.13})$$

This formula is the experimental cornerstone of the search for a single quantum emitter. Indeed, once properly normalized, the  $g^{(2)}(\tau)$  function at  $\tau = 0$  can be divided in two categories depending on the value of  $\mu$ :

$$g^{(2)}(0) < 0.5 \implies \mu < 2 \implies \text{single emitter} \quad (\text{A.14})$$

$$g^{(2)}(0) \geq 0.5 \implies \mu \geq 2 \implies \text{multiple emitters} \quad (\text{A.15})$$

The relation (A.13) can be used to estimate the number of emitters under the excitation spot, assuming that the emitters are of same nature and emit light in the same proportion.

### Conclusion

In conclusion, we have derived the classical and quantum expression of the second-order correlation function which provide a set of tools to experimentally evaluate a source of light. Indeed, based on the value at zero delay of the histogram representing  $g^{(2)}(\tau)$ , we can distinguish between classical light and quantum light, and in the latter case between a single-emitter emission and multiple-emitters emission.

## Effect of the IRF on the histogram of photon correlations

### B.1 Position of the problem

IN Section 2.4.2, we have established the following expression for the second-order correlation function in the case of a three-level model:

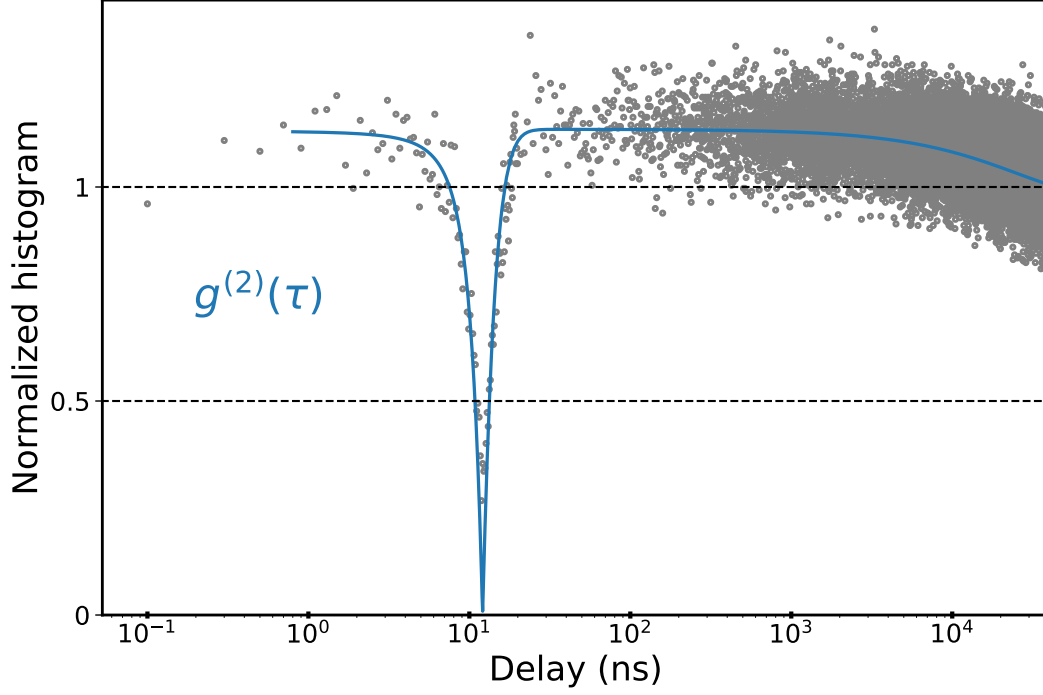
$$g^{(2)}(\tau) = 1 - (1 + a) \exp(-\lambda_1 \tau) + a \exp(-\lambda_2 \tau) \quad . \quad (\text{B.1})$$

At  $\tau = 0$  the function gives a zero value, expressing the fact that for a single quantum emitter the photons are perfectly anti-correlated. Fig B.1 shows a long-time scale recording of  $g^{(2)}(\tau)$  and the corresponding fit using the function of Eq (B.1). We observe a discrepancy between data and fit at zero delay (here the zero delay is represented by  $\tau_d = 12$  ns, the electronic delay added experimentally in order to record the value of  $g^{(2)}(\tau)$  for negative delay).

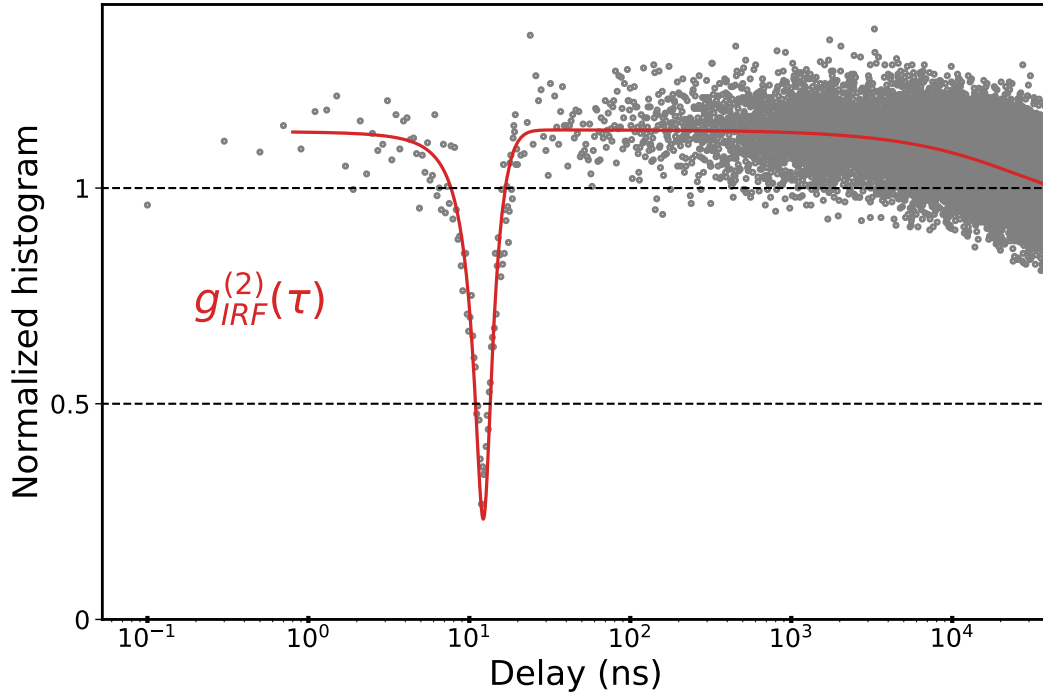
This difference can be explained by PL background with poissonian distribution that originates from the environment of the defect and thus decreases the purity of the single-photon source. However, in the case of high signal-to-background ratio, it is usually due to the instrument response function (IRF) of the detection setup. Indeed, when the emission dynamics of the quantum system probed by the photon correlation measurements has a radiative lifetime in the order of the width of the IRF, the value at zero delay will never reached 0, no matter how large is the signal-to-background ratio. In order to assess the purity of the quantum light source, the fitting function of the histogram has to take into consideration the IRF. The measurement of the IRF of the setup is described in Section 2.3.2. Its profile is of Gaussian type with FWHM = 0.880 ns, or  $\sigma = \text{FWHM}/(2\sqrt{2 \ln 2}) \approx 0.374$  ns. The gaussian function is expressed as follows:

$$\text{IRF}(t) = \frac{1}{\sigma\sqrt{2\pi}} \exp\left(-\frac{t^2}{2\sigma^2}\right) \quad . \quad (\text{B.2})$$

To account for the IRF in the fitting procedure of the histogram of photon correlations, one should calculate the convolution of  $g^{(2)}(\tau)$  of Eq (B.1) with the IRF of Eq (B.2). With the electronic delay  $\tau_d$ , negative delays are also recorded thus absolute value must be taken for the variable  $\tau$ . We calculate below the convoluted function with  $\tau_d = 0$  for simplicity, and reintroduce it at the end.


**Figure B.1**

$g^{(2)}(\tau)$  curve fitting using Eq (B.1) without taking the IRF of the detection setup into account. Grey circle are experimental data and blue solid line is the fit.


**Figure B.2**

$g^{(2)}(\tau)$  curve fitting using Eq (B.17) with taking the IRF of the detection setup into account. Grey circle are experimental data and red solid line is the fit.

## B.2 Convolution of $g^{(2)}(\tau)$ and the IRF

Using the notation introduced in Eq (2.22) Section 2.4.3, we have:

$$g_{IRF}^{(2)}(\tau) = [g^{(2)} * IRF](\tau) \quad , \quad (B.3)$$

$$= \int_{-\infty}^{+\infty} d\tau' \frac{1}{\sigma\sqrt{2\pi}} e^{-\frac{(\tau-\tau')^2}{2\sigma^2}} \times \left[ 1 - (1+a)e^{-\lambda_1|\tau'|} + ae^{-\lambda_2|\tau'|} \right] \quad . \quad (B.4)$$

Then, we obtain the three terms:

$$g_{IRF}^{(2)}(\tau) = \frac{1}{\sigma\sqrt{2\pi}} \int_{-\infty}^{+\infty} d\tau' e^{-\frac{(\tau-\tau')^2}{2\sigma^2}} + \frac{1+a}{\sigma\sqrt{2\pi}} \int_{-\infty}^{+\infty} d\tau' e^{-\frac{(\tau-\tau')^2}{2\sigma^2}} \times e^{-\lambda_1|\tau'|} \\ + \frac{a}{\sigma\sqrt{2\pi}} \int_{-\infty}^{+\infty} d\tau' e^{-\frac{(\tau-\tau')^2}{2\sigma^2}} \times e^{-\lambda_2|\tau'|} \quad . \quad (B.5)$$

The first term of Eq (B.5) is a simple normalized Gaussian integral, thus:

$$\frac{1}{\sigma\sqrt{2\pi}} \int_{-\infty}^{+\infty} d\tau' e^{-\frac{(\tau-\tau')^2}{2\sigma^2}} = 1 \quad . \quad (B.6)$$

The two other terms of Eq (B.5) are similar and we detail below the calculation for the first one, with the constant factor in front of the integral left aside:

$$\int_{-\infty}^{+\infty} d\tau' e^{-\frac{(\tau-\tau')^2}{2\sigma^2}} \times e^{-\lambda_1|\tau'|} = \underbrace{\int_{-\infty}^0 d\tau' e^{-\frac{(\tau-\tau')^2}{2\sigma^2}} \times e^{-\lambda_1(-\tau')}}_{(I)} + \underbrace{\int_0^{+\infty} d\tau' e^{-\frac{(\tau-\tau')^2}{2\sigma^2}} \times e^{-\lambda_1\tau'}}_{(II)} \quad (B.7)$$

We first treat the term (I) of Eq (B.7):

$$(I) = \int_{-\infty}^0 d\tau' e^{-\frac{(\tau-\tau')^2}{2\sigma^2}} \times e^{-\lambda_1(-\tau')} \quad , \quad (B.8)$$

$$= \int_0^{+\infty} d\tau' e^{-\frac{(\tau+\tau')^2}{2\sigma^2}} \times e^{-\lambda_1\tau'} \quad , \quad (B.9)$$

$$= \int_{\tau}^{+\infty} d\tau' e^{-\frac{\tau'^2}{2\sigma^2}} \times e^{-\lambda_1\tau'} \times e^{\lambda_1\tau} \quad , \quad (B.10)$$

$$= e^{\lambda_1\tau} \int_{\tau}^{+\infty} d\tau' e^{-\frac{1}{2\sigma^2}[(\tau'+\lambda_1\sigma^2)^2 - \lambda_1^2\sigma^4]} \quad , \quad (B.11)$$

$$= e^{\lambda_1\tau} e^{\frac{\lambda_1^2\sigma^2}{2}} \int_{\tau}^{+\infty} d\tau' e^{-\left(\frac{\tau'+\lambda_1\sigma^2}{\sigma\sqrt{2}}\right)^2} \quad , \quad (B.12)$$

$$= e^{\lambda_1\tau} e^{\frac{\lambda_1^2\sigma^2}{2}} \sigma\sqrt{2} \int_{\frac{\tau+\lambda_1\sigma^2}{\sigma\sqrt{2}}}^{+\infty} d\tau' e^{-\tau'^2} \quad , \quad (B.13)$$

$$(I) = e^{\lambda_1\tau} e^{\frac{\lambda_1^2\sigma^2}{2}} \frac{\sigma\sqrt{2\pi}}{2} \times \text{Erfc}\left(\frac{\tau + \lambda_1\sigma^2}{\sigma\sqrt{2}}\right) \quad . \quad (B.14)$$



Where  $\text{Erfc}(x)$  is the complementary function of the  $\text{Erf}(x)$  function:

$$\text{Erfc}(x) = 1 - \text{Erf}(x) = 1 - \frac{2}{\sqrt{\pi}} \int_0^x e^{-t^2} dt = \frac{2}{\sqrt{\pi}} \int_x^{+\infty} e^{-t^2} dt . \quad (\text{B.15})$$

We note that the term (II) of Eq (B.7) is similar to Eq (B.9) with only  $\tau$  changed to  $-\tau$  in the exponential function. Using the same variable substitutions, we find for term (II):

$$(\text{II}) = e^{-\lambda_1 \tau} e^{\frac{\lambda_1^2 \sigma^2}{2}} \frac{\sigma \sqrt{2\pi}}{2} \times \text{Erfc} \left( \frac{-\tau + \lambda_1 \sigma^2}{\sigma \sqrt{2}} \right) . \quad (\text{B.16})$$

The second term of Eq (B.5) is finally obtained by multiplying [(I) + (II)] by the constant factor  $\frac{1+a}{\sigma \sqrt{2\pi}}$ . The third term is similar with only  $\lambda_1$  changed in  $\lambda_2$ .

---

The fitting function  $g_{IRF}^{(2)}(\tau)$ , reintroducing the electronic delay  $\tau_d$ , finally reads:

$$\begin{aligned} g_{IRF}^{(2)}(\tau) = & 1 - \frac{(1+a)}{2} e^{\frac{\lambda_1^2 \sigma^2}{2}} \left[ \text{Erfc} \left( \frac{\tau - \tau_d + \lambda_1 \sigma^2}{\sigma \sqrt{2}} \right) e^{\lambda_1(\tau - \tau_d)} \right. \\ & \left. + \text{Erfc} \left( \frac{-(\tau - \tau_d) + \lambda_1 \sigma^2}{\sigma \sqrt{2}} \right) e^{-\lambda_1(\tau - \tau_d)} \right] \\ & + \frac{a}{2} e^{\frac{\lambda_2^2 \sigma^2}{2}} \left[ \text{Erfc} \left( \frac{\tau - \tau_d + \lambda_2 \sigma^2}{\sigma \sqrt{2}} \right) e^{\lambda_2(\tau - \tau_d)} + \text{Erfc} \left( \frac{-(\tau - \tau_d) + \lambda_2 \sigma^2}{\sigma \sqrt{2}} \right) e^{-\lambda_2(\tau - \tau_d)} \right] . \end{aligned} \quad (\text{B.17})$$


---

Using the above function to fit the histogram of photon correlations, with  $\sigma$  fixed by the experimental measurement of the IRF, we get a very good match with the histogram at zero delay, as illustrated on Fig B.2. The small gap between the fitting function and the histogram at zero delay attests that the single-photon source is very pure, and that the deviation to  $g^{(2)}(0) = 0$  is mainly due to the IRF of the detection setup.

## Bibliography

- [1] T. H. Maiman. “Optical and Microwave-Optical Experiments in Ruby”. In: *Physical Review Letters* 4.11 (June 1, 1960), pp. 564–566. DOI: [10.1103/PhysRevLett.4.564](https://doi.org/10.1103/PhysRevLett.4.564). URL: <https://link.aps.org/doi/10.1103/PhysRevLett.4.564>.
- [2] G. Binnig and H. Rohrer. “Scanning tunneling microscopy”. In: *Surface Science* 126.1 (Mar. 2, 1983), pp. 236–244. ISSN: 0039-6028. DOI: [10.1016/0039-6028\(83\)90716-1](https://doi.org/10.1016/0039-6028(83)90716-1). URL: <http://www.sciencedirect.com/science/article/pii/0039602883907161>.
- [3] Christian Kurtsiefer, Sonja Mayer, Patrick Zarda, and Harald Weinfurter. “Stable Solid-State Source of Single Photons”. In: *Physical Review Letters* 85.2 (July 10, 2000), pp. 290–293. DOI: [10.1103/PhysRevLett.85.290](https://doi.org/10.1103/PhysRevLett.85.290). URL: <https://link.aps.org/doi/10.1103/PhysRevLett.85.290>.
- [4] W. Pfaff, B. J. Hensen, H. Bernien, S. B. van Dam, M. S. Blok, T. H. Taminiau, M. J. Tiggelman, R. N. Schouten, M. Markham, D. J. Twitchen, and R. Hanson. “Unconditional quantum teleportation between distant solid-state quantum bits”. In: *Science* 345.6196 (Aug. 1, 2014), pp. 532–535. ISSN: 0036-8075, 1095-9203. DOI: [10.1126/science.1253512](https://doi.org/10.1126/science.1253512). URL: <https://science.sciencemag.org/content/345/6196/532>.
- [5] L. Rondin, J.-P. Tetienne, T. Hingant, J.-F. Roch, P. Maletinsky, and V. Jacques. “Magnetometry with nitrogen-vacancy defects in diamond”. In: *Reports on Progress in Physics* 77.5 (May 2014), p. 056503. ISSN: 0034-4885. DOI: [10.1088/0034-4885/77/5/056503](https://doi.org/10.1088/0034-4885/77/5/056503). URL: <https://doi.org/10.1088/0034-4885/77/5/056503>.
- [6] S. Castelletto, B. C. Johnson, V. Ivády, N. Stavrias, T. Umeda, A. Gali, and T. Ohshima. “A silicon carbide room-temperature single-photon source”. In: *Nature Materials* 13.2 (Feb. 2014), pp. 151–156. ISSN: 1476-4660. DOI: [10.1038/nmat3806](https://doi.org/10.1038/nmat3806). URL: <https://www.nature.com/articles/nmat3806>.
- [7] A. Lohrmann, S. Castelletto, J. R. Klein, T. Ohshima, M. Bosi, M. Negri, D. W. M. Lau, B. C. Gibson, S. Praver, J. C. McCallum, and B. C. Johnson. “Activation and control of visible single defects in 4H-, 6H-, and 3C-SiC by oxidation”. In: *Applied Physics Letters* 108.2 (Jan. 11, 2016), p. 021107. ISSN: 0003-6951. DOI: [10.1063/1.4939906](https://doi.org/10.1063/1.4939906). URL: <https://aip.scitation.org/doi/abs/10.1063/1.4939906>.

- [8] Kenji Watanabe, Takashi Taniguchi, and Hisao Kanda. “Direct-bandgap properties and evidence for ultraviolet lasing of hexagonal boron nitride single crystal”. In: *Nature Materials* 3.6 (June 2004), pp. 404–409. ISSN: 1476-4660. DOI: [10.1038/nmat1134](https://doi.org/10.1038/nmat1134). URL: <https://www.nature.com/articles/nmat1134>.
- [9] Dinh Loc Duong, Seok Joon Yun, and Young Hee Lee. “van der Waals Layered Materials: Opportunities and Challenges”. In: *ACS Nano* 11.12 (Dec. 26, 2017), pp. 11803–11830. ISSN: 1936-0851. DOI: [10.1021/acsnano.7b07436](https://doi.org/10.1021/acsnano.7b07436). URL: <https://doi.org/10.1021/acsnano.7b07436>.
- [10] A. K. Geim and I. V. Grigorieva. “Van der Waals heterostructures”. In: *Nature* 499.7459 (July 2013), pp. 419–425. ISSN: 1476-4687. DOI: [10.1038/nature12385](https://doi.org/10.1038/nature12385). URL: <https://www.nature.com/articles/nature12385>.
- [11] Bettina V. Lotsch. “Vertical 2D Heterostructures”. In: *Annual Review of Materials Research* 45.1 (2015), pp. 85–109. DOI: [10.1146/annurev-matsci-070214-020934](https://doi.org/10.1146/annurev-matsci-070214-020934). URL: <https://doi.org/10.1146/annurev-matsci-070214-020934>.
- [12] Hyunseob Lim, Seong In Yoon, Gwangwoo Kim, A-Rang Jang, and Hyeon Suk Shin. “Stacking of Two-Dimensional Materials in Lateral and Vertical Directions”. In: *Chemistry of Materials* 26.17 (Sept. 9, 2014), pp. 4891–4903. ISSN: 0897-4756. DOI: [10.1021/cm502170q](https://doi.org/10.1021/cm502170q). URL: <https://doi.org/10.1021/cm502170q>.
- [13] S. J. Haigh, A. Gholinia, R. Jalil, S. Romani, L. Britnell, D. C. Elias, K. S. Novoselov, L. A. Ponomarenko, A. K. Geim, and R. Gorbachev. “Cross-sectional imaging of individual layers and buried interfaces of graphene-based heterostructures and superlattices”. In: *Nature Materials* 11.9 (Sept. 2012), pp. 764–767. ISSN: 1476-4660. DOI: [10.1038/nmat3386](https://doi.org/10.1038/nmat3386). URL: <https://www.nature.com/articles/nmat3386>.
- [14] C. R. Dean, A. F. Young, I. Meric, C. Lee, L. Wang, S. Sorgenfrei, K. Watanabe, T. Taniguchi, P. Kim, K. L. Shepard, and J. Hone. “Boron nitride substrates for high-quality graphene electronics”. In: *Nature Nanotechnology* 5.10 (Oct. 2010), pp. 722–726. ISSN: 1748-3395. DOI: [10.1038/nnano.2010.172](https://doi.org/10.1038/nnano.2010.172). URL: <https://www.nature.com/articles/nnano.2010.172>.
- [15] Giovanni Scuri, You Zhou, Alexander A. High, Dominik S. Wild, Chi Shu, Kristiaan De Greve, Luis A. Jauregui, Takashi Taniguchi, Kenji Watanabe, Philip Kim, Mikhail D. Lukin, and Hongkun Park. “Large Excitonic Reflectivity of Monolayer MoSe<sub>2</sub> Encapsulated in Hexagonal Boron Nitride”. In: *Physical Review Letters* 120.3 (Jan. 18, 2018), p. 037402. DOI: [10.1103/PhysRevLett.120.037402](https://doi.org/10.1103/PhysRevLett.120.037402). URL: <https://link.aps.org/doi/10.1103/PhysRevLett.120.037402>.
- [16] Tianhua Ren and Kian Ping Loh. “On-chip integrated photonic circuits based on two-dimensional materials and hexagonal boron nitride as the optical confinement layer”. In: *Journal of Applied Physics* 125.23 (June 20, 2019), p. 230901. ISSN: 0021-8979. DOI: [10.1063/1.5096195](https://doi.org/10.1063/1.5096195). URL: <https://aip.scitation.org/doi/full/10.1063/1.5096195>.

- [17] Song Liu, Rui He, Zhipeng Ye, Xiaozhang Du, Jingyu Lin, Hongxing Jiang, Bin Liu, and James H. Edgar. “Large-Scale Growth of High-Quality Hexagonal Boron Nitride Crystals at Atmospheric Pressure from an Fe–Cr Flux”. In: *Crystal Growth & Design* 17.9 (Sept. 6, 2017), pp. 4932–4935. ISSN: 1528-7483. DOI: [10.1021/acs.cgd.7b00871](https://doi.org/10.1021/acs.cgd.7b00871). URL: <https://doi.org/10.1021/acs.cgd.7b00871>.
- [18] Joo Song Lee, Soo Ho Choi, Seok Joon Yun, Yong In Kim, Stephen Boandoh, Ji-Hoon Park, Bong Gyu Shin, Hayoung Ko, Seung Hee Lee, Young-Min Kim, Young Hee Lee, Ki Kang Kim, and Soo Min Kim. “Wafer-scale single-crystal hexagonal boron nitride film via self-collimated grain formation”. In: *Science* 362.6416 (Nov. 16, 2018), pp. 817–821. ISSN: 0036-8075, 1095-9203. DOI: [10.1126/science.aau2132](https://science.sciencemag.org/content/362/6416/817). URL: <https://science.sciencemag.org/content/362/6416/817>.
- [19] W. H. Balmain. “XLVI. Observations on the formation of compounds of boron and silicon with nitrogen and certain metals”. In: *The London, Edinburgh, and Dublin Philosophical Magazine and Journal of Science* 21.138 (Oct. 1, 1842), pp. 270–277. ISSN: 1941-5966. DOI: [10.1080/14786444208621545](https://doi.org/10.1080/14786444208621545). URL: <https://doi.org/10.1080/14786444208621545>.
- [20] *Carborundum Company / Encyclopedia.com*. URL: <https://www.encyclopedia.com/books/politics-and-business-magazines/carborundum-company>.
- [21] Sedat Alkoy, Cetin Toy, Turgay Gönül, and Adnan Tekin. “Crystallization behavior and characterization of turbostratic boron nitride”. In: *Journal of the European Ceramic Society* 17.12 (Jan. 1, 1997), pp. 1415–1422. ISSN: 0955-2219. DOI: [10.1016/S0955-2219\(97\)00040-X](http://www.sciencedirect.com/science/article/pii/S095522199700040X). URL: <http://www.sciencedirect.com/science/article/pii/S095522199700040X>.
- [22] R. H. Wentorf. “Condensed Systems at High Pressures and Temperatures”. In: *The Journal of Physical Chemistry* 63.11 (Nov. 1959), pp. 1934–1940. ISSN: 0022-3654, 1541-5740. DOI: [10.1021/j150581a033](https://pubs.acs.org/doi/abs/10.1021/j150581a033). URL: <https://pubs.acs.org/doi/abs/10.1021/j150581a033>.
- [23] F. P. Bundy and R. H. Wentorf. “Direct Transformation of Hexagonal Boron Nitride to Denser Forms”. In: *The Journal of Chemical Physics* 38.5 (Mar. 1, 1963), pp. 1144–1149. ISSN: 0021-9606. DOI: [10.1063/1.1733815](https://aip.scitation.org/doi/abs/10.1063/1.1733815). URL: <https://aip.scitation.org/doi/abs/10.1063/1.1733815>.
- [24] Vladimir L. Solozhenko. “Boron nitride phase diagram. State of the art”. In: *High Pressure Research* 13.4 (Mar. 1, 1995), pp. 199–214. ISSN: 0895-7959. DOI: [10.1080/08957959508200884](https://doi.org/10.1080/08957959508200884). URL: <https://doi.org/10.1080/08957959508200884>.
- [25] Simon Larach and Ross E. Shrader. “Multiband Luminescence in Boron Nitride”. In: *Physical Review* 104.1 (Oct. 1, 1956), pp. 68–73. ISSN: 0031-899X. DOI: [10.1103/PhysRev.104.68](https://link.aps.org/doi/10.1103/PhysRev.104.68). URL: <https://link.aps.org/doi/10.1103/PhysRev.104.68>.
- [26] A. Katzir, J. T. Suss, A. Zunger, and A. Halperin. “Point defects in hexagonal boron nitride. I. EPR, thermoluminescence, and thermally-stimulated-current measurements”. In: *Physical Review B* 11.6 (Mar. 15, 1975), pp. 2370–2377. DOI: [10.1103/PhysRevB.11.2370](https://link.aps.org/doi/10.1103/PhysRevB.11.2370). URL: <https://link.aps.org/doi/10.1103/PhysRevB.11.2370>.

- [27] Takashi Kuzuba, Koh Era, Toshihiko Ishii, Tadao Sato, and Minoru Iwata. “Electron-phonon interactions in layered hexagonal boron nitride”. In: *Physica B+C* 105.1 (May 1, 1981), pp. 339–342. ISSN: 0378-4363. DOI: [10.1016/0378-4363\(81\)90271-0](https://doi.org/10.1016/0378-4363(81)90271-0). URL: <http://www.sciencedirect.com/science/article/pii/0378436381902710>.
- [28] *h-BN - Hexagonal Boron Nitride*. URL: <http://www.hqgraphene.com/h-BN.php>.
- [29] Jin-Cheng Zheng, Liang Zhang, A. V. Kretinin, S. V. Morozov, Yi Bo Wang, Tun Wang, Xiaojun Li, Fei Ren, Jingyu Zhang, Ching-Yu Lu, Jia-Cing Chen, Miao Lu, Hui-Qiong Wang, A. K. Geim, and K. S. Novoselov. “High thermal conductivity of hexagonal boron nitride laminates”. In: *2D Materials* 3.1 (Jan. 2016), p. 011004. ISSN: 2053-1583. DOI: [10.1088/2053-1583/3/1/011004](https://doi.org/10.1088/2053-1583/3/1/011004). URL: <https://doi.org/10.1088%2F2053-1583%2F3%2F1%2F011004>.
- [30] S. Hu, M. Lozada-Hidalgo, F. C. Wang, A. Mishchenko, F. Schedin, R. R. Nair, E. W. Hill, D. W. Boukhvalov, M. I. Katsnelson, R. a. W. Dryfe, I. V. Grigorieva, H. A. Wu, and A. K. Geim. “Proton transport through one-atom-thick crystals”. In: *Nature* 516.7530 (Dec. 2014), pp. 227–230. ISSN: 1476-4687. DOI: [10.1038/nature14015](https://doi.org/10.1038/nature14015). URL: <https://www.nature.com/articles/nature14015>.
- [31] Andres Castellanos-Gomez. “Why all the fuss about 2D semiconductors?” In: *Nature Photonics* 10 (Mar. 31, 2016), pp. 202–204. ISSN: 1749-4893. DOI: [10.1038/nphoton.2016.53](https://doi.org/10.1038/nphoton.2016.53). URL: <https://www.nature.com/articles/nphoton.2016.53>.
- [32] Joshua D. Caldwell, Igor Aharonovich, Guillaume Cassabois, James H. Edgar, Bernard Gil, and D. N. Basov. “Photonics with hexagonal boron nitride”. In: *Nature Reviews Materials* 4.8 (Aug. 2019), pp. 552–567. ISSN: 2058-8437. DOI: [10.1038/s41578-019-0124-1](https://doi.org/10.1038/s41578-019-0124-1). URL: <https://www.nature.com/articles/s41578-019-0124-1>.
- [33] Mark Zastrow. “Meet the crystal growers who sparked a revolution in graphene electronics”. In: *Nature* 572 (Aug. 21, 2019), pp. 429–432. DOI: [10.1038/d41586-019-02472-0](https://doi.org/10.1038/d41586-019-02472-0). URL: <http://www.nature.com/articles/d41586-019-02472-0>.
- [34] R. S. Pease. “An X-ray study of boron nitride”. In: *Acta Crystallographica* 5.3 (May 2, 1952), pp. 356–361. ISSN: 0365-110X. DOI: [10.1107/S0365110X52001064](https://doi.org/10.1107/S0365110X52001064). URL: <http://scripts.iucr.org/cgi-bin/paper?a00642>.
- [35] T. Q. P. Vuong, G. Cassabois, P. Valvin, V. Jacques, A. Van Der Lee, A. Zobelli, K. Watanabe, T. Taniguchi, and B. Gil. “Phonon symmetries in hexagonal boron nitride probed by incoherent light emission”. In: *2D Materials* 4.1 (2017), p. 011004. ISSN: 2053-1583. DOI: [10.1088/2053-1583/4/1/011004](https://doi.org/10.1088/2053-1583/4/1/011004). URL: <https://doi.org/10.1088%2F2053-1583%2F4%2F1%2F011004>.
- [36] *Hybridation sp<sup>2</sup>*. URL: [https://www.aclg.be/Create/GeometrieMoleculaireMolOrg\\_CG/page\\_16.htm](https://www.aclg.be/Create/GeometrieMoleculaireMolOrg_CG/page_16.htm).

- [37] R. J. Jiménez-Riobóo, L. Artús, R. Cuscó, T. Taniguchi, G. Cassaboïs, and B. Gil. “In- and out-of-plane longitudinal acoustic-wave velocities and elastic moduli in h-BN from Brillouin scattering measurements”. In: *Applied Physics Letters* 112.5 (Jan. 29, 2018), p. 051905. ISSN: 0003-6951. DOI: [10.1063/1.5019629](https://doi.org/10.1063/1.5019629). URL: <https://aip.scitation.org/doi/10.1063/1.5019629>.
- [38] S. Matt Gilbert, Thang Pham, Mehmet Dogan, Sehoon Oh, Brian Shevitski, Gabe Schumm, Stanley Liu, Peter Ercius, Shaul Aloni, Marvin L. Cohen, and Alex Zettl. “Alternative stacking sequences in hexagonal boron nitride”. In: *2D Materials* 6.2 (Mar. 2019), p. 021006. ISSN: 2053-1583. DOI: [10.1088/2053-1583/ab0e24](https://doi.org/10.1088/2053-1583/ab0e24). URL: <https://doi.org/10.1088/2053-1583/ab0e24>.
- [39] Alexey Bosak, Jorge Serrano, Michael Krisch, Kenji Watanabe, Takashi Taniguchi, and Hisao Kanda. “Elasticity of hexagonal boron nitride: Inelastic x-ray scattering measurements”. In: *Physical Review B* 73.4 (Jan. 19, 2006), p. 041402. DOI: [10.1103/PhysRevB.73.041402](https://link.aps.org/doi/10.1103/PhysRevB.73.041402). URL: <https://link.aps.org/doi/10.1103/PhysRevB.73.041402>.
- [40] M. Chubarov, H. Pedersen, H. Högborg, Zs Czigany, and A. Henry. “Chemical vapour deposition of epitaxial rhombohedral BN thin films on SiC substrates”. In: *CrystEngComm* 16.24 (2014), pp. 5430–5436. DOI: [10.1039/C4CE00381K](https://pubs.rsc.org/en/content/articlelanding/2014/ce/c4ce00381k). URL: <https://pubs.rsc.org/en/content/articlelanding/2014/ce/c4ce00381k>.
- [41] Linfeng Ye, Feng Liang, Lei Zhao, Xuan He, Wei Fang, Hui Chen, Xin Wang, Jinfeng Wu, and Shihua An. “Catalyzed synthesis of rhombohedral boron nitride in sodium chloride molten salt”. In: *Ceramics International* 42.10 (Aug. 1, 2016), pp. 11626–11633. ISSN: 0272-8842. DOI: [10.1016/j.ceramint.2016.04.062](http://www.sciencedirect.com/science/article/pii/S0272884216304564). URL: <http://www.sciencedirect.com/science/article/pii/S0272884216304564>.
- [42] Phuong Vuong. “Optical spectroscopy of boron nitride heterostructures”. thesis. Montpellier, Oct. 24, 2018. URL: <http://www.theses.fr/2018MONT075>.
- [43] D. A. Evans, A. G. McGlynn, B. M. Towlson, M. Gunn, D. Jones, T. E. Jenkins, R. Winter, and N. R. J. Poolton. “Determination of the optical band-gap energy of cubic and hexagonal boron nitride using luminescence excitation spectroscopy”. In: *Journal of Physics: Condensed Matter* 20.7 (Jan. 2008), p. 075233. ISSN: 0953-8984. DOI: [10.1088/0953-8984/20/7/075233](https://doi.org/10.1088/0953-8984/20/7/075233). URL: <https://doi.org/10.1088/0953-8984/20/7/075233>.
- [44] A. Segura, R. Cuscó, T. Taniguchi, K. Watanabe, G. Cassaboïs, B. Gil, and L. Artús. “Nonreversible Transition from the Hexagonal to Wurtzite Phase of Boron Nitride under High Pressure: Optical Properties of the Wurtzite Phase”. In: *The Journal of Physical Chemistry C* 123.33 (Aug. 22, 2019), pp. 20167–20173. ISSN: 1932-7447. DOI: [10.1021/acs.jpcc.9b06163](https://doi.org/10.1021/acs.jpcc.9b06163). URL: <https://doi.org/10.1021/acs.jpcc.9b06163>.
- [45] E. Doni and G. Pastori Parravicini. “Energy bands and optical properties of hexagonal boron nitride and graphite”. In: *Il Nuovo Cimento B (1965-1970)* 64.1 (Nov. 1, 1969), pp. 117–144. ISSN: 1826-9877. DOI: [10.1007/BF02710286](https://doi.org/10.1007/BF02710286). URL: <https://doi.org/10.1007/BF02710286>.



- [46] Pere Miró, Martha Audiffred, and Thomas Heine. “An atlas of two-dimensional materials”. In: *Chemical Society Reviews* 43.18 (Aug. 18, 2014), pp. 6537–6554. ISSN: 1460-4744. DOI: [10.1039/C4CS00102H](https://doi.org/10.1039/C4CS00102H). URL: <https://pubs.rsc.org/en/content/articlelanding/2014/cs/c4cs00102h>.
- [47] Giorgia Fugallo, Matteo Aramini, Jaakko Koskelo, Kenji Watanabe, Takashi Taniguchi, Mikko Hakala, Simo Huotari, Matteo Gatti, and Francesco Sottile. “Exciton energy-momentum map of hexagonal boron nitride”. In: *Physical Review B* 92.16 (Oct. 21, 2015), p. 165122. DOI: [10.1103/PhysRevB.92.165122](https://doi.org/10.1103/PhysRevB.92.165122). URL: <https://link.aps.org/doi/10.1103/PhysRevB.92.165122>.
- [48] Jaakko Koskelo, Giorgia Fugallo, Mikko Hakala, Matteo Gatti, Francesco Sottile, and Pierluigi Cudazzo. “Excitons in van der Waals materials: From monolayer to bulk hexagonal boron nitride”. In: *Physical Review B* 95.3 (Jan. 17, 2017), p. 035125. DOI: [10.1103/PhysRevB.95.035125](https://doi.org/10.1103/PhysRevB.95.035125). URL: <https://link.aps.org/doi/10.1103/PhysRevB.95.035125>.
- [49] Kin Fai Mak, Changgu Lee, James Hone, Jie Shan, and Tony F. Heinz. “Atomically Thin MoS<sub>2</sub>: A New Direct-Gap Semiconductor”. In: *Physical Review Letters* 105.13 (Sept. 24, 2010), p. 136805. DOI: [10.1103/PhysRevLett.105.136805](https://doi.org/10.1103/PhysRevLett.105.136805). URL: <https://link.aps.org/doi/10.1103/PhysRevLett.105.136805>.
- [50] Weijie Zhao, Zohreh Ghorannevis, Lei Qiang Chu, Minglin Toh, Christian Kloc, Ping-Heng Tan, and Goki Eda. “Evolution of Electronic Structure in Atomically Thin Sheets of WS<sub>2</sub> and WSe<sub>2</sub>”. In: *ACS Nano* 7.1 (Jan. 22, 2013), pp. 791–797. ISSN: 1936-0851. DOI: [10.1021/nn305275h](https://doi.org/10.1021/nn305275h). URL: <https://doi.org/10.1021/nn305275h>.
- [51] Yi Zhang, Tay-Rong Chang, Bo Zhou, Yong-Tao Cui, Hao Yan, Zhongkai Liu, Felix Schmitt, James Lee, Rob Moore, Yulin Chen, Hsin Lin, Horng-Tay Jeng, Sung-Kwan Mo, Zahid Hussain, Arun Bansil, and Zhi-Xun Shen. “Direct observation of the transition from indirect to direct bandgap in atomically thin epitaxial MoSe<sub>2</sub>”. In: *Nature Nanotechnology* 9.2 (Feb. 2014), pp. 111–115. ISSN: 1748-3395. DOI: [10.1038/nnano.2013.277](https://doi.org/10.1038/nnano.2013.277). URL: <https://www.nature.com/articles/nnano.2013.277>.
- [52] Ignacio Gutiérrez Lezama, Ashish Arora, Alberto Ubaldini, Céline Barreateau, Enrico Giannini, Marek Potemski, and Alberto F. Morpurgo. “Indirect-to-Direct Band Gap Crossover in Few-Layer MoTe<sub>2</sub>”. In: *Nano Letters* 15.4 (Apr. 8, 2015), pp. 2336–2342. ISSN: 1530-6984. DOI: [10.1021/nl5045007](https://doi.org/10.1021/nl5045007). URL: <https://doi.org/10.1021/nl5045007>.
- [53] C. Elias, P. Valvin, T. Pelini, A. Summerfield, C. J. Mellor, T. S. Cheng, L. Eaves, C. T. Foxon, P. H. Beton, S. V. Novikov, B. Gil, and G. Cassabois. “Direct band-gap crossover in epitaxial monolayer boron nitride”. In: *Nature Communications* 10.1 (June 14, 2019), p. 2639. ISSN: 2041-1723. DOI: [10.1038/s41467-019-10610-5](https://doi.org/10.1038/s41467-019-10610-5). URL: <https://www.nature.com/articles/s41467-019-10610-5>.



- [54] Fulvio Paleari, Thomas Galvani, Hakim Amara, François Ducastelle, Alejandro Molina-Sánchez, and Ludger Wirtz. “Excitons in few-layer hexagonal boron nitride: Davydov splitting and surface localization”. In: *2D Materials* 5.4 (Aug. 14, 2018), p. 045017. ISSN: 2053-1583. DOI: [10.1088/2053-1583/aad586](https://doi.org/10.1088/2053-1583/aad586). URL: <http://stacks.iop.org/2053-1583/5/i=4/a=045017?key=crossref.d4ed3c3461abd8c6f845f8038fdb2ec>.
- [55] G. Cassaboïs, P. Valvin, and B. Gil. “Hexagonal boron nitride is an indirect bandgap semiconductor”. In: *Nature Photonics* 10.4 (Apr. 2016), pp. 262–266. ISSN: 1749-4885, 1749-4893. DOI: [10.1038/nphoton.2015.277](https://doi.org/10.1038/nphoton.2015.277). URL: <http://www.nature.com/articles/nphoton.2015.277>.
- [56] Ramon Cuscó, Bernard Gil, Guillaume Cassaboïs, and Luis Artús. “Temperature dependence of Raman-active phonons and anharmonic interactions in layered hexagonal BN”. In: *Physical Review B* 94.15 (Oct. 20, 2016), p. 155435. DOI: [10.1103/PhysRevB.94.155435](https://doi.org/10.1103/PhysRevB.94.155435). URL: <https://link.aps.org/doi/10.1103/PhysRevB.94.155435>.
- [57] T. Q. P. Vuong, G. Cassaboïs, P. Valvin, V. Jacques, R. Cuscó, L. Artús, and B. Gil. “Overtones of interlayer shear modes in the phonon-assisted emission spectrum of hexagonal boron nitride”. In: *Physical Review B* 95.4 (Jan. 17, 2017), p. 045207. DOI: [10.1103/PhysRevB.95.045207](https://doi.org/10.1103/PhysRevB.95.045207). URL: <https://link.aps.org/doi/10.1103/PhysRevB.95.045207>.
- [58] T. Q. P. Vuong, G. Cassaboïs, P. Valvin, S. Liu, J. H. Edgar, and B. Gil. “Exciton-phonon interaction in the strong-coupling regime in hexagonal boron nitride”. In: *Physical Review B* 95.20 (May 26, 2017), p. 201202. DOI: [10.1103/PhysRevB.95.201202](https://doi.org/10.1103/PhysRevB.95.201202). URL: <https://link.aps.org/doi/10.1103/PhysRevB.95.201202>.
- [59] Yutaka Toyozawa. “Theory of Line-Shapes of the Exciton Absorption Bands”. In: *Progress of Theoretical Physics* 20.1 (July 1, 1958), pp. 53–81. ISSN: 0033-068X. DOI: [10.1143/PTP.20.53](https://doi.org/10.1143/PTP.20.53). URL: <https://academic.oup.com/ptp/article/20/1/53/1937228>.
- [60] Léonard Schué, Lorenzo Sponza, Alexandre Plaud, Hakima Bensalah, Kenji Watanabe, Takashi Taniguchi, François Ducastelle, Annick Loiseau, and Julien Barjon. “Bright Luminescence from Indirect and Strongly Bound Excitons in h-BN”. In: *Physical Review Letters* 122.6 (Feb. 12, 2019), p. 067401. DOI: [10.1103/PhysRevLett.122.067401](https://doi.org/10.1103/PhysRevLett.122.067401). URL: <https://link.aps.org/doi/10.1103/PhysRevLett.122.067401>.
- [61] E. Cannuccia, B. Monserrat, and C. Attacalite. “Theory of phonon-assisted luminescence in solids: Application to hexagonal boron nitride”. In: *Physical Review B* 99.8 (Feb. 8, 2019), p. 081109. DOI: [10.1103/PhysRevB.99.081109](https://doi.org/10.1103/PhysRevB.99.081109). URL: <https://link.aps.org/doi/10.1103/PhysRevB.99.081109>.
- [62] Fulvio Paleari, Henrique P. C. Miranda, Alejandro Molina-Sánchez, and Ludger Wirtz. “Exciton-Phonon Coupling in the Ultraviolet Absorption and Emission Spectra of Bulk Hexagonal Boron Nitride”. In: *Physical Review Letters* 122.18 (May 7, 2019), p. 187401. DOI: [10.1103/PhysRevLett.122.187401](https://doi.org/10.1103/PhysRevLett.122.187401). URL: <https://link.aps.org/doi/10.1103/PhysRevLett.122.187401>.

- [63] G. Cassaboïs, P. Valvin, and B. Gil. “Intervalley scattering in hexagonal boron nitride”. In: *Physical Review B* 93.3 (Jan. 28, 2016), p. 035207. DOI: [10.1103/PhysRevB.93.035207](https://doi.org/10.1103/PhysRevB.93.035207). URL: <https://link.aps.org/doi/10.1103/PhysRevB.93.035207>.
- [64] M. Hulin. “Selection Rules for Two-Phonon Absorption Processes”. In: *physica status solidi (b)* 21.2 (1967), pp. 607–618. ISSN: 1521-3951. DOI: [10.1002/pssb.19670210219](https://doi.org/10.1002/pssb.19670210219). URL: <https://onlinelibrary.wiley.com/doi/abs/10.1002/pssb.19670210219>.
- [65] P. Jaffrennou, J. Barjon, T. Schmid, L. Museur, A. Kanaev, J.-S. Lauret, C. Y. Zhi, C. Tang, Y. Bando, D. Golberg, B. Attal-Tretout, F. Ducastelle, and A. Loiseau. “Near-band-edge recombinations in multiwalled boron nitride nanotubes: Cathodoluminescence and photoluminescence spectroscopy measurements”. In: *Physical Review B* 77.23 (June 16, 2008), p. 235422. DOI: [10.1103/PhysRevB.77.235422](https://doi.org/10.1103/PhysRevB.77.235422). URL: <https://link.aps.org/doi/10.1103/PhysRevB.77.235422>.
- [66] Romain Bourrellier, Michele Amato, Luiz Henrique Galvão Tizei, Christine Giorgetti, Alexandre Gloter, Malcolm I. Heggie, Katia March, Odile Stéphan, Lucia Reining, Mathieu Kociak, and Alberto Zobelli. “Nanometric Resolved Luminescence in h-BN Flakes: Excitons and Stacking Order”. In: *ACS Photonics* 1.9 (Sept. 17, 2014), pp. 857–862. DOI: [10.1021/ph500141j](https://doi.org/10.1021/ph500141j). URL: <https://doi.org/10.1021/ph500141j>.
- [67] Romain Bourrellier, Sophie Meuret, Anna Tararan, Odile Stéphan, Mathieu Kociak, Luiz H. G. Tizei, and Alberto Zobelli. “Bright UV Single Photon Emission at Point Defects in h-BN”. In: *Nano Letters* 16.7 (July 13, 2016), pp. 4317–4321. ISSN: 1530-6984. DOI: [10.1021/acs.nanolett.6b01368](https://doi.org/10.1021/acs.nanolett.6b01368). URL: <https://doi.org/10.1021/acs.nanolett.6b01368>.
- [68] T. Q. P. Vuong, G. Cassaboïs, P. Valvin, A. Ouerghi, Y. Chassagneux, C. Voisin, and B. Gil. “Phonon-Photon Mapping in a Color Center in Hexagonal Boron Nitride”. In: *Physical Review Letters* 117.9 (Aug. 25, 2016), p. 097402. DOI: [10.1103/PhysRevLett.117.097402](https://doi.org/10.1103/PhysRevLett.117.097402). URL: <https://link.aps.org/doi/10.1103/PhysRevLett.117.097402>.
- [69] Kamil Koronski, Agata Kaminska, Nikolai D. Zhigadlo, Christine Elias, Guillaume Cassaboïs, and Bernard Gil. “Spontaneous emission of color centers at 4eV in hexagonal boron nitride under hydrostatic pressure”. In: *Superlattices and Microstructures* 131 (July 1, 2019), pp. 1–7. ISSN: 0749-6036. DOI: [10.1016/j.spmi.2019.05.018](https://doi.org/10.1016/j.spmi.2019.05.018). URL: <http://www.sciencedirect.com/science/article/pii/S0749603619308043>.
- [70] G. Kern, G. Kresse, and J. Hafner. “Ab initio calculation of the lattice dynamics and phase diagram of boron nitride”. In: *Physical Review B* 59.13 (Apr. 1, 1999), pp. 8551–8559. DOI: [10.1103/PhysRevB.59.8551](https://doi.org/10.1103/PhysRevB.59.8551). URL: <https://link.aps.org/doi/10.1103/PhysRevB.59.8551>.

- [71] Z. Remes, M. Nesladek, K. Haenen, K. Watanabe, and T. Taniguchi. “The optical absorption and photoconductivity spectra of hexagonal boron nitride single crystals”. In: *physica status solidi (a)* 202.11 (2005), pp. 2229–2233. ISSN: 1862-6319. DOI: [10.1002/pssa.200561902](https://doi.org/10.1002/pssa.200561902). URL: <https://onlinelibrary.wiley.com/doi/abs/10.1002/pssa.200561902>.
- [72] L. Ju, J. Velasco Jr, E. Huang, S. Kahn, C. Nosiola, Hsin-Zon Tsai, W. Yang, T. Taniguchi, K. Watanabe, Y. Zhang, G. Zhang, M. Crommie, A. Zettl, and F. Wang. “Photoinduced doping in heterostructures of graphene and boron nitride”. In: *Nature Nanotechnology* 9.5 (May 2014), pp. 348–352. ISSN: 1748-3395. DOI: [10.1038/nnano.2014.60](https://doi.org/10.1038/nnano.2014.60). URL: <https://www.nature.com/articles/nnano.2014.60>.
- [73] Romain Bourrellier. “Luminescence at Defects in h-BN : Excitons at Stacking Faults and Single Photon Emitters”. thesis. Paris 11, Oct. 28, 2014. URL: <http://www.theses.fr/2014PA112285>.
- [74] A.K. Dąbrowska, K. Pakuła, R. Bożek, J.G. Rousset, D. Ziółkowska, K. Gołasa, K.P. Korona, A. Wyszomolek, and R. Stępniewski. “Structural and Optical Properties of Boron Nitride Grown by MOVPE”. In: *Acta Physica Polonica A* 129.1 (Jan. 2016), A–129–A–131. ISSN: 0587-4246, 1898-794X. DOI: [10.12693/APhysPolA.129.A-129](https://doi.org/10.12693/APhysPolA.129.A-129). URL: <http://przyrbwn.icm.edu.pl/APP/PDF/129/a129z1ap32.pdf>.
- [75] Dillon Wong, Jairo Velasco Jr, Long Ju, Juwon Lee, Salman Kahn, Hsin-Zon Tsai, Chad Germany, Takashi Taniguchi, Kenji Watanabe, Alex Zettl, Feng Wang, and Michael F. Crommie. “Characterization and manipulation of individual defects in insulating hexagonal boron nitride using scanning tunnelling microscopy”. In: *Nature Nanotechnology* 10.11 (Nov. 2015), pp. 949–953. ISSN: 1748-3395. DOI: [10.1038/nnano.2015.188](https://doi.org/10.1038/nnano.2015.188). URL: <https://www.nature.com/articles/nnano.2015.188>.
- [76] R. M. Feenstra, J. M. Woodall, and G. D. Pettit. “Observation of bulk defects by scanning tunneling microscopy and spectroscopy: Arsenic antisite defects in GaAs”. In: *Physical Review Letters* 71.8 (Aug. 23, 1993), pp. 1176–1179. DOI: [10.1103/PhysRevLett.71.1176](https://doi.org/10.1103/PhysRevLett.71.1176). URL: <https://link.aps.org/doi/10.1103/PhysRevLett.71.1176>.
- [77] K. Teichmann, M. Wenderoth, S. Loth, R. G. Ulbrich, J. K. Garleff, A. P. Wijnheijmer, and P. M. Koenraad. “Controlled Charge Switching on a Single Donor with a Scanning Tunneling Microscope”. In: *Physical Review Letters* 101.7 (Aug. 15, 2008), p. 076103. DOI: [10.1103/PhysRevLett.101.076103](https://doi.org/10.1103/PhysRevLett.101.076103). URL: <https://link.aps.org/doi/10.1103/PhysRevLett.101.076103>.
- [78] Toan Trong Tran, Kerem Bray, Michael J. Ford, Milos Toth, and Igor Aharonovich. “Quantum emission from hexagonal boron nitride monolayers”. In: *Nature Nanotechnology* 11.1 (Jan. 2016), pp. 37–41. ISSN: 1748-3395. DOI: [10.1038/nnano.2015.242](https://doi.org/10.1038/nnano.2015.242). URL: <https://www.nature.com/articles/nnano.2015.242>.

- [79] L. J. Martínez, T. Pelini, V. Waselowski, J. R. Maze, B. Gil, G. Cassaboïs, and V. Jacques. “Efficient single photon emission from a high-purity hexagonal boron nitride crystal”. In: *Physical Review B* 94.12 (Sept. 22, 2016), p. 121405. DOI: [10.1103/PhysRevB.94.121405](https://doi.org/10.1103/PhysRevB.94.121405). URL: <https://link.aps.org/doi/10.1103/PhysRevB.94.121405>.
- [80] Toan Trong Tran, Christopher Elbadawi, Daniel Totonjian, Charlene J. Lobo, Gabriele Grosso, Hyowon Moon, Dirk R. Englund, Michael J. Ford, Igor Aharonovich, and Milos Toth. “Robust Multicolor Single Photon Emission from Point Defects in Hexagonal Boron Nitride”. In: *ACS Nano* 10.8 (Aug. 23, 2016), pp. 7331–7338. ISSN: 1936-0851. DOI: [10.1021/acsnano.6b03602](https://doi.org/10.1021/acsnano.6b03602). URL: <https://doi.org/10.1021/acsnano.6b03602>.
- [81] Zav Shotan, Harishankar Jayakumar, Christopher R. Consideine, Mažena Mackoït, Helmut Fedder, Jörg Wrachtrup, Audrius Alkauskas, Marcus W. Doherty, Vinod M. Menon, and Carlos A. Meriles. “Photoinduced Modification of Single-Photon Emitters in Hexagonal Boron Nitride”. In: *ACS Photonics* 3.12 (Dec. 21, 2016), pp. 2490–2496. DOI: [10.1021/acsp Photonics.6b00736](https://doi.org/10.1021/acsp Photonics.6b00736). URL: <https://doi.org/10.1021/acsp Photonics.6b00736>.
- [82] Nathan Chejanovsky, Mohammad Rezai, Federico Paolucci, Youngwook Kim, Torsten Rendler, Wafa Rouabeh, Felipe Fávaro de Oliveira, Patrick Herlinger, Andrej Denisenko, Sen Yang, Ilja Gerhardt, Amit Finkler, Jurgen H. Smet, and Jörg Wrachtrup. “Structural Attributes and Photodynamics of Visible Spectrum Quantum Emitters in Hexagonal Boron Nitride”. In: *Nano Letters* 16.11 (Nov. 9, 2016), pp. 7037–7045. ISSN: 1530-6984. DOI: [10.1021/acs.nanolett.6b03268](https://doi.org/10.1021/acs.nanolett.6b03268). URL: <https://doi.org/10.1021/acs.nanolett.6b03268>.
- [83] Nicholas R. Jungwirth, Brian Calderon, Yanxin Ji, Michael G. Spencer, Michael E. Flatté, and Gregory D. Fuchs. “Temperature Dependence of Wavelength Selectable Zero-Phonon Emission from Single Defects in Hexagonal Boron Nitride”. In: *Nano Letters* 16.10 (Oct. 12, 2016), pp. 6052–6057. ISSN: 1530-6984. DOI: [10.1021/acs.nanolett.6b01987](https://doi.org/10.1021/acs.nanolett.6b01987). URL: <https://doi.org/10.1021/acs.nanolett.6b01987>.
- [84] Annemarie L. Exarhos, David A. Hopper, Richard R. Grote, Audrius Alkauskas, and Lee C. Bassett. “Optical Signatures of Quantum Emitters in Suspended Hexagonal Boron Nitride”. In: *ACS Nano* 11.3 (Mar. 28, 2017), pp. 3328–3336. ISSN: 1936-0851. DOI: [10.1021/acsnano.7b00665](https://doi.org/10.1021/acsnano.7b00665). URL: <https://doi.org/10.1021/acsnano.7b00665>.
- [85] Gabriele Grosso, Hyowon Moon, Benjamin Lienhard, Sajid Ali, Dmitri K. Efetov, Marco M. Furchi, Pablo Jarillo-Herrero, Michael J. Ford, Igor Aharonovich, and Dirk Englund. “Tunable and high-purity room temperature single-photon emission from atomic defects in hexagonal boron nitride”. In: *Nature Communications* 8.1 (Sept. 26, 2017), pp. 1–8. ISSN: 2041-1723. DOI: [10.1038/s41467-017-00810-2](https://doi.org/10.1038/s41467-017-00810-2). URL: <https://www.nature.com/articles/s41467-017-00810-2>.

- [86] Annemarie L. Exarhos, David A. Hopper, Raj N. Patel, Marcus W. Doherty, and Lee C. Bassett. “Magnetic-field-dependent quantum emission in hexagonal boron nitride at room temperature”. In: *Nature Communications* 10.1 (Jan. 15, 2019), p. 222. ISSN: 2041-1723. DOI: [10.1038/s41467-018-08185-8](https://doi.org/10.1038/s41467-018-08185-8). URL: <https://www.nature.com/articles/s41467-018-08185-8>.
- [87] S. Reich, A. C. Ferrari, R. Arenal, A. Loiseau, I. Bello, and J. Robertson. “Resonant Raman scattering in cubic and hexagonal boron nitride”. In: *Physical Review B* 71.20 (May 4, 2005), p. 205201. DOI: [10.1103/PhysRevB.71.205201](https://doi.org/10.1103/PhysRevB.71.205201). URL: <https://link.aps.org/doi/10.1103/PhysRevB.71.205201>.
- [88] M. Nirmal, B. O. Dabbousi, M. G. Bawendi, J. J. Macklin, J. K. Trautman, T. D. Harris, and L. E. Brus. “Fluorescence intermittency in single cadmium selenide nanocrystals”. In: *Nature* 383.6603 (Oct. 1996), pp. 802–804. ISSN: 1476-4687. DOI: [10.1038/383802a0](https://doi.org/10.1038/383802a0). URL: <https://www.nature.com/articles/383802a0>.
- [89] Robert M. Dickson, Andrew B. Cubitt, Roger Y. Tsien, and W. E. Moerner. “On/off blinking and switching behaviour of single molecules of green fluorescent protein”. In: *Nature* 388.6640 (July 1997), pp. 355–358. ISSN: 1476-4687. DOI: [10.1038/41048](https://doi.org/10.1038/41048). URL: <https://www.nature.com/articles/41048>.
- [90] Sumin Choi, Brett C. Johnson, Stefania Castelletto, Cuong Ton-That, Matthew R. Phillips, and Igor Aharonovich. “Single photon emission from ZnO nanoparticles”. In: *Applied Physics Letters* 104.26 (June 30, 2014), p. 261101. ISSN: 0003-6951. DOI: [10.1063/1.4872268](https://doi.org/10.1063/1.4872268). URL: <https://aip.scitation.org/doi/full/10.1063/1.4872268>.
- [91] Jean Comtet, Evgenii Glushkov, Vytautas Navikas, Jiandong Feng, Vitaliy Babenko, Stephan Hofmann, Kenji Watanabe, Takashi Taniguchi, and Aleksandra Radenovic. “Wide-Field Spectral Super-Resolution Mapping of Optically Active Defects in Hexagonal Boron Nitride”. In: *Nano Letters* 19.4 (Apr. 10, 2019), pp. 2516–2523. ISSN: 1530-6984. DOI: [10.1021/acs.nanolett.9b00178](https://doi.org/10.1021/acs.nanolett.9b00178). URL: <https://doi.org/10.1021/acs.nanolett.9b00178>.
- [92] I. Aharonovich, S. Castelletto, D. A. Simpson, C.-H. Su, A. D. Greentree, and S. Praver. “Diamond-based single-photon emitters”. In: *Reports on Progress in Physics* 74.7 (June 2011), p. 076501. ISSN: 0034-4885. DOI: [10.1088/0034-4885/74/7/076501](https://doi.org/10.1088/0034-4885/74/7/076501). URL: <https://doi.org/10.1088/0034-4885/74/7/076501>.
- [93] C. Bradac, T. Gaebel, N. Naidoo, M. J. Sellars, J. Twamley, L. J. Brown, A. S. Barnard, T. Plakhotnik, A. V. Zvyagin, and J. R. Rabeau. “Observation and control of blinking nitrogen-vacancy centres in discrete nanodiamonds”. In: *Nature Nanotechnology* 5.5 (May 2010), pp. 345–349. ISSN: 1748-3395. DOI: [10.1038/nnano.2010.56](https://doi.org/10.1038/nnano.2010.56). URL: <https://www.nature.com/articles/nnano.2010.56>.
- [94] Toan Trong Tran, Cameron Zachreson, Amanuel Michael Berhane, Kerem Bray, Russell Guy Sandstrom, Lu Hua Li, Takashi Taniguchi, Kenji Watanabe, Igor Aharonovich, and Milos Toth. “Quantum Emission from Defects in Single-Crystalline Hexagonal Boron Nitride”. In: *Physical Review Applied* 5.3 (Mar. 10, 2016), p. 034005. DOI: [10.1103/PhysRevApplied.5.034005](https://doi.org/10.1103/PhysRevApplied.5.034005). URL: <https://link.aps.org/doi/10.1103/PhysRevApplied.5.034005>.



- [95] M. Jaros and S. F. Ross. “Calculations of impurity states in semiconductors: I”. In: *Journal of Physics C: Solid State Physics* 6.10 (May 1973), pp. 1753–1762. ISSN: 0022-3719. DOI: [10.1088/0022-3719/6/10/010](https://doi.org/10.1088/0022-3719/6/10/010). URL: <https://doi.org/10.1088/0022-3719/6/10/010>.
- [96] L. Rondin, G. Dantelle, A. Slablab, F. Grosshans, F. Treussart, P. Bergonzo, S. Perruchas, T. Gacoin, M. Chaigneau, H.-C. Chang, V. Jacques, and J.-F. Roch. “Surface-induced charge state conversion of nitrogen-vacancy defects in nanodiamonds”. In: *Physical Review B* 82.11 (Sept. 28, 2010), p. 115449. DOI: [10.1103/PhysRevB.82.115449](https://link.aps.org/doi/10.1103/PhysRevB.82.115449). URL: <https://link.aps.org/doi/10.1103/PhysRevB.82.115449>.
- [97] M. V. Hauf, B. Grotz, B. Naydenov, M. Dankerl, S. Pezzagna, J. Meijer, F. Jelezko, J. Wrachtrup, M. Stutzmann, F. Reinhard, and J. A. Garrido. “Chemical control of the charge state of nitrogen-vacancy centers in diamond”. In: *Physical Review B* 83.8 (Feb. 14, 2011), p. 081304. DOI: [10.1103/PhysRevB.83.081304](https://link.aps.org/doi/10.1103/PhysRevB.83.081304). URL: <https://link.aps.org/doi/10.1103/PhysRevB.83.081304>.
- [98] Bernhard Grotz, Moritz V. Hauf, Markus Dankerl, Boris Naydenov, Sébastien Pezzagna, Jan Meijer, Fedor Jelezko, Jörg Wrachtrup, Martin Stutzmann, Friedemann Reinhard, and Jose A. Garrido. “Charge state manipulation of qubits in diamond”. In: *Nature Communications* 3 (Mar. 6, 2012), p. 729. ISSN: 2041-1723. DOI: [10.1038/ncomms1729](https://www.nature.com/articles/ncomms1729). URL: <https://www.nature.com/articles/ncomms1729>.
- [99] C. Schreyvogel, V. Polyakov, R. Wunderlich, J. Meijer, and C. E. Nebel. “Active charge state control of single NV centres in diamond by in-plane Al-Schottky junctions”. In: *Scientific Reports* 5 (July 16, 2015), p. 12160. ISSN: 2045-2322. DOI: [10.1038/srep12160](https://www.nature.com/articles/srep12160). URL: <https://www.nature.com/articles/srep12160>.
- [100] Mandy L. Y. Sin, Vincent Gau, Joseph C. Liao, David A. Haake, and Pak Kin Wong. “Active Manipulation of Quantum Dots using AC Electrokinetics”. In: *The Journal of Physical Chemistry C* 113.16 (Apr. 23, 2009), pp. 6561–6565. ISSN: 1932-7447. DOI: [10.1021/jp9004423](https://doi.org/10.1021/jp9004423). URL: <https://doi.org/10.1021/jp9004423>.
- [101] Rodney Loudon. *The Quantum Theory of Light*. Google-Books-ID: AEkfajgql-doC. OUP Oxford, Sept. 7, 2000. 454 pp. ISBN: 978-0-19-158978-2.
- [102] R. Hanbury Brown and R. Q. Twiss. “LXXIV. A new type of interferometer for use in radio astronomy”. In: *The London, Edinburgh, and Dublin Philosophical Magazine and Journal of Science* 45.366 (July 1, 1954), pp. 663–682. ISSN: 1941-5982. DOI: [10.1080/14786440708520475](https://doi.org/10.1080/14786440708520475). URL: <https://doi.org/10.1080/14786440708520475>.
- [103] R. Hanbury Brown and R. Q. Twiss. “A Test of a New Type of Stellar Interferometer on Sirius”. In: *Nature* 178.4541 (Nov. 1956), pp. 1046–1048. ISSN: 1476-4687. DOI: [10.1038/1781046a0](https://www.nature.com/articles/1781046a0). URL: <https://www.nature.com/articles/1781046a0>.

- [104] Gerhard Rempe, Herbert Walther, and Norbert Klein. “Observation of quantum collapse and revival in a one-atom maser”. In: *Physical Review Letters* 58.4 (Jan. 26, 1987), pp. 353–356. DOI: [10.1103/PhysRevLett.58.353](https://doi.org/10.1103/PhysRevLett.58.353). URL: <https://link.aps.org/doi/10.1103/PhysRevLett.58.353>.
- [105] Th. Basché, W. E. Moerner, M. Orrit, and H. Talon. “Photon antibunching in the fluorescence of a single dye molecule trapped in a solid”. In: *Physical Review Letters* 69.10 (Sept. 7, 1992), pp. 1516–1519. DOI: [10.1103/PhysRevLett.69.1516](https://doi.org/10.1103/PhysRevLett.69.1516). URL: <https://link.aps.org/doi/10.1103/PhysRevLett.69.1516>.
- [106] Serge Reynaud. “La fluorescence de résonance : Etude par la méthode de l’atome habillé”. In: *Annales de Physique* 8 (1983), pp. 315–370. ISSN: 0003-4169, 1286-4838. DOI: [10.1051/anphys/198308080315](https://doi.org/10.1051/anphys/198308080315). URL: <https://www.annphys.org/articles/anphys/abs/1983/01/anphys19830808p315/anphys19830808p315.html>.
- [107] L. Fleury, J.-M. Segura, G. Zumofen, B. Hecht, and U. P. Wild. “Nonclassical Photon Statistics in Single-Molecule Fluorescence at Room Temperature”. In: *Physical Review Letters* 84.6 (Feb. 7, 2000), pp. 1148–1151. ISSN: 0031-9007, 1079-7114. DOI: [10.1103/PhysRevLett.84.1148](https://doi.org/10.1103/PhysRevLett.84.1148). URL: <https://link.aps.org/doi/10.1103/PhysRevLett.84.1148>.
- [108] Frank Diedrich and Herbert Walther. “Nonclassical radiation of a single stored ion”. In: *Physical Review Letters* 58.3 (Jan. 19, 1987), pp. 203–206. DOI: [10.1103/PhysRevLett.58.203](https://doi.org/10.1103/PhysRevLett.58.203). URL: <https://link.aps.org/doi/10.1103/PhysRevLett.58.203>.
- [109] A. Beveratos, S. Kühn, R. Brouri, T. Gacoin, J.-P. Poizat, and P. Grangier. “Room temperature stable single-photon source”. In: *The European Physical Journal D - Atomic, Molecular, Optical and Plasma Physics* 18.2 (Feb. 1, 2002), pp. 191–196. ISSN: 1434-6079. DOI: [10.1140/epjd/e20020023](https://doi.org/10.1140/epjd/e20020023). URL: <https://doi.org/10.1140/epjd/e20020023>.
- [110] Alexios Beveratos. “Sources à boîtes quantiques semiconductrices pour la nanophotonique et l’information quantique aux longueurs d’onde des télécommunications”. PhD thesis. Feb. 14, 2005. URL: <http://www.theses.fr/076117308>.
- [111] S. C. Kitson, P. Jonsson, J. G. Rarity, and P. R. Tapster. “Intensity fluctuation spectroscopy of small numbers of dye molecules in a microcavity”. In: *Physical Review A* 58.1 (July 1, 1998), pp. 620–627. DOI: [10.1103/PhysRevA.58.620](https://doi.org/10.1103/PhysRevA.58.620). URL: <https://link.aps.org/doi/10.1103/PhysRevA.58.620>.
- [112] Martin Berthel, Oriane Mollet, Géraldine Dantelle, Thierry Gacoin, Serge Huant, and Aurélien Drezet. “Photophysics of single nitrogen-vacancy centers in diamond nanocrystals”. In: *Physical Review B* 91.3 (Jan. 14, 2015), p. 035308. DOI: [10.1103/PhysRevB.91.035308](https://doi.org/10.1103/PhysRevB.91.035308). URL: <https://link.aps.org/doi/10.1103/PhysRevB.91.035308>.
- [113] *Igor Pro from WaveMetrics / Igor Pro by WaveMetrics*. URL: <https://www.wavemetrics.com/>.



- [114] E. Wu, Vincent Jacques, Heping Zeng, Philippe Grangier, François Treussart, and Jean-François Roch. “Narrow-band single-photon emission in the near infrared for quantum key distribution”. In: *Optics Express* 14.3 (Feb. 6, 2006), pp. 1296–1303. ISSN: 1094-4087. DOI: [10.1364/OE.14.001296](https://doi.org/10.1364/OE.14.001296). URL: <https://www.osapublishing.org/oe/abstract.cfm?uri=oe-14-3-1296>.
- [115] Niko Nikolay, Noah Mendelson, Ersan Özelci, Bernd Sontheimer, Florian Böhm, Günter Kewes, Milos Toth, Igor Aharonovich, and Oliver Benson. “Direct Measurement of Quantum Efficiency of Single Photon Emitters in Hexagonal Boron Nitride”. In: *arXiv:1904.08531 [cond-mat, physics:physics]* (Apr. 17, 2019). arXiv: [1904.08531](https://arxiv.org/abs/1904.08531). URL: <http://arxiv.org/abs/1904.08531>.
- [116] Nathan Chejanovsky, Amlan Mukherjee, Youngwook Kim, Andrej Denisenko, Amit Finkler, Takashi Taniguchi, Kenji Watanabe, Durga Bhaktavatsala Rao Dasari, Jurgen H Smet, and Jörg Wrachtrup. “Single spin resonance in a van der Waals embedded paramagnetic defect”. In: *arXiv:1901.05952 [cond-mat]* (), p. 22.
- [117] Sherif Abdulkader Tawfik, Sajid Ali, Marco Fronzi, Mehran Kianinia, Toan Trong Tran, Catherine Stampfl, Igor Aharonovich, Milos Toth, and Michael J. Ford. “First-principles investigation of quantum emission from hBN defects”. In: *Nanoscale* 9.36 (Sept. 21, 2017), pp. 13575–13582. ISSN: 2040-3372. DOI: [10.1039/C7NR04270A](https://doi.org/10.1039/C7NR04270A). URL: <https://pubs.rsc.org/en/content/articlelanding/2017/nr/c7nr04270a>.
- [118] Feng Wu, Andrew Galatas, Ravishankar Sundararaman, Dario Rocca, and Yuan Ping. “First-principles engineering of charged defects for two-dimensional quantum technologies”. In: *Physical Review Materials* 1.7 (Dec. 6, 2017), p. 071001. DOI: [10.1103/PhysRevMaterials.1.071001](https://doi.org/10.1103/PhysRevMaterials.1.071001). URL: <https://link.aps.org/doi/10.1103/PhysRevMaterials.1.071001>.
- [119] Mehdi Abdi, Jyh-Pin Chou, Adam Gali, and Martin B. Plenio. “Color Centers in Hexagonal Boron Nitride Monolayers: A Group Theory and Ab Initio Analysis”. In: *ACS Photonics* 5.5 (May 16, 2018), pp. 1967–1976. DOI: [10.1021/acsphotonics.7b01442](https://doi.org/10.1021/acsphotonics.7b01442). URL: <https://doi.org/10.1021/acsphotonics.7b01442>.
- [120] Koh Era, Fujio Minami, and Takashi Kuzuba. “Fast luminescence from carbon-related defects of hexagonal boron nitride”. In: *Journal of Luminescence* 24-25 (Nov. 1, 1981), pp. 71–74. ISSN: 0022-2313. DOI: [10.1016/0022-2313\(81\)90223-4](https://doi.org/10.1016/0022-2313(81)90223-4). URL: <http://www.sciencedirect.com/science/article/pii/0022231381902234>.
- [121] P. J. Dean. “Photoluminescence as a diagnostic of semiconductors”. In: *Progress in Crystal Growth and Characterization*. Special Issue on Characterization 5.1 (Jan. 1, 1982), pp. 89–174. ISSN: 0146-3535. DOI: [10.1016/0146-3535\(82\)90010-7](https://doi.org/10.1016/0146-3535(82)90010-7). URL: <http://www.sciencedirect.com/science/article/pii/0146353582900107>.

- [122] T. B. Hoffman, B. Clubine, Y. Zhang, K. Snow, and J. H. Edgar. “Optimization of Ni–Cr flux growth for hexagonal boron nitride single crystals”. In: *Journal of Crystal Growth*. The 19th American Conference on Crystal Growth and Epitaxy in conjunction with The 16th US Biennial Workshop on Organometallic Vapor Phase Epitaxy 393 (May 1, 2014), pp. 114–118. ISSN: 0022-0248. DOI: [10.1016/j.jcrysgr.2013.09.030](https://doi.org/10.1016/j.jcrysgr.2013.09.030). URL: <http://www.sciencedirect.com/science/article/pii/S0022024813006313>.
- [123] Song Liu, Rui He, Lianjie Xue, Jiahao Li, Bin Liu, and James H. Edgar. “Single Crystal Growth of Millimeter-Sized Monoisotopic Hexagonal Boron Nitride”. In: *Chemistry of Materials* 30.18 (Sept. 25, 2018), pp. 6222–6225. ISSN: 0897-4756. DOI: [10.1021/acs.chemmater.8b02589](https://doi.org/10.1021/acs.chemmater.8b02589). URL: <https://doi.org/10.1021/acs.chemmater.8b02589>.
- [124] T. Q. P. Vuong, S. Liu, A. Van der Lee, R. Cuscó, L. Artús, T. Michel, P. Valvin, J. H. Edgar, G. Cassabois, and B. Gil. “Isotope engineering of van der Waals interactions in hexagonal boron nitride”. In: *Nature Materials* 17.2 (Feb. 2018), pp. 152–158. ISSN: 1476-4660. DOI: [10.1038/nmat5048](https://doi.org/10.1038/nmat5048). URL: <https://www.nature.com/articles/nmat5048>.
- [125] Takashi Taniguchi and Kenji Watanabe. “Synthesis of high-purity boron nitride single crystals under high pressure by using Ba–BN solvent”. In: *Journal of Crystal Growth* 303.2 (May 15, 2007), pp. 525–529. ISSN: 0022-0248. DOI: [10.1016/j.jcrysgr.2006.12.061](https://doi.org/10.1016/j.jcrysgr.2006.12.061). URL: <https://www.sciencedirect.com/science/article/pii/S0022024807000486>.
- [126] C. Attaccalite, M. Bockstedte, A. Marini, A. Rubio, and L. Wirtz. “Coupling of excitons and defect states in boron-nitride nanostructures”. In: *Physical Review B* 83.14 (Apr. 29, 2011), p. 144115. DOI: [10.1103/PhysRevB.83.144115](https://doi.org/10.1103/PhysRevB.83.144115). URL: <https://link.aps.org/doi/10.1103/PhysRevB.83.144115>.
- [127] Luc Museur, Eduard Feldbach, and Andrei Kanaev. “Defect-related photoluminescence of hexagonal boron nitride”. In: *Physical Review B* 78.15 (Oct. 16, 2008), p. 155204. DOI: [10.1103/PhysRevB.78.155204](https://doi.org/10.1103/PhysRevB.78.155204). URL: <https://link.aps.org/doi/10.1103/PhysRevB.78.155204>.
- [128] *Welcome to Python.org*. Python.org. URL: <https://www.python.org/>.
- [129] *Leading Optical Product Design Software for Engineering Teams - Zemax*. URL: <https://www.zemax.com/>.
- [130] Tatiana Korona and Michał Chojecki. “Exploring point defects in hexagonal boron-nitrogen monolayers”. In: *International Journal of Quantum Chemistry* 119.14 (2019), e25925. ISSN: 1097-461X. DOI: [10.1002/qua.25925](https://doi.org/10.1002/qua.25925). URL: <https://onlinelibrary.wiley.com/doi/abs/10.1002/qua.25925>.
- [131] A. J. Stone and D. J. Wales. “Theoretical studies of icosahedral C<sub>60</sub> and some related species”. In: *Chemical Physics Letters* 128.5 (Aug. 1, 1986), pp. 501–503. ISSN: 0009-2614. DOI: [10.1016/0009-2614\(86\)80661-3](https://doi.org/10.1016/0009-2614(86)80661-3). URL: <http://www.sciencedirect.com/science/article/pii/0009261486806613>.

- [132] Ondrej L. Krivanek, Matthew F. Chisholm, Valeria Nicolosi, Timothy J. Pennycook, George J. Corbin, Niklas Dellby, Matthew F. Murfitt, Christopher S. Own, Zoltan S. Szilagyi, Mark P. Oxley, Sokrates T. Pantelides, and Stephen J. Pennycook. “Atom-by-atom structural and chemical analysis by annular dark-field electron microscopy”. In: *Nature* 464.7288 (Mar. 2010), pp. 571–574. ISSN: 1476-4687. DOI: [10.1038/nature08879](https://doi.org/10.1038/nature08879). URL: <https://www.nature.com/articles/nature08879>.
- [133] Mazena Mackoit-Sinkeviciene, Marek Maciaszek, Chris G. Van de Walle, and Audrius Alkauskas. “Carbon dimer defect as a source of the 4.1 eV luminescence in hexagonal boron nitride”. In: *arXiv:1907.02303 [cond-mat]* (July 4, 2019). arXiv: [1907.02303](https://arxiv.org/abs/1907.02303). URL: <http://arxiv.org/abs/1907.02303>.
- [134] X. Z. Du, J. Li, J. Y. Lin, and H. X. Jiang. “The origin of deep-level impurity transitions in hexagonal boron nitride”. In: *Applied Physics Letters* 106.2 (Jan. 12, 2015), p. 021110. ISSN: 0003-6951. DOI: [10.1063/1.4905908](https://doi.org/10.1063/1.4905908). URL: <https://aip.scitation.org/doi/abs/10.1063/1.4905908>.
- [135] Shigefusa F. Chichibu, Youichi Ishikawa, Hiroko Kominami, and Kazuhiko Hara. “Nearly temperature-independent ultraviolet light emission intensity of indirect excitons in hexagonal BN microcrystals”. In: *Journal of Applied Physics* 123.6 (Feb. 9, 2018), p. 065104. ISSN: 0021-8979. DOI: [10.1063/1.5021788](https://doi.org/10.1063/1.5021788). URL: <https://aip.scitation.org/doi/10.1063/1.5021788>.
- [136] Emi Tsushima, Takuya Tsujimura, and Takashi Uchino. “Enhancement of the deep-level emission and its chemical origin in hexagonal boron nitride”. In: *Applied Physics Letters* 113.3 (July 16, 2018), p. 031903. ISSN: 0003-6951. DOI: [10.1063/1.5038168](https://doi.org/10.1063/1.5038168). URL: <https://aip.scitation.org/doi/10.1063/1.5038168>.
- [137] L. Weston, D. Wickramaratne, M. Mackoit, A. Alkauskas, and C. G. Van de Walle. “Native point defects and impurities in hexagonal boron nitride”. In: *Physical Review B* 97.21 (June 18, 2018), p. 214104. DOI: [10.1103/PhysRevB.97.214104](https://doi.org/10.1103/PhysRevB.97.214104). URL: <https://link.aps.org/doi/10.1103/PhysRevB.97.214104>.
- [138] Manuel Cardona and M. L. W. Thewalt. “Isotope effects on the optical spectra of semiconductors”. In: *Reviews of Modern Physics* 77.4 (Nov. 7, 2005), pp. 1173–1224. DOI: [10.1103/RevModPhys.77.1173](https://doi.org/10.1103/RevModPhys.77.1173). URL: <https://link.aps.org/doi/10.1103/RevModPhys.77.1173>.
- [139] C. Chartrand, L. Bergeron, K. J. Morse, H. Riemann, N. V. Abrosimov, P. Becker, H.-J. Pohl, S. Simmons, and M. L. W. Thewalt. “Highly enriched  $^{28}\text{Si}$  reveals remarkable optical linewidths and fine structure for well-known damage centers”. In: *Physical Review B* 98.19 (Nov. 5, 2018), p. 195201. DOI: [10.1103/PhysRevB.98.195201](https://doi.org/10.1103/PhysRevB.98.195201). URL: <https://link.aps.org/doi/10.1103/PhysRevB.98.195201>.
- [140] Andreas Dietrich, Kay D Jahnke, Jan M Binder, Tokuyuki Teraji, Junichi Isoya, Lachlan J Rogers, and Fedor Jelezko. “Isotopically varying spectral features of silicon-vacancy in diamond”. In: *New Journal of Physics* 16.11 (Nov. 11, 2014), p. 113019. ISSN: 1367-2630. DOI: [10.1088/1367-2630/16/11/113019](https://doi.org/10.1088/1367-2630/16/11/113019). URL:

- <http://stacks.iop.org/1367-2630/16/i=11/a=113019?key=crossref.82aa49b97773b65bb6774d744bd5a404>.
- [141] Hisamitsu Akamaru, Akifumi Onodera, Tadashi Endo, and Osamu Mishima. “Pressure dependence of the optical-absorption edge of AlN and graphite-type BN”. In: *Journal of Physics and Chemistry of Solids* 63.5 (May 1, 2002), pp. 887–894. ISSN: 0022-3697. DOI: [10.1016/S0022-3697\(01\)00244-X](https://doi.org/10.1016/S0022-3697(01)00244-X). URL: <http://www.sciencedirect.com/science/article/pii/S002236970100244X>.
- [142] A. Segura, R. Cuscó, T. Taniguchi, K. Watanabe, G. Cassaboïs, B. Gil, and L. Artús. “High-Pressure Softening of the Out-of-Plane A<sub>2u</sub>(Transverse-Optic) Mode of Hexagonal Boron Nitride Induced by Dynamical Buckling”. In: *The Journal of Physical Chemistry C* 123.28 (July 18, 2019), pp. 17491–17497. ISSN: 1932-7447. DOI: [10.1021/acs.jpcc.9b04582](https://doi.org/10.1021/acs.jpcc.9b04582). URL: <https://doi.org/10.1021/acs.jpcc.9b04582>.
- [143] S. Meuret, L. H. G. Tizei, T. Cazimajou, R. Bourrellier, H. C. Chang, F. Treussart, and M. Kociak. “Photon Bunching in Cathodoluminescence”. In: *Physical Review Letters* 114.19 (May 11, 2015), p. 197401. DOI: [10.1103/PhysRevLett.114.197401](https://doi.org/10.1103/PhysRevLett.114.197401). URL: <https://link.aps.org/doi/10.1103/PhysRevLett.114.197401>.
- [144] Alberto Zobelli, Steffi Y. Woo, Luiz H. G. Tizei, Nathalie Brun, Anna Tararan, Xiaoyan Li, Odile Stéphan, Mathieu Kociak, and Marcel Tencé. “Spatial and spectral dynamics in STEM hyperspectral imaging using random scan patterns”. In: *arXiv:1909.07842 [cond-mat, physics:physics]* (Sept. 17, 2019). arXiv: [1909.07842](https://arxiv.org/abs/1909.07842). URL: <http://arxiv.org/abs/1909.07842>.
- [145] Sumin Choi, Toan Trong Tran, Christopher Elbadawi, Charlene Lobo, Xuewen Wang, Saulius Juodkazis, Gediminas Seniutinas, Milos Toth, and Igor Aharonovich. “Engineering and Localization of Quantum Emitters in Large Hexagonal Boron Nitride Layers”. In: *ACS Applied Materials & Interfaces* 8.43 (Nov. 2, 2016), pp. 29642–29648. ISSN: 1944-8244. DOI: [10.1021/acsami.6b09875](https://doi.org/10.1021/acsami.6b09875). URL: <https://doi.org/10.1021/acsami.6b09875>.
- [146] X. T. Zou and L. Mandel. “Photon-antibunching and sub-Poissonian photon statistics”. In: *Physical Review A* 41.1 (Jan. 1, 1990), pp. 475–476. DOI: [10.1103/PhysRevA.41.475](https://doi.org/10.1103/PhysRevA.41.475). URL: <https://link.aps.org/doi/10.1103/PhysRevA.41.475>.
- [147] A. Migdall, S. V. Polyakov, J. Fan, J. C. Bienfang. *Single-Photon Generation and Detection: Physics and Applications*. Vol. 45. Experimental methods in the physical sciences. Google-Books-ID: gERMqvh2OjAC. Academic Press, Nov. 29, 2013. 593 pp. ISBN: 978-0-12-387696-6.
- [148] Cécile DeWitt-Morette, A Blandin, and Claude Cohen-Tannoudji. *Optique et électronique quantiques: quantum optics and electronics : lectures delivered at Les Houches during the 1964 session of the Summer School of Theoretical Physics University of Grenoble*. OCLC: 1103630647. New York: Gordon and Breach, 1965.